

# Probing the Inner Accretion Flow Properties Around Black Holes with X-ray Observations

Thesis by  
Yanjun Xu

In Partial Fulfillment of the Requirements for the  
Degree of  
Doctor of Philosophy

The logo for the California Institute of Technology (Caltech), featuring the word "Caltech" in a bold, orange, sans-serif font.

CALIFORNIA INSTITUTE OF TECHNOLOGY  
Pasadena, California

2021  
Defended May 19, 2021

© 2021

Yanjun Xu

ORCID: 0000-0003-2443-3698

All rights reserved except where otherwise noted.

## ACKNOWLEDGEMENTS

First and foremost, I would like to express gratitude to my parents and grandparents for being extra supportive of me in all aspects of my life, allowing entire freedom for me to explore and pursue paths that I have been interested in ever since my childhood. And special thanks to my mom for being my best friend, and being always interested in my work although she probably would not pay much attention to astrophysics otherwise.

I am sincerely grateful to my Ph.D. advisor Prof. Fiona Harrison for her guidance and support of me through my years in graduate school, and for her always being a open-minded and inclusive resource to talk to and discuss scientific problems with. I am also eternally grateful for her constant determination and efforts to lead me to become a confident and independent researcher.

I am very grateful to Prof. Jon Miller, Prof. Andy Fabian, and Dr. John Tomsick for carefully reading my papers, always offering insightful and helpful comments and discussions, and being supportive of me to pursue a scientific career. My thanks also go to everyone else in the *NuSTAR* team at Caltech, from whom I learned a lot when working with them, especially to Dr. Karl Froster for helping schedule my *NuSTAR* observations. And I want to thank Dr. Dominic Walton, Dr. Mislav Baloković, Dr. Lian Tao, Dr. Felix Fürst, and Dr. Murray Brightman for teaching me about the basics of X-ray data analysis at the start of my Ph.D. I thank Prof. Phil Hopkins, Prof. Chris Martin, and Prof. Alan Weinstein for serving on my thesis committee and providing helpful advice. And I am grateful to my undergraduate research advisors Prof. Tinggui Wang and Prof. Linqing Wen for inspiring my interest in high energy astrophysics and continuing to offer me valuable advice over the years.

I am lucky to have many supportive friends, Xiangcheng Ma, Xinghao Zhou, Songming Du, Feng Bi, Dan Zhou, and Sanle Hu among others, at Caltech from the beginning of my graduate study. Many thanks to them for kindly picking me up from the airport on my first day at Caltech, helping me settle into the new environment, and taking me out for dinner every weekend for almost two years until I earned the skill to drive in LA traffic (and helping with that too). And thanks to Jamie Rankin, Aaron Pearlman, Matt Hartley, and Sean Pike for being my good office mates for many years.

Last, I hold sincere gratitude to the faculty and staff at Caltech for undertaking tireless administrative efforts to make student life as normal as possible during the COVID-19 period, without which this thesis could not have been finished in time. I also hold sincere gratitude to anyone continuing their hard work during this unprecedentedly difficult time, of which I may be aware or not, to keep our everyday life going and strengthen our faith in the good sides of humanity despite all the uncertainties in life.

## ABSTRACT

Accretion, governed by gravity, is a fundamental source of energy in the universe. Accretion is important to the growth and evolution of black holes, as well as the structure in the universe on larger scales. Accretion disks around supermassive black holes are likely to have produced most of the ionizing radiation in the universe since the epoch of reionization. Outflows launched from the accretion disk of black holes, either in the form of disk winds or jets, provide a feedback mechanism that plays an important role in the co-evolution of black holes and their host galaxies. It has been decades since the fundamental theories about black hole accretion were established. Black hole accretion has been widely studied in active galactic nuclei (AGNs) and black hole binaries ever since the early days of X-ray astronomy. However, important questions still remain regarding the fundamental physical properties of black holes, the structure and geometry of accretion disks and coronae, and the nature of disk winds and jets.

In this thesis, I report results from recent X-ray observations of an ultra-luminous infrared galaxy with a central AGN, IRAS 05189–2524, and several black hole X-ray binaries (or black hole candidates for those currently lacking dynamical mass determinations), IGR J17091–3624, MAXI J1535–571, Swift J1658.2–4242, MAXI J1631–479, and MAXI J1820+070. Most of the black hole X-ray binaries studied in this thesis were uncatalogued sources and were discovered as bright Galactic X-ray transients over the past few years, offering great opportunities for investigating black hole accretion with high quality datasets. The launch of the *NuSTAR* telescope in 2012 has brought the advanced capabilities of performing high sensitivity observations in the hard X-ray band and remaining free from pile-up for bright Galactic sources, providing new angles for the detailed study of observational phenomena around both supermassive and stellar-mass accreting black holes. I study the inner accretion flow properties around black holes in the above objects by conducting spectral and timing analyses of the *NuSTAR* observations and the simultaneous soft X-ray band data from the *Swift* or *XMM-Newton* telescope. I have searched for and analyzed various accretion related observational features in these systems (disk reflection spectra, ionized absorption caused by disk winds, quasi periodic oscillations (QPOs) in the X-ray light curves, and unusual aperiodic flux variations or accretion state changes), and interpret the results in terms of the physical properties about the inner accretion flows and the central black holes.

By modeling the relativistic disk reflection spectra, I have found that the inner edge of the optically-thick accretion disk is truncated in IGR J17091–3624 during the bright hard state, in MAXI J1631–479 during the very high state, and in MAXI J1820+070 during the faint hard state, whereas the inner accretion disk is consistent with extending down to the ISCO in MAXI J1535–571 and Swift J1658.2–4242 during their bright hard states, and in MAXI J1631–479 during its soft state. Based on all the observational evidence gathered in this thesis, the general picture about the accretion flow geometry at different accretion states seems to be more complicated than that from previously well accepted theoretical predictions. In addition, I have measured the black holes spins and inner accretion disk inclinations for IRAS 05189–2524, MAXI J1535–571, Swift J1658.2–4242, and MAXI J1631–479 using the disk reflection modeling method, where the central black holes are all found to be rapidly spinning. There are also evidence for strong disk winds detected in the X-ray spectra of some of the objects studied in this thesis with interesting implications. I summarize my studies of these individual objects at the end of this thesis in a more broader context of the characteristic behaviors of the population and their general physical implications, and discuss about the possibilities of extending my research in this direction with the upcoming new X-ray missions.

## PUBLISHED CONTENT AND CONTRIBUTIONS

Xu Y., Harrison F. A., Tomsick J. A., Hare J. et al. (2020). “Evidence for Disk Truncation at Low Accretion States of the Black Hole Binary MAXI J1820+070 Observed by *NuSTAR* and *XMM-Newton*.” *The Astrophysical Journal*, 893(1): 42. doi: 10.3847/1538–4357/ab7cdb.

Y.X. participated in the conception of the project, proposed for the observations, analyzed the data, and wrote the manuscript.

Xu Y., Harrison F. A., Tomsick J. A., Walton D. J. et al. (2020). “Studying the Reflection Spectra of the New Black Hole X-Ray Binary Candidate MAXI J1631–479 Observed by *NuSTAR*.” *The Astrophysical Journal*, 893(1):30. doi: 0.3847/1538–4357/ab7dc0.

Y.X. participated in the conception of the project, proposed for the observations, analyzed the data, and wrote the manuscript.

Xu Y., Harrison F. A., Tomsick J. A., Barret D. et al. (2019). “Broadband X-Ray Spectral and Timing Analyses of the Black Hole Binary Candidate Swift J1658.2–4242: Rapid Flux Variation and the Turn-on of a Transient QPO.” *The Astrophysical Journal*, 879(2):93. doi: 0.3847/1538–4357/ab24bf.

Y.X. participated in the conception of the project, proposed for the observations, performed data analyses, provided physical interpretation of the results, and wrote the manuscript.

Xu Y., Harrison F. A., Kennea J. A., Walton D. J. et al. (2018). “The Hard State of the Highly Absorbed High Inclination Black Hole Binary Candidate Swift J1658.2–4242 Observed by *NuSTAR* and *Swift*.” *The Astrophysical Journal*, 865(1):18. doi: 0.3847/1538–4357/aada03.

Y.X. participated in the conception of the project, proposed for the observations, analyzed the data, and wrote the manuscript.

Xu Y., Harrison F. A., García J. A., Fabian A. C. et al. (2018). “Reflection Spectra of the Black Hole Binary Candidate MAXI J1535–571 in the Hard State Observed by *NuSTAR*.” *The Astrophysical Journal Letters*, 852(2):L34. doi: 10.3847/2041–8213/aaa4b2.

Y.X. participated in the conception of the project, analyzed the data, and wrote the manuscript.

Xu Y., García J. A., Fürst F., Harrison F. A. (2017). “Spectral and Timing Properties of IGR J17091–3624 in the Rising Hard State During Its 2016 Outburst.” *The Astrophysical Journal*, 851(2):103. doi: 0.3847/1538–4357/aa9ab4.

Y.X. participated in the conception of the project, analyzed the data, and wrote the manuscript.

Xu Y., Baloković M., Walton D. J., Harrison F. A. et al. (2017). “Evidence for Relativistic Disk Reflection in the Seyfert 1h Galaxy/ULIRG IRAS 05189–2524 Observed by *NuSTAR* and *XMM-Newton*.” *The Astrophysical Journal*, 837(1):21. doi: 0.3847/1538–4357/aa5df4.

Y.X. participated in the conception of the project, analyzed the data, and wrote the manuscript.

# TABLE OF CONTENTS

<b>Acknowledgements</b> . . . . .	iii
<b>Abstract</b> . . . . .	v
<b>Published Content and Contributions</b> . . . . .	vii
<b>Table of Contents</b> . . . . .	ix
<b>List of Illustrations</b> . . . . .	xi
<b>List of Tables</b> . . . . .	xiv
<b>Chapter I: Introduction</b> . . . . .	1
1.1 High Energy Astrophysics in the X-ray Waveband . . . . .	1
1.2 Black Hole Systems as X-ray Sources . . . . .	2
1.3 Investigating the Inner Accretion Flow Properties around Black Holes via X-ray Spectral and Timing Analyses . . . . .	15
1.4 Thesis Outline . . . . .	23
<b>Chapter II: Evidence for Relativistic Disk Reflection in the Seyfert 1h Galaxy/ULIRG IRAS 05189–2524 Observed by <i>NuSTAR</i> and <i>XMM-Newton</i></b> . . . . .	25
2.1 Introduction . . . . .	25
2.2 Data Reduction . . . . .	27
2.3 Spectral Analysis . . . . .	28
2.4 Discussion . . . . .	36
2.5 Summary and Conclusion . . . . .	40
<b>Chapter III: Spectral and Timing Properties of IGR J17091–3624 in the Rising Hard State During its 2016 Outburst</b> . . . . .	42
3.1 Introduction . . . . .	42
3.2 Observations and Data Reduction . . . . .	44
3.3 Analysis . . . . .	47
3.4 Discussion . . . . .	60
3.5 Summary and Conclusion . . . . .	67
<b>Chapter IV: Reflection Spectra of the Black Hole Binary Candidate MAXI J1535–571 in the Hard State Observed by <i>NuSTAR</i></b> . . . . .	69
4.1 Introduction . . . . .	69
4.2 Observation and Data Reduction . . . . .	71
4.3 Spectral Modeling . . . . .	71
4.4 Discussion and Conclusions . . . . .	79
<b>Chapter V: The Hard State of the Highly Absorbed High Inclination Black Hole Binary Candidate Swift J1658.2–4242 Observed by <i>NuS- TAR</i> and <i>Swift</i></b> . . . . .	82
5.1 Introduction . . . . .	83
5.2 Observations and Data Reduction . . . . .	84
5.3 Light Curves . . . . .	85

5.4 Spectral Analysis . . . . .	87
5.5 Low-frequency QPO . . . . .	97
5.6 Discussion . . . . .	99
<b>Chapter VI: Broadband X-ray Spectral and Timing Analyses of the Black Hole Binary Candidate Swift J1658.2–4242: Rapid Flux Variation and the Turn-on of a Transient QPO . . . . .</b>	<b>102</b>
6.1 Introduction . . . . .	103
6.2 Observations and Data Reduction . . . . .	105
6.3 Variability . . . . .	107
6.4 Spectral Analysis . . . . .	113
6.5 Discussion . . . . .	121
6.6 Summary . . . . .	128
<b>Chapter VII: Studying the Reflection Spectra of the New Black Hole X-Ray Binary Candidate MAXI J1631–479 Observed by <i>NuSTAR</i>: A Variable Broad Iron Line Profile . . . . .</b>	<b>130</b>
7.1 Introduction . . . . .	131
7.2 Observations and Data Reduction . . . . .	132
7.3 Spectral Modeling . . . . .	135
7.4 Discussion . . . . .	148
7.5 Conclusion . . . . .	155
<b>Chapter VIII: Evidence for Disk Truncation at Low Accretion States of the Black Hole Binary MAXI J1820+070 Observed by <i>NuSTAR</i> and <i>XMM-Newton</i> . . . . .</b>	<b>157</b>
8.1 Introduction . . . . .	157
8.2 Observation and Data Reduction . . . . .	159
8.3 Spectral Analysis . . . . .	161
8.4 Timing Analysis . . . . .	167
8.5 Discussion and Conclusion . . . . .	167
<b>Chapter IX: Summary and Future Prospects . . . . .</b>	<b>174</b>
9.1 Summary of Previous Research . . . . .	174
9.2 Future Prospects . . . . .	180
<b>Bibliography . . . . .</b>	<b>188</b>

## LIST OF ILLUSTRATIONS

<i>Number</i>	<i>Page</i>
1.1 AGN SED and schematic representation of AGN structures. . . . .	6
1.2 SED of Cygnus X-1 and schematic representation of the structure of a black hole X-ray binary. . . . .	9
1.3 Representative X-ray spectra of an AGN and a black hole X-ray binary.	10
1.4 Representative spectral and timing properties of a black hole X-ray binary during different accreting states. . . . .	12
1.5 A schematic representation of the disk-jet coupling model in a black hole X-ray binary. . . . .	13
1.6 An illustration of the physical mechanisms shaping the broad Fe $K\alpha$ line with the broad Fe $K\alpha$ emission line and narrow disk wind ab- sorption features observed in an AGN. . . . .	18
1.7 A schematic presentation of the measurement of the spin of a black hole based on the relativistic disk reflection spectrum. . . . .	19
1.8 A schematic diagram of the disk truncation model for black hole X- ray binaries and AGNs at different mass accretion rates. . . . .	20
2.1 Spectral fitting of IRAS 05189–2524 with the phenomenological re- flection model. . . . .	30
2.2 Possible absorption features in the residuals of the absorbed power- law model. . . . .	31
2.3 Spectral fitting of IRAS 05189–2524 with self-consistent disk reflec- tion models. . . . .	35
2.4 Constraints on the black hole spin of IRAS 05189–2524 from spec- tral modeling. . . . .	38
2.5 Spectral residuals of the absorption-dominated models. . . . .	39
3.1 <i>Swift</i> monitoring of the 2016 outburst of IGR J17091–3624. . . . .	45
3.2 IGR J17091–3624 spectra observed by <i>NuSTAR</i> modeled with the absorbed power-law model. . . . .	48
3.3 Residuals of the IGR J17091–3624 spectra from the unblurred re- flection model. . . . .	50
3.4 IGR J17091–3624 spectra with the best-fit models. . . . .	51

3.5	Constraints of the inner disk radius in IGR J17091–3624 from spectral modeling. . . . .	52
3.6	<i>NuSTAR</i> CPDS of IGR J17091–3624 with best-fit models in the $\nu P_\nu$ representation. . . . .	57
3.7	<i>NuSTAR</i> CPDS of IGR J17091–3624 generated in two energy intervals. . . . .	58
3.8	Relation of spectral and timing properties with the source flux. . . . .	62
3.9	The relation of the inner disk radius measured from spectral modeling with that inferred from QPO. . . . .	66
4.1	MAXI and Swift/BAT monitoring light curves of MAXI J1535–571. . . . .	72
4.2	<i>NuSTAR</i> spectra of MAXI J1535–571 in the hard state. . . . .	73
4.3	Ratio plots of the reflection modeling and the best fit model. . . . .	76
4.4	$\Delta\chi^2$ plots for the black hole spin and the inner accretion disk radius from spectral modeling. . . . .	78
5.1	<i>Swift</i> monitoring of the outburst of Swift J1658.2–4242. . . . .	86
5.2	<i>NuSTAR</i> light curves and hardness ratios of Swift J1658.2–4242. . . . .	87
5.3	<i>NuSTAR</i> spectra of Swift J1658.2–4242 during the hard state. . . . .	89
5.4	Broad-band X-ray spectra of Swift J1658.2–4242 with the best-fit model. . . . .	91
5.5	Constraints of the velocity shift of the ionized absorber. . . . .	94
5.6	The dipping spectra of Swift J1658.2–4242 compared with the persistent spectra. . . . .	96
5.7	Power spectrum of Swift J1658.2–4242 from the <i>NuSTAR</i> observation with the QPO. . . . .	98
6.1	Long term <i>Swift</i> light curves and HID of Swift J1658.2–4242. . . . .	106
6.2	X-ray light curves of Swift J1658.2–4242 from the joint <i>NuSTAR</i> and <i>XMM-Newton</i> observations. . . . .	108
6.3	Dynamical <i>NuSTAR</i> power spectrum of Swift J1658.2–4242. . . . .	110
6.4	Time-averaged power spectra of Swift J1658.2–4242 in the intermediate state. . . . .	112
6.5	<i>NuSTAR</i> spectra of Swift J1658.2–4242 during the intermediate state. . . . .	115
6.6	The broadband X-ray spectra of Swift J1658.2–4242 in the intermediate state with best-fit models. . . . .	119
7.1	MAXI and <i>Swift</i> /BAT monitoring light curves of MAXI J1631–479. . . . .	133
7.2	<i>NuSTAR</i> spectra of MAXI J1631–479 in the disk dominant and the power-law dominant state. . . . .	137
7.3	Variations in the profile and the strength of the Fe $K\alpha$ line. . . . .	138

7.4	<i>NuSTAR</i> spectra of MAXI J1631–479 with the best-fit models. . . . .	141
7.5	Broad iron line profiles of MAXI J1631–479 observed during the disk dominant state corrected for narrow absorption and emission features. . . . .	145
7.6	Constraints of the black hole spin parameter and inner accretion disk radius. . . . .	150
8.1	Long-term <i>Swift</i> monitoring light curve of the outburst of MAXI J1820+070. . . . .	160
8.2	<i>NuSTAR</i> and <i>XMM-Newton</i> spectra of the MAXI J1820+070 in the LHS. . . . .	163
8.3	Confidence contours of the inner disk radius and the disk inclination. . . . .	166
8.4	<i>NuSTAR</i> and <i>XMM-Newton</i> PSD of MAXI J1820+070 in the LHS. . . . .	168
8.5	A comparison of the Fe $K\alpha$ line profile of MAXI J1820+070 observed at different epochs, and the evolution of the inner accretion disk radius with the Eddington ratio. . . . .	169
9.1	Schematic illustrations of a wobbling jet and a warped accretion disk. . . . .	181
9.2	The effective areas of high-resolution X-ray spectroscopy instruments aboard currently operating and future X-ray missions. . . . .	183
9.3	Example Fe $K\alpha$ emission line profiles arising from warped accretion disks. . . . .	185

## LIST OF TABLES

<i>Number</i>	<i>Page</i>
2.1 Spectral models used to fit IRAS 05189–2524 . . . . .	29
2.2 Spectral fitting of IRAS 05189–2524 : Part I. . . . .	31
2.3 Spectral fitting of IRAS 05189–2524 : Part II. . . . .	34
3.1 <i>NuSTAR</i> and simultaneous <i>Swift</i> observations of IGR J17091–3624. . . . .	46
3.2 Best-fit parameters of the disk reflection models. . . . .	55
3.3 Fitting results of <i>NuSTAR</i> CPDS in different energy bands. . . . .	59
4.1 Best-fit model parameters of MAXI J1535–571. . . . .	75
5.1 Spectral fitting of Swift J1658.2–4242 in the hard state. . . . .	90
6.1 Power spectra properties of Swift J1658.2–4242. . . . .	111
6.2 Spectral fitting results of Swift J1658.2–4242: Part I. . . . .	116
6.3 Spectral fitting results of Swift J1658.2–4242: Part II. . . . .	123
7.1 <i>NuSTAR</i> observations of MAXI J1631–479. . . . .	134
7.2 Spectral fitting of MAXI J1631–479 (disk dominant state). . . . .	143
7.3 Spectral fitting of MAXI J1631–479 (power-law dominant state). . . . .	147
8.1 Energy spectral parameters of MAXI J1820+070 in the LHS. . . . .	164

*Chapter 1*

## INTRODUCTION

**1.1 High Energy Astrophysics in the X-ray Waveband**

I begin this thesis by some historical notes of X-ray astronomy. X-ray astronomy started after World War II when military rockets got repurposed to lift radiation detectors above the atmosphere. The atmosphere of the Earth is opaque to X-rays due to photoelectric absorption by the atoms in the molecular gases. The first extrasolar X-ray source was detected in 1962 during a rocket flight by a team led by Riccardo Giacconi in the constellation of Scorpius, Sco X-1. Before that, X-ray observations were expected to focus on the study of active stars, with fluxes scaled from that of the solar corona, the only known X-ray source then. Sco X-1 was later confirmed to be an accreting neutron star fed by a companion star, continuing to be the brightest persistent extrasolar X-ray source nowadays only briefly outshone by bright X-ray transients. The X-ray sky was systematically explored by the first dedicated X-ray astronomy satellite *Uhuru* launch in 1970. Among *Uhuru* discoveries include the detections of X-ray pulsations in Cen X-3 and Her X-1 (therefore probably many of the most luminous galactic sources are neutron star X-ray binaries), extended X-ray emission from galaxy clusters, and the identification of Cygnus X-1 and its recognition as the first strong candidate to contain a black hole. The early days of explorations in the 60s and 70s established X-ray astronomy as a major branch of astrophysics, showing that the X-ray band is rich for astrophysical study in light of the detections of supernova remnants, nearby radio galaxies, highly variable stellar X-ray sources, and the diffuse X-ray background.

X-rays typically refer to photons in the energy range of 0.1–100 keV, further divided into soft (below 10 keV) and hard (above 10 keV) X-ray bands. The fundamental distinction between soft and hard X-rays can be understood from the basic property of normal solids. Typical atomic spacings in solids are  $\sim 1\text{\AA}$ , the distance when interpreted as a wavelength corresponds to photons with the energy of  $\sim 10\text{ keV}$ . It is therefore difficult to make materials that reflect hard X-ray photons and focus hard X-rays. The early type of technology used for X-ray astronomy are the non-imaging, collimated proportional counters. While having a large collecting area, such instruments also suffered from large background rates, both due to particles

and X-ray emission from objects other than the intended targets, and hence had limited sensitivities. They are therefore suitable for the study of bright X-ray sources (of order  $10^{-11}$  erg cm $^{-2}$  s $^{-1}$  or higher), usually nearby Galactic targets. Imaging X-ray telescopes with CCD detectors, the operating *XMM-Newton* and *Chandra* telescopes can reach flux levels below  $10^{-14}$  erg cm $^{-2}$  s $^{-1}$  in the 0.3–10 keV band, good for detecting and spatially resolving extragalactic sources. And for X-rays above 10 keV, given that it is difficult to focus hard X-ray photons, one successful alternative is to use coded mask aperture. Instruments based on this technology, such as the present *INTEGRAL* and Burst Alert Telescope (BAT) aboard *Swift*, typically have a large field of view and localization can be achieved to several arcminutes after specialized processing. More recently, X-ray focusing telescope technology has been extended to hard X-rays by multi-layer coating on *NuSTAR*, which uses CZT detectors.

This thesis is made up of X-ray spectral and timing studies of several stellar-mass black holes in our Galaxy and one extragalactic supermassive black hole. I use data from pointed observations by the *Nuclear Spectroscopic Telescope Array (NuSTAR)*, which is the first focusing hard X-ray telescope and thus reaching unprecedently high sensitivity in the hard X-ray band of 3–79 keV (Harrison et al., 2013). To achieve a broad X-ray band coverage, simultaneous X-ray observations of *XMM-Newton* (Jansen et al., 2001) or *Swift* (Gehrels et al., 2004) were scheduled. The EPIC instrument aboard *XMM-Newton* (Strüder et al., 2001; Turner et al., 2001) and XRT aboard *Swift* (Burrows et al., 2005) cover the energy band of 0.2–10 keV. And thanks to the wide field X-ray monitoring capabilities of *Swift*/BAT (Krimm et al., 2013) in hard X-rays and MAXI (Matsuoka et al., 2009) in soft X-rays, several new black hole transients were found in our Galaxy during the past few years, which formed the majority of the targets investigated in this thesis.

## 1.2 Black Hole Systems as X-ray Sources

Black holes, while themselves are black, become powerful engines outstandingly bright in X-rays when undergoing accretion. Accreting powered black holes are the most luminous long-lived objects of radiation in the universe. The accretion process heats up the gas falling into the black holes to exceedingly high temperatures producing X-ray emission, forming a circumstellar disk structure around the central engines. Therefore, the studies regarding black holes using X-ray observations are essentially focused on the studies of the accretion flow properties around black

holes, bearing certain implications regarding the nature of the black holes and the co-evolution relationship of the black holes with their larger environments.

X-ray is known as one of the most efficient electromagnetic wavelengths to discover and study black holes. In the X-ray band, black holes have been confidently detected in two mass ranges, i.e., stellar mass black holes ( $\sim 5\text{--}30 M_{\odot}$ ), and supermassive black holes ( $\sim 10^5\text{--}10^{10} M_{\odot}$ ). Observational studies of accreting black holes have been widely conducted on these two mass scales, the former mostly found in black hole X-ray binaries, and the latter mostly detected as active galactic nuclei (AGNs) lying in the center of large galaxies. In the Milky Way, most known black hole X-ray binaries were discovered as X-ray novae, they go into recurrent outbursts due to thermal-viscous instabilities in the accretion disk (Frank et al., 2002), with the total rate of  $\sim 2\text{--}3$  outbursts per year. And Cygnus X-1, being the first source widely accepted to be a black hole, is still the only confirmed persistent black hole X-ray binary in our Galaxy. There are currently about 60 known Galactic black hole X-ray binaries (including black hole candidates), the number is slowly increasing with new X-ray transients discovered by wide-field monitoring X-ray telescopes (Corral-Santana et al., 2016). Limited by the capability of the current generation of telescopes, the study of black hole X-ray binaries are heavily concentrated on Galactic sources, and only several extragalactic counterparts in nearby galaxies may be considered as nearly equally well studied, e.g., LMC X-1, M33 X-7. Therefore, we probably still do not have enough evidence (or at least the potential to obtain much more information!) to tell how different the two populations really are, or to answer the question of what kind of impacts the galactic environment have on these stellar mass black holes. It might be an intriguing subject as we gain better abilities to discover, resolve, and perform followup observations of these extragalactic black hole X-ray transients in the future with advances in instrumentation. Due to their high luminosities, the study of AGNs have been more versatile. AGNs has been widely studied in the X-ray band through systematical surveys of focusing X-ray telescopes, from the local universe to the current record of the most distant AGNs detected to the redshift of  $z \sim 7$  (Page et al., 2014; Bañados et al., 2018), and thus they are believed to be promising probes of some important cosmological problems (see the references in e.g., Hickox & Alexander, 2018).

There have also been efforts to detect intermediate-mass black holes ( $\sim 10^2\text{--}10^5 M_{\odot}$ ), which are believed to fill the gap between the two classes and have important implications about the black hole formation channels. But definite evidence for the

existence of intermediate-mass black holes have been scarce. Comparatively, the most convincing case so far is the recent gravitational wave event GW190521 detected by LIGO, caused by the merger of two black holes, weighing  $85 M_{\odot}$  and  $65 M_{\odot}$ , with the resulting black hole weighing  $142 M_{\odot}$  (Abbott et al., 2020a). Beforehand, the most promising candidates for intermediate-mass black holes consist of HLX-1 in the galaxy ESO 243–49 (Farrell et al., 2009), and some of the brightest ultra-luminous X-ray sources (ULXs), i.e., M82 X-1 (Matsumoto et al., 2001), which become obvious targets of interest because of their offset from the galactic center and their high X-ray luminosities, which exceed that expected in a  $10 M_{\odot}$  black hole. However, there have been increasing evidence that at least a significant fraction of ULXs are neutron stars accreting at super-Eddington rates (e.g., Bachetti et al., 2014; King & Lasota, 2020).

This thesis consists of detailed studies of one AGN in the Ultra Luminous InfraRed Galaxy (ULIRG), IRAS 05189–2524, and several recently discovered black hole X-ray binaries, IGR J17091–3624, MAXI J1535–571, Swift J1658.2–4242, MAXI J1631–479, and MAXI J1820+070. The studies are concentrated on the X-ray band to reveal the properties of the innermost part of the accretion flow around black holes using X-ray observations. I start here with a brief introduction of the basic structures of AGNs and black hole X-ray binaries, and their properties across the electromagnetic spectrum with a focus on the X-ray band, to place my studies in a broad context of relevance.

### 1.2.1 Active Galactic Nucleus

Numerous types of AGN have been defined based on their rich observed characteristics (see Padovani et al., 2017, for details). Two of the common classifications are the Seyfert 1 and the Seyfert 2 galaxies (Seyfert galaxies are the less luminous and more local type of AGNs with host galaxies clearly visible, as opposed to quasars), the former showing broad ( $1,000\text{--}20,000 \text{ km s}^{-1}$ ) and the latter containing strong, relatively narrow ( $300\text{--}1,000 \text{ km s}^{-1}$ ) permitted and semiforbidden emission lines on top of the near-infrared (NIR)-optical-ultraviolet (UV) spectral continua. There are also definitions of subgroups between these two types, Seyfert 1.5, Seyfert 1.8, or Seyfert 1.9 etc., referring to the relative intensity of the broad and narrow components of the Balmer lines. According to the unified model of AGN (see Netzer, 2015, for a review), the differences are due to variations in the level of obscuration at different viewing angles, thus different degrees of absorption are also present in the X-ray spectra. The unified model of AGN contains sev-

eral components/structures: a subparsec-rotation-dominated accretion flow (either the optically-thick accretion disk or the optically-thin advection dominated accretion flow), a central jet perpendicular to the accretion disk, high-density dust-free gas clouds (the broad-line region, BLR) moving at roughly Keplerian velocities at  $\sim 0.01\text{--}1$  pc from the black hole, an axisymmetric dusty structure at  $\sim 0.1\text{--}10$  pc (torus), and lower-density lower-velocity ionized gas (the narrow-line region, NLR) extending from outside the torus to  $\sim 10^2\text{--}10^3$  pc (see Figure 1.1). The unified model of AGN successfully combines most of the subgroup of AGNs into a general picture with a small number of physical parameters: the torus inclination to the line of sight and the source luminosity. And the nature of the central obscurer, the torus, is still debated, and is generally believed to be related to the growth of supermassive black holes (e.g., Hopkins et al., 2012; Wada, 2012).

The high-energy photons produced in the accretion flows and jets around supermassive black holes get absorbed and reflected off by different structures of AGNs from inside out, producing reemission, making AGNs a type of astronomical object that is bright across a very broad range in the electromagnetic spectrum. The accretion of gas around the supermassive black hole produces an optically-thick accretion disk that emits thermally at a wide range of temperatures, with the temperature being an inverse function of the distance from the black hole. For a typical AGN accretion disk, the range of gas temperatures is around  $10^4\text{--}10^5$  K, and therefore the majority of the emission is at UV–optical wavelengths in the spectral shape of a multi-color blackbody. The X-ray emission is thought to arise from the so-called “corona” (see Section 1.3.1 for a more detailed discussion of the corona) above the accretion disk at the vicinity of the black hole, and is predominantly produced by inverse Compton scattering of photons from the accretion disk in the spectral shape approximated by a cutoff power law. Synchrotron emission from the jet is the dominant component in the radio band, and the associated synchrotron self-Compton (SSC) emission dominates the  $\gamma$ -ray band (see Blandford et al., 2019, for a recent review). In the IR, emission mostly comes from reprocess of photons from the central source by dust in the torus. There is also a component known as the soft excess in many AGNs as an excess of X-ray emission below 1 keV. The origin of this feature remains debated, as several models have been suggested to explain it, including high energy tail of the thermal disk component, warm Comptonization of the UV-optical disk photons, blurred ionized reflection, and complex absorption (e.g., Gierliński & Done, 2004; Mehdipour et al., 2011; Boissay et al., 2016). On top of the spectral continuum, there are emission and absorption lines arising from

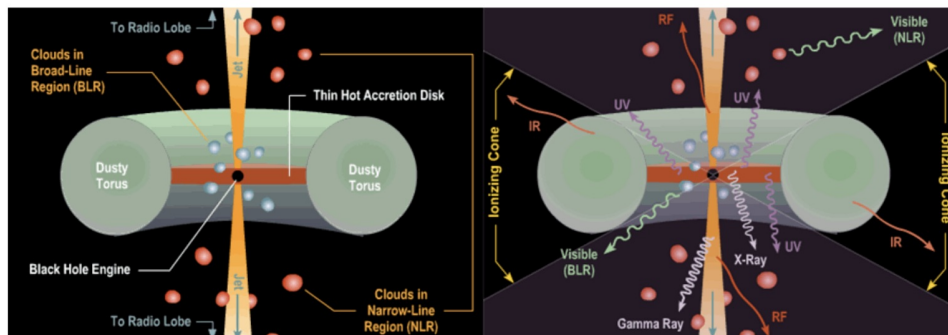
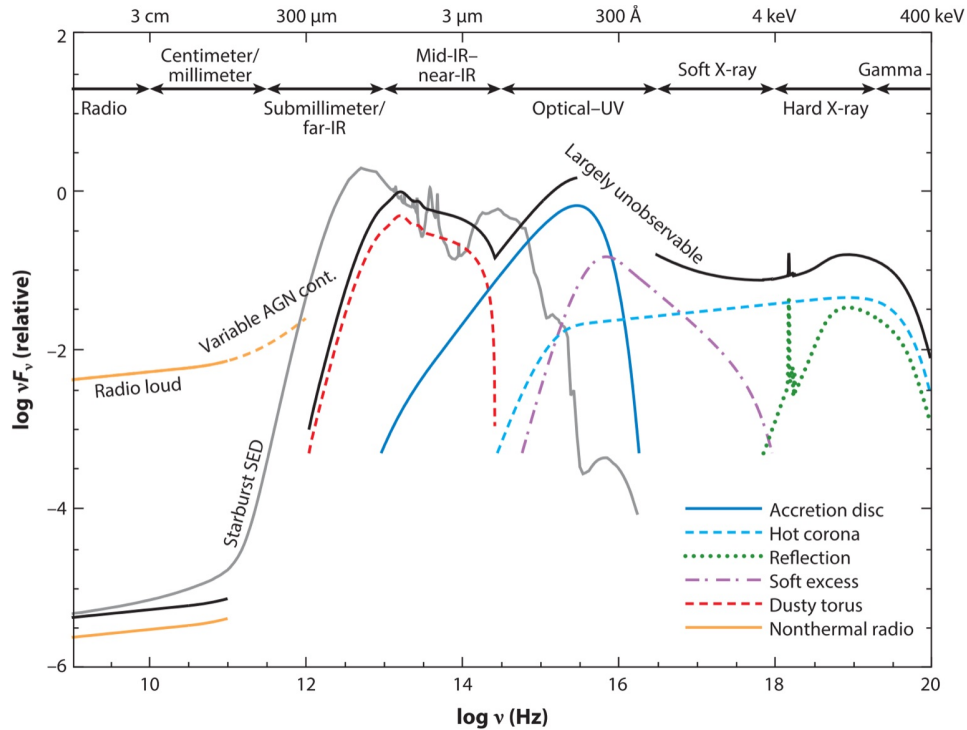


Figure 1.1: Upper panel: Schematic representation of the spectral energy distribution (SED) of an AGN (black curve), separated into the main physical components (colored curves) and compared to the SED of a star-forming galaxy (gray curve). Figure from Hickox & Alexander (2018). Lower panel: Schematic representation of the AGN physical model, broadly illustrating the key components with their corresponding emission components. Image credit: Brooks/Cole Thomson Learning via AstronomyOnline.org.

reprocessing (absorption/reradiation/reflection) of the illumination from the central engine by the surface layers of the accretion disk or more distant structures in an AGN: notably, fluorescent lines in the X-ray band (Fe  $K\alpha$  being the strongest), various broad permitted and narrow forbidden emission lines produced by photoionization in the UV/optical band, and the associated absorption features caused by ionized absorbers along the line of sight (see details in Krolik, 1998, Chapter 10, 11, and 12).

In the X-ray band, the prominent spectral components in an AGN are the soft excess below 1 keV, the coronal emission in the approximate shape of a cutoff power-law extending to high energies, the reflection component including the Fe  $K\alpha$  line around 6–7 keV, the Fe K edge, and the Compton reflection hump peaking around 30 keV (see Figure 1.3, left panel). The Compton reflection hump arises from a combinational effect of absorption and Compton recoil. If the Fe K line is produced in the inner accretion disk, the line would be significantly broadened by relativistic effects in the vicinity of a black hole (see Section 1.3.1 for detailed explanations). There are occasionally weaker lines detected, the Fe L lines, or the C, N, O lines between 0.3 to 1.0 keV, but line blending could be severe in that energy range (Ballantyne et al., 2002). The Fe K lines are always the most prominent ones due to the high cosmic Fe abundance and the high fluorescence yield of electrons transiting to fill the Fe K shell. In the soft X-ray band, the spectrum of an AGN usually contains dilution from hot gas and binary emission in the galaxies, and is sometimes further modified by absorption of warm materials.

Black holes powered by accretion are highly variable sources, both for AGNs and black hole X-ray binaries, displaying significant aperiodic or quasi-periodic variabilities over a wide range of time scales. The origin of the intrinsic fluctuations in the lightcurves are typically attributed to a superposition of random pulses, i.e., shot noise (e.g., Terrell, 1972; Lehto, 1989), invoking accretion disk turbulence (Nowak & Wagoner, 1995), magnetic flares in the disk corona (Poutanen & Fabian, 1999), or magnetohydrodynamic instabilities of the inner disk (Hawley & Krolik, 2001) as possible physical causes. Variabilities are believed to be a useful probe for investigating the central structures around black holes, which typically cannot be resolved by telescopes due to their small sizes. Both AGNs and black hole X-ray binaries display characteristic features in their power density spectra (see Section 1.3.2 for more details), and more sophisticated techniques are sometimes required to maximize our ability to extract information encoded in the lightcurves of these

accreting black hole systems: e.g., the rms/covariance spectrum, which isolates out the spectral component responsible for the flux variations; the time lag analysis (either the lag between the spectral continuum and the emission lines in the optical-UV-X-ray band, or the lag between the optical and the IR continuum emission), providing a means to estimate the light-travel time/distance from the central illuminating source and the reprocessing materials, and the sign of the time lag between two adjacent energy bands (e.g., the soft and the hard X-ray band) are usually used to indicate the direction that instability propagates (the absolute time lag involved in this case is determined by the physical propagation mechanism). The characteristic time scales in accreting black holes scale positively with the black hole mass, and is also known to scale negatively with the accretion rate (e.g., McHardy, 2010). Therefore, it is usually more promising to conduct variability studies on narrow-line Seyfert 1 galaxies (NLSy1s), which are known as bright small-mass supermassive black holes ( $\sim 10^6$ – $10^8 M_\odot$ ) with high accretion rates (e.g., Komossa, 2008), as the long time scale associated with supermassive black holes is a common observational obstacle. In some sense, what may be related are the studies of tidal disruption events (TDEs), which are caused by stars in the immediate vicinity of supermassive black holes with the mass of  $10^6$ – $10^8 M_\odot$  ripped apart by the tidal forces of the black holes (Rees, 1988, and see Komossa, 2015 for a recent review on observations). The temporal high accretion rates obviously cannot be sustained, making them slowly decaying transient sources and offering good opportunities for the study of accretion phenomena related to variabilities.

### 1.2.2 Black Hole X-ray Binary

There are broad similarities in the behaviors between black hole X-ray binaries and AGNs. It is believed that the physical processes occurring in accretion flows around the black holes in these objects are essentially the same, but should be scaled in some appropriate manner given the significant differences in black hole masses. And due to their large distinctions in luminosities and variation time scales, we should naturally expect the studies of AGNs and black hole X-ray binaries to suffer from different observational biases, which probably in some way exaggerate the actual differences of the two classes.

According to the standard black hole accretion disk model, the characteristic disk temperature scales inversely with the black hole mass (Novikov & Thorne, 1973; Shakura & Sunyaev, 1973; Pringle, 1981). The thermal disk emission from black hole X-ray binaries is known to peak in the soft X-rays, higher than that from AGNs,

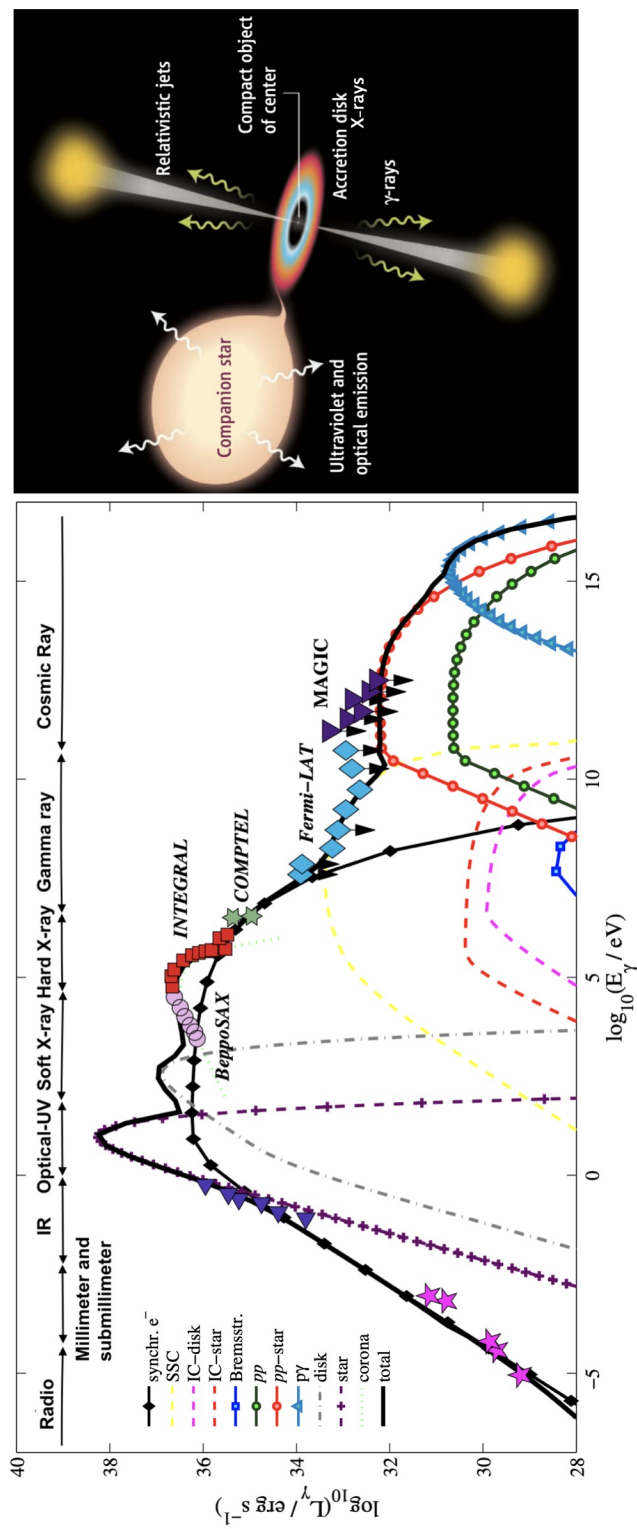


Figure 1.2: Left: The spectral energy distribution of the black hole binary Cygnus X-1 with best-fit models from Pepe et al. (2015). Down-pointing arrows indicate upper limits. Right: Schematic representation of the structure of a black hole X-ray binary, image from Mirabel (2006).

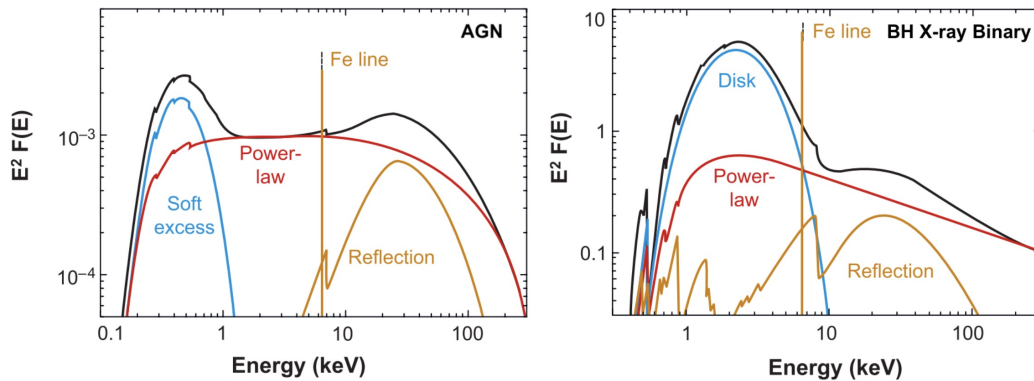


Figure 1.3: Representative X-ray spectra of an unobscured AGN and a black hole X-ray binary. The relativistic effects that shape the Fe K line and reflection continuum have not been included. Figure from Miller (2007).

and therefore the accretion disk is also expected to be more ionized in black hole X-ray binaries. Similar to AGNs, there is also a coronal component in the spectral shape of a cutoff power-law dominating the hard X-ray band. X-ray binaries are also known to produce powerful jets, hence the name “microquasars,” and jet emission typically dominating the IR and  $\gamma$ -ray band (see Figure 1.2). Although there is accumulating evidence that some black hole X-ray binaries may be heavily obscured or at least being so during some phases of their evolution cycle (e.g., Corral-Santana et al., 2013; Motta et al., 2017; Miller et al., 2020), there is generally no ubiquitous torus-like obscuration component known in these systems. Also, the emission in the UV-optical band of black hole X-ray binaries is often diluted by light from the companion stars to some level, depending on the type of the companion star and the relative brightness of the accretion-powered black hole. Therefore, the study of accretion phenomena in these stellar-mass black holes has been rather restricted to the X-ray band, whereas for AGNs, considerable amount of work (if not more) can be conducted in the UV-optical band and also through reproduced emission in the IR.

In the X-ray spectrum of a black hole X-ray binary, the representative spectral components are the thermal disk emission peaking in the soft energy band, a power-law coronal component, and the reflection component (see Figure 1.3, right panel). There are also relatively narrow absorption features indicating disk winds superimposed on the spectral continuum, whose occurrence is believed to be associated with the accretion states. Most known black hole binaries in our Galaxy are found near the galactic plane, so their X-ray spectra in the soft X-ray band are usually

significantly absorbed by the interstellar medium (ISM) along the line of sight. In addition, dust in the ISM scatters X-ray photons, producing structures (dust scattering halos) that cannot always be resolved, modifying the observed soft band spectra of black hole X-ray binaries in a more complicated way (e.g., Predehl & Schmitt, 1995; Draine, 2003). We note that high extinctions also make it difficult to identify the companion stars in the optical/IR band in many cases, prohibiting accurate dynamical measurements of the mass of the central compact objects and the determination of their distances. As a result, the classification of a newly discovered X-ray transient as a black hole candidate is usually based on its phenomenological behaviors.

From observations at the electromagnetic wavelengths, almost all stellar-mass black holes are found as X-ray transients that go into recurrent outbursts due to thermal-viscous instabilities in the accretion disk (the so-called X-ray novae), and the majority of bright X-ray novae found in our Galaxy are identified as black hole candidates. However, the confirmation of a single X-ray nova as a stellar-mass black hole is not straightforward, considering that they often lack direct dynamical mass measurements. Black hole and neutron star X-ray binaries share a lot of similarities in terms of accretion, and they are known to reach similar flux levels. The existence of a solid stellar surface and magnetic fields in an accreting neutron star creates more variations in its observational phenomena in the X-rays, and thus making some neutron star X-ray binaries appear more similar to their black hole counterparts than others. In general, the detection of coherent pulsations or thermonuclear X-ray bursts are the definite indications for a neutron star. If no such behaviors are detected and if the source displays characteristic state transitions and spectral and timing behaviors consistent with known black holes during outbursts, it is considered as a black hole X-ray binary candidate (see van der Klis, 2006). X-ray binaries are divided into high-mass and low-mass ones (HMXBs and LMXBs, respectively) according to the mass of the companion star feeding the relativistic compact object. Statistically, most X-ray novae ( $\sim 75\%$ ) are LMXBs with the central object being a black hole where mass transfer occurs via Roche lobe overflow (Tanaka & Shibazaki, 1996). Whereas, most known neutron star X-ray binaries are persistent sources (see King et al., 1996 for a discussion of the conditions for being persistent or transient sources), and most HMXBs are known to be pulsating neutron stars with strong magnetic fields (van Paradijs, 1998). We note that there are always certain fractions of exceptions, and caution should be taken as this general trend is

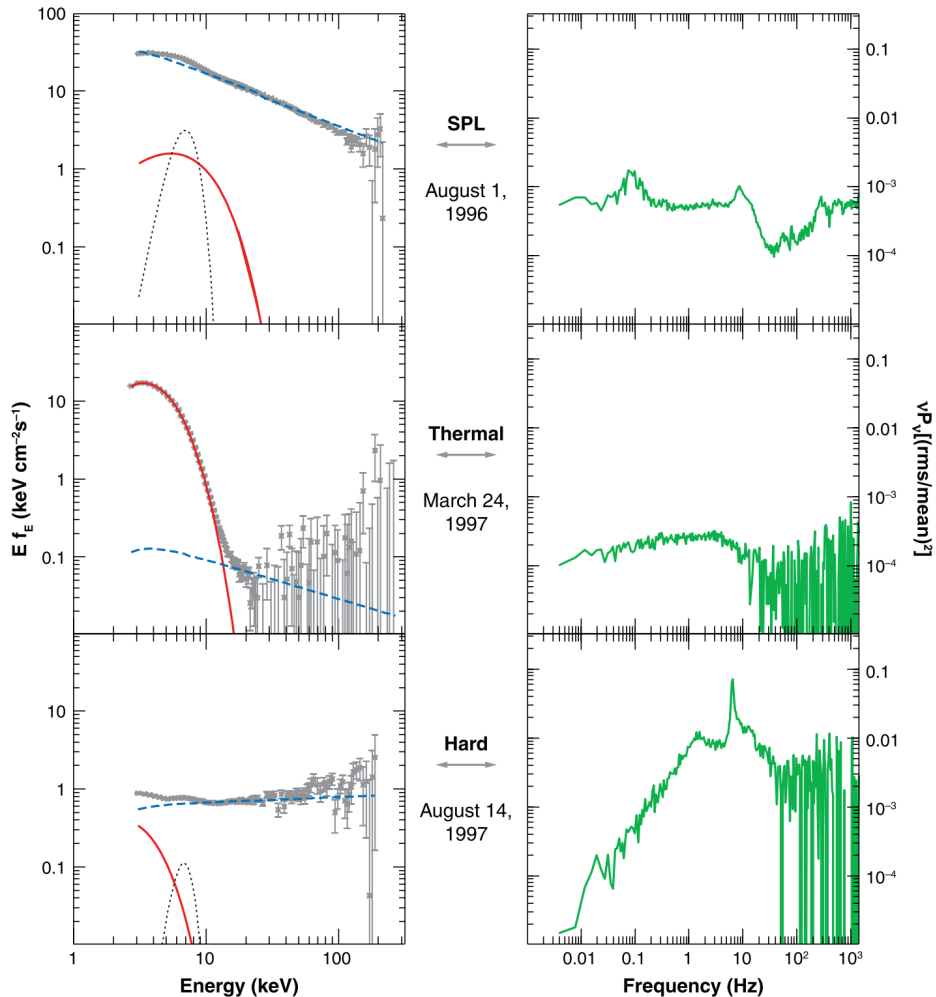


Figure 1.4: Sample energy spectra and power density spectra of GRO J1655–40 observed by *RXTE*, illustrating the representative spectral and timing properties of a black hole X-ray binary during different accreting states: steep power-law state (SPL), high/soft state (thermal), and low/hard state (hard). Left panels show the spectral energy distribution decomposed into three components: a thermal disk component (red solid), a power-law component (blue dashed), and a broad Fe  $K\alpha$  line (black dotted). Right panels show their corresponding power density spectra. Figure from Remillard & McClintock (2006).

based on observations of a considerably small sample of stellar-mass black holes and in a relatively homogeneous environment, our Milky Way.

Black hole X-ray binaries are ideal targets for the study of rapid variations and state transitions arising from the accretion flows around black holes. For a black hole X-ray transient, its X-ray flux/accretion rate varies by several orders of magnitude during an outburst. The typical duration of an outburst (a few months) makes it convenient to track the state transitions, which are characterized by different patterns in the X-ray spectral and timing behaviors. The outburst commonly starts with a

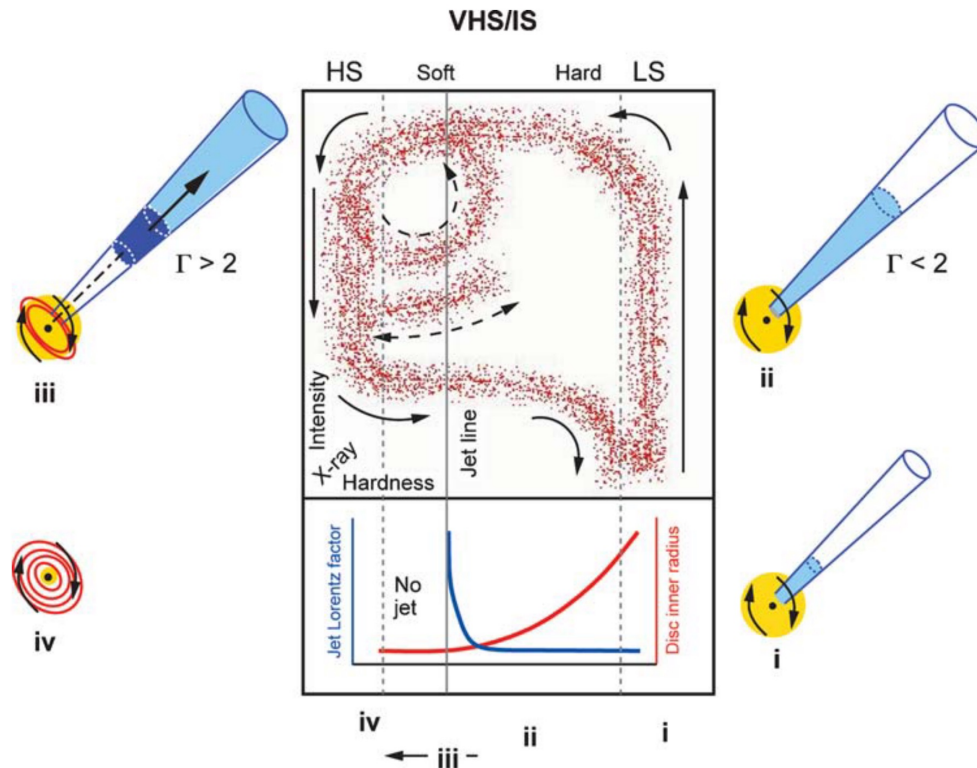


Figure 1.5: A schematic representation of the disk-jet coupling model in a black hole X-ray binary from Fender et al. (2004). The top panel shows its evolutionary tracks in the hardness intensity diagram (HID). The X-ray accretion states are labeled: the high/soft state (HS), the very high state or the intermediate state (VHS/IS), and the low/hard state (LS). The lower panel indicates variations of the bulk Lorentz factor ( $\Gamma$ ) of the jet with spectral hardness. The sketches around the outside illustrate the concept of the relative contributions of the jet (blue), the corona (yellow), and the accretion disc (red) at these different stages in the model.

hard state and transitions to the soft state as the source brightens, and goes back into the hard state close to the end of the outburst. There are also some intermediate states less clearly defined close to the hard-to-soft state transitions. The soft state energy spectrum, which is commonly dominated by thermal disk emission with the characteristic temperature of  $\sim 1$  keV, is usually observed when the source is bright, thereby prompting the name “high/soft state.” The hard state spectrum, typically dominated by a power-law component with the photon index of  $\sim 1.7$ , is generally seen when the source is fainter, hence the name “low/hard state.” In this state, the disk appears much cooler and weaker. There is a less commonly observed state named the “very high state.” It is characterized by a relatively high luminosity and an energy spectrum comprised of both a thermal component and a power-law component that is steeper than the hard state power-law (see Remillard & McClint-

tock, 2006 for a review on the accretion states of black hole X-ray binaries, and see Figure 1.4 for their characteristic behaviors in the spectral and timing aspects). The different accretion states also show distinct timing behaviors, manifesting in the power density spectra (PDS; see also Section 1.3.2 for more details). In general, the intrinsic variabilities of the source are high in the hard state ( $\sim 30\text{--}40\%$ ), and much lower in the soft state. In the PDS of a black hole X-ray binary, narrow peaks, the so-called quasi-periodic oscillations (QPOs), are frequently detected on top of the spectral continuum during the hard state and the intermediate states, and vanish as the source enters the soft state. There are detailed classifications on the various types of QPOs. Because their frequencies can be accurately measured, the association of certain types of QPOs with specific accreting states or state transitions suggests that QPOs could be a key ingredient in understanding the underlying physical conditions of these states. It is interesting to note that a few changing-look AGNs have also been detected to display state transitions in the X-ray band similar to those observed in black hole X-ray binaries, which have been proposed to be triggered by certain instabilities (e.g., Noda & Done, 2018; Ruan et al., 2019; Ricci et al., 2020). However, AGNs in general are relatively constant objects; most do not show significant variability on humanly accessible time scales.

The hardness intensity diagram (HID) is a tool commonly used to investigate the state changes in accreting objects, which is a plot of the X-ray intensity versus hardness ratio (HR), i.e., the ratio of detector counts in two energy bands. The HID is also used to illustrate the “unified model for radio jets” in black hole X-ray binaries as proposed by Fender et al. (2004). See Figure 1.5 for a schematic presentation for the relationship between jets and accretion states, which shows qualitatively how the jet Lorentz factor and the morphology of the jet evolve with changes in the accretion state in a black hole binary. The summarized general trend of the unified model is that during the rising phase of an outburst, the steady slower-moving optically-thick jet, known to be associated with the canonical low/hard state, persists while the X-ray spectrum initially softens. Subsequently, the jet becomes unstable, and a powerful optically-thin radio outburst occurs, associated with the soft X-ray peak at the end of softening corresponding to the very high state. The soft state afterwards are not associated with core radio emission. The investigation of the relation between the jet and the disk during accretion state changes provides clues about the physics of jet launching mechanisms (e.g., Fender et al., 2004). The studies of jets in accreting systems is by itself a comprehensive subject, which I am not going to expand upon any further. What is related to the topic of disk-jet cou-

pling is the role of disk winds during the accretion state transitions, as jets and disk winds are both believed to carry away the available accretion power in accreting systems (see the review Fabian, 2012 for details). There is some evidence showing that strong disk winds and jets might be mutually exclusive, with jets and disk winds being prevalent during the hard and the soft state, respectively (e.g., Miller et al., 2008; Neilsen & Lee, 2009; Ponti et al., 2012).

### **1.3 Investigating the Inner Accretion Flow Properties around Black Holes via X-ray Spectral and Timing Analyses**

There are various data analysis techniques that have been widely applied to analyzing X-ray observational data of accreting black holes, in order to reveal the physical properties of the inner accretion flows where X-ray emission originates. The general approach is similar to any field of research in astrophysics: choosing the best astronomical objects to study, analyzing the observational data to reveal key signatures, comparing the results with theoretical predictions to draw conclusions about the physical processes involved, or directly fitting the data with models from theoretical simulations to measure key physical parameters of interest. Some diagnostic features from accreting black holes that can be revealed from X-ray spectral and timing analyses have been mentioned in the previous sections of general introductions of AGNs and black hole X-ray binaries. This section focuses on the use of these features to probe the underlying physical processes in the inner accretion flows, which are widely used in the following chapters of this thesis. In addition, some of the theoretical models proposed and open questions remaining are discussed with references included.

#### **1.3.1 Disk Reflection and Disk Wind Features**

The study of relativistic disk reflection features started with the discussion about the existence of relativistically broadened and asymmetric Fe  $K\alpha$  lines in the X-ray spectra of accreting black holes. A broad Fe  $K\alpha$  line was first detected in the black hole X-ray binary Cygnus X-1 by *EXOSAT* (Barr et al., 1985), which was interpreted as a relativistic line in the vicinity of a black hole in Fabian et al. (1989). The predicted asymmetric line profile was then clearly resolved by *ASCA* in the Seyfert 1 galaxy MCG-6-30-15 in Tanaka et al. (1995). The extended red wing in the Fe  $K\alpha$  line profile strongly suggests that the emission arises from the innermost region of a relativistic accretion disk within deep gravitational potential, providing evidence for the central object being a black hole. Subsequently, such broadened

and asymmetric Fe  $K\alpha$  lines have been detected in a number of Seyfert 1 galaxies by *ASCA*, *XMM-Newton*, and *Suzaku* (e.g., Nandra et al., 1997; Nandra et al., 2007; Patrick et al., 2012; Walton et al., 2013). But for many years, such investigations in black hole X-ray binaries were limited by instrumental capabilities due to several factors. CCD detectors (e.g., *XMM-Newton* EPIC) were easily piled-up at the typical high flux level of Galactic black hole X-ray binaries, and proportional counter detectors (e.g., *Ginga* LAC and *RXTE* PCA) suffered from poor energy resolution and general uncertainties in their response matrices. Since the launch of *NuSTAR* (Harrison et al., 2013), it has become the suitable instrument to conduct the study of relativistic reflection features in black hole X-ray binaries as well as AGNs, because of its high sensitivity, moderate energy resolution, broad energy coverage (covering both the Fe K and the Compton hump energy ranges), and the ability to stay free from pile up for bright sources with triggered readout.

The basic physics of X-ray reflection and Fe line fluorescence is well summarized in Fabian et al. (2000), and can be understood in the form of a hard X-ray power-law continuum (emission from the corona) illuminating a semi-infinite slab of cold gas (accretion disk). In some cases, a useful simplified picture is assumed that the corona is of a lamppost geometry on the spin axis of the black hole illuminating the accretion disk (e.g., Martocchia & Matt, 1996; Miniutti et al., 2004). When a hard X-ray photon enters the slab, it is subject to a number of possible interactions: Compton scattering by free or bound electrons, photoelectric absorption followed by fluorescent line emission, or photoelectric absorption followed by Auger de-excitation. A given incident photon is either destroyed by Auger de-excitation, scattered out of the slab, or reprocessed into a fluorescent line photon which escapes the slab. Due to the energy dependence of photoelectric absorption, incident soft X-rays are mostly absorbed, whereas hard photons are rarely absorbed and tend to Compton scatter back out of the slab. Above energies of several tens of keV, Compton recoil reduces the backscattered photon flux. These effects give the reflection spectrum a broad hump-like shape, the so-called “Compton reflection hump.” In addition, there is an emission line spectrum resulting primarily from fluorescent  $K\alpha$  lines of the most abundant metals, with the Fe  $K\alpha$  line being the strongest. The fluorescent Fe K line is produced when a K-shell electron of an Fe atom (or ion) is ejected following photoelectric absorption of an X-ray photon above 7.1 keV, and then an L-shell electron drops into the K-shell releasing energy as an emission line photon. The reflection component is superposed on the direct power-law primary continuum. As a result, the main observables of the reflection are an Fe  $K\alpha$  line

at 6–7 keV (energy depending on the ionization status) and the Compton reflection hump peaking around 20–30 keV.

The Fe  $K\alpha$  line is intrinsically a relatively narrow line, hence the broad profile of the line probes the dynamics of the accretion disk. Thermal and turbulent broadening are generally not believed to be the dominant factors here. The line profile is shaped by the effects of Doppler shifts and gravitational redshifting (see Figure 1.6, left panel). In a non-relativistic disk, each radius of the disk produces a symmetric double-horned line profile corresponding to emission from materials on both the approaching and receding side. Near a black hole, where the orbital velocities of the disk are mildly relativistic, special relativistic beaming enhances the blue peak of the line from each radius. Finally, the comparable influences of the transverse Doppler effect and gravitational redshifting shift the contribution from each radius to a lower energy. Summing the line emission from all radii of the relativistic disk gives a skewed and highly broadened line profile. The key physical parameters shaping the relativistic disk reflection features (dominated by the shape of the skewed iron line) are the inclination of accretion disk, the ionization status of the accretion disk, the inner radius of the optically-thick accretion disk (how close to the black hole the line emission comes from), and the disk emissivity profile (how much line flux is emitted at each disk radius); see detailed discussions in Fabian et al. (2000). The emissivity profile is essentially related to the illuminating pattern of accretion disk from the corona, which is believed to encode information about the geometry and dynamics of the corona (e.g., Wilkins & Fabian, 2012). The radius of the innermost stable circular orbit (ISCO) around a black hole decreases with the black hole spin. Since the line profile is sensitive to the innermost radius of fluorescent line emission, this provides a method to estimate the inner edge of the optically-thick accretion disk, and the spin of the black hole if the radius is consistent with the ISCO (see the review Miller, 2007 for details, and see Figure 1.7). Since the skewed shape of the Fe  $K\alpha$  line is believed to be driven by the GR effects in the strong-field regime, the technique is widely applicable to both AGNs and black hole X-ray binaries, and has the advantage that it does not rely on independent measurements of other physical parameters of the systems, such as the mass and the distance.

As illustrated above, the relativistic disk reflection features are promising probes for investigating the geometry and (possibly) dynamics about the accretion disk and the illuminating corona, which have broad implications in the astrophysical context.

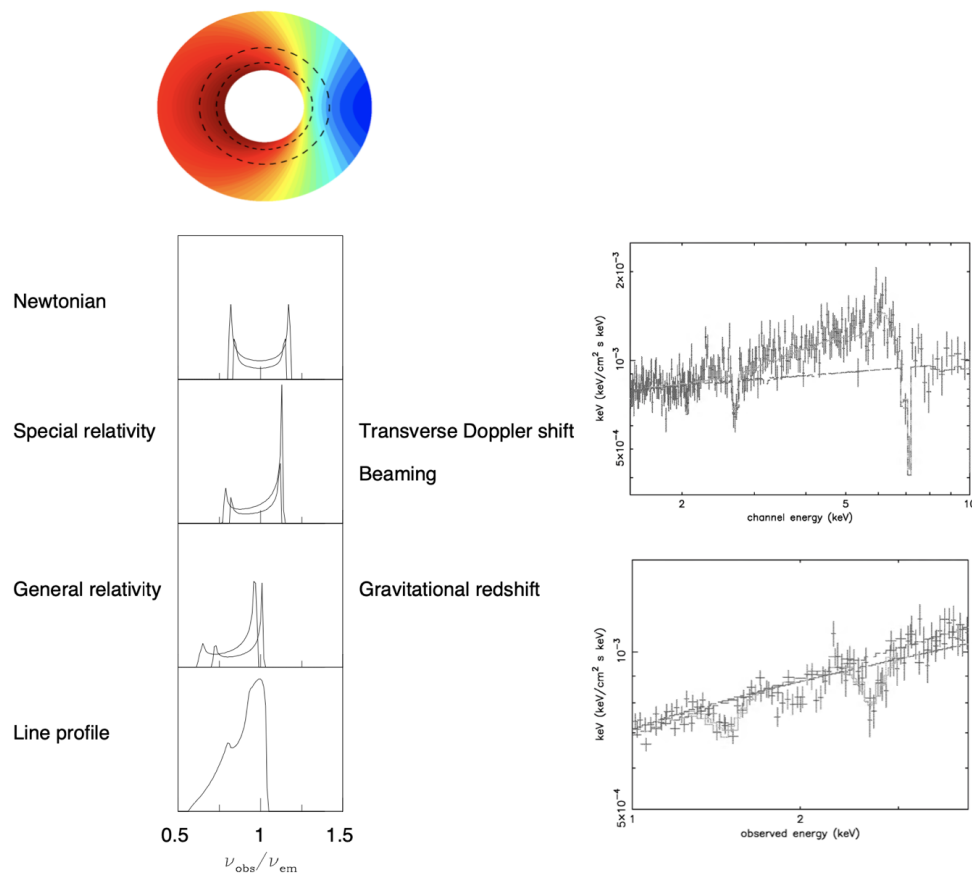


Figure 1.6: An illustration of the physical mechanisms shaping the broad Fe  $K\alpha$  line with the broad Fe  $K\alpha$  emission line and narrow disk wind absorption features observed in an AGN. Left panels: Physical mechanisms shaping the broad Fe  $K\alpha$  line. The panels from top to bottom show the symmetric double peaked profiles generated from two narrow annuli in a non-relativistic disk, the profiles with the effects of transverse Doppler shifting and relativistic beaming included, the profiles further including gravitational redshifting, and the final broad skewed line profile by summing up emission from different radii (figure from Fabian et al., 2000). Right panels: Broad Fe  $K\alpha$  emission line along with narrow absorption lines from Fe XXVI, S XVI, and Mg XII observed in the quasar PG 1121+143 by *XMM-Newton* in Pounds et al. (2003).

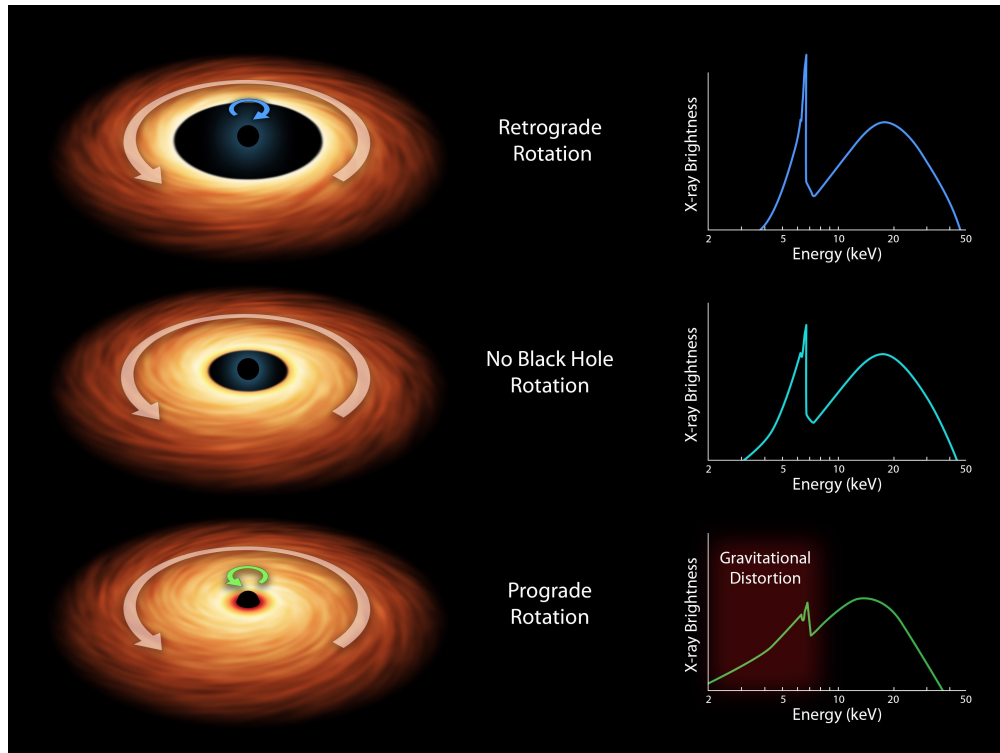


Figure 1.7: A schematic presentation of the measurement of the spin of a black hole based on the relativistic disk reflection spectrum. The degree of gravitational distortion on the disk reflection features in the X-ray spectrum depends on the location of the inner edge of the optically-thick accretion disk, which is believed to be determined by the black hole spin in cases where the disk is not truncated. Image credit: NASA/JPL-Caltech.

The accreting geometry of black holes at different accreting rates is not well understood. Black hole accretion is generally studied in two regimes: cold accretion flows of optically-thick material at high mass accretion rates and hot optically-thin accretion flows at low mass accretion rates, and the latter is thought to be made up of advection-dominated accretion flows (ADAFs). Specifically, models with different accretion flow geometries have been proposed to explain black hole accretion at different Eddington rates (see Yuan & Narayan, 2014, for a recent review). One of the popular geometry for black hole at relatively low accretion rates is the truncated thin disk plus hot accretion flow model, i.e., a two-zone accretion flow model consisting of a cool optically-thick geometrically-thin disk at large radii and a hot optically-thick geometrically-thick accretion flow at small radii, and the degree of disk truncation depends on the mass accretion rate and the accretion state (e.g., Shapiro et al., 1976; Esin et al., 1997, and see Figure 1.8). We note that there are also some more complicated variations proposed recently invoking, e.g., recondensation of gas onto an inner disk under the ADAF (Meyer et al., 2007;

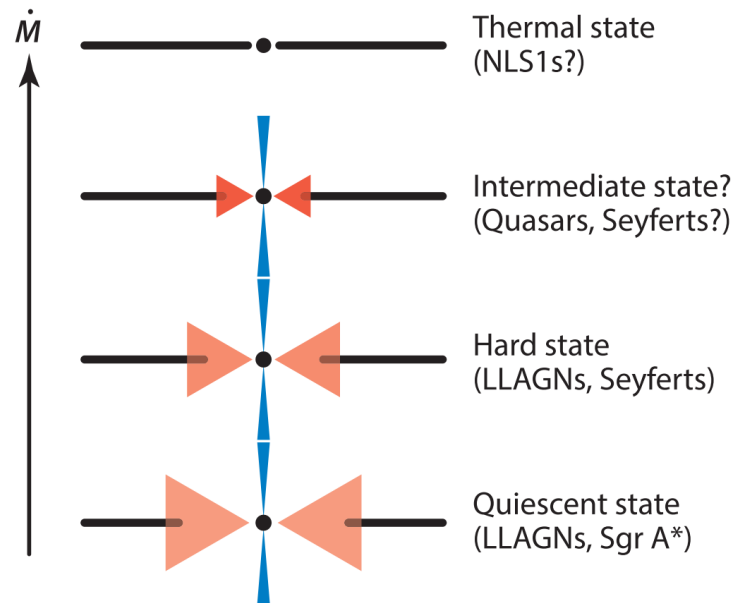


Figure 1.8: A schematic diagram showing accretion flow configurations at different accretion states of a black hole X-ray binary, as a function of the mass accretion rate  $\dot{M}$  (based on the disk truncation model in Esin et al., 1997; figure from Yuan & Narayan, 2014). Possibly equivalent AGN classes are indicated in parentheses. Red triangles indicate the hot accretion flow, whereas thick black horizontal lines represent the standard thin disk. The transition radius where the thin disk is truncated is predicted to shrink with increasing mass accretion rate. The disk truncation radius can be measured by modeling the relativistic disk reflection features in the X-ray spectra of black hole X-ray binaries and AGNs.

Meyer-Hofmeister et al., 2009). In general, the model has been successful in many aspects and in accommodating some observational facts, but this picture still in general lacks solid observational support and requires further scrutiny. The disk reflection features in the X-ray spectra of both AGNs and black hole binaries should be considered as one of most rigorous tools for observational tests. The physical properties of the corona and its relationship with the jet and the hot phases of the accretion flow is a debated topic, which is also naturally related to the geometry of the corona. The corona in the vicinity of a black hole usually refers to the part responsible for the hard X-ray power-law emission in the X-ray spectra of AGNs and black hole X-ray binaries, it is believed to be an optically-thin structure made up of hot electrons Comptonizing thermal disk photons. In the truncated disk model, the corona is thought to be associated with the inner hot accretion flow. In untruncated disk models, the corona is either proposed to have a slab geometry (heated by magnetic reconnection) or be a patchy corona (made up of individual magnetic flares) above the accretion disk, or act as the base of the jet. There is certain evi-

dence in favor and against each scenario, and there is currently no coherent answer to the question about the origin of the corona (see discussions and references in Done et al., 2007 Section 4 or Yuan & Narayan, 2014 Section 4.2). It is unlikely that the debate will be resolved on a pure theoretical/simulative basis, thus it awaits constraints from future observations, and X-ray polarimetry may be an upcoming new window for looking at this problem (e.g., Malzac, 2018).

In addition to disk reflection, ionized absorptions lines are also frequently found prominent atomic features in the X-ray spectra of accreting black holes, signaling outflowing materials along the line of sight. The first evidence for ionized absorption in the X-ray spectrum of an AGN was reported by Halpern (1984) comparing spectra of the quasar MR 2251–178 during two epochs with the *Einstein* satellite. The data showed a change in the soft X-ray band, which was interpreted as an ionized cloud crossing the continuum source. The presence of highly ionized plasma in X-ray binaries was first clearly observed in GRO J1655–40 (Ueda et al., 1998) and GRS 1915+105 (Kotani et al., 2000) by *ASCA*, showing narrow absorption lines that were identified with absorption from Fe XXV (rest-frame energy at 6.7 keV) and Fe XXVI (rest-frame energy at 6.97 keV). The advent of the higher energy resolution grating spectrometers aboard *Chandra* and *XMM-Newton* provided a revolution in such studies of disk winds in both AGNs and black hole X-ray binaries as these are usually quite narrow features, revealing absorption in the Fe K band as well as in softer energy ranges, composed of a number of lines and edges from different elements at different ionization states (e.g., Pounds et al., 2003; Miller et al., 2008, 2015a; Parker et al., 2017). The energies of these lines were commonly found to be systematically blue-shifted compared to the expected values, indicating that the absorption materials were likely from winds outflowing from the central regions of black holes. Modeling of the absorption line complex gives a measurement of the gas density, the column density, the outflowing velocity, and the degree of ionization of the absorber. Photoionized absorbers are thought to be ubiquitous in accreting systems, and have been detected in more than half of local Seyfert galaxies. They are also frequently detected in black hole X-ray binaries as transient features, whose appearance is related to the accretion states (e.g., Ponti et al., 2012; Díaz Trigo & Boirin, 2016). The observed wind features are usually thought to be associated with the companion stars in HMXBs. Whereas in LMXBs, they are considered to originate from the accretion disks, in which cases they are more likely to be detected in systems viewed near edge-on due to the wide opening angles of the winds when they are launched from the accretion disks (Frank et al., 1987). In addition, a more

extreme type of outflows, referred to as Ultra-Fast Outflows (UFOs), have been recently found in a number of AGNs; these are broad absorption features characterized by high ionization status and mild relativistic velocities (e.g., Tombesi et al., 2011, 2013; Nardini et al., 2015). These features are of particular interest because they are believed to be launched from the inner accretion disks and the energetics involved are high.

Disk winds are an important element when studying accretion phenomena around compact objects. Powerful winds driven by AGNs are often considered to play a fundamental role in the co-evolution of supermassive black holes and their host galaxies. In general, disk winds are believed to have important effects on the accretion efficiency in black holes across the mass scale. They could lead to instabilities in the accretion flows (Begelman et al., 1983) or trigger accretion state changes (Shields et al., 1986). Accretion disk winds could be driven by thermal, radiative, or magnetic pressure; details about the launch and propagation mechanisms of outflowing winds at different scales in these systems are currently not clearly understood, which require systematic inputs from further observations and theoretical simulations.

### 1.3.2 Power Density Spectrum

Rapid aperiodic variabilities arisen from the immediate vicinity of black holes are observed in the X-ray light curves of both AGNs and black hole X-ray binaries. Time analysis techniques in the Fourier domain are required for the study of such fast variabilities of accreting black holes. One of the basic tools commonly used is the power density spectrum (PDS; e.g., Leahy et al., 1983), which calculates the variation power at each frequency. Accreting black holes are known to display distinct behaviors in the PDS during different accretion states (See Figure 1.4). The continuum power in the PDS is of interest for both its shape and its integrated amplitude. The latter is usually expressed in the units of the root-mean-square (rms) fluctuations, scaled to the mean count rates and providing a measurement of the general variability of the source. Black hole X-ray binaries are known to exhibit transient, discrete features known as quasi-periodic oscillations (QPOs), which are prominent narrow peaks on top of the noise continuum in the PDS. QPOs are usually modeled with Lorentzian functions in the PDS, while we note that coherent pulsations should be in the shape of Dirac delta functions. Recently, QPOs have also been detected in the NLSy1 RE J1034+396 with the characteristic frequencies being a lot lower than those observed in stellar-mass black holes (Gierliński

et al., 2008). Such detections are challenging as long and extensive monitoring observations are required to reach the sensitivity, and also selection effects should be important here as QPOs are known to be accretion state dependent. In black hole X-ray binaries, QPOs have also been detected in UV-optical-IR bands (e.g., Hynes et al., 2003; Gandhi et al., 2010), whose origin (the jet or the outer parts of the accretion disk) and the connection with the QPOs found in X-rays are still debated (e.g., Veledina et al., 2013). In addition, the bend time scales of the PDS are also characteristic features of interest. The break frequency at the low frequency end of the PDS is known to scale with the QPO frequency (e.g., Wijnands & van der Klis, 1999). There is evidence that the break frequency of the PDS is positively correlated with the black hole mass, but is negatively correlated with the accretion rate, indicating that the break frequency may be associated with the inner edge of the accretion disk (McHardy, 2010). There are also occasionally broad peaks detected in the PDS, but such features lack systematic studies and are poorly understood.

QPOs were first identified in accreting white dwarfs and neutron stars, and then in black hole systems more than 30 years ago. QPOs found in black hole X-ray binaries are rich in phenomenology, detected from the frequency range of mHz to kHz. They are classified into various types, whose occurrence depends on accretion states, and are believed to have different physical origins (Remillard & McClintock, 2006). Many models have been proposed to explain the physical origin of QPOs detected in the X-ray band, which invoke either general relativistic effects or instabilities in the accretion flows (see Ingram & Motta, 2020, for a recent review on QPOs). In general, X-ray timing is believed to be a useful method to commensurate the findings from X-ray spectral analysis. Spectral analysis (especially line profile modeling) probes the dynamics of the accretion flow and features in the timing analysis highlight characteristic time scales. Essentially, they are both related to the size of the corresponding X-ray emission region. It has been proposed that QPOs and break frequencies in the PDS could potentially offer independent methods to measure the inner radius of the accretion disk, and the black hole mass and spin. However, despite being strong and easily measurable, the physical origins of these timing features are elusive and their association with the basic physical properties of the black hole is still unclear.

#### **1.4 Thesis Outline**

The main content of this thesis presents results from recent X-ray observations of an AGN (Chapter 2) and several Galactic black hole X-ray binaries (Chapter 3 to

8) using *NuSTAR*, *Swift*, and *XMM-Newton*. Each chapter is dedicated to the study of a single source, presenting the detailed data analysis procedures and the physical interpretations based on the observational data. I summarize the results in Chapter 9 in a more general context regarding the common characteristics of the population of accreting black holes studied in X-rays, with a discussion about prospects to extend my research using future X-ray telescopes.

## EVIDENCE FOR RELATIVISTIC DISK REFLECTION IN THE SEYFERT 1H GALAXY/ULIRG IRAS 05189–2524 OBSERVED BY *NUSTAR* AND *XMM-NEWTON*

Xu Y., Baloković M., Walton D. J., Harrison F. A. et al. (2017). “Evidence for Relativistic Disk Reflection in the Seyfert 1h Galaxy/ULIRG IRAS 05189–2524 Observed by *NuSTAR* and *XMM-Newton*.” *The Astrophysical Journal*, 837(1):21. DOI: 0.3847/1538–4357/aa5df4.

### Abstract

We present a spectral analysis of the *NuSTAR* and *XMM-Newton* observations of the Seyfert 1h galaxy/ULIRG IRAS 05189–2524 taken in 2013. We find evidence for relativistic disk reflection in the broadband X-ray spectrum: a highly asymmetric broad Fe  $K\alpha$  emission line extending down to 3 keV and a Compton scattering component above 10 keV. Physical modeling with a self-consistent disk reflection model suggests the accretion disk is viewed at an intermediate angle with a super-solar iron abundance, and a mild constraint can be put on the high-energy cutoff of the power-law continuum. We test the disk reflection modeling under different absorption scenarios. A rapid black hole spin is favored, however we cannot place a model-independent tight constraint on the value. The high reflection fraction ( $R_{\text{ref}} \simeq 2.0\text{--}3.2$ ) suggests that the coronal illuminating source is compact and close to the BH (lying within  $8.7 R_g$  above the central BH), where light-bending effects are important.

**Keywords:** accretion, accretion disks – black hole physics – galaxies: active – galaxies: individual (IRAS 05189–2524) – galaxies: Seyfert – X-rays: galaxies

### 2.1 Introduction

The hard X-ray continuum emission of active galactic nuclei (AGNs) is believed to be produced in the corona via thermal Comptonization of ultraviolet (UV) radiation from the accretion disk (e.g., Haardt & Maraschi, 1993). This continuum emission is subsequently reprocessed by dense material either from the accretion disk or distant structures such as the dusty torus or the broad line region (BLR), producing the characteristic reflected X-ray spectrum (e.g., George & Fabian, 1991). Fluorescent

spectral lines, line edges, and a Compton hump are typical features of the reflected X-ray spectrum. Fe  $K\alpha$  is the most prominent spectral line in the X-ray band due to its high cosmic abundance and fluorescent yield. The line emission from the innermost regions of the accretion disk is relativistically broadened by the combined effects of Doppler shifts and gravitational redshift (Fabian et al., 1989; Laor, 1991), which skew the line profile into an extended red wing. Assuming the accretion disk extends down to the innermost stable orbit (ISCO), which is determined by the spin of the black hole (BH), a relativistically broadened Fe  $K\alpha$  line could be used as a probe of the BH spin.

So far, broad Fe  $K\alpha$  lines have been detected in many AGNs (e.g. Tanaka et al., 1995; Nandra et al., 2007; Risaliti et al., 2013; Walton et al., 2013); these are mostly Seyfert 1–1.5 galaxies with only a few absorbed Seyfert 2 galaxies showing such features: e.g., IRAS 18325–5926 (Iwasawa et al., 1996), IRAS 00521–7054 (Tan et al., 2012). *XMM-Newton* and *Suzaku* observations of IRAS 00521–7054 revealed a possibly strong and broad Fe  $K\alpha$  line favoring a high BH spin, however the broad line could also be artificially produced by a combination of partial covering absorbers (Tan et al., 2012; Ricci et al., 2014). With high-quality broadband X-ray data and multi-epoch observations, BH spins have been robustly constrained in some nearby obscured Seyferts (e.g., Seyfert 1.9 galaxy NGC 1365, Risaliti et al., 2013; Walton et al., 2014), but the measurement is still difficult for these obscured objects.

IRAS 05189–2524 is an ultraluminous infrared galaxy (ULIRG) with  $\log(L_{\text{IR}}/L_{\odot}) = 12.16$  (U et al., 2012) and hosts a Compton-thin AGN at redshift  $z = 0.0426$ . While originally classified as Seyfert 2 (Veilleux et al., 1995), broad polarized Balmer lines were detected (Young et al., 1996) and near-infrared spectroscopy revealed broad Paschen lines (Veilleux et al., 1999; Severgnini et al., 2001), indicating the existence of a hidden BLR. Therefore, it has been more accurately classified as a hidden broad line Seyfert 1 galaxy (Seyfert 1h galaxy/S1h) (Véron-Cetty & Véron, 2006), which defines the kind of Seyfert 2s having the spectra of Seyfert 1s in the polarized light.

In the X-ray band, IRAS 05189–2524 is one of the most luminous ULIRGs in the sky, which are typically merger systems undergoing rapid star-forming activities. IRAS 05189–2524 is likely a late stage merger of two spiral galaxies (Sanders et al., 1988). Its X-ray emission is dominated by the central AGN rather than starburst activities (Veilleux et al., 1999). Iron emission has been detected in IRAS 05189–

2524 from previous X-ray observations by *Beppo-SAX* (Severgnini et al., 2001) and *Suzaku* (Teng et al., 2009), but the general line profile was not resolved. The source went through a major spectral change during the 2006 *Suzaku* observation when the 2–10 keV flux dropped by a factor of  $\sim 30$ , which could be explained by an increase in the absorption column density or the change of the intrinsic AGN luminosity (Teng et al., 2009). At a galactic scale, high-velocity outflows of ionized (Westmoquette et al., 2012; Bellocchi et al., 2013), neutral (Rupke et al., 2005; Teng et al., 2013; Rupke & Veilleux, 2015), and molecular (Veilleux et al., 2013) gas have been observed.

Outflows have been recognized as a signature of AGN feedback, which is believed to play an important role in the co-evolution of AGNs and their host galaxies. Evidence for multi-phase outflowing gas has been observed in AGNs on a wide range of spatial scales from that of the central accretion disk to large-scale molecular outflows. If outflows at different scales are all AGN-driven, linking them could help unveil the expansion mechanism of the wind. Such studies have been conducted on ULIRGs IRAS 11119+3257 (Tombesi et al., 2015) and Mrk 231 (Feruglio et al., 2015). In the X-ray band, there is growing evidence for ultra-fast outflows (UFOs) with the typical velocities of  $\sim 0.1\text{--}0.2 c$ , detected by fitting blue-shifted Fe K-shell absorption lines between 7 and 10 keV (e.g., Pounds et al., 2003; Tombesi et al., 2010; Pounds & King, 2013). In the case of PDS 456, a P-Cygni-like profile was observed, demonstrating a powerful wide angle outflow (Nardini et al., 2015).

In this paper, we report evidence for relativistic disk reflection in IRAS 05189–2524 based on analysis of the broadband X-ray spectrum from *NuSTAR* and *XMM-Newton*. In Section 2.2, we describe the observations and the data reduction. Section 2.3 provides the details of our spectral fitting. We present a discussion of the results in Section 2.4 and summarize our results in Section 2.5.

## 2.2 Data Reduction

IRAS 05189–2524 was observed with *NuSTAR* (Harrison et al., 2013) and *XMM-Newton* (Jansen et al., 2001) in 2013 as a part of the *NuSTAR* ULIRG survey (Teng et al., 2015) and the *NuSTAR* survey of *Swift*/BAT AGN (Baloković et al., in prep.). *NuSTAR* observed the source at two epochs: on 2013 February 20 (OBSID 60002027002) and on 2013 October 2 (consecutive OBSIDs 60002027004 and 60002027005) with the exposures of 23.1 ks, 25.4 ks, and 8.3 ks, respectively. The *XMM-Newton* observation (OBSID 0722610101) with an exposure time of 37.8 ks

was coordinated with the second *NuSTAR* observation. The dataset was previously analyzed in the *NuSTAR* ULIRG survey (Teng et al., 2015), with the focus on uncovering the obscuration levels and intrinsic luminosities of several nearby ULIRGs. We reduced the data following the data processing description in Teng et al. (2015).

### 2.2.1 NuSTAR

The data were processed using v.1.6.0 of the NuSTARDAS pipeline with *NuSTAR* CALDB v20160731. For each observation, the source spectra were extracted at the position of IRAS 05189–2524 within the radius of 60". Corresponding background spectra were extracted from source-free areas on the same chip using polygonal regions. As discussed in Teng et al. (2015), the *NuSTAR* data show minor count rate variability (~20%) and no obvious change in spectral shape between the two epochs. Therefore, we combined the three *NuSTAR* observations using the ADDSPEC script in HEASoft v6.19 to maximize the signal-to-noise ratio (S/N) of the spectra. We binned the data taking into account the background level to provide a nearly constant S/N over the *NuSTAR* bandpass, with a minimum S/N of 3, and median S/Ns of 5.5 and 5.3 for the two focal plane modules (FPMA and FPMB).

### 2.2.2 XMM-Newton

The *XMM-Newton* observation was reduced with the *XMM-Newton* Science Analysis System v14.0.0 following standard procedures. The raw event files were filtered using EPCHAIN and EMCHAIN to produce cleaned event lists for each of the EPIC-pn (Strüder et al., 2001) and EPIC-MOS (Turner et al., 2001) detectors, respectively. Science products were then produced using XMMSELECT, considering only single and double events for EPIC-pn, and single to quadruple events for EPIC-MOS. We extracted the source from a circular region of radius 40", while background was estimated from a large region of blank sky on the same detector as IRAS 05189–2524. Instrumental response files were generated with RMFGEN and ARFGEN for each detector. The good exposure is ~31 ks for EPIC-pn and ~36 ks for each of the two EPIC-MOS detectors. After performing the reduction separately for MOS1 and MOS2, we combined these data into a single spectrum using ADDASCASPEC. The MOS and PN spectra were grouped to have 25 counts per bin.

## 2.3 Spectral Analysis

We model the time-averaged *NuSTAR* and *XMM-Newton* spectra jointly in XSPEC v12.9.0 (Arnaud, 1996) using the  $\chi^2$  statistics. All uncertainties of the spectral pa-

Table 2.1: XSPEC Models

Model	XSPEC Components	Spectral Range
1	zpcfabs*powerlaw + mekal	0.3–30 keV
2	zpcfabs*(pexrav + zgauss) + mekal	0.3–30 keV
3a	zpcfabs*relxillp	2–30 keV
3b	(partcov*tbnew_feo)*relxillp	2–30 keV
4a	zpcfabs*XSTAR*relxillp	2–30 keV
4b	(partcov*tbnew_feo)*XSTAR*relxillp	2–30 keV

rameters are reported at the 90% confidence level. Cross-normalization constants are allowed to vary freely for *NuSTAR* FPMB and *XMM-Newton* MOS and PN, and assumed to be unity for FPMA. The values are within  $\sim 10\%$  of unity, as expected from Madsen et al. (2015b). For all the spectral fitting, we take into account the Galactic absorption by modifying the spectrum with a TBabs absorption model (Wilms et al., 2000). The Galactic column density is set to  $N_{\text{H,gal}} = 1.66 \times 10^{20} \text{ cm}^{-2}$  (Kalberla et al., 2005). We begin our spectral analysis of the broadband X-ray spectrum considering the band from 0.3 keV to 30 keV, as it becomes background-dominated above 30 keV. We first fit the spectrum with a power-law model subject to one partial covering neutral absorber modeled with zpcfabs, plus a mekal line emission model with its elemental abundances fixed at solar values (model 1, XSPEC models are listed in Table 2.1). The mekal component is used to model the thermal plasma contribution from the host galaxy. We find the best fit (reduced chi-square  $\chi^2/\text{d.o.f.} = 1425.8/1049$ ) with a photon index  $\Gamma = 2.29 \pm 0.04$  and a mekal temperature  $kT = 0.092_{-0.005}^{+0.010}$  keV. The covering fraction of the neutral absorber is well constrained as 98.89%, therefore contribution from the scattered power-law component is negligible above  $\sim 2$  keV. For simplicity, we fix the value at 99% from here on.

The data/model ratio plot shows strong signatures of disk reflection (Figure 2.1, panel b): a broad iron line peaking around 6.7 keV in the source rest-frame with a skewed shape extending down to  $\sim 3$  keV and residuals above 10 keV from the Compton reflection. In addition, there are possible absorption features of blue-shifted Fe K lines in both the *NuSTAR* and the *XMM-Newton* spectra, with the most evident absorption troughs lying in the vicinity of the Fe K-edge around 7.3 keV (Figure 2.2).

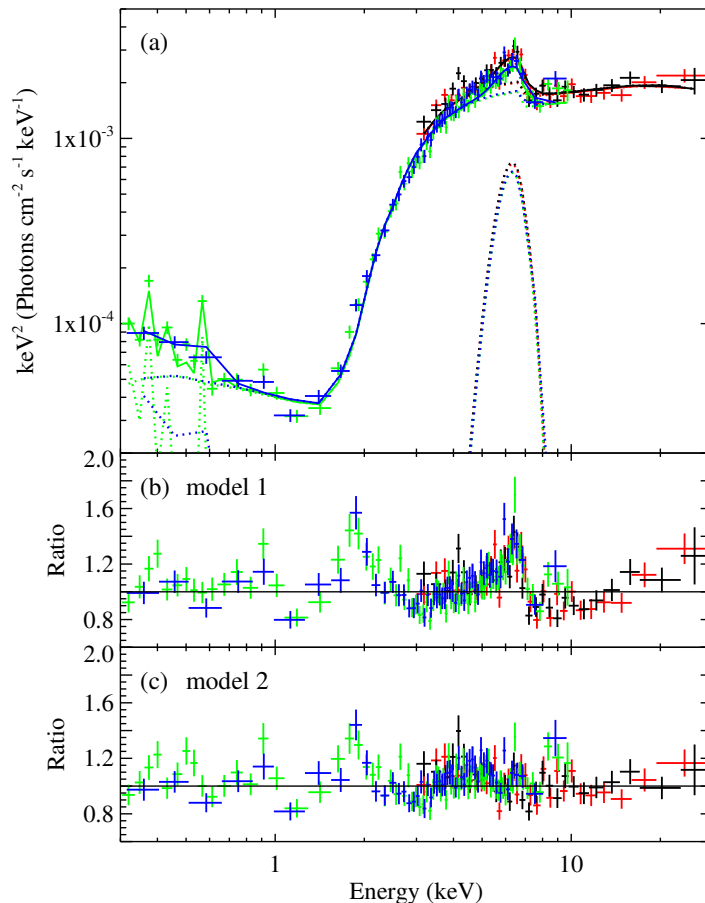


Figure 2.1: Spectral fitting of IRAS 05189–2524 with the phenomenological reflection model. (a) *XMM-Newton* PN (green), MOS (blue), *NuSTAR* FPMA (red) and FPMB (black) spectra of IRAS 05189–2524, with the best-fit phenomenological reflection model (model 2). (b) Data/model ratio after fitting an absorbed power-law plus a soft mekal component to the 0.3–30 keV spectrum (model 1). (c) Residuals of the phenomenological reflection model (model 2). The data are rebinned for display clarity.

### 2.3.1 Phenomenological Reflection Model

We then test fitting the reflection features with a phenomenological model by adding a neutral reflection component `pexrav` (Magdziarz & Zdziarski, 1995) and one Gaussian emission line with variable width using the model `zgauss` (model 2, see table 2.2). We freeze the centroid of the Gaussian emission line at 6.4 keV, the disk inclination angle at the default value ( $\cos i = 0.45$ ), the iron abundance at solar and include no high-energy cutoff (`foldE = 0`), as this simple model is not sensitive to these parameters. The fit is improved considerably with  $\Delta\chi^2/\Delta\text{d.o.f} = -231/-2$ . A broad Gaussian line with line width  $\sigma = 0.71^{+0.13}_{-0.11}$  keV and equivalent width (EW)  $\simeq 0.60$  keV is required to provide a decent fit for the iron line emission feature in the

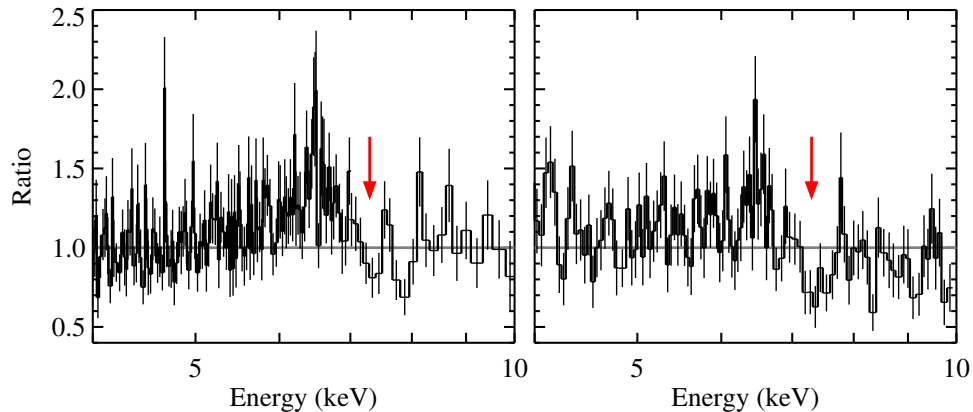


Figure 2.2: Possible absorption features between 7 keV and 8 keV marked by arrows in the residual plots of the absorbed power-law model (model 1). Left panel: *XMM-Newton* PN spectrum; right panel: *NuSTAR* FPMB spectrum.

Table 2.2: Spectral Fitting of IRAS 05189–2524 : Part I

Component	Parameter	Model 1	Model 2
ZPCFABS	$N_{\text{H}} (\times 10^{22} \text{ cm}^{-2})$	$8.82^{+0.27}_{-0.26}$	$8.30 \pm 0.21$
	$f_{\text{abs}}(\%)$	$98.89^{+0.08}_{-0.09}$	99*
POWER-LAW	$\Gamma$	$2.29 \pm 0.04$	...
MEKAL	kT (keV)	$0.092^{+0.010}_{-0.005}$	$0.087^{+0.006}_{-0.009}$
PEXRAV	$\Gamma$	...	$2.47 \pm 0.04$
	$R_{\text{ref}}$	...	$1.48^{+0.53}_{-0.44}$
ZGAUSS	LineE (keV)	...	6.40*
	$\sigma$ (keV)	...	$0.71^{+0.13}_{-0.11}$
$\chi^2/\text{d.o.f}$		1425.8/1049	1194.8/1047

Model 1 and model 2 fit the 0.3–30 keV broadband spectrum from *NuSTAR* and *XMM-Newton*. Parameters with  $\star$  are fixed values.

spectrum. However, a clear excess still remains in the residuals between 3 and 6 keV as would be expected from the red wing of a relativistically broadened iron line (Figure 2.1, panel c). Model 2 also gives a very steep power-law of  $\Gamma = 2.47 \pm 0.04$ . We do not attempt to interpret the intrinsic continuum steepness at this point, as this is only a phenomenological model.

We note that for both the simple absorbed power-law and the phenomenological reflection model, at least two extra emission features are present in the residuals around 0.9 and 1.9 keV. The 0.9 keV excess might be associated with O Ly $\alpha$  or Fe–L shell emissions, and the feature around 1.9 keV could be caused by ionized Si emis-

sion lines. The excesses cannot be adequately fitted with simple Gaussian emission line models, as they could be a complicated combination of ionized absorption, over-abundant metal lines and X-ray contribution from the high mass X-ray binary population in the star-forming regions. X-ray point-source emission correlates with galaxy star forming rate (SFR) in star-forming galaxies (Lehmer et al., 2010). At an SFR of  $\sim 80 M_{\odot} \text{ yr}^{-1}$  (Westmoquette et al., 2012), the 2–10 keV luminosity from the binary population is estimated to be  $1.4 \times 10^{41} \text{ ergs s}^{-1}$ , about 1% of the total luminosity, which is enough to dominate the soft emission of IRAS 05189–2524. Therefore, the soft part of the spectrum likely helps little to constrain the X-ray continuum from the AGN. In order to avoid the possible situation where the soft emission from the host galaxy is driving our modeling of the disk reflection features, we ignore the data below 2 keV from here on.

### 2.3.2 Self-consistent Disk Reflection Models

In Teng et al. (2015), the authors attempted to explain the reflection features observed in IRAS 05189–2524 by neutral reflection from the torus, which is commonly the case for Compton-thick AGNs. However, they found that neither the MYTorus (Murphy & Yaqoob, 2009) nor BNTorus model (Brightman & Nandra, 2011) could provide an adequate fit for the broadband spectrum, which ruled out the possibility of distant reflection. In order to explore the relativistic reflection hypothesis, we replace the `pexrav` and `zgauss` components in the phenomenological model with the self-consistent relativistic reflection model `relxill` (Dauser et al., 2014; García et al., 2014) (model 3a, see Table 2.2). We use `relxilllp` in the `relxill` model family, instead of using an empirical emissivity law; the emissivity is calculated directly in the lamp post geometry (Dauser et al., 2013). `Relxilllp` calculates a self-consistent reflection fraction. This could help us constrain the BH spin by shrinking the parameter space, as results with unphysical solutions of low BH spins with high reflection fractions can be ruled out by the assumption of a lamp-post geometry (for discussion, see Dauser et al., 2014). In order to measure the BH spin, we assume that the inner disk radius extends down to the ISCO. We fix the outer radius at the default value of  $400 R_g$  ( $R_g \equiv GM/c^2$  is the gravitational radius) as the model is not sensitive to this parameter, and the cutoff energy is allowed to vary in the fitting.

The `relxilllp` model yields a good fit to the 2–30 keV spectrum with  $\chi^2/\text{d.o.f.} = 862.0/859$  and no obvious excess in the residuals (Figure 2.3, panel b). The intrinsic X-ray continuum is steep, with the power-law photon index  $\Gamma = 2.04^{+0.02}_{-0.03}$ .

It is in the upper range of the photon index distribution observed in local Seyfert galaxies (e.g. Nandra & Pounds, 1994; Winter et al., 2009; Rivers et al., 2013), but less extreme than the previously published values for IRAS 05189–2524: e.g.  $\Gamma = 2.68_{-0.13}^{+0.30}$  (Teng et al., 2009),  $\Gamma = 2.51 \pm 0.02$  (Teng et al., 2015). Albeit lacking high quality data above 30 keV, the model is able to put a modest constraint on the high-energy cutoff  $E_{\text{cut}} = 55_{-7}^{+10}$  keV, as discussed in García et al. (2015a). Such sensitivity could come partly from the low energy part of the reflection spectrum ( $< 3$  keV). The location of the primary radiation source is found to be close to the disk  $h = 2.39_{-0.32}^{+0.80} R_g$ , with a rapid BH spin (dimensionless spin parameter  $a = 0.96_{-0.03}^{+0.02}$ ), and the self-consistent reflection fraction derived by the model is high ( $R_{\text{ref}} = 3.24$ ). The best-fit results also find an intermediate inclination of  $\theta = 42 \pm 2$  degrees and an ionization parameter<sup>1</sup>  $\log \xi = 3.02 \pm 0.02$  erg cm s<sup>-1</sup> for the accretion disk. We note that the iron abundance  $A_{\text{Fe}}$  is unusually high with best-fit value hitting the upper bound of the model of 10. But if we fix the iron abundance at solar in the `relxilllp` model, the fitting degrades considerably ( $\Delta\chi^2 \sim 130$ ) with a visible excess in the Fe K band.

A super-solar metal abundance is not uncommon among ULIRGs (e.g., Rupke et al., 2008). In the case of IRAS 05189–2524, based on the diagnostics of [N II]/H $\alpha$ , [S II]/H $\alpha$ , and [O I]/H $\alpha$  line ratios, an uncommonly high metallicity ( $>4Z_{\odot}$ )<sup>2</sup> is estimated for the outer galactic disk, or else some peculiar ionization effects are needed to explain the line ratio measurements (Westmoquette et al., 2012). If the metallicity is indeed high on the galactic scale in IRAS 05189–2524, it is more physically consistent to use neutral absorption models with super-solar abundances in our spectral fitting, as neutral absorbers normally reside far from the central BH.

In an attempt to further constrain the iron abundance, we tie the iron abundances of the neutral absorber and the disk reflection component by replacing the `zpcfabs` model with an improved model for neutral absorption `tbnew_feo`<sup>3</sup> convolved with the partial covering model `partcov` (model 3b, see Table 2.3). Both Fe and O abundances are variable parameters in the `tbnew_feo` model. We freeze the O abundance at solar, since it would not have a significant influence on our spectral fitting above 2 keV. As a result, the model finds a best-fit iron abundance  $A_{\text{Fe}} = 5.5_{-1.1}^{+2.5}$ , which is consistent with the measurement from Westmoquette et al. (2012). This

<sup>1</sup>The ionization parameter  $\xi = 4\pi F_x/n$ , where  $F_x$  is the ionizing flux and  $n$  is the gas density.

<sup>2</sup>Only an upper limit was put on the metallicity because the line ratios were outside the range predicted by the photoionization, shock, or AGN models used in the paper.

<sup>3</sup><http://pulsar.sternwarte.uni-erlangen.de/wilms/research/tbabs/>

Table 2.3: Spectral Fitting of IRAS 05189–2524 : Part II  
Self-consistent Disk Reflection Models

Component	Parameter	Model 3a	Model 3b	Model 4a	Model 4b
ZPCFABS	$N_{\text{H}} (\times 10^{22} \text{ cm}^{-2})$	$7.17^{+0.17}_{-0.16}$	$4.20^{+0.21}_{-0.27}$	$7.15^{+0.62}_{-0.53}$	$4.33^{+0.98}_{-0.33}$
	$f_{\text{abs}} (\%)$	99*	99*	99*	99*
	$A_{\text{Fe}}$	...	$5.5^{+2.5}_{-1.1}$	...	$5.0^{+u}_{-0.7}$
XSTAR	$N_{\text{H}} (\times 10^{22} \text{ cm}^{-2})$	...	...	$0.27^{+0.37}_{-0.27}$	$1.44^{+1.56}_{-1.44}$
	$\log \xi (\text{erg cm s}^{-1})$	...	...	$3.20^{+1.26}_{-0.68}$	$3.17^{+0.28}_{-0.39}$
	$V_{\text{out}} (\text{c})$	...	...	$0.13^{+0.02}_{-0.06}$	$0.12^{+0.02}_{-0.01}$
	$A_{\text{Fe}}$	...	...	$10.0^{+u}_{-3.3}$	$5.0^{+u}_{-0.7}$
RELXILLLP	$h (\text{GM}/\text{c}^2)$	$2.39^{+0.80}_{-0.32}$	$4.70^{+4.04}_{-1.99}$	$3.00^{+1.48}_{-0.87}$	$4.08^{+2.16}_{-1.60}$
	$a (\text{cJ}/\text{GM}^2)$	$0.96^{+0.02}_{-0.03}$	$0.96^{+u}_{-0.94}$	$0.96^{+u}_{-0.07}$	$0.98^{+u}_{-0.61}$
	$\theta (^{\circ})$	$42 \pm 2$	$44^{+2}_{-5}$	$41^{+5}_{-2}$	$51^{+4}_{-5}$
	$\Gamma$	$2.04^{+0.02}_{-0.03}$	$1.79^{+0.17}_{-0.14}$	$2.00^{+0.17}_{-0.19}$	$1.74^{+0.18}_{-0.17}$
	$\log \xi (\text{erg cm s}^{-1})$	$3.02 \pm 0.02$	$3.12^{+0.22}_{-0.11}$	$3.06 \pm 0.07$	$3.23^{+0.14}_{-0.18}$
	$A_{\text{Fe}}$	$10.0^{+u}_{-1.3}$	$5.5^{+2.5}_{-1.1}$	$10.0^{+u}_{-3.3}$	$5.0^{+u}_{-0.7}$
	$E_{\text{cut}} (\text{keV})$	$55^{+10}_{-7}$	$34^{+21}_{-10}$	$59^{+111}_{-24}$	$33^{+21}_{-10}$
$\chi^2/\text{d.o.f}$	862.0/859	860.6/859	854.8/856	854.7/856	

Model 3–4 fit the broadband spectrum with the part below 2.0 keV ignored. Parameters with  $\star$  are fixed values. Iron abundances ( $A_{\text{Fe}}$ ) are linked during the spectral fitting. Values with uncertainty marked with  $+u$  denote 90% confidence limits in excess of the upper bound of the model.

model provides a slightly better fit for the data ( $\chi^2/\text{d.o.f.} = 860.6/859$ ), with a higher coronal height  $h = 4.70^{+4.04}_{-1.99}$ , a less steep power-law continuum ( $\Gamma = 1.79^{+0.17}_{-0.14}$ ) and a cutoff at  $34^{+21}_{-10}$  keV, even lower than in the previous model. As a result, the reflection fraction is reduced to  $R_{\text{ref}} = 1.99$ . We note that here the cutoff energy is uncommonly low for an AGN, even compared with the lowest *NuSTAR* measurements (e.g., Ursini et al., 2015; Tortosa et al., 2017). This model generally has more uncertainty in the parameters, most notably, it places no constraint on the BH spin. Although the metallicities in the whole galaxy should be related, there is no solid justification to assume that the metallicities are the same in the BH vicinity and in the outer disk of the galaxy. However, we believe it is a reasonable simplification given the data quality; untying the iron abundances brings no obvious improvement to the fitting.

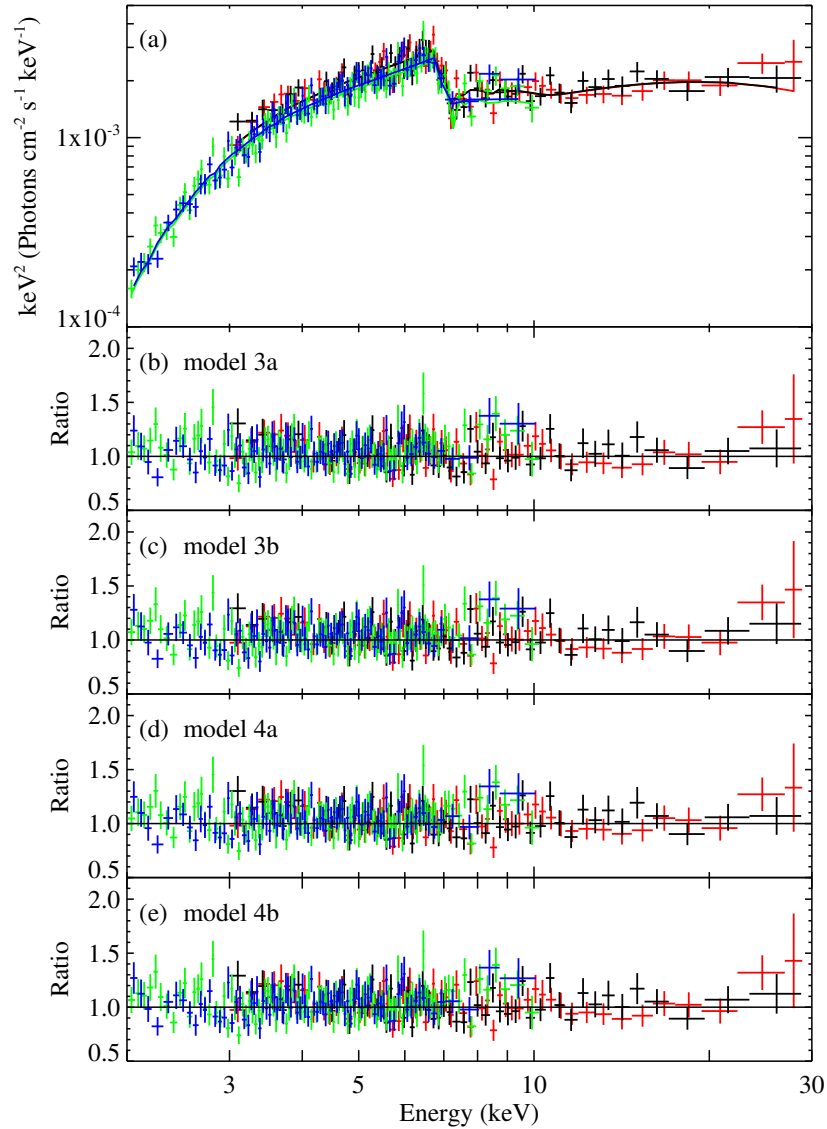


Figure 2.3: Spectral fitting of IRAS 05189–2524 with self-consistent disk reflection models. (a) *XMM-Newton* and *NuSTAR* spectra of IRAS 05189–2524 with the relativistic disk reflection model 4b. (b)–(e) Data/model ratio plots after fitting for the disk reflection component under four different absorption scenarios: (b) one neutral absorber with a solar iron abundance; (c) one neutral absorber with a variable iron abundance; (b) one neutral absorber with a solar iron abundance + one ionized absorber; (c) one neutral absorber with a variable iron abundance + one ionized absorber. The data are rebinned for display clarity. See Table 2.1 for the list of XSPEC models.

Given the possible ionized absorption features in the Fe K band and motivated by the presence of large-scale outflows in the host galaxy (e.g., Westmoquette et al., 2012; Bellocchi et al., 2013; Rupke & Veilleux, 2015), we add an ionized absorption component to account for any outflowing ionized absorbers. We modify the spectrum with an ionized absorption table model calculated by the XSTAR code (Kallman & Bautista, 2001) and tie its iron abundance with that of the `relxilllp` component. It is a physically reasonable requirement, since if the wind has extreme velocity, it most likely arises from the accretion disk, thus the same chemical abundances would naturally be expected. We first assume that the partial covering neutral absorber has a solar iron abundance (model 4a, see Table 2.3). The fitting results reveal an ionized absorber with a velocity  $v_{\text{out}} = 0.13_{-0.06}^{+0.02} c$  in the source rest-frame, which is well above the typical outflowing velocities of warm absorbers, about the common value found for UFOs (e.g., Tombesi et al., 2010). With an ionization parameter  $\log \xi = 3.06 \pm 0.07 \text{ erg cm s}^{-1}$ , the absorption should be dominated by Fe XXV. However the detection of a high-velocity ionized outflow is not significant, as it only brings marginal improvement to the fitting  $\Delta\chi^2/\Delta\text{d.o.f} = -7.2/-3$  and the difference not visually evident in the ratio plot. Other best-fit parameters are consistent with model 3a (without the ionized absorber). A rapidly spinning BH with  $a > 0.89$  is required to provide an adequate fit for the data.

We then reintroduce the neutral absorption model with a variable iron abundance (model 4b, see Table 2.3), and force the iron abundances of the disk reflection, the outflowing wind, and the neutral absorber to be the same. The model brings no further improvement for the fitting. But again, it reduces the iron abundance  $A_{\text{Fe}}$  to  $\sim 5$ , and since the iron abundance and the column density in the XSTAR model are degenerate parameters, the column density of the ionized outflow is estimated to be higher. Best-fit parameters of the disk reflection agree well with those given by model 3b, except for a slightly higher inclination of  $\theta = 51_{-5}^{+4}$  degrees. Only a low BH spin can be ruled out at the 90% confidence level by this model.

## 2.4 Discussion

We test four models under different absorption scenarios to physically fit for the disk reflection features in IRAS 05189–2524, which provide good and comparable fits to the 2–30 keV broadband spectrum (for details, see Table 2.3 and Figure 2.3). With the covering fraction of the neutral absorber fixed at 99%, there is also no large discrepancy in the continuum below 2 keV. Based on the limited S/N of the spectrum, we cannot distinguish which model better describes the data. A super-solar neutral

absorber is a reasonable requirement by the metallicity measurement of the galaxy from the literature, and it reduces the disk iron abundance to a less extreme value. However, detailed modeling of the intrinsic absorption causes apparent difficulty in disentangling the parameter degeneracies. Adding an ionized absorber modeled by XSTAR helps to account for the possible features of a high-velocity outflow in the Fe K band, but is not statistically strongly required. For three out of the four models, we can rule out a slow or retrograde BH spin at the 90% confidence level. In model 3a and 4a, a rapidly spinning BH is favored (for the spin constraints, see Figure 2.4). In addition, we consider the possible contribution from distant reflection produced in the torus or BLR, but including an extra `xillver` component does not improve the fitting.

#### 2.4.1 Super-solar Iron Abundance

In our spectral analysis of IRAS 05189–2524, all acceptable fits require a super-solar iron abundance for the disk reflection component, but the value is not very well constrained. The primary effect of the iron abundance parameter is to change the relative strength of the iron line and the Compton hump. Because of the low net number counts at the high energy end of the *NuSTAR* spectra, the shape of the Compton hump is not well constrained, which could make it difficult to obtain a tight constraint of the iron abundance. We note that a similar over-abundance in iron has been reported in a number of AGNs (e.g., Risaliti et al., 2009; Patrick et al., 2011) and stellar-mass BHs (e.g., García et al., 2015b), with the examples of well-known narrow-line Seyfert 1 galaxies (NLSy1s) 1H 0707–495 (Dauser et al., 2012; Kara et al., 2015) and IRAS 13224–3809 (Fabian et al., 2013). In the case of IRAS 05189–2524, the galaxy is undergoing intense star formation, so it is expected to be iron enriched. Since super-solar metallicities were indicated via spatially resolved optical spectroscopy in the outer disk and the nuclear region of the galaxy (Westmoquette et al., 2012), it is physically reasonable for the iron abundance to be high in the accretion disk.

#### 2.4.2 Absorption-dominated Models

Absorption from material lying relatively distant from the BH has frequently been proposed as an alternative interpretation of relativistic disk reflection (e.g., Miller et al., 2008, 2009). To investigate whether the excesses in the Fe K band and above 10 keV observed in IRAS 05189–2524 can be fully accounted by absorption-dominated models (without the reflection component), we test modeling the 2–

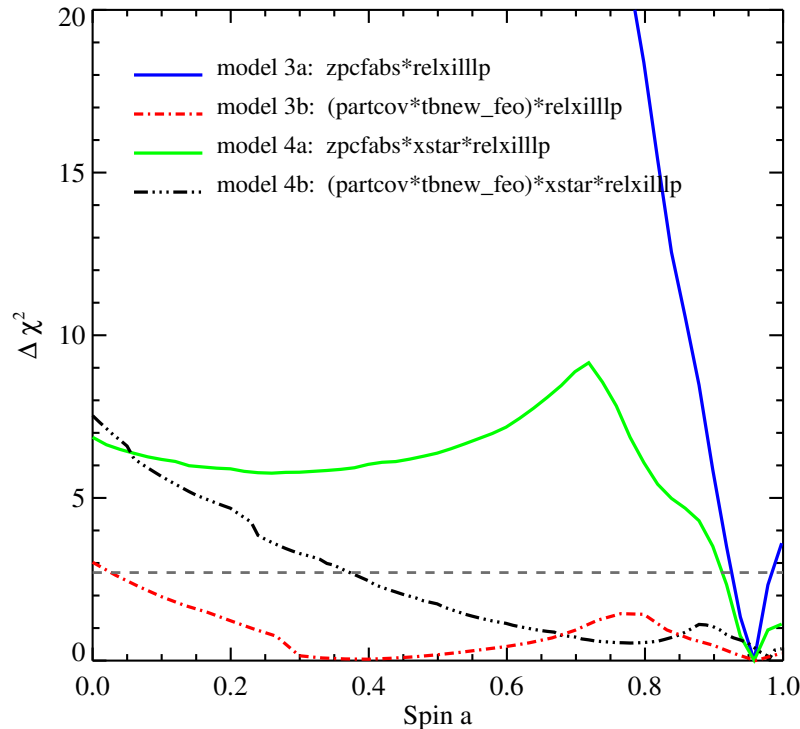


Figure 2.4:  $\Delta\chi^2$  as a function of BH spin for the relativistic disk reflection modeling under four different absorption scenarios. The dashed line marks the 90% confidence limit. Model 3a and 4a favor a high BH spin of  $a \gtrsim 0.9$ . The constraint weakens considerably when we consider a variable iron abundance for the neutral absorber in model 3b and 4b.

30 keV spectrum with single and dual partial covering neutral absorption models with variable iron abundances. For the single-absorber model<sup>4</sup>, we fix the covering fraction at 99% to avoid large deviation from the data below 2 keV, the same way as in all the previous modeling. With  $\Delta\chi^2 = 215.6$  compared to model 3b, this scenario can be easily ruled out. The dual-absorber model<sup>5</sup> with an iron abundance  $A_{\text{Fe}} = 2.2^{+0.2}_{-0.4}$  provides a better fit for the data, which requires one full covering absorber with the column density  $N_{\text{H,abs1}} = 6.01^{+0.14}_{-0.93} \times 10^{22} \text{ cm}^{-2}$  and another of the coverage fraction  $f_{\text{abs2}} = 64 \pm 5\%$  with  $N_{\text{H,abs2}} = 1.92^{+0.58}_{-0.18} \times 10^{23} \text{ cm}^{-2}$ . However, it is still statistically worse than the reflection-dominated model with  $\Delta\chi^2 = 75.6$ . The model leaves a broad excess in the Fe K band and also fails to produce the shape of the Compton hump above 10 keV (see Figure 2.5(b)), resembling the case in NGC 1365 (Risaliti et al., 2013).

<sup>4</sup>(partcov\*tbnew\_feo)\*powerlaw

<sup>5</sup>(partcov\*tbnew\_feo)\*(partcov\*tbnew\_feo)\*powerlaw

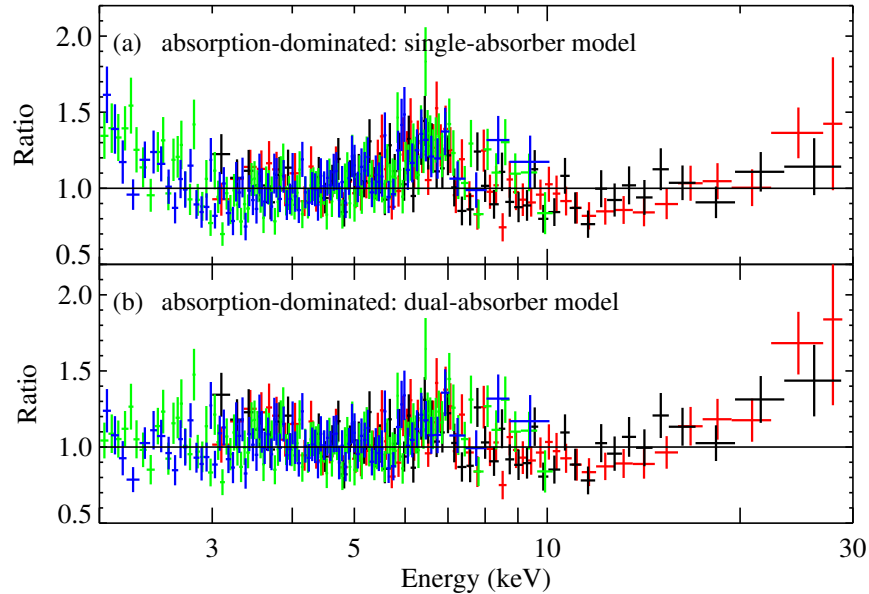


Figure 2.5: Data/model ratio plots of the absorption-dominated models: (a) one neutral partial covering absorber with the covering fraction fixed at 99% and a variable iron abundance; (b) two partial covering absorbers of free covering fractions and linked iron abundances. The data are rebinned for display clarity.

### 2.4.3 Eddington Ratio and Outflow

The time-averaged X-ray flux of IRAS 05189–2524 observed by *NuSTAR* is  $7.1 \times 10^{-12}$  ergs cm $^{-2}$  s $^{-1}$  in the 2–30 keV band, corresponding to an intrinsic luminosity of  $3.0 \times 10^{43}$  ergs s $^{-1}$  during the 2013 observation. Using the central velocity dispersions measured from the Ca II Triplet line widths (Rothberg et al., 2013) and the  $M_{\text{BH}}-\sigma$  relation (Tremaine et al., 2002), the BH mass of IRAS 05189–2524 is estimated to be  $M_{\text{BH}} = 4.2 \times 10^8 M_{\odot}$ . We note that the BH mass derived from the Ca II Triplet here is more than ten times larger than the value measured from CO band heads in the near infrared (Dasyra et al., 2006). As discussed in Dasyra et al. (2006), CO band heads are often representative of young stellar populations, which could lead to systematically lower BH masses for ULIRGs. Combined with the bolometric luminosity inferred from the infrared (Teng et al., 2015), IRAS 05189–2524 is measured to be accreting at an Eddington rate  $\lambda_{\text{Edd}} = L_{\text{bol}}/L_{\text{Edd}}$  of 0.12. Based on the correlation between the photon indexes and the Eddington ratios of AGNs (Shemmer et al., 2008; Brightman et al., 2013, 2016), a photon index of  $\Gamma \sim 2.0$  would be expected. The photon index obtained by our disk reflection modeling with a low cutoff energy is  $\Gamma \simeq 1.7 - 2.0$ , which is consistent with the expected value given the scatter of the relation.

In our spectral modeling, we did not detect significant disk winds. Fitting the possible absorption features in the spectrum with a simple Gaussian absorption line using the `gabs` model would reach similar  $\chi^2$  as the physical XSTAR grid, with the best-fit line centroid at  $\sim 7.33$  keV. Although the effect of this ionized absorber on the continuum is subtle, we include it in the spectral fitting, as even mild absorption lying around the Fe K-edge could influence the BH spin measurement, which is sensitive to the profile of the broad iron line. The power of an outflow scales with the amount of matter being ejected (King & Pounds, 2015). With the rather small column density measured for the ionized absorption compared with that of massive disk winds found in other AGNs (e.g., IRAS 11119+3257, Tombesi et al., 2015), even if an UFO indeed existed in IRAS 05189–2524 at the epoch of the observation, it was probably not energetic enough to have a large impact on its galactic environment.

## 2.5 Summary and Conclusion

We detect disk reflection features of a broad iron line and a Compton reflection hump in IRAS 05189–2524, a Seyfert 1h galaxy and ULIRG, from the *NuSTAR* and *XMM-Newton* data taken in 2013. With the broadband X-ray spectrum, an alternative dual partial covering absorber explanation can be ruled out. Physically modeling with the self-consistent relativistic reflection model `relxilllp` finds that the reflection is likely to be generated from the inner range of a rapidly spinning BH. The high reflection fraction measured ( $R_{\text{ref}} \simeq 2.0\text{--}3.2$ ) indicates that the reflection area is close to the BH, where relativistic light bending effects boost the reflection signature (Miniutti & Fabian, 2004), suggesting the coronal illuminating source is compact. However, due to the complex effects from neutral and ionized absorption and the limited S/N data, parameter degeneracies preclude putting a tight, model-independent estimation on the BH spin.

As a merger system, IRAS 05189–2524 is an interesting target for the spin measurement, as BH spins are believed to encode information about the galaxy evolution history (Berti & Volonteri, 2008), and ULIRGs have been proposed as an important transition phase in the hierarchical evolution model of galaxies (Hopkins et al., 2006; Sanders et al., 1988). Simulations predict it is uncommon for mergers to yield large spins, unless alignment of the spins of the merging BHs with the orbital angular momentum is very efficient (Berti & Volonteri, 2008).

With Fe K band absorption features marginally evident in the residuals, the detection of a high-velocity ionized wind is not statistically significant. Also, we find that the iron abundance of the neutral absorber is strongly degenerated with the BH spin. Future observations with higher S/N data could help disentangle the reflection component from the underlying continuum and the various absorption effects. Assuming the source remains at the flux level observed in 2013, if the ionized absorption indeed exists in IRAS 05189–2524, simulations indicate that the XSTAR component would be significantly required by datasets with more than  $\sim 2$  times of exposure, leading to a  $>3\sigma$  detection of the ionized absorption features. With longer observations (500 ks *NuSTAR* and 300 ks *XMM-Newton* exposures), it would be possible to obtain the BH spin to within  $\sim 30\%$  of uncertainty under all the different absorption scenarios we have discussed above.

### **Acknowledgments**

We thank the anonymous referee for helpful comments that improved the paper. M. B. acknowledges support from NASA Headquarters under the NASA Earth and Space Science Fellowship Program, grant NNX14AQ07H. This work was supported under NASA Contract No. NNG08FD60C, and made use of data obtained with *NuSTAR*, a project led by Caltech, funded by NASA, and managed by NASA/JPL, and has utilized the NUSTARDAS software package, jointly developed by the ASDC (Italy) and Caltech (USA). We thank the *NuSTAR* Operations, Software, and Calibration teams for support with the execution and analysis of these observations. This research has also made use of data obtained with *XMM-Newton*, an ESA science mission with instruments and contributions directly funded by ESA Member States.

## SPECTRAL AND TIMING PROPERTIES OF IGR J17091–3624 IN THE RISING HARD STATE DURING ITS 2016 OUTBURST

Xu Y., García J. A., Fürst F., Harrison F. A. (2017). “Spectral and Timing Properties of IGR J17091–3624 in the Rising Hard State During Its 2016 Outburst.” *The Astrophysical Journal*, 851(2):103. doi: 0.3847/1538–4357/aa9ab4.

### Abstract

We present a spectral and timing study of the *NuSTAR* and *Swift* observations of the black hole candidate IGR J17091–3624 in the hard state during its outburst in 2016. Disk reflection is detected in each of the *NuSTAR* spectra taken in three epochs. Fitting with relativistic reflection models reveals that the accretion disk is truncated during all epochs with  $R_{\text{in}} > 10 r_{\text{g}}$ , with the data favoring a low disk inclination of  $\sim 30^\circ$ – $40^\circ$ . The steepening of the continuum spectra between epochs is accompanied by a decrease in the high energy cut-off: the electron temperature  $kT_e$  drops from  $\sim 64$  keV to  $\sim 26$  keV, changing systematically with the source flux. We detect type-C QPOs in the power spectra with frequency varying between 0.131 Hz and 0.327 Hz. In addition, a secondary peak is found in the power spectra centered at about 2.3 times the QPO frequency during all three epochs. The nature of this secondary frequency is uncertain, however a non-harmonic origin is favored. We investigate the evolution of the timing and spectral properties during the rising phase of the outburst and discuss their physical implications.

**Keywords:** accretion, accretion disks – black hole physics – X-rays: binaries – X-rays: individual (IGR J17091–3624)

### 3.1 Introduction

Most Galactic black hole binaries detected to date are transient X-ray sources that exhibit recurrent bright outbursts. During the onset of the month-to-year long outbursts, the sources transition from the low/hard state to the high/soft state through relatively short-lived intermediate states. In the hard state, the sources typically have hard spectra with a power-law index  $\Gamma \sim 1.7$  and the thermal disk component is cool and faint (usually not detected above 2 keV). In the frequency domain, type-C quasi-periodic oscillations (QPOs) ranging in frequency from  $\sim 0.1$ –10 Hz have

been frequently detected, and they are considered as potential probes of the strong-gravity dominated flow dynamics (see Remillard & McClintock, 2006; Fender & Belloni, 2012, for relevant reviews).

The standard paradigm of accretion disks in black hole binaries is that the inner disk radius extends to the innermost stable circular orbit (ISCO) in the soft state, whereas it is truncated at a larger distance during the hard state. There are two methods widely used to measure the inner disk radius from X-ray spectral modeling: determining the disk emission area from its thermal disk blackbody component (e.g., Zhang et al., 1997; McClintock et al., 2014), or estimating the relativistic distortion effects on the disk reflection features (e.g., Fabian et al., 1989; Reynolds, 2014).

While it is generally well supported by observations that the disk radius extends to the ISCO at high accretion rates in the soft state (e.g., Steiner et al., 2010; Tomsick et al., 2014; Walton et al., 2016), the disk truncation interpretation of the hard state spectrum is still highly debated (e.g., Kolehmainen et al., 2014; Fürst et al., 2015; García et al., 2015b). Cool disks are common in the brightest phases of the hard state; modeling thermal continuum emission in this state is difficult, but some continua point to small inner disk radii (e.g., Miller et al., 2006b; Rykoff et al., 2007; Reynolds & Miller, 2013). Evidence that disks may remain at the ISCO in bright phases of the hard state also comes from reflection spectroscopy (e.g., Miller et al., 2015b). In addition, it has been noticed that the measurements of truncated disks could be biased by photon pile-up distortions in some cases (e.g., Miller et al., 2010), with the best evidence of disk truncation (a narrow Fe K line) only observed in GX 339-4 by *Suzaku* at the luminosity approximately an order of magnitude below the brightest parts of the hard state (Tomsick et al., 2009). With the high sensitivity of *NuSTAR* for reflection spectroscopy and its triggered read-out (Harrison et al., 2013), new observations in the hard state can help to better understand the disk evolution of black hole binaries.

IGR J17091–3624 is a transient Galactic black hole candidate discovered with *INTEGRAL* in 2003 (Kuulkers et al., 2003). During its brightest outburst in 2011 (Krimm et al., 2011), IGR J17091–3624 was regularly monitored with *Swift* and *Rossi X-ray Timing Explorer*. The source revealed a rich variety of variability behavior, with both low- and high-frequency QPOs detected (Altamirano et al., 2011a; Rodriguez et al., 2011; Altamirano & Belloni, 2012). After following the canonical evolution track for a black hole candidate at the beginning of the outburst, the

source entered the soft state and was found to display a number of peculiar variability patterns. Most notably, the so-called “heartbeat” or  $\rho$  state was detected, which had only been seen previously in the bright Galactic binary GRS 1915+105 (Altamirano et al., 2011b). In addition, several new variability states were recently discovered in IGR J17091–3624 that had never been reported in GRS 1915+105 (Pahari et al., 2012; Court et al., 2017).

Despite its similar timing properties to GRS 1915+105, IGR J17091–3624 is more than 10–50 times fainter. Assuming that the exceptional variability patterns are a result of emitting close to the Eddington limit, IGR J17091–3624 either hosts an extremely small black hole  $<3 M_{\odot}$  (for a distance of less than 17 kpc), or is very distant (Altamirano et al., 2011b). However, both scenarios are in tension with other independent observations: for example, based on the empirical relations between the photon index and QPO frequency combined with constraints from spectral modeling, the black hole mass of IGR J17091–3624 is estimated to be in the range of  $8.7 M_{\odot}$  to  $15.6 M_{\odot}$  (Iyer et al., 2015); meanwhile, the source distance inferred from simultaneous multi-wavelength observations is between  $\sim 11$  to  $\sim 17$  kpc (Rodríguez et al., 2011). Assumptions about other properties of the system, such as a low black hole spin or a high disk inclination have been invoked to help reconcile this discrepancy (Capitanio et al., 2012; Rao & Vadawale, 2012). So far, with no direct measurement of the basic properties of IGR J17091–3624 (the distance, the inclination, and the black hole mass and spin all remain unknown), it is difficult to distinguish among the different scenarios proposed and investigate the physical origin of its peculiar behavior.

In February 2016, IGR J17091–3624 started to show renewed activity (Miller et al., 2016a), and subsequent Swift monitoring confirmed that the source rose through the hard state before transitioning to the soft state at a comparable flux level with its outburst in 2011. In this paper, we perform spectral and timing analyses of three *NuSTAR* and simultaneous *Swift* observations taken during the rising phase of the hard state. In Section 3.2, we describe the observations and the data reduction. Section 3.3 provides the details of our spectral fitting and timing analyses. We present a discussion in Section 3.4 and summarize our results in Section 3.5.

### 3.2 Observations and Data Reduction

IGR J17091–3624 was observed by *NuSTAR* (Harrison et al., 2013) three times in the hard state during the rising phase of its 2016 outburst, on March 7, 12, and

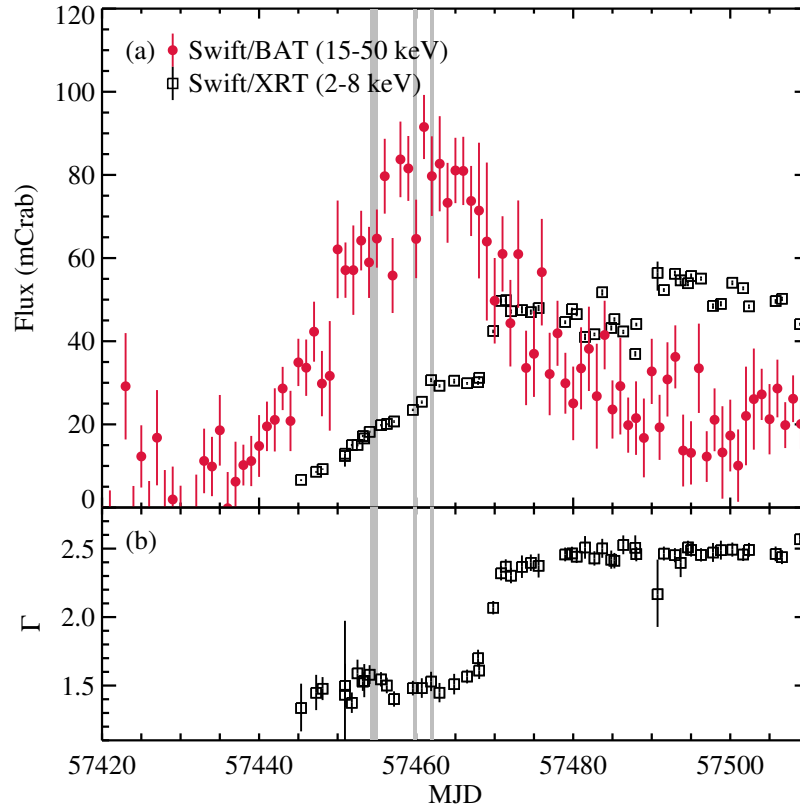


Figure 3.1: *Swift* monitoring of the 2016 outburst of IGR J17091–3624. (a) *Swift* monitoring of the 2016 outburst of IGR J17091–3624. The 15–50 keV BAT light curve is from the *Swift*/BAT hard X-Ray monitor, which is rescaled to the unit mCrab based on the Crab rates in the instrument band (Krimm et al., 2013). The XRT light curve is converted to mCrab from the energy flux in 2–8 keV. (b) Photon index derived by fitting the *Swift*/XRT data with an absorbed power-law model. The gray shaded areas mark the three *NuSTAR* observations, which caught the source in the hard state before it started to enter the soft state around MJD 57470.

14, about one week before the source started to enter the soft state (see Table 3.1 for the list of observations considered in this work). *Swift*/XRT monitored the entire outburst of IGR J17091–3624 with frequent 1–2 ks snapshots from February 26 to October 4. Figure 3.1 shows the evolution of the soft and hard X-ray band flux during the outburst measured by the *Swift* X-ray Telescope (XRT) (Burrows et al., 2005) and Burst Alert Telescope (BAT) (Krimm et al., 2013). The *Swift*/XRT data were taken in the Windowed Timing mode to avoid photon pile-up. There are simultaneous *Swift*/XRT data for all the three *NuSTAR* observations, providing coverage of the soft X-ray band (see Table 3.1).

Table 3.1: *NuSTAR* and Simultaneous *Swift* Observations

Epoch	Instrument	ObsID	Start Time (UTC)	E. T. (ks)	C. R. (s <sup>-1</sup> )
1	<i>NuSTAR</i>	80001041002	2016-03-07 02:01	43.3	16.5
	<i>Swift</i> /XRT	00031921099	2016-03-07 01:49	1.46	7.3
2	<i>NuSTAR</i>	80202014002	2016-03-12 14:11	20.2	21.4
	<i>Swift</i> /XRT	00031921104	2016-03-12 13:53	1.95	8.9
3	<i>NuSTAR</i>	80202014004	2016-03-14 19:26	20.7	23.6
	<i>Swift</i> /XRT	00031921106	2016-03-14 21:39	1.03	10.4

The exposure time and count rates of *NuSTAR* quoted here are the values from FPMA.

### 3.2.1 *NuSTAR*

We processed the *NuSTAR* data using v.1.6.0 of the NuSTARDAS pipeline with *NuSTAR* CALDB v20170120. After the standard data cleaning and filtering, the total exposure time is 43.3 ks, 20.2 ks, and 20.7 ks for the three observations. For each observation, the source spectra and light curves were extracted at the position of IGR J17091–3624 within the radius of 100'' from the two *NuSTAR* focal plane modules (FPMA and FPMB). Corresponding background spectra were extracted from source-free areas on the same chip using polygonal regions. In the first *NuSTAR* observation (ObsID 80001041002), the source region was contaminated by the stray light from a nearby bright source GX 349+2. In this case, we also placed the background region in the part of the field illuminated by the stray light. We note the influence from the stray light is minimal, as the background only contributes  $\sim 2\%$  to the total count rate. The *NuSTAR* spectra were grouped to have a signal-to-noise (S/N) ratio of at least 20 per bin after background subtraction.

For the *NuSTAR* timing analysis, we first applied barycenter correction to the event files to transfer the photon arrival times to the barycenter of the solar system using JPL Planetary Ephemeris DE-200. We then generated cross-power density spectra (CPDS) using MaLTPyNT (Bachetti, 2015) from the cleaned event files. MaLTPyNT, developed for *NuSTAR* timing analysis, properly treats orbital gaps and uses the CPDS as a proxy for the power density spectrum. The CPDS uses the signals from two independent focal plane modules, FPMA and FPMB, and the real part of the CPDS provides a measure of the signal that is in phase between the two modules. Thus, this method helps to remove the spurious distortion to the power-density spectrum introduced by the instrumental dead time (for details, see Bachetti et al., 2015). We generated the CPDS with the binning time of  $2^{-8}$  s and in 512 s

long intervals. For all the power spectra, we used the root-mean-square (rms) normalization, and geometrically rebinned the power spectra with a factor of 1.03 to increase the S/N of the frequency bins and produce nearly equally spaced bins in the logarithmic scale.

### 3.2.2 Swift

The *Swift*/XRT data were processed using `xrtpipeline` v.0.13.2 with XRT CALDB v20160609 to produce clean event files. We extracted the source spectra with `xselect` from a circular region with a radius of 20 pixels centered on the position of IGR J17091–3624. The background was extracted from an annulus area with the inner and outer radii of 80 pixels and 120 pixels, respectively. The data were filtered for grade 0 events only and we used `swxwt0s6_20131212v015.rmf` for the response matrix. Ancillary response files were generated with `xrtmkarf` incorporating exposure maps to correct for the bad columns. Finally, we rebinned the data to have a S/N greater than 5 for each energy bin.

## 3.3 Analysis

### 3.3.1 Spectral Modeling

We model the simultaneous *NuSTAR* and *Swift*/XRT spectra in XSPEC v12.9.0n (Arnaud, 1996) using  $\chi^2$  statistics. For spectral fitting, we adopt the cross-sections from Verner et al. (1996) and abundances from Wilms et al. (2000). All parameter uncertainties are reported at the 90% confidence level for one parameter of interest. Cross-normalization constants are allowed to vary freely for *NuSTAR* FPMB and *Swift*/XRT, and assumed to be unity for FPMA. The values are within 5% of unity for Epoch 1 and Epoch 2, as expected from Madsen et al. (2015b). In Epoch 3, the *Swift* normalization is  $\sim 13\%$  higher than *NuSTAR*. We note that it is probably caused by the exposure correction uncertainty when the source lies close to the CCD bad columns, which is sensitive to the exact source position and can be affected by the spacecraft pointing stability<sup>1</sup>.

All three *NuSTAR* observations detect IGR J17091–3624 across the entire instrument bandpass. To highlight the reflection features, we fit the *NuSTAR* spectra with a simple absorbed power-law model, `TBabs*powerlaw` in XSPEC, using only data in the 3–5 keV and 8–12 keV energy ranges. As shown in Figure 3.2, the residuals display asymmetric broad iron lines around 4–7 keV and show evidence for changes in the cut-off energy as the source luminosity increases. From this simple model,

<sup>1</sup>[http://www.swift.ac.uk/analysis/xrt/digest\\_sci.php](http://www.swift.ac.uk/analysis/xrt/digest_sci.php)

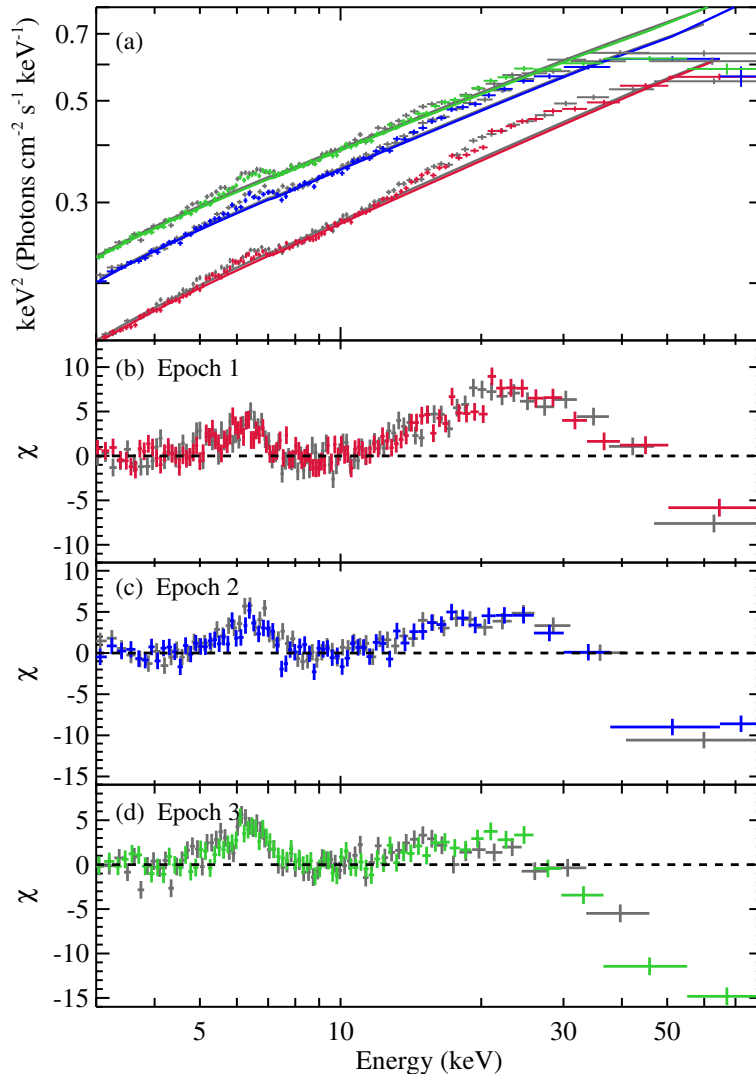


Figure 3.2: IGR J17091–3624 spectra observed by *NuSTAR* modeled with the absorbed power-law model. (a) Unfolded IGR J17091–3624 spectra from the three *NuSTAR* observations. (b)–(d) Residuals in  $\chi$  from the simple absorbed power-law model. FPMA spectra taken in Epoch 1, 2, and 3 are marked in red, blue, and green, respectively. For comparison, FPMB spectra are all in gray. The data are rebinned for display clarity.

we also detect a slight steepening in the power-law slope:  $\Gamma$  increases from  $\sim 1.55$  to  $\sim 1.60$  from Epoch 1 to Epoch 3. No parameter uncertainties are calculated here as the fits are too poor to determine meaningful parameter uncertainties.

### 3.3.1.1 Joint Fits with Disk Reflection Models

Given the disk reflection features observed (see Figure 3.2), we model the *NuSTAR* and *Swift* spectra simultaneously with the self-consistent reflection model `relxill`

v0.5b (Dauser et al., 2014; García et al., 2014). We fit the *NuSTAR* and *Swift* spectra in the bands 3–79 keV and 1–10 keV, respectively. We ignore the *Swift* data below 1 keV to avoid possible low-energy residuals known to be present in the XRT Windowed Timing mode data of some absorbed sources<sup>2</sup>. We note that due to the relative weakness of the disk reflection component, as displayed in Figure 3.2(a), reflection features are not detected by *Swift*. Although measurements of the reflection spectra are dominated by the *NuSTAR* data, extending the spectral fitting to the soft energy band helps to constrain the absorption column density and the general continuum slope.

We first fit the data with the unblurred version of the reflection model `xillver` (García & Kallman, 2010) multiplied by a model that accounts for neutral Galactic absorption: `TBabs*xillver`. To maximize the parameter constraints, we jointly fit the spectra taken at the three epochs and link the values for the absorption column density  $N_{\text{H}}$ , the iron abundance  $A_{\text{Fe}}$  and the disk inclination  $i$ , which are normally expected to remain constant. Other relevant parameters (the ionization parameter  $\xi$ , photon index  $\Gamma$ , high energy cut-off,  $E_{\text{cut}}$  and reflection fraction  $R_{\text{ref}}$ ) are allowed to vary between epochs. The best-fit result yields the reduced-chi-square  $\chi^2_{\nu} = \chi^2/\nu = 3851.1/3629 = 1.061$ , where  $\nu$  is the number of degrees of freedom. The model leaves obvious residuals in the Fe K band (see Figure 3.3), suggesting that relativistic blurring is required to provide an adequate fit for the data.

### 3.3.1.2 Power-law Emissivity Index

In order to account for the relativistic effects and to better describe the changes in the high energy rollover as displayed in Figure 3.1, we fit the spectra with the relativistic reflection model `relxillCp` (Model 1a). It uses a thermally Comptonized input continuum `nthcomp` (Zdziarski et al., 1996; Życki et al., 1999) and parameterizes the high energy cut-off by the coronal electron temperature  $kT_e$ . The disk emissivity profile in `relxillCp` is described by a broken power law with three parameters: the inner and the outer emissivity indices  $q_{\text{in,out}}$  and the break radius  $R_{\text{br}}$ . We assume a canonical emissivity profile  $\epsilon(r) \propto r^{-3}$  by fixing both  $q_{\text{in}}$  and  $q_{\text{out}}$  at 3, which is expected for the outer parts of a standard Shakura–Sunyaev disk (Dauser et al., 2013). If  $q_{\text{in}}$  and  $R_{\text{br}}$  are allowed to vary individually for each epoch, the fit would not be improved and the data cannot constrain the extra parameters. We fix the outer disk radius at  $400 R_{\text{g}}$  and allow the inner disk radius  $R_{\text{in}}$  to vary to test the

<sup>2</sup>[http://www.swift.ac.uk/analysis/xrt/digest\\_cal.php](http://www.swift.ac.uk/analysis/xrt/digest_cal.php)

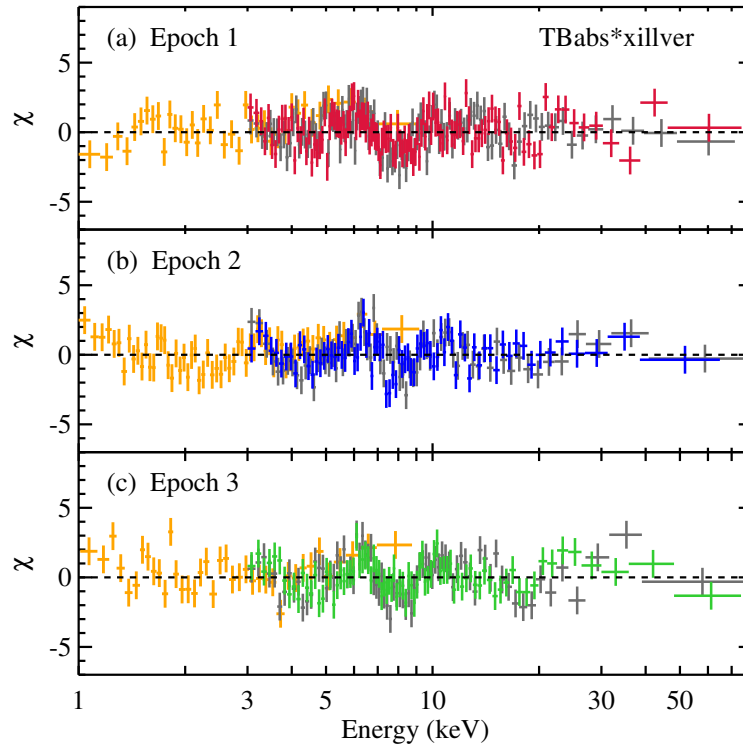


Figure 3.3: Residuals of IGR J17091–3624 spectra from the unblurred reflection model. The same color scheme is used as in Figure 3.2 for the *NuSTAR* data. *Swift*/XRT spectra are all plotted in yellow. The plots are in units of  $\chi$  so that *Swift* residuals are of comparable magnitude with *NuSTAR*.

disk truncation hypothesis. There is no well-constrained black hole spin measurement for IGR J17091–3624; previous estimates range from a low or negative spin (Rao & Vadawale, 2012) to a high spin (Reis et al., 2012). We first simply fix the dimensionless spin parameter  $a$  ( $a \equiv cJ/GM^2$ ) at its maximum value of 0.998. As demonstrated below, the choice of spin does not significantly affect our results.

The broad-band X-ray spectra can be well fitted by Model 1a with no obvious residuals (Figure 3.4). The reduced-chi-square is very close to unity ( $\chi^2_{\nu} = 3627.0/3626 = 1.000$ ), indicating statistically a very good fit. Using the relativistic reflection model improves the fit significantly by  $\Delta\chi^2 = 224$  compared to the unblurred reflection model. The only excess noticeable is around 3.0–3.5 keV in the *NuSTAR* spectra at Epoch 2 (Figure 3.4(c)), which is possibly related to small calibration uncertainties near the edge of the instrument bandpass and is not statistically important. We include this part in the spectral modeling as it helps to constrain the overall power-law slope. The soft disk component is either too cool to contribute much above 1 keV or intrinsically too faint to be detected by *Swift*/XRT, and a disk blackbody component

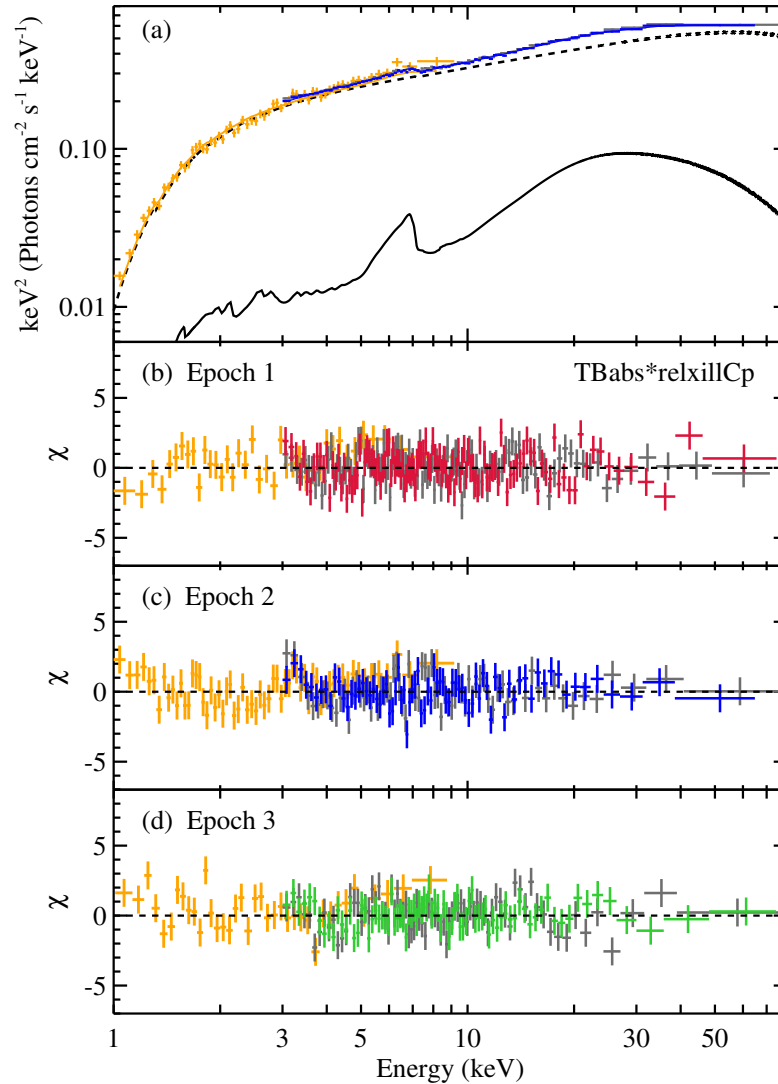


Figure 3.4: IGR J17091–3624 spectra with the best-fit models. (a) Unfolded *NuSTAR* and *Swift* spectra with Model 1a. For clarity, only the Epoch 2 data are displayed. Black solid and dashed lines indicate the relative contributions from the disk reflection and the coronal continuum in Model 1a. The normalization of the plotted model is the value corresponding to FPMA. (b)–(d) Residuals of Model 1a at the three epochs. The same color scheme is used as in Figure 3.4.

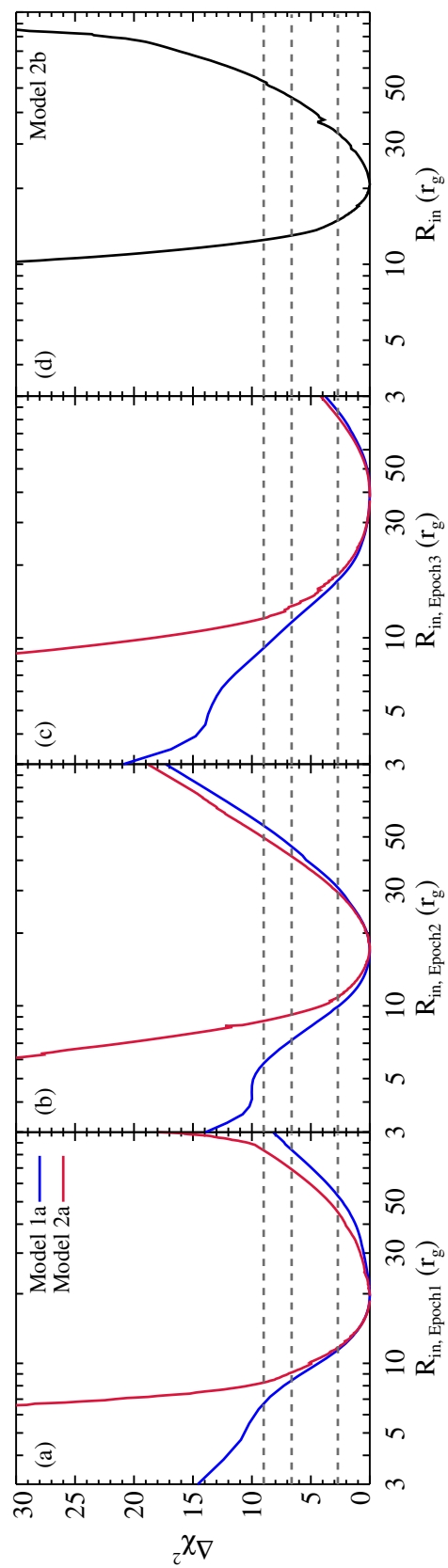


Figure 3.5:  $\Delta\chi^2$  contours of the inner disk radius  $R_{\text{in}}$  obtained from Model 1a, 2a and 2b. The dashed lines indicate the 90%, 99%, and  $3\sigma$  confidence levels for one parameter of interest.

is not required by our spectral modeling. From the best-fit parameters, we confirm the relatively high obscuration in IGR J17091–3624, with the equivalent hydrogen column density  $N_{\text{H}} = (1.58 \pm 0.03) \times 10^{22} \text{ cm}^{-2}$ , consistent with previous measurements (e.g., Rodriguez et al., 2011; Capitanio et al., 2012). After including the reflection component in the spectral fitting, we measure a slightly steeper power-law index ( $\Gamma \simeq 1.67\text{--}1.70$ ) compared to the simple absorbed power-law model. We confirm the existence of the high energy cut-off in the spectra, with the relatively low coronal temperature<sup>3</sup>  $kT_{\text{e}} = 64_{-15}^{+46} \text{ keV}$ ,  $32_{-4}^{+6} \text{ keV}$ , and  $26_{-2}^{+3} \text{ keV}$  for Epoch 1, 2, and 3, respectively.

As for the key reflection parameters: the ionization parameter  $\xi^4$  increases with source flux from Epoch 1 to Epoch 3; an abundance of  $A_{\text{Fe}} = 0.78_{-0.13}^{+0.10}$  (in units of solar value) is derived for the accretion disk and the disk is estimated to be viewed at a low inclination angle  $i = 37_{-4}^{+3}$ ; the measured inner disk radius is  $R_{\text{in,Epoch1}} = 20_{-8}^{+33} r_{\text{g}}$ ,  $R_{\text{in,Epoch2}} = 17_{-7}^{+14} r_{\text{g}}$ , and  $R_{\text{in,Epoch3}} = 40_{-22}^{+47} r_{\text{g}}$  (see Table 3.2 for a list of the best-fit parameters).

The accretion disk is considered truncated if the inner edge of the disk is located outside the ISCO. The radius of the ISCO is a function of the black hole spin, and its value decreases monotonically from  $9 r_{\text{g}}$  ( $r_{\text{g}} \equiv GM/C^2$  is the gravitational radius) for an extreme retrograde spinning black hole to  $1.235 r_{\text{g}}$  for a black hole with a maximum positive spin. The lower limits of the inner disk radius from Model 1a are all in excess of  $10 r_{\text{g}}$  at the 90% confidence level and radii smaller than  $6 r_{\text{g}}$  can be ruled out at  $3\sigma$  (see Figure 3.5), which points to the truncated disk scenario.

The reflection fraction  $R_{\text{ref}}$  is defined to be the ratio of the coronal intensity illuminating the disk to that reaching the observer (Dauser et al., 2016). The low reflection fraction measured ( $R_{\text{ref}} \sim 0.15\text{--}0.26$ ) suggests the photon reprocessing is free from the strong light-bending effects in the vicinity of the black hole, also consistent with a truncated accretion disk. To investigate the effect of the black hole spin on the fitting results, we fix  $a$  at  $-0.998$ ,  $0$ , and  $0.998$  respectively, and obtain basically identical fits for all other parameters. Therefore, we note that the reflection modeling is simply not sensitive to the spin parameter, which is to be expected when the disk is truncated at this level. By fixing  $R_{\text{in}}$  at the ISCO and in turn fitting for the black hole spin,  $a$ , would yield a worse fit by  $\Delta\chi^2 \simeq 20$  with  $a$  pegged at  $-0.998$ .

<sup>3</sup>Approximately, the exponential rollover energy  $E_{\text{c}}$  of the thermally Comptonized continuum is related to the electron temperature  $kT_{\text{e}}$  as  $E_{\text{c}} = 2\text{--}3 kT_{\text{e}}$ .

<sup>4</sup>The ionization parameter  $\xi = 4\pi F_{\text{x}}/n$ , where  $F_{\text{x}}$  is the ionizing flux and  $n$  is the gas density.

This indicates that the fitting is attempting to find a larger inner disk radius than the maximum value allowed for the ISCO, which is also evidence for a truncated disk.

In Model 1a, we assume that the iron abundance, inclination, and absorption column density remain constant through the outburst, which can be an over-simplification in some cases. For instance, a strongly warped disk could cause the apparent disk inclination to vary with radius. Evidence for disk warping has been found in e.g., Cyg X-1, for which the inner disk and the orbital plane inclination are found to disagree by  $\sim 10^\circ\text{--}15^\circ$  (Tomsick et al., 2014; Walton et al., 2016). We explore this possibility by fitting independently the disk inclination parameter  $i$  at the three epochs (Model 1b). This only improves the fitting marginally with two extra free parameters  $\Delta\chi^2/\Delta\nu = -4.3/-2$ . The best-fit inner disk radius at Epoch 3 is a bit lower, about the same value at Epoch 2 (although still consistent with Model 1a results within errors). This is more reasonable, as an obvious increase of the inner radius returned by Model 1a is not expected given the short time interval between the later two observations. However, since there is no clear indication for a change in the inner disk radius between epochs, disk warping is not explicitly required to describe the data.

### 3.3.1.3 Lamppost Geometry

The characteristic reflection spectra in black hole binaries are believed to be produced by reprocessing of the hard X-ray continuum generated by a centrally located corona. In principle, information about the geometry of the corona can be extracted from the disk reflection spectrum. In the previous section, we measured a change in the electron temperature  $kT_e$ , implying an evolving corona. In an attempt to further explore the possible changes in the accretion geometry, we assume a lamppost geometry for the corona by using the `relxilllpCp` reflection model. Instead of assigning a specific emissivity profile, `relxilllpCp` characterizes the reflection spectrum assuming a point source located in the rotational axis at a height  $h$ . The lamppost model `relxilllpCp` can self-consistently calculate the reflection fraction  $R_{\text{ref}}$  given a certain combination of spin, inner disk radius, and coronal height, which places an extra constraint on the fitting (see Dauser et al., 2014, for a discussion). We first fix the spin parameter  $a$  at the maximum, and allow both the inner disk radius and the lamppost height to vary freely between epochs (Model 2a). The lamppost model results in a good fit to the data with  $\chi^2_\nu = 3626.9/3626 = 1.000$ . The best-fit parameters are consistent with the results from the `relxillCp` model

Table 3.2: Best-fit Parameters of the Disk Reflection Models

Epoch	$N_{\text{H}}$ ( $\times 10^{22}$ cm $^2$ )	$q_{\text{in}}$	$q_{\text{out}}$	$h$ ( $r_{\text{g}}$ )	$i$ ( $^{\circ}$ )	$R_{\text{in}}$ ( $r_{\text{g}}$ )	$a$	$\Gamma$	$\log \xi$ (log[erg cm s $^{-1}$ ])	$A_{\text{Fe}}$	$k_{\text{Te}}$ (keV)	$R_{\text{ref}}$
Model 1a: TBABS*RELXILLCP												
1	3*	3*	...	(37 $^{+8}_{-5}$ ) $^l$	20 $^{+33}_{-8}$	0.998*	1.674 $^{+0.008}_{-0.009}$	1.95 $^{+0.41}_{-0.18}$	(0.74 $^{+0.10}_{-0.15}$ ) $^l$	64 $^{+46}_{-15}$	0.26 $\pm$ 0.03	
2	...	3*	3*	...	...	17 $^{+14}_{-7}$	0.998*	1.680 $^{+0.012}_{-0.010}$	2.73 $^{+0.08}_{-0.21}$	...	32 $^{+6}_{-4}$	0.19 $^{+0.06}_{-0.04}$
3	...	3*	3*	...	...	40 $^{+47}_{-22}$	0.998*	1.698 $^{+0.009}_{-0.008}$	2.75 $\pm$ 0.09	...	26 $^{+3}_{-2}$	0.15 $^{+0.04}_{-0.03}$
$\chi^2/\nu$ 3627.0/3626(1.000)												
Model 1b: TBABS*RELXILLCP ( $i$ allowed to vary between epochs)												
1	(1.56 $\pm$ 0.03) $^l$	3*	3*	...	34 $^{+8}_{-6}$	17 $^{+24}_{-6}$	0.998*	1.672 $\pm$ 0.009	2.07 $^{+0.34}_{-0.26}$	(0.74 $^{+0.16}_{-0.14}$ ) $^l$	69 $^{+11}_{-7}$	0.24 $^{+0.04}_{-0.03}$
2	...	3*	3*	...	42 $^{+11}_{-7}$	21 $^{+20}_{-10}$	0.998*	1.683 $^{+0.012}_{-0.010}$	2.72 $^{+0.07}_{-0.30}$	...	33 $^{+6}_{-4}$	0.21 $^{+0.07}_{-0.05}$
3	...	3*	3*	...	29 $^{+21}_{-8}$	21 $^{+77}_{-9}$	0.998*	1.696 $^{+0.010}_{-0.009}$	2.79 $^{+0.16}_{-0.08}$	...	26 $^{+3}_{-2}$	0.13 $^{+0.04}_{-0.03}$
$\chi^2/\nu$ 3623.7/3624(1.000)												
Model 2a: TBABS*RELXILLCP												
1	(1.59 $\pm$ 0.03) $^l$	...	...	9.4 $^{+29.3}_{-4.6}$	(36 $^{+5}_{-2}$ ) $^l$	19 $^{+21}_{-8}$	0.998*	1.673 $\pm$ 0.008	2.04 $^{+0.31}_{-0.29}$	(0.73 $\pm$ 0.13) $^l$	67 $^{+39}_{-17}$	0.51
2	...	...	...	5.7 $^{+6.5}_{-3.0}$	...	18 $^{+8}_{-7}$	0.998*	1.680 $^{+0.010}_{-0.009}$	2.74 $^{+0.07}_{-0.20}$	...	33 $^{+6}_{-4}$	0.40
3	...	...	...	11.9 $^{+20.2}_{-7.8}$	...	39 $^{+21}_{-20}$	0.998*	1.698 $\pm$ 0.008	2.75 $^{+0.09}_{-0.08}$	...	26 $^{+3}_{-2}$	0.31
$\chi^2/\nu$ 3626.9/3626(1.000)												
Model 2b: TBABS*RELXILLCP ( $R_{\text{in}}$ linked for all epochs)												
1	(1.59 $\pm$ 0.03) $^l$	...	...	10.3 $^{+3.3}_{-2.5}$	(35 $\pm$ 4) $^l$	(21 $^{+11}_{-6}$ ) $^l$	0.998*	1.673 $^{+0.006}_{-0.008}$	2.04 $^{+0.30}_{-0.29}$	(0.72 $^{+0.12}_{-0.13}$ ) $^l$	67 $^{+35}_{-17}$	0.50
2	...	...	...	6.6 $^{+7.3}_{-3.0}$	...	...	0.998*	1.678 $\pm$ 0.009	2.74 $^{+0.08}_{-0.19}$	...	33 $^{+5}_{-4}$	0.36
3	...	...	...	5.5 $^{+7.1}_{-2.4}$	...	...	0.998*	1.700 $^{+0.009}_{-0.008}$	2.79 $^{+0.10}_{-0.06}$	...	26 $^{+3}_{-2}$	0.31
$\chi^2/\nu$ 3629.3/3628(1.000)												

Frozen parameters are marked with asterisks. Superscripts  $l$  indicate the parameters whose values are linked at the three epochs. For all models, the outer disk radius  $R_{\text{out}}$  is fixed at 400  $r_{\text{g}}$  and the black hole spin  $a$  is fixed at 0.998. As discussed in the text, altering the spin parameter  $a$  causes no significant change to the fitting result.

in general, and we find a coronal height of  $\sim 10 r_g$  (see Table 3.2). As the disk is truncated and given the data quality, the modeling is not sensitive to the high emissivity close to the black hole that would result from a low lamppost height. The inner disk radius and the lamppost position cannot be simultaneously constrained to test a plausible change in the parameters.

Since the values of the inner disk radius at the three epochs are all consistent within errors, we make an attempt to achieve a better constraint on  $h$  by tying together  $R_{\text{in}}$  at the three epochs in a joint fit (Model 2b). This yields an equally acceptable fit with  $\chi^2_{\nu} = 3629.3/3628 = 1.000$ . The coronal height  $h$  is measured to be  $h_{\text{Epoch1}} = 10.3^{+3.3}_{-2.5} r_g$ ,  $h_{\text{Epoch2}} = 6.6^{+7.3}_{-3.0} r_g$ , and  $h_{\text{Epoch3}} = 5.5^{+7.1}_{-2.4} r_g$ , with  $R_{\text{in}}$  staying at  $21^{+11}_{-6} r_g$ . We note that the constraint on  $h$  here is most likely driven by the decrease of the reflection fraction from Epoch 1 to Epoch 3. As the spin and the inner disk radius are both assumed to remain constant, the different reflection fractions can only be accounted for by the change in the lamppost position in the lamppost model. In this case, the reflection fraction returned by our model fits correlates positively with the coronal height. This trend is opposite to that expected if the disk extends down to the ISCO. When the accretion disk is truncated, more photons are lost with a lower coronal height, because light-bending in the strong gravitational field focuses more X-rays to the innermost regions that will not be reflected by the truncated disk. This trend of the reflection fraction, also observed in the fits with Model 1a, is yet another indication for the moderate truncation of the accretion disk.

### 3.3.2 Timing Analysis

Low frequency QPOs observed in black hole binaries are classified into different types, namely type-A, type-B, and type-C, based on their characteristics in the power spectra and are related to different spectral states (e.g., see Casella et al.; Casella et al., 2004; 2005). In the hard state, type-C QPOs are most commonly found, which are variable and highly coherent peaks on top of strong flat-topped noise. A type-C QPO is evident in the CPDS generated in the full energy band (3–79 keV) from our *NuSTAR* observations of IGR J17091–3624 (see Figure 3.6).

We model the *NuSTAR* CPDS of the three epochs in XSPEC jointly with a unit response file. We use a multi-Lorentzian model, which is commonly used to fit the power spectra of black hole binaries (e.g., Nowak, 2000; Pottschmidt et al., 2003). The model consists of two zero-centered Lorentzians for the underlying broad component, plus one Lorentzian for the fundamental QPO and two for possible sub-

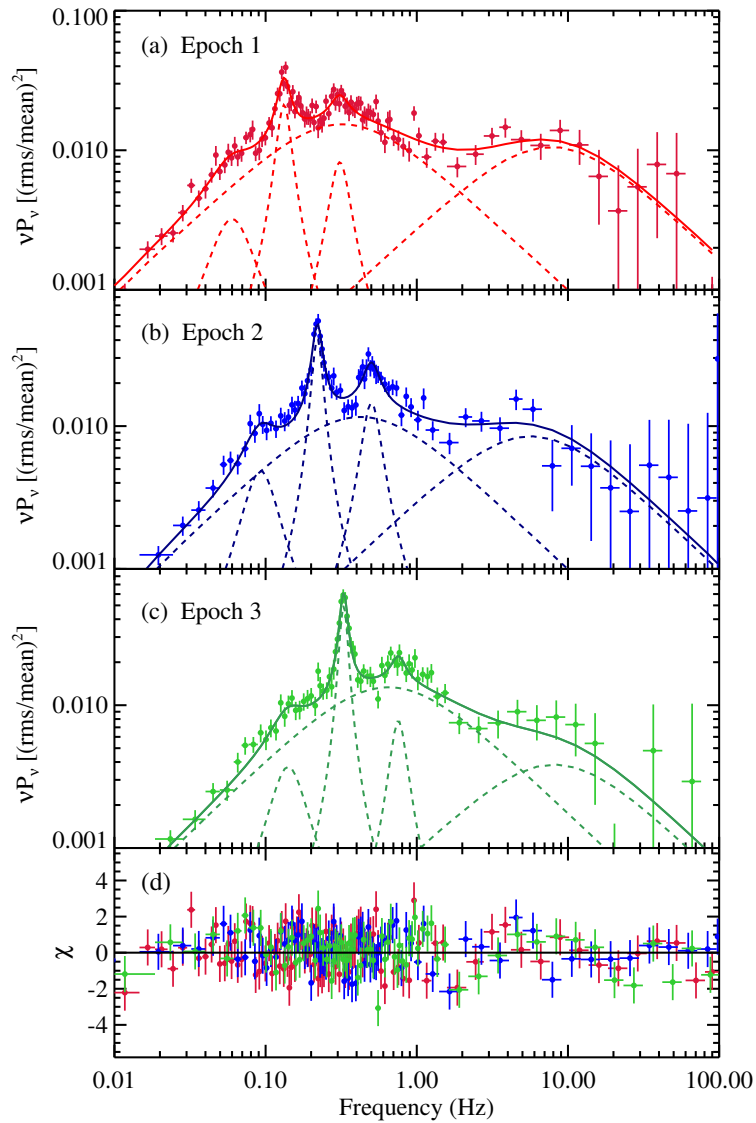


Figure 3.6: *NuSTAR* CPDS of IGR J17091–3624 with best-fit models in the  $\nu P_\nu$  representation. (a)–(c) *NuSTAR* CPDS and best-fit model in the  $\nu P_\nu$  representation. The CPDS are calculated using data from the full energy band (3–79 keV). Same color scheme is used as in the previous figures: data taken in Epoch 1, 2, 3 are plotted in red, blue, and green, respectively. A type-C QPO variable in frequency along with a secondary peak around 2.3 times the QPO frequency are detected. The dashed lines indicate the best-fit Lorentzian profiles. (d) Residuals of the best-fit model that includes five Lorentzians. The data are rebinned for display clarity.

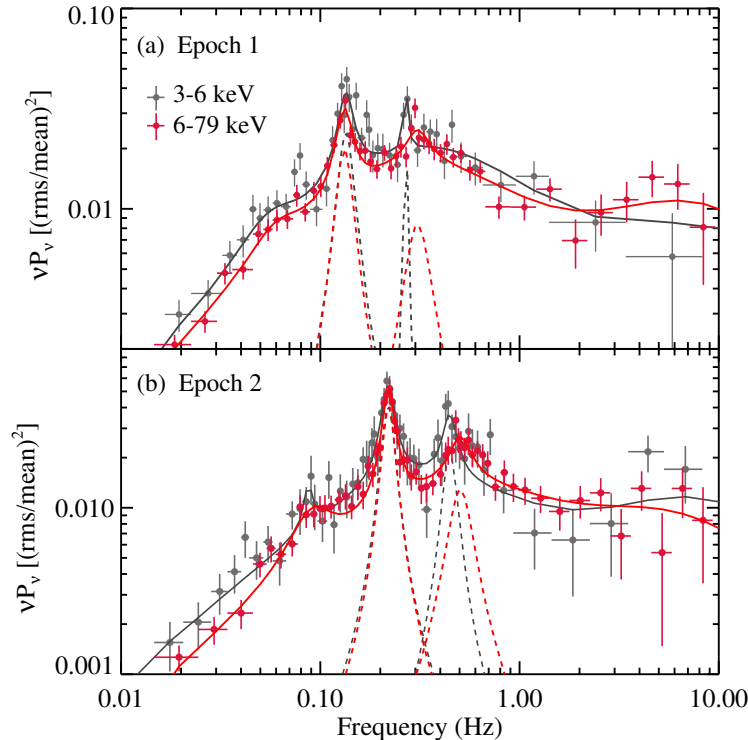


Figure 3.7: CPDS generated in two energy intervals: 3–6 keV (gray) and 6–79 keV (red). Panel (a) and (b) are the data taken from the the first and the second *NuSTAR* observations. The dotted lines indicate the best-fit Lorentzian profiles for the type-C QPO and the secondary frequency.

and super- harmonics. This provides an adequate fit for the power spectra, with  $\chi^2_v = 829.9/798 = 1.04$ , leaving no obvious excess (see Figure 3.6). The Lorentzian used to fit for the possible sub-harmonic is less significant compared to other components, and the centroid frequency and the line width cannot be very well constrained. Therefore, we focus our discussion on the two more significant peaks in the CPDS. The type-C QPO frequency  $\nu_0$  is well measured to be  $0.131 \pm 0.002$  Hz,  $0.219 \pm 0.002$  Hz, and  $0.327 \pm 0.002$  Hz, with the rms amplitude of  $6.1 \pm 0.6\%$ ,  $7.3 \pm 0.5\%$ , and  $7.3 \pm 0.4\%$  for Epoch 1 to 3, respectively. No significant deviation in the QPO frequency is observed during any of the three individual *NuSTAR* observations. The relatively low type-C QPO frequencies are consistent with the values found during the onset of the 2011 outburst of IGR J17091–3624 (Rodríguez et al., 2011; Iyer et al., 2015). However, by adopting the disk reflection model, we measure a slightly higher photon index of  $\Delta\Gamma \sim 0.2$  from the energy spectra when about the same QPO frequencies are detected, compared to Iyer et al. (2015) who used different spectral models.

Table 3.3: Fitting Results of the *NuSTAR* CPDS in Different Energy Bands

Epoch	Energy (keV)	$\nu_0$ (Hz)	$\nu_1$ (Hz)	$P(\nu_1)$
1	3.0–79.0	$0.131 \pm 0.002$	$0.31 \pm 0.01$	$5.3\sigma$
	3.0–6.0	$0.134^{+0.004}_{-0.003}$	$0.270^{+0.006}_{-0.004}$	$2.0\sigma$ ( $2.4\sigma$ )
	6.0–79.0	$0.131 \pm 0.002$	$0.30^{+0.02}_{-0.01}$	$3.9\sigma$
2	3.0–79.0	$0.219 \pm 0.002$	$0.50 \pm 0.01$	$7.6\sigma$
	3.0–6.0	$0.218 \pm 0.004$	$0.45^{+0.03}_{-0.02}$	$3.6\sigma$
	6.0–79.0	$0.220 \pm 0.002$	$0.50 \pm 0.01$	$5.1\sigma$
3	3.0–79.0	$0.327 \pm 0.002$	$0.76^{+0.05}_{-0.04}$	$4.0\sigma$
	3.0–6.0	$0.327 \pm 0.004$	...	$< 95\%$ ( $79\%$ )
	6.0–79.0	$0.327 \pm 0.003$	$0.70^{+0.05}_{-0.04}$	$2.7\sigma$ ( $2.6\sigma$ )

$\nu_0$  and  $\nu_1$  denote the type-C QPO and the secondary frequency.  $P(\nu_1)$  is the significance of the secondary frequency determined by the F-test. For comparison, significances calculated by simulations (1000 trials) are listed in parentheses.

As displayed in Figure 3.6, there is a secondary peak at higher frequencies than the type-C QPO in all three datasets. Such feature is commonly associated with the first QPO harmonic, which occurs at twice the fundamental QPO frequency. However, this secondary frequency  $\nu_1$  is measured to be centered at  $0.31 \pm 0.01$  Hz,  $0.50 \pm 0.01$  Hz, and  $0.76^{+0.05}_{-0.04}$  Hz at Epoch 1, 2, and 3, respectively.  $\nu_1$  is about 2.3 times the type-C QPO frequency, making them unlikely to be harmonically related. Although some small residuals can be seen in the fit of the power-spectra (e.g., around 0.3 Hz in Figure 3.6(b)), they are probably because the underlying continuum cannot be perfectly described by two Lorentzians and would not affect the measurement of the secondary frequency. When modeling the CPDS, the Lorentzian width of the secondary peak cannot always be constrained within a reasonable value. In order to obtain a reasonable fit, we set an upper limit of 0.2 Hz for the Lorentzian FWHM. This feature is detected at  $\gtrsim 4\sigma$  confidence level in all epochs, and is most significant at Epoch 2 with the detection at  $7.6\sigma^5$ . Although its origin is unclear, we note this is not caused by instrumental effects, as its characteristic frequency is increasing between epochs.

<sup>5</sup>All significances here are estimated with the F-test, based on the improvement in  $\chi^2$  by adding a Lorentzian component for the secondary peak in the fit model. For low significance cases, we test the significances further with Monte Carlo simulations using the `simftest` script in `xspec`. The results agree with those calculated by the simple F-test.

We also investigate the energy dependence of the CPDS. In order to allow for enough statistics in each energy band, we only calculate the CPDS in two energy intervals: 3–6 keV (low) and 6–79 keV (high). The type-C QPO frequency basically remains constant in the two energy bands. The only noteworthy difference is evidence for an apparent shift of the secondary frequency, which is present at Epoch 1 and 2 (see Figure 3.7). In the high energy band, this secondary frequency is detected at  $3.9\sigma$  and  $5.1\sigma$  in Epoch 1 and Epoch 2, respectively; while it becomes considerably weaker at lower energies, the confidence levels are  $2.0\sigma$  in Epoch 1 and  $3.6\sigma$  in Epoch 2. The fitting finds different values for the secondary frequency  $\nu_1$  in the two energy bands: at lower energies, we measure  $\nu_{1,\text{Epoch1}} = 0.270_{-0.004}^{+0.006}$  Hz,  $\nu_{1,\text{Epoch2}} = 0.45_{-0.02}^{+0.03}$  Hz; whereas  $\nu_1$  derived from the high energy band agrees with the full-band results (see Table 3.3 for a list of frequencies and significances). We note that  $\nu_1$  in the 3–6 keV band is roughly two times the type-C QPO frequency, consistent with that of a conventional first harmonic. If the secondary frequency  $\nu_1$  is required to be the same in the two energy bands, the overall fit would worsen by  $\Delta\chi^2_{\text{Epoch1}} \simeq 8$ ,  $\Delta\chi^2_{\text{Epoch2}} \simeq 5$ . In the Epoch 3 data, the secondary peak is the weakest and cannot be detected above the 95% confidence level in the low energy band. The absence of the same pattern in Epoch 3 could imply it is transient, or it just lacks the statistics to be detected as the power spectrum becomes noisy close to the high frequency end. In addition, we calculate the lag-frequency spectra between the two energy bands. The time lags are consistent with zero around the QPO frequencies.

### 3.4 Discussion

We have presented a multi-epoch X-ray analysis of the galactic black hole candidate IGR J17091–3624 in the rising hard state using data taken by *NuSTAR* and *Swift*. The data is free from pile-up issues at the count rate level during the observations. The broadband X-ray spectra display broadly similar shapes, revealing a blurred reflection component on top of a cut-off power-law continuum, with no significant detection of the soft disk emission. We model the multi-epoch energy spectra jointly with four different relativistic reflection model setups, assuming either a constant emissivity index or a steep emissivity profile from a lamppost geometry. The models all provide adequate fits for the data and yield consistent results (see Table 3.2). During the spectral modeling, we allow key parameters governing the inner disk properties to vary between epochs. Timing analysis of the *NuSTAR* data reveals a type-C QPO in the power spectra that increases in frequency from Epoch 1 to Epoch 3. We also detect a secondary frequency at about 2.3 times the type-C

QPO frequency, inconsistent with the conventional frequency expected from QPO super-harmonics, possibly an independent second frequency of the system.

### 3.4.1 Properties of the Inner Accretion Disk

Our reflection modeling finds the accretion disk to be truncated. The lower limits of the inner disk radius are all in excess of  $10 r_g$ , which is larger than the maximum ISCO radius corresponding to a retrograde spin. We have also demonstrated that the choice of black hole spin has negligible effects on the measurement of disk truncation in our case. The best-fit values for the inner disk radius are around  $17 - 40 r_g$ . Considering the parameter uncertainties, the truncation radius is at the level of a few tens of gravitational radii. Due to controversies over the source distance and the black hole mass, the Eddington ratio of the source during our observations is uncertain. It can be estimated if we assume IGR J17091–3624 emits at the Eddington limit during its “heartbeat” state. From Altamirano et al. (2011b), the 2–50 keV source flux was  $\sim 4 \times 10^{-9} \text{ erg cm}^{-2} \text{ s}^{-1}$  when GRS 1915+105 like variabilities were detected. For a crude estimation, taking a bolometric correction factor of 3, we find an Eddington fraction  $\lambda = L_{1-100 \text{ keV}}/L_{\text{Edd}} \sim 20\text{--}30\%$  at the time of the *NuSTAR* observations (the source flux only increases by  $\sim 50\%$  from Epoch 1 to 3 as shown in Figure 3.8). Therefore, our results are currently consistent with the disk still being truncated at a considerable level during the bright phase of the outburst ( $L/L_{\text{Edd}} \gg 1\%$ ), although we stress that the exact value for the Eddington ratio is highly uncertain.

We obtain an abundance of  $A_{\text{Fe}} \simeq 0.7$  for the accretion disk from the spectral fitting. Super-solar abundances of  $A_{\text{Fe}} \sim 3\text{--}5$  have been frequently required in the reflection modeling of Galactic black hole binaries: e.g., Cyg X–1 (Fürst et al., 2015; Parker et al., 2015; Fürst et al., 2016b; Walton et al., 2016), GX 339–4 (Tomsick et al., 2014; García et al., 2015b), and GRS 1739–278 (Miller et al., 2015b). The lower elemental abundance for IGR J17091–3624 could result from the weak Fe K line/edge relative to the Compton hump.

A face-on geometry is favored for IGR J17091–3624 with a low inclination of  $i \simeq 30^\circ\text{--}40^\circ$ . A high inclination ( $>65^\circ$ ) can be excluded by all models at  $> 90\%$  confidence level (see Table 3.2), and in the best constrained case (Model 2b), this can be ruled out at  $>5\sigma$ . A low inclination is in contrast with several previous estimations. Capitanio et al. (2012) proposed IGR J17091–3624 could be a highly inclined system, as the faintness of the source could be ascribed to the spectral deformation

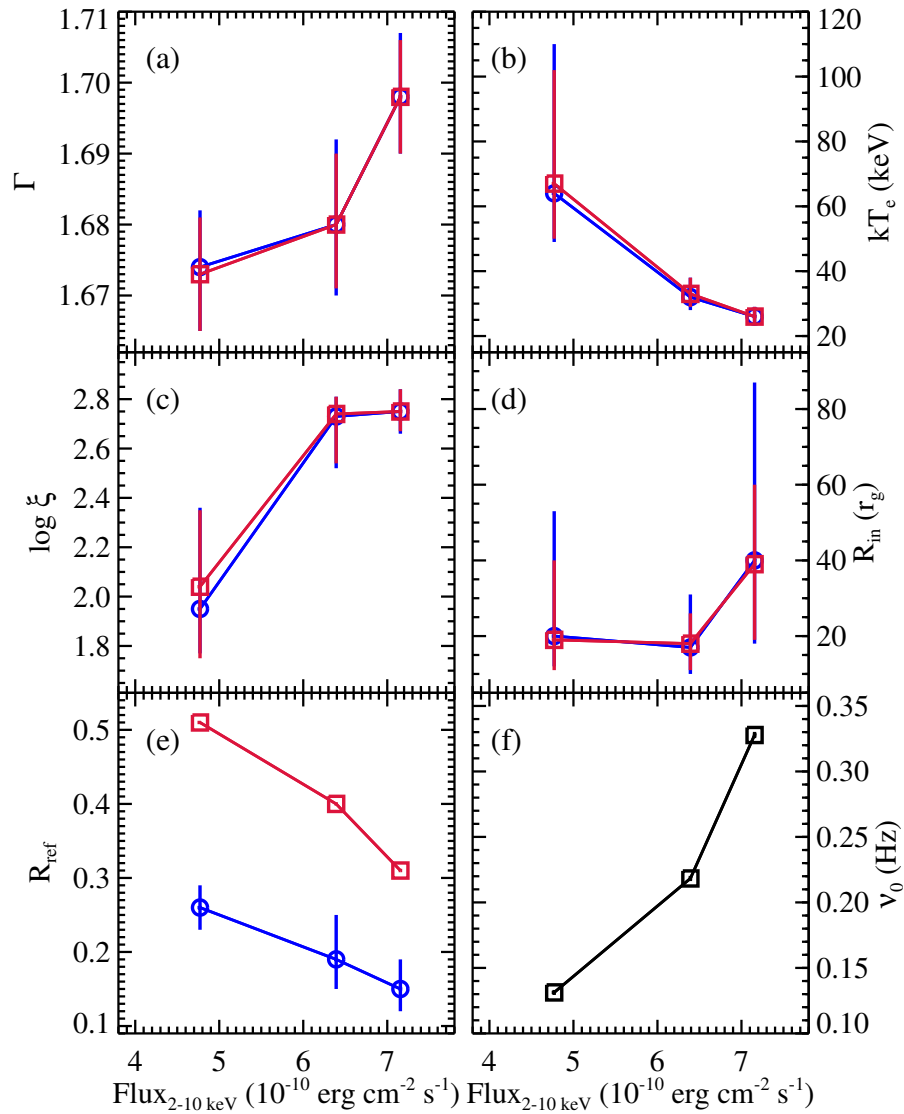


Figure 3.8: Relation of spectral and timing properties with the source flux. Blue circles are best-fit parameters from Model 1a, red squares are the results from Model 2a that assumes a lamppost geometry. There are no error bars for the reflection fraction  $R_{\text{ref}}$  from Model 2a in panel (e), as the values are calculated self-consistently by the model from a combination of  $a$ ,  $R_{\text{in}}$ , and  $h$ .

effects due to a high inclination angle. Rao & Vadawale (2012) performed a phase-resolved spectral fitting of the heartbeat oscillations of IGR J17091–3624 observed with *Rossi X-ray Timing Explorer* and *XMM-Newton* with a multi-temperature disk blackbody and a power-law component, and their results favor a high inclination of  $\sim 70^\circ$ . In addition, high velocity outflows have been observed in IGR J17091–3624 by *Chandra* (King et al., 2012), that are usually expected from nearly edge-on systems. Suggestions of a high inclination for IGR J17091–3624 also come from its general similarities with GRS 1915+105, that has been measured to have an inclination angle of  $\sim 65^\circ$ – $75^\circ$  (e.g., Middleton et al., 2006; Miller et al., 2013).

A warped accretion disk could be one possible explanation for this discrepancy. All previous arguments for the high inclination are based on the soft state properties of IGR J17091–3624, while our measurements indicating a low inclination are from the hard state. From the standard diagram for black hole binaries, the inner disk radius is believed to move inward towards the ISCO during the transition from the hard state to the soft state, the inner edge of the accretion disk can appear to be viewed at different angles if the disk is strongly warped: the inner part is aligned with the black hole spin while the outer part is tilted, aligned with the binary orbital axis. This misalignment is believed to be driven by the precessional torque from the Lense-Thirring effect (Bardeen & Petterson, 1975). Location of the transition of orientations can reach a steady state and is at  $\sim 10$ – $20 r_g$  as shown by recent simulations (Nealon et al., 2015), which is relevant to the scale of truncation radius discussed here. Therefore, the viewing angle  $30^\circ$ – $40^\circ$  we measured might be the orbital inclination or it might be somewhere in between the orbital and inner disk inclinations. Unfortunately, as we have not detected significant changes in the inner disk radius considering the error range, it is not possible to test this hypothesis via spectral fitting within the timespan of our observations.

### 3.4.2 Origin of the Secondary Frequency

Regarding the nature of the peak around 2.3 times the fundamental frequency, the basic question is whether it is harmonically related to the type-C QPO frequency or not. Harmonics of low-frequency QPOs have been discovered from a number of Galactic black hole binaries, and have been used as an additional probe to investigate the physical origins of QPOs (e.g. Axelsson et al., 2014; Ingram & van der Klis, 2015; Axelsson & Done, 2016). While the fundamental QPO and its harmonics have been found to display different behaviors (e.g., the energy dependence of phase lags and amplitudes), the ratio of the fundamental and first harmonic fre-

quency has been always found at 1:2 (e.g., Rodriguez et al., 2002; Casella et al., 2005; Ingram & van der Klis, 2015). However, based on the measurements from the full-band CPDS of IGR J17091–3624, the frequency ratio of the secondary peak and the type-C QPO  $\nu_1/\nu_0$  is  $2.37 \pm 0.08$ ,  $2.28 \pm 0.05$ ,  $2.32 \pm 0.02$  for Epoch 1 to 3, respectively, making it inappropriate to associate the secondary frequency with the first QPO harmonic.

In the low energy band (3–6 keV) CPDS, the secondary peak is found at the conventional value of two times the QPO frequency. We note that instead of being an apparent shift of the secondary frequency detected in the full band, it is possible that this is the real first harmonic. It is not unusual for the super-harmonic to be more prominent in the lower energy band while it is undetected at higher energies, as the harmonic energy spectrum has been found to be systematically softer than that of the fundamental QPO. This is likely a result of the inhomogeneity of the Comptonizing region generating the QPOs (Axelsson et al., 2014; Axelsson & Done, 2016). Also, the harmonic features are usually transient, which could explain why it is not detected in the soft band CPDS at Epoch 3.

The secondary frequency at about 2.3 times the type-C frequency is consistently detected in the 6–79 keV and full energy band, indicating that it is dominated by hard X-ray photons. One possibility is that higher energy photons are generated at a smaller distance from the black hole where the times scales are shorter, corresponding to a higher QPO frequency. Pairs of non-harmonically related QPOs have been simultaneously discovered during the 2005 outburst of GRO J1655–40, which were identified as a type-C QPO and a type-B QPO (Motta et al., 2012). However, the secondary frequency detected in IGR J17091–3624 is unlikely a type-B QPO, since type-B QPOs are normally detected at higher frequencies around  $\sim 5$ –6 Hz and when the source is at a higher hardness ratio (e.g., Casella et al., 2004, 2005). Although GRO J1655–40 is not an exact analog to that discussed here, it indicates that there are multiple mechanisms generating the low-frequency QPOs in black hole binaries. Currently there is no consensus about the nature of low frequency QPOs. If the secondary frequency discussed here is indeed not harmonically related with the type-C QPO, its origin is rather uncertain, but it should be an independent frequency that increases with the type-C QPO frequency.

### 3.4.3 Evolution of the Spectral and Timing Properties

The 2–10 keV flux of IGR J17091–3624 increased by  $\sim 50\%$  during the time span of our three *NuSTAR* observations. We observe several parameters from the spectral and timing analysis to change systematically with the source flux (see Figure 3.8).

The evolution in the spectral fitting parameters is broadly similar to what has been found in the systematic study of GX 339–4 recently with *Rossi X-ray Timing Explorer* (García et al., 2015b). The ionization parameter increases with the source flux, which is naturally expected given the definition of the ionization parameter  $\xi^2$ . Regarding the two parameters governing the general curvature of the continuum, the photon index  $\Gamma$  increases whereas the electron temperature  $kT_e$  decreases with rising source flux. The slope of the thermal Comptonized continuum is described by an asymptotic power-law with photon index  $\Gamma$  in the `nthcomp` model, which depends on the electron scattering optical depth  $\tau_e$  and the electron temperature  $kT_e$  (Lightman & Zdziarski, 1987). Therefore, optical depth  $\tau_e$  can be estimated from  $\Gamma$  and  $kT_e$ <sup>6</sup>, and we find  $\tau_{e,\text{Epoch1}} \simeq 1.95$ ,  $\tau_{e,\text{Epoch2}} \simeq 3.13$ ,  $\tau_{e,\text{Epoch3}} \simeq 3.51$ . The measurements suggest that the corona is cooling more efficiently by Compton up-scattering more photons as the source flux increases, which is also physically consistent with the increase in the electron opacity.

The type-C QPO frequency is known to be well correlated with the general changes in the energy spectra, e.g., photon index, strength of the thermal disk component (Remillard & McClintock, 2006). One promising explanation for the low-frequency QPO is the Lense-Thirring precession of an inner hot flow of a truncated disk, which correlates the increase of the QPO frequency with the inward motion of the inner edge of the accretion disk (e.g., Ingram et al., 2009; Ingram & Done, 2011). The model assigns the nodal precession frequency to the origin of type-C QPOs. In principle, it is possible to test the consistency of this QPO model using spectral-timing methods. We make a simple comparison of the QPO frequency  $\nu_0$  and the inner disk radius  $r_{\text{in}}$  to the theoretical calculation of the nodal precession frequency  $\nu_{\text{nod}}$  from Ingram & Motta (2014). Since neither the black hole spin  $a$  nor mass  $m$  is known for the system, we calculate the theoretical curve for several combinations of these parameters (see Figure 3.9). However, the inner disk radius measured at the three epochs overlaps with each other within errors and no clear trend can be inferred from the three data points. It is clear from Figure 3.9 that in order to detect possible tension between the spectral and timing results in the frame of the QPO

<sup>6</sup>We use equation (1) in García et al. (2015b) for the calculation.

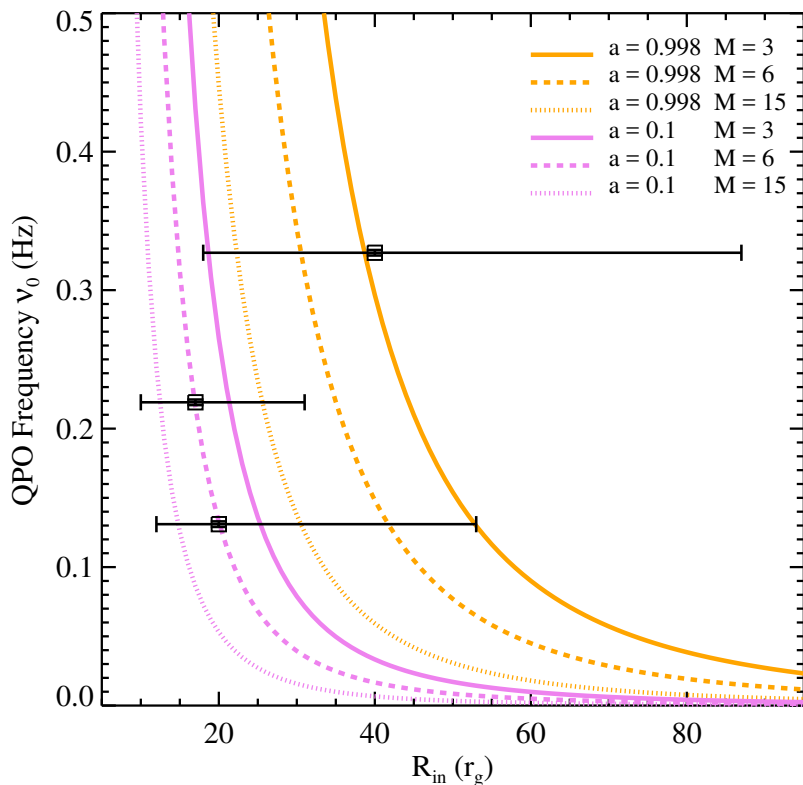


Figure 3.9: Black square points mark the inner disk radius  $R_{\text{in}}$  and the type-C QPO frequency  $\nu_0$  measured at the three epochs, the errors are clearly dominated by the measurement of disk truncation. For comparison, theoretical curves of the nodal precession frequency based on the Lense-Thirring precession model are plotted.

model, e.g., whether the inner disk radius changes in step with the QPO frequency, the inner disk radius must be constrained to be better than  $\sim 5 r_g$ .

The anti-correlation of the reflection fraction with the source flux has also been observed and discussed in García et al. (2015b), although we note that the reflection fraction is defined differently here. From the lamppost geometry, the decrease of the reflection fraction in IGR J17091–3624 can be self-consistently explained by a reduction of the lamppost height assuming the inner disk radius remains constant (as the case with Model 2b), which can still be valid if the inner disk is moving inward as predicted by the QPO model. This only works if the corona has a compact size compared to the level of disk truncation. In this scenario, because there is no inner disk to reflect the emission, a lower source height means that a larger fraction of the photons that would have been reflected by an inner disk reaching the ISCO are now lost in the gap between the disk and the horizon, reducing the reflection

fraction. We note that the decrease of the reflection fraction could also be caused by the beaming effect of an outflowing corona (Beloborodov, 1999; Malzac et al., 2001). However, it is difficult to explore this scenario with our limited S/N data, since additional parameters such as the corona velocity and geometric extent should be considered.

### 3.5 Summary and Conclusion

We have undertaken a multi-epoch analysis of the *NuSTAR* and *Swift* observations of the black hole candidate IGR J17091–3624 in the rising hard state during its 2016 outburst. Reflection features are detected in the *NuSTAR* spectra, enabling us to constrain the inner accretion properties from relativistic reflection modeling. Reflection models assuming a constant emissivity index or a lamppost geometry yield consistent results: the accretion disk is truncated at the level of a few tens of gravitational radii at all epochs, and is viewed at a low inclination angle of  $\sim 30^\circ$ – $40^\circ$ . Our modeling also implies that the reflection spectrum is not sensitive to the specific disk emissivity profile when the disk is truncated. Several parameters from the spectral fitting (the photon index  $\Gamma$ , the coronal temperature  $kT_e$ , the ionization parameter  $\xi$  and the reflection fraction  $R_{\text{ref}}$ ) are observed to evolve systematically with the source flux, which is consistent with the standard picture of a black hole binary going into an outburst.

A type-C QPO is robustly detected in the *NuSTAR* data, with the frequency varying from 0.131 Hz to 0.327 Hz. The Lense-Thirring precession model predicts moderate truncation regardless of the black hole mass and spin. It also predicts a relatively small change in  $R_{\text{in}}$  with QPO frequency. Unfortunately, there is no clear evidence for a corresponding change in the disk truncation radius predicted by the model, as the inner disk radius cannot be well constrained from the reflection modeling, but the results are generally consistent with the model within errors. A secondary peak is detected at around 2.3 times the type-C frequency in the power spectra at all epochs, which we note is unlikely to be a QPO harmonic, but instead an independent frequency of the system. If true, this would add to the peculiarity of IGR J17091–3624 in its variability behavior. Lacking enough statistics for more detailed timing analysis, the nature of this secondary frequency remains uncertain.

### Acknowledgments

We thank the anonymous referee for detailed and helpful comments. D.J.W. acknowledges support from an STFC Ernest Rutherford Fellowship. This work was

supported under NASA contract No. NNG08FD60C and made use of data from the *NuSTAR* mission, a project led by the California Institute of Technology, managed by the Jet Propulsion Laboratory, and funded by the National Aeronautics and Space Administration. We thank the *NuSTAR* Operations, Software, and Calibration teams for support with the execution and analysis of these observations. This research has made use of the *NuSTAR* Data Analysis Software (NuSTARDAS), jointly developed by the ASI Science Data Center (ASDC, Italy) and the California Institute of Technology (USA).

REFLECTION SPECTRA OF THE BLACK HOLE BINARY  
CANDIDATE MAXI J1535–571 IN THE HARD STATE  
OBSERVED BY *NUSTAR*

Xu Y., Harrison F. A., García J. A., Fabian A. C. et al. (2018). “Reflection Spectra of the Black Hole Binary Candidate MAXI J1535–571 in the Hard State Observed by *NuSTAR*.” *The Astrophysical Journal Letters*, 852(2):L34. doi: 10.3847/2041–8213/aaa4b2.

**Abstract**

We report on a *NuSTAR* observation of the recently discovered bright black hole candidate MAXI J1535–571. *NuSTAR* observed the source on MJD 58003 (five days after the outburst was reported). The spectrum is characteristic of a black hole binary in the hard state. We observe clear disk reflection features, including a broad Fe  $K\alpha$  line and a Compton hump peaking around 30 keV. Detailed spectral modeling reveals narrow Fe  $K\alpha$  line complex centered around 6.5 keV on top of the strong relativistically broadened Fe  $K\alpha$  line. The narrow component is consistent with distant reflection from moderately ionized material. The spectral continuum is well described by a combination of cool thermal disk photons and a Comptonized plasma with the electron temperature  $kT_e = 19.7 \pm 0.4$  keV. An adequate fit can be achieved for the disk reflection features with a self-consistent relativistic reflection model that assumes a lamp-post geometry for the coronal illuminating source. The spectral fitting measures a black hole spin  $a > 0.84$ , inner disk radius  $R_{\text{in}} < 2.01 r_{\text{ISCO}}$ , and a lamp-post height  $h = 7.2^{+0.8}_{-2.0} r_g$  (statistical errors, 90% confidence), indicating no significant disk truncation and a compact corona. Although the distance and mass of this source are not currently known, this suggests the source was likely in the brighter phases of the hard state during this *NuSTAR* observation.

**Keywords:** accretion, accretion disks — black hole physics — X-rays: binaries

#### 4.1 Introduction

MAXI J1535–571 was discovered by MAXI/GSC (Negoro et al., 2017) and Swift/BAT (Kennea et al., 2017) as an uncatalogued hard X-ray transient located near the Galactic plane on September 2, 2017. Subsequent monitoring in X-ray and radio

indicates behavior consistent with other known black hole transients, making it a strong black hole binary candidate (e.g., Negoro et al., 2017; Russell et al., 2017). The optical and near-infrared counterparts were identified (Dincer, 2017; Scaringi & ASTR211 Students, 2017). The source was reported to begin the hard-to-soft state transition around September 10 (Kennea, 2017; Nakahira et al., 2017), soon followed by the detection of low-frequency quasi-periodic oscillations (QPOs) by *Swift*/XRT (Mereminskiy & Grebenev, 2017). The X-ray flux level of MAXI J1535–571 rose rapidly, reaching  $\sim 5$  Crab in the MAXI/GSC band, making it one of the brightest black hole binary candidates known. At the time of this work the source is still in outburst and continues to evolve.

During a typical outburst, black hole binaries undergo a transition from the low/hard to the high/soft state through relatively short-lived intermediate states (see Remillard & McClintock, 2006, for a review). This process is believed to be associated with changes in the accretion flow geometry at the vicinity of the black hole. It is generally well accepted that the inner disk extends to the innermost stable circular orbit (ISCO) in the soft state. Since the black hole angular momentum sets the location of the ISCO radius, estimations of the black hole spin are possible via X-ray spectroscopy, which has been achieved either by modeling the thermal disk (e.g., Zhang et al., 1997) or the disk reflection component (e.g., Fabian et al., 1989). In addition, from the relativistic reflection spectrum, information can be obtained about the nature of the illuminating source commonly referred to as the “corona” (e.g., Miller et al., 2015b; Walton et al., 2017).

The interpretation of the hard state spectrum is still highly debated. The disk accretion model given by Esin et al. (1997) suggests the inner disk is truncated and replaced by an advection-dominated accretion flow at low mass accretion rates in the low/hard state. A recessed disk has also been invoked to explain the behavior of low-frequency QPOs commonly found in the hard state (e.g., Ingram et al., 2009, 2016). There have been efforts to measure the inner disk radius in the hard state through reflection modeling (e.g., Fürst et al., 2015; García et al., 2015b). However, controversies remain about the radius of truncation and when disk truncation occurs in terms of the Eddington ratio. The results in some cases have been questioned because of photon pile-up issues at high count rates (e.g., Done & Diaz Trigo, 2010; Miller et al., 2010).

With high sensitivity, broad bandpass and triggered read-out free from pile-up distortion, the *Nuclear Spectroscopic Telescope Array* (*NuSTAR*, Harrison et al., 2013)

is ideal for studying reflection in Galactic binaries. Recent *NuSTAR* observations of several black hole binaries in the bright hard state revealed very broad iron lines (Miller et al., 2013, 2015b), which are among the best evidence for lack of disk truncation. New observations of black hole binaries in outburst are important for understanding the accretion geometry in the hard state.

## 4.2 Observation and Data Reduction

MAXI J1535–571 was observed by *NuSTAR* (Harrison et al., 2013) starting on 2017 September 7 (MJD 58003) at 18:41:09 UT under a DDT request (OBSID 90301013002). We processed the *NuSTAR* data using v.1.6.0 of the NuSTAR-DAS pipeline with *NuSTAR* CALDB v20170817. After filtering background flares due to enhanced solar activity by setting `saacalc=2`, `saamode = OPTIMIZED`, and `tentacle = no` in NUPIPELINE, and the correction for dead time, the effective exposure times are 8.7 ks and 9.1 ks for the two focal plane modules FPMA and FPMB, respectively. The spectra were extracted from a circular region of the radius 180'' centered on the source location. We chose the background from a blank region on the detector furthest from source location to avoid source photons. The spectra were grouped to have a signal-to-noise (S/N) ratio of at least 30 per bin.

As shown in Figure 4.1, the *NuSTAR* observation caught MAXI J1535–571 in the hard state before the spectrum began to soften. The source flux rose quickly during the observation, the dead time corrected FPMA count rate increased from  $\sim 750$  cts  $s^{-1}$  to  $\sim 900$  cts  $s^{-1}$  from the start to the end of the exposure, exceeding the Crab count rate ( $\sim 500$  cts  $s^{-1}$ ) in the *NuSTAR* band (Madsen et al., 2015a). We only consider time-averaged spectra in this work, as there is no significant change in the hardness ratio (Figure 4.1(c)). We model the *NuSTAR* spectra using XSPEC v12.9.0n (Arnaud, 1996) using  $\chi^2$  statistics, and adopt the cross-sections from Verner et al. (1996) and abundances from Wilms et al. (2000). All parameter uncertainties are reported at the 90% confidence level for one parameter of interest. A cross-normalization constant is allowed to vary freely for FPMB and is assumed to be unity for FPMA.

## 4.3 Spectral Modeling

A clear reflection component is present in the *NuSTAR* spectra. To highlight the reflection features, we first fit the spectra with an absorbed cutoff power-law model, `TBabs*cutoffpl` in XSPEC notation, only considering the energy intervals of 3–4, 8–12, 40–79 keV. This approximate fit requires a power-law index  $\Gamma \sim 1.6$  and

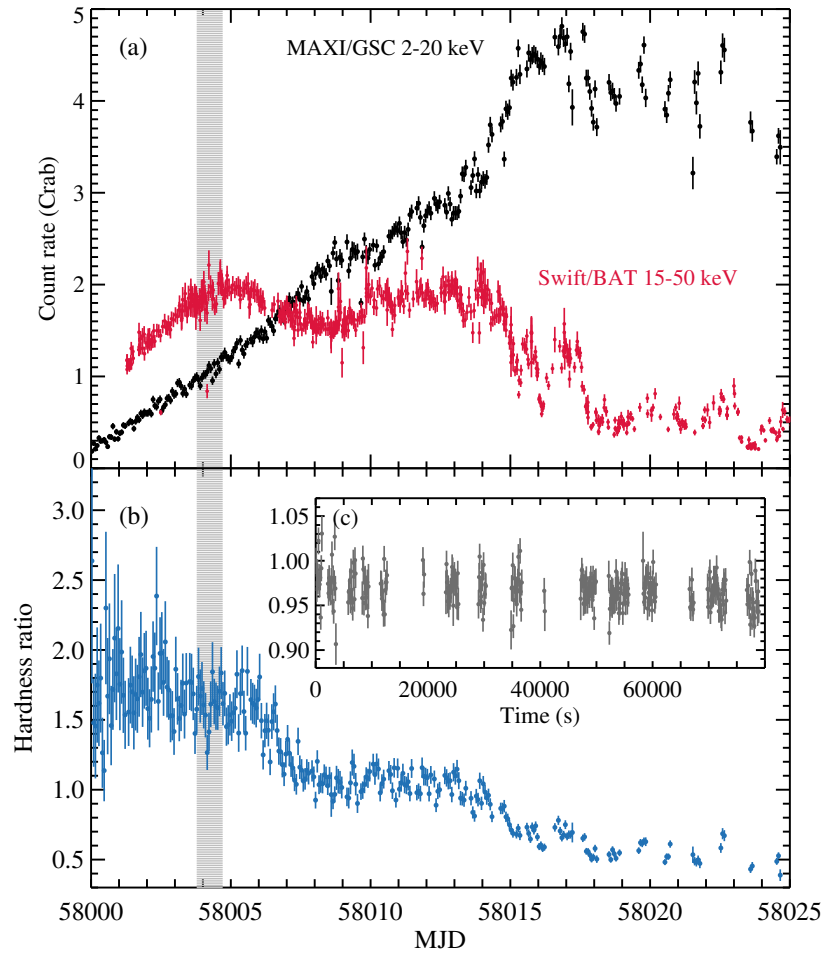


Figure 4.1: MAXI and Swift/BAT monitoring light curves of MAXI J1535-571. (a) MAXI/GSC (black) and Swift/BAT (red) orbital light curves of MAXI, scaled to the Crab count rates in the corresponding instrument bands (only BAT data points with  $S/N > 7$  are included). The gray shaded area marks the duration of the *NuSTAR* observation. (b) MAXI hardness ratio calculated from count rates (4–20 / 2–4 keV). (c) *NuSTAR* hardness ratio in 100s bins (count rates, 6–10 / 3–6 keV).

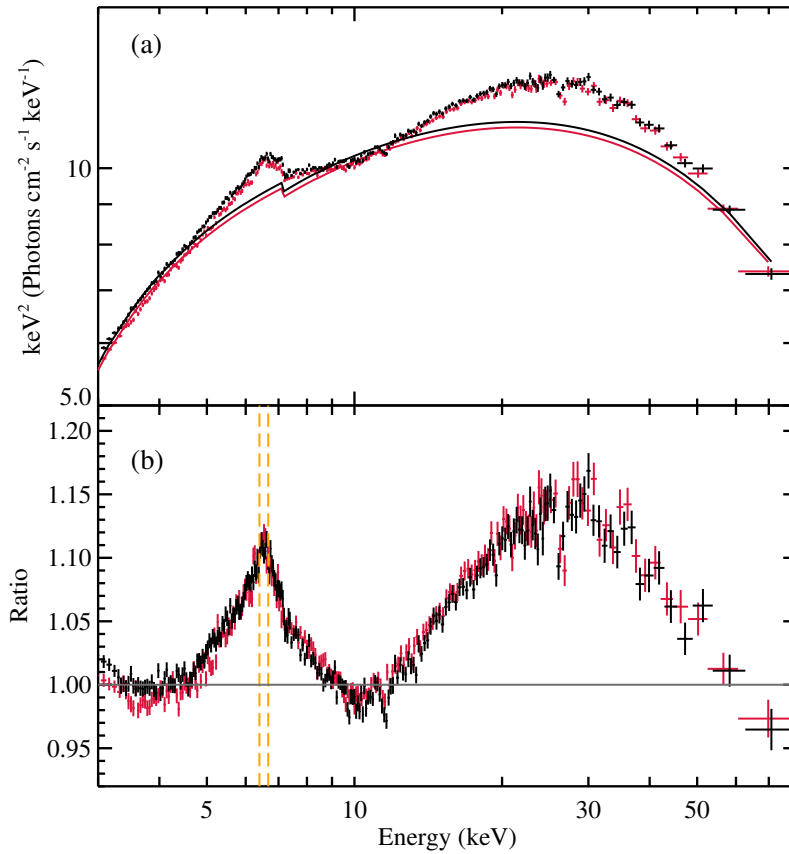


Figure 4.2: *NuSTAR* spectra of MAXI J1535–571 in the hard state. (a) Unfolded *NuSTAR* spectra of MAXI J1535–571. FPMA and FPMB data are plotted in black and red, respectively. (b) Data/model residuals to an absorbed cutoff power-law model. The narrow core of the iron line peaks at  $\sim 6.5$  keV. The energies of neutral Fe K $\alpha$  (6.4 keV) and Fe XXV K $\alpha$  (6.7 keV) are marked in orange dashed lines.

high-energy cutoff at  $E_{\text{cut}} \sim 60$  keV. As displayed in Figure 4.2, a broad iron line extending down to about 4.5 keV and a Compton hump peaking around 30 keV is evident. In addition, a sharp Fe K-edge can be seen at 7.1 keV, indicating strong absorption.

In the residuals, we also notice narrow dips in the spectra at 11.5 and 26.5 keV, which would only be obvious in bright sources with high S/N data. Whether these are instrumental related is unclear and currently under investigation. We ignore the corresponding energy bins in the spectral fitting from here on. There is also a slight difference ( $\sim 1\%$ ) between FPMA and FPMB below 5 keV as can be seen in Figure 4.2(b), which is within the calibration accuracy of *NuSTAR* (Madsen et al., 2015b). In order to improve the fitting statistics, we account for this discrepancy by fitting the photon-index,  $\Gamma$ , of FPMA and FPMB independently. In all fits in this

work, the difference in  $\Gamma$  is minimal (within 0.01) and would not influence other parameters. Therefore we only report the value of  $\Gamma$  from FPMA.

Motivated by the low high-energy cutoff, we model the continuum with the thermal Comptonization model `nthcomp` (Zdziarski et al., 1996; Życki et al., 1999). The shape of thermal Comptonization is significantly different from a cutoff power-law even below 80 keV (Zdziarski et al., 2003). To minimize the number of free parameters, we first fit the disk reflection assuming a “lamp-post” geometry, where the corona is a point source located on the spin axis of the black hole at a height,  $h$ , above the accretion disk. The source emissivity profile can be self-consistently calculated with the lamp-post assumption given the location of the illuminating source (Dauser et al., 2013). We use the lamp-post model `relxilllpCp` in the `relxill` model family (Dauser et al., 2014; García et al., 2014), which internally includes a `nthcomp` continuum. The reflection fraction can be self-consistently determined in `relxilllpCp` based on the inner disk radius  $R_{\text{in}}$ , the spin parameter  $a$ , and the lamp-post height  $h$  from ray-tracing calculations, which helps to constrain the geometry of the system and rules out some unphysical parts of the parameter space (see Dauser et al., 2014, for a discussion). We fit for  $a$  and  $R_{\text{in}}$  simultaneously, and freeze the outer edge of accretion disk,  $R_{\text{out}}$ , at  $400 r_g$ , where  $r_g$  is the gravitational radius defined as  $r_g \equiv GM/c^2$ ). In addition, we include possible contribution from reprocessing by distant material using an unblurred reflection model `xillverCp` (García & Kallman, 2010) to account for the narrow core of the Fe  $K\alpha$  line. We first assume the distant reprocessing to be neutral by fixing  $\log \xi = 0$  (where the ionization parameter  $\xi \equiv L/nR^2$ ,  $L$  is the ionizing luminosity,  $n$  is the gas density and  $R$  is the distance to the ionizing source), as neutral narrow Fe  $K\alpha$  lines have been commonly found in bright Galactic binaries (e.g., Parker et al., 2015; Walton et al., 2016). The iron abundance  $A_{\text{Fe}}$  and the input continuum in `xillverCp` are linked with those in the disk reflection component. The total model setup is `TBabs*(relxilllpCp+xillverCp)` (Model 1).

As shown in Figure 4.3 (left panel), Model 1 fails to adequately fit the spectral continuum, leaving obvious excesses at both the soft and hard end of the *NuSTAR* energy band. The reduced  $\chi^2_\nu$  ( $\chi^2/\nu$  where  $\nu$  is the number of degrees of freedom) is  $1986/1371 = 1.45$ . The fit can be greatly improved by adding a multi-color disk blackbody component: `TBabs*(relxilllpCp+xillverCp+diskbb)` (Model 2), with  $\chi^2_\nu = 1586/1369 = 1.16$ . A disk component is not evident in the *Swift*/XRT data as of September 11 (Kennea, 2017), which may be due to the high level of

Table 4.1: Best-fit Model Parameters

Component	Parameter	Model 3	Model 4
TBABS	$N_{\text{H}} (\times 10^{22} \text{ cm}^{-2})$	$8.2^{+0.3}_{-0.6}$	$7.2 \pm 0.3$
DISKBB	$kT_{\text{in}} (\text{keV})$	$0.43 \pm 0.01$	$0.40 \pm 0.01$
	Norm ( $10^5$ )	$1.07^{+0.20}_{-0.07}$	$1.2^{+0.6}_{-0.3}$
RELXILL(LP)CP	$h (r_{\text{g}})$	$7.2^{+0.8}_{-2.0}$	...
	$q_{\text{in}}$	...	$> 9.2$
	$q_{\text{out}}$	...	$3^*$
	$R_{\text{br}} (r_{\text{g}})$	...	$10^*$
	$a (cJ/GM^2)$	$> 0.84$	$> 0.987$
	$R_{\text{in}} (r_{\text{ISCO}})$	$< 2.01$	$< 1.22$
	$i (^\circ)$	$57^{+1}_{-2}$	$75^{+2}_{-4}$
	$\Gamma$	$1.815^{+0.005}_{-0.008}$	$1.862^{+0.014}_{-0.016}$
	$\log \xi (\log [\text{erg cm s}^{-1}])$	$3.69 \pm 0.04$	$3.19^{+0.21}_{-0.15}$
	$A_{\text{Fe}} (\text{solar})$	$1.4^{+0.3}_{-0.1}$	$0.8 \pm 0.1$
	$kT_{\text{e}} (\text{keV})$	$19.7 \pm 0.4$	$21.9 \pm 1.2$
	$R_{\text{ref}}$	1.55	$0.60^{+0.06}_{-0.10}$
	Norm	$0.129^{+0.006}_{-0.009}$	$0.089^{+0.007}_{-0.008}$
XILLVERCP	$\log \xi (\log [\text{erg cm s}^{-1}])$	$2.35^{+0.10}_{-0.08}$	$2.32^{+0.10}_{-0.14}$
	Norm ( $10^{-3}$ )	$7.8^{+1.0}_{-0.7}$	$17^{+3}_{-5}$
	$\chi^2/\nu$	1538/1368	1515/1367
	$F_{3-10 \text{ keV}} (\text{erg cm}^{-2} \text{ s}^{-1})^{\text{a}}$	$1.67 \times 10^{-8}$	
	$F_{10-79 \text{ keV}} (\text{erg cm}^{-2} \text{ s}^{-1})^{\text{b}}$	$3.62 \times 10^{-8}$	
	$F_{0.1-500 \text{ keV}} (\text{erg cm}^{-2} \text{ s}^{-1})^{\text{c}}$	$8.10 \times 10^{-8}$	$7.82 \times 10^{-8}$

Frozen parameters are marked with asterisks. There is no error estimation for  $R_{\text{ref}}$  in Model 3, as the parameter is self-consistently calculated in the lamp-post geometry. <sup>a,b</sup> Absorbed flux calculated from the normalization of FPMA. <sup>c</sup> Unabsorbed flux.

obscuration. However, we note that the contribution from the thermal disk is important for an adequate fit even at higher energies, because it allows for a harder continuum. There are still some residuals left, a narrow peak between 6 to 7 keV (see Figure 4.3). As can be seen in Figure 4.2(b), the narrow core of the iron line actually peaks between 6.4 keV (neutral Fe  $K\alpha$ ) and 6.7 keV (Fe XXV  $K\alpha$ ), indicating that the distant reprocessing is most likely ionized. Therefore, we leave the ionization parameter to vary freely in `xillverCp` (Model 3).

Model 3 yields a reasonable fit,  $\chi^2/\nu = 1538/1368 = 1.12$  with no obvious residuals (see Figure 4.3). Allowing the distant reflection component to be ionized brings an

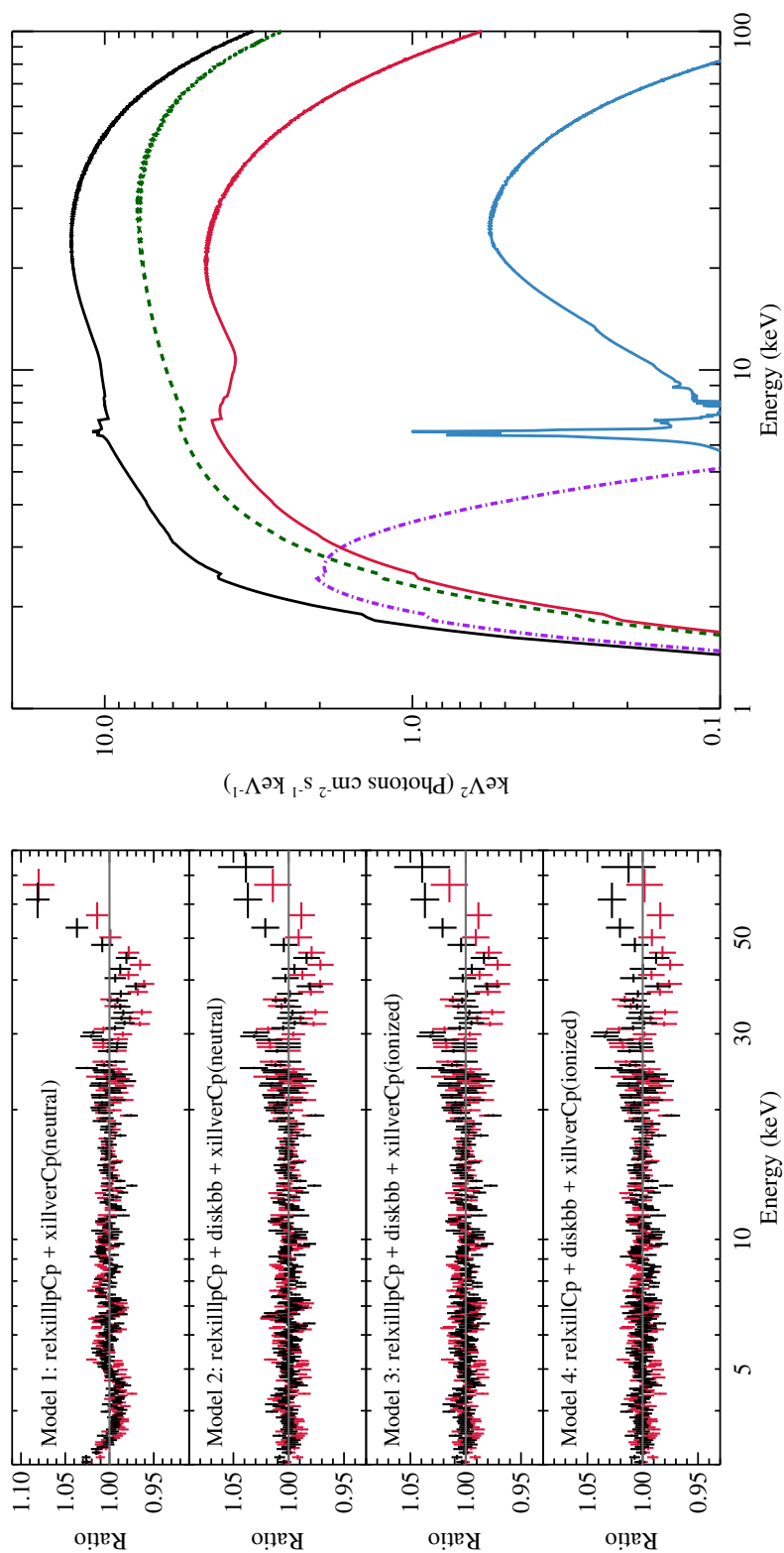


Figure 4.3: Ratio plots of the reflection modeling and the best fit model. Left: Ratio plots of the reflection modeling and the best fit model. The spectra are rebinned for display clarity. Right: Contributions from different spectral components in Model 3. The total model is marked in black solid lines, together with the thermal disk (purple), Comptonization continuum (dark green), disk reflection (red), and distant reflection (blue).

improvement of  $\Delta\chi^2 = 48$  for one additional parameter, with the ionization parameter for the distant reprocessing material measured as  $\log \xi = 2.35_{-0.08}^{+0.10}$ , indicating that the narrow core is actually a blend of Fe K line complex (which are not well separated by *NuSTAR*). The relative contributions from different components are plotted in Figure 4.3 (right panel). The Comptonization model `nthcomp` describes the incident continuum by the asymptotic photon-index,  $\Gamma$ , and the electron temperature,  $kT_e$ , which are well measured to be  $1.815_{-0.008}^{+0.005}$  and  $19.7 \pm 0.4$  keV, respectively. We note the value of  $kT_e$  here is as observed, not in the source frame. The model also finds an inclination angle of  $i = 57_{-2}^{+1^\circ}$ , an iron abundance  $A_{\text{Fe}} = 1.4_{-0.1}^{+0.3}$  (in solar units), and an accretion disk ionization parameter  $\log \xi = 3.69 \pm 0.04$  (see Table 4.1).

In addition, the disk reflection modeling indicates a relatively low lamp-post height of  $h = 7.2_{-2.0}^{+0.8} r_g$ . The constraints on the spin,  $a$ , and inner disk radius,  $R_{\text{in}}$ , are plotted in Figure 4.4. Here we measure  $R_{\text{in}}$  in units of  $r_{\text{ISCO}}$  to better test whether the disk is truncated as the black hole spin is not known a priori. The radius of the ISCO is a function of the black hole spin, decreasing monotonically from  $6 r_g$  for a Schwarzschild black hole to  $1.235 r_g$  for a black hole with the maximum spin parameter of 0.998. The results are strongly inconsistent with a significantly truncated accretion disk scenario, with the best-fit parameters  $a > 0.84$  and  $R_{\text{in}} < 2.01 r_{\text{ISCO}}$ . The  $\Delta\chi^2$  contour flattens down at the regime of high  $a$  and low  $R_{\text{in}}$  (Figure 4.4), which is expected as the two parameters are degenerate, both controlling the absolute position of the inner disk radius. The reflection fraction  $R_{\text{ref}}$  given by the lamp-post model is 1.55, defined to be the ratio of the coronal intensity illuminating the disk to that reaching the observer (Dauser et al., 2016). A high reflection fraction is an indicator of strong light bending effects, resulting from a combination of a low corona height, a small inner disk radius, and a high spin. Fitting for the reflection fraction as a free parameter does not result in a significantly improved fit.

The model also confirms the obscured nature of the source with the absorption column density  $N_{\text{H}} = 8.2_{-0.6}^{+0.3} \times 10^{22} \text{ cm}^{-2}$ . The value is higher than that reported by *Swift*/XRT ( $N_{\text{H}} = 3.6 \pm 0.2 \times 10^{22} \text{ cm}^{-2}$ , Kennea, 2017), but a higher  $N_{\text{H}}$  is expected in order to obtain a similar spectral shape with an extra thermal disk component included; a high  $N_{\text{H}}$  was also reported by preliminary results from ( $N_{\text{H}} = 4.89 \pm 0.06 \times 10^{22} \text{ cm}^{-2}$ , Gendreau et al., 2017). We note that the values of  $N_{\text{H}}$  reported here were measured at different epochs, thus the difference could possibly be due to variations in the intrinsic absorption column during the outburst (e.g., Walton et al.,

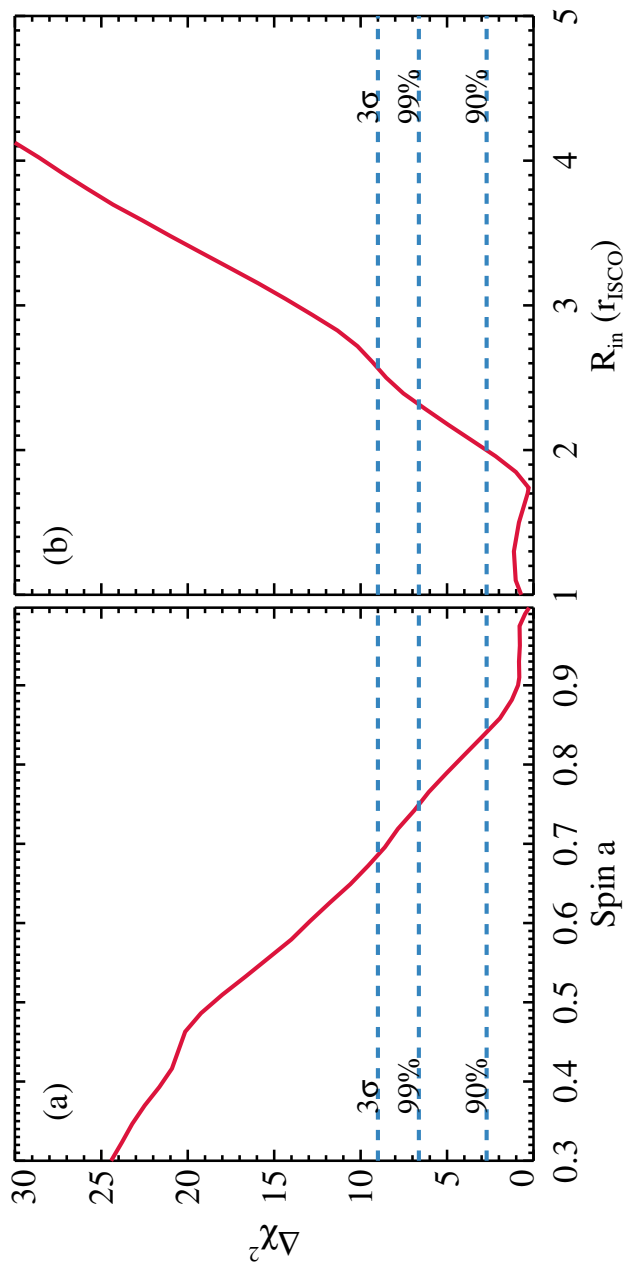


Figure 4.4:  $\Delta\chi^2$  plots for the black hole spin parameter  $a$  and inner accretion disk radius  $R_{\text{in}}$  from Model 3. The dashed lines mark the 90%, 99%, and  $3\sigma$  confidence levels for one parameter of interest.

2017). The inner disk temperature measured is  $kT_{\text{in}} = 0.43 \pm 0.01$  keV, which is somewhat higher than the values of several well-known black hole binaries in the hard state (e.g., Reynolds et al., 2010; Basak & Zdziarski, 2016). An alternative interpretation to the soft emission is to invoke a soft Comptonization component (e.g., Di Salvo et al., 2001). We explored this possibility by including an extra `nthcomp` model following Basak et al. (2017), but it brings no further improvement to the fit and causes no significant change in other parameters. In addition, we notice that the low-energy end of the spectra includes minor contributions from a dust scattering halo. Therefore, we stress that without soft band coverage, an accurate and unbiased determination of the disk temperature and absorption column density is difficult, but this uncertainty has negligible influence on the reflection parameters as the spectra can be well fitted above 5 keV without a thermal disk or soft Comptonization component, and the other parameters remain unchanged.

To explore the disk emissivity beyond the assumption from a lamp-post geometry, we use a broken power-law emissivity profile ( $\epsilon(r) \propto r^{-q}$ ) in the `relxillCp` model, which is described by the inner and outer emissivity indexes  $q_{\text{in,out}}$  and a break radius  $R_{\text{br}}$  (Model 4). The best-fit inner emissivity index,  $q_{\text{in}}$ , is pegged at the upper limit of 10, whereas  $q_{\text{out}}$  and  $R_{\text{br}}$  cannot be constrained. Thus we fix  $q_{\text{out}}$  at 3 as expected in the Newtonian case, and  $R_{\text{br}}$  at  $10 r_{\text{g}}$ . The model yields a broadly similar solution to the lamp-post model (see Table 4.1), also prefers a rapid black hole spin and a inner disk radius close to the ISCO. The reflection fraction in `relxillCp` is defined differently from the `relxilllpCp`, and the values are not directly comparable (for a detailed explanation, see Dauser et al., 2016). The extremely high emissivity index makes the model highly sensitive to the position of the inner radius, resulting in much tighter statistical constraints on  $a$  and  $R_{\text{in}}$ . However, the extreme value of the emissivity index could be an indication that the broken power-law is an overly simplified description of the complicated emissivity profile. Also, although this results in a better fit, we note that the main difference of Model 3 and Model 4 lies in the high energy tail (see Figure 4.3, left panel), where FPMA and FPMB data do not match perfectly, indicating that the difference of the two models is close to the instrumental calibration accuracy. Therefore, we focus our discussion on the results from Model 3.

#### 4.4 Discussion and Conclusions

We have performed a spectral analysis of the *NuSTAR* observation of the recently discovered black hole binary candidate MAXI J1535–571 in the bright hard state.

Spectral fitting with relativistic reflection models measures a high black hole spin of  $a > 0.84$  and a small inner disk radius  $R_{\text{in}} < 2.01 r_{\text{ISCO}}$ . It supports that the inner edge of the accretion disk remains close to the ISCO at the bright hard state of MAXI; the result is independent of whether a lamp-post coronal geometry is assumed or not. We measure a high reflection fraction  $R_{\text{ref}} = 1.55$ , which can be self-consistently described in the lamp-post model as the result of strong light bending effects near the black hole. Our spin constraint is consistent with the preliminary results reported by a observation in the intermediate state (Gendreau et al., 2017). With basic properties of the binary system unknown (i.e., distance, black hole mass, orbital period), the exact Eddington ratio at the time of the observation is unclear. Assuming a distance of 8 kpc as the source direction is close to the Galactic center, we measure the source luminosity  $L_{0.1-500 \text{ keV}} \sim 6 \times 10^{38} \text{ erg s}^{-1}$ , which is about half the Eddington luminosity for a  $10 M_{\odot}$  black hole <sup>1</sup>.

In addition, we measure a lamp-post height of  $h = 7.2_{-2.0}^{+0.8} r_g$  and an electron temperature of  $kT_e = 19.7 \pm 0.4 \text{ keV}$ , suggesting a compact and relatively cool corona. Low coronal temperatures, or equivalently low values for the high-energy cutoff, have so far been robustly measured in several black hole binaries during bright hard states with *NuSTAR* (e.g., Miller et al., 2013, 2015b). Evidence has been found previously that the coronal temperature decreases during the rising phase of the hard state (e.g., Joinet et al., 2008; Motta et al., 2009; García et al., 2015b) and the high-energy cutoff disappears at the time of state transition (e.g., Belloni et al., 2006), which signals a dramatic changes in the coronae.

A weak narrow Fe  $K\alpha$  component is required for an adequate fit of the *NuSTAR* data, which can be well described by a moderately ionized unblurred reflection model *xillverCp*. A high resolution systematic study of Fe lines in X-ray binaries using *Chandra*/HETGS reveals that narrow Fe fluorescence emission is ubiquitous in high-mass X-ray binaries, but rare in low-mass X-ray binaries (Torrejón et al., 2010). It is unclear where the moderately ionized distant reprocessing material is located in MAXI. The best-fit absorption column density  $N_{\text{H}} = 8.2_{-0.6}^{+0.3} \times 10^{22} \text{ cm}^{-2}$  is higher than the expected value for the Galactic absorption column,  $N_{\text{H,Gal}} = 1.43 \times 10^{22} \text{ cm}^{-2}$  (Kalberla et al., 2005). The extra obscuration is most likely intrinsic, which might be an indication of a complicated structure for the binary system. It is possible that the ionized reflection comes from the outer regions of a flared disk or the tilted outer part of a warped disk. Ionized narrow Fe  $K\alpha$  lines could also

---

<sup>1</sup> $L$  here is about the highest observed among black hole binaries in the hard state, and a few tens times higher than that in the hard state of Cygnus X-1.

be produced in disk winds (e.g., Miller et al., 2015b; King et al., 2015), but is less likely in this case as there is no evidence for absorption lines and source is measured to be viewed at high inclination.

In light of the detection of QPOs reported in later observations (Gendreau et al., 2017; Mereminskiy & Grebenev, 2017), we perform a search for possible QPOs in the frequency range of 0.1 Hz to 500 Hz in the *NuSTAR* power spectra, but obtain no significant detection, which is not uncommon considering the transient nature of the QPO behavior.

### **Acknowledgments**

We thank the referee for constructive comments that improved the paper. D.J.W. acknowledges support from STFC Ernest Rutherford Fellowship. J.A.G. acknowledges support from NASA Grant No. 80NSSC17K0515 and Alexander von Humboldt Foundation. This work was supported under NASA contract No. NNG08-FD60C and made use of data from the *NuSTAR* mission, a project led by the California Institute of Technology, managed by the Jet Propulsion Laboratory, and funded by the National Aeronautics and Space Administration. We thank the *NuSTAR* Operations, Software, and Calibration teams for support with the execution and analysis of these observations. This research has made use of the *NuSTAR* Data Analysis Software (NuSTARDAS), jointly developed by the ASI Science Data Center (ASDC, Italy) and the California Institute of Technology (USA).

THE HARD STATE OF THE HIGHLY ABSORBED HIGH  
INCLINATION BLACK HOLE BINARY CANDIDATE SWIFT  
J1658.2–4242 OBSERVED BY *NUSTAR* AND *SWIFT*

Xu Y., Harrison F. A., Kennea J. A., Walton D. J. et al. (2018). “The Hard State of the Highly Absorbed High Inclination Black Hole Binary Candidate Swift J1658.2–4242 Observed by *NuSTAR* and *Swift*.” *The Astrophysical Journal*, 865(1):18. DOI: 0.3847/1538–4357/aada03.

**Abstract**

We present a spectral and timing analysis of the newly reported Galactic X-ray transient Swift J1658.2–4242 observed by *NuSTAR* and *Swift*. The broad-band X-ray continuum is typical of a black hole binary in the bright hard state, with a photon index of  $\Gamma = 1.63 \pm 0.02$  and a low coronal temperature of  $kT_e = 22 \pm 1$  keV, corresponding to a low spectral cutoff well constrained by *NuSTAR*. Spectral modeling of the relativistic disk reflection features, consisting of a broad Fe  $K\alpha$  line and the Compton reflection hump, reveals that the black hole is rapidly spinning with the spin parameter of  $a^* > 0.96$ , and the inner accretion disk is viewed at a high inclination angle of  $i = 64_{-3}^{+2^\circ}$  (statistical errors, 90% confidence). The high inclination is independently confirmed by dips in the light curves, which can be explained by absorbing material located near the disk plane temporarily obscuring the central region. In addition, we detect an absorption line in the *NuSTAR* spectra centered at  $7.03_{-0.03}^{+0.04}$  keV. If associated with ionized Fe K absorption lines, this provides evidence for the presence of outflowing material in the low/hard state of a black hole binary candidate. A timing analysis shows the presence of a type-C QPO in the power spectrum, with the frequency increasing from  $\sim 0.14$  Hz to  $\sim 0.21$  Hz during the single *NuSTAR* exposure. Our analysis reveals that Swift J1658.2–4242 displays characteristics typical for a black hole binary that is viewed at a high inclination angle, making it a good system for studying the accretion geometry in black hole binaries.

**Keywords:** accretion, accretion disks – X-rays: binaries – X-rays: individual (Swift J1658.2–4242)

## 5.1 Introduction

Most Galactic black hole binaries are discovered as X-ray transients that go into recurrent outbursts. During a typical outburst, a black hole binary transitions from the low/hard state (power-law component dominates the energy spectrum with a hard photon index) to the high/soft state (thermal disk component dominates) as the source flux increases (see Remillard & McClintock, 2006, for a review). The changes in the spectral shape are believed to be associated with the evolution of the accretion geometry. One hypothesis that has been widely explored is that the inner disk extends to the innermost stable circular orbit (ISCO) in the soft state, whereas is truncated at a larger radius in the hard state (e.g., Esin et al., 1997; Done et al., 2007). However, it has been suggested from observations that the inner disk extends down to the ISCO in the hard state of black hole binaries in several cases (e.g., Miller et al., 2002, 2006a). Whether the accretion disk is truncated can be determined by measuring the degree of relativistic distortion of the Fe  $K\alpha$  emission line, which comes from reflection of the central emission by the inner accretion disk (e.g., Fabian et al., 1989). Recently, *NuSTAR* observations of several black hole binaries in the bright hard state revealed very broad Fe  $K\alpha$  lines (Miller et al., 2015b; El-Batal et al., 2016; Xu et al., 2018b). As *NuSTAR* spectra are free from pile-up distortions even at high count rates typical of Galactic X-ray binaries, these results clearly challenge the disk truncation interpretation of the hard state.

Mass outflows are important phenomena in the study of accretion processes. Equatorial disk winds, identified by narrow absorption lines from highly ionized iron (mostly Fe XXV and Fe XXVI), have been observed in a number of black hole binaries in the soft state, and are more likely to be observed in high inclination systems (e.g., Neilsen & Lee, 2009; King et al., 2014; Miller et al., 2015a). Detailed studies of several well-known black hole binaries indicate that the presence of accretion disk winds appears to be anti-correlated with relativistic jets (e.g., Neilsen & Lee, 2009; Miller et al., 2012). The disk wind is thought to be responsible for carrying away a considerable amount of kinetic energy when the jet switches off in the high/soft state. During typical low/hard states when the source Eddington ratio is relatively low, however, collimated radio jets are ubiquitous, and disk wind features are either absent or at least much weaker, thus making the detection difficult (e.g., Ponti et al., 2012; Miller et al., 2012).

Swift J1658.2–4242 is a newly discovered X-ray transient in the Galactic plane. The first reported detection was made by *Swift*/BAT (Krimm et al., 2013) on February

16, 2018. The source was detected by *INTEGRAL* during its observations of the Galactic center field on February 13, 2018, with a spectral hardness typical for black hole binaries in the hard state (Grebenev et al., 2018; Grinberg et al., 2018). Subsequent radio observations by ATCA imply that the source is a black hole binary at a distance of greater than 3 kpc (Russell et al., 2018). Low frequency quasi-periodic oscillations (QPOs) increasing in frequency were detected by *NuSTAR* (Xu et al., 2018a) and *AstroSAT* (Beri et al., 2018). X-ray spectra from *Swift*/XRT reveal that the source is highly absorbed, with an absorption column density of  $N_{\text{H}} > 10^{23} \text{ cm}^{-2}$  (Lien et al., 2018). In addition, several dips were observed from initial analysis of the *NuSTAR* data (Xu et al., 2018a), similar to those detected in known dipping low-mass X-ray binaries (LMXBs) (e.g., Tomsick et al., 1998; Díaz Trigo et al., 2009; Kuulkers et al., 2013). Dips in the light curves of black hole and neutron star binaries are signatures of high inclination ( $i > 65^\circ$ ). They are thought to originate from obscuring material located at the thick outer region of the accretion disk in LMXBs (White & Swank, 1982; Frank et al., 1987); while in HMXBs, dips can be explained by obscuration by the stellar wind from the donor star.

In this paper, we present a spectral and timing analysis of the newly discovered black hole binary candidate Swift J1658.2–4242, using simultaneous *NuSTAR* and *Swift* observations that caught the source in the hard state. The paper is structured as follows: in Section 5.2, we describe the observations and the data reduction details; we present the results of our spectral modeling and timing analysis in Section 5.3, 5.4, and 5.5, and discuss the results in Section 5.6.

## 5.2 Observations and Data Reduction

Swift J1658.2–4242 was observed by *NuSTAR* (Harrison et al., 2013) on February 16, 2018 starting at 23:26:09 UT for an exposure of 33.3 ks per module (OBSID: 90401307002). The observation was approved through DDT time, and was taken on the same day that the outburst was first reported. We reduced the *NuSTAR* data following standard procedure using NuSTARDAS pipeline v.1.6.0 and CALDB v20170817. The source spectra were extracted from a circular region with the radius of  $150''$  from the two *NuSTAR* focal plane modules (FPMA and FPMB). Corresponding background spectra were extracted using polygonal regions from source-free areas in the detectors. We also extracted spectra from mode 6 data following the procedures described in Walton et al. (2016), which yielded an extra  $\sim 3.6$  ks of data when an aspect solution was not available from the on board star

tracker CHU4. We grouped the *NuSTAR* spectra with a signal-to-noise ratio (S/N) of 20 per energy bin.

The outburst of Swift J1658.2–4242 was monitored by *Swift*/XRT (Burrows et al., 2005). The XRT observation (OBSID: 00810300002) overlapping with the *NuSTAR* observation used in this paper was taken in the Windowed Timing (WT) mode to avoid photon pile-up. The XRT observation was taken around the middle of the *NuSTAR* exposure, starting from 10:38:52 UT to 16:43:57 UT on February 17, 2018. We reduced the the *Swift*/XRT data using `xrtpipeline` v.0.13.2 with CALDB v20171113. We extracted the source spectrum from a circular region with the radius of  $70''$ , and the background was extracted from an annulus area with the inner and outer radii of  $200''$  and  $300''$ , respectively. After standard data filtering, the total exposure time is 3.9 ks. The XRT spectrum was rebinned to have at a S/N of of least 5 per bin.

### 5.3 Light Curves

Evolution of the flux of Swift J1658.2–4242 since the beginning of the outburst observed by *Swift*/XRT and BAT is shown in Figure 5.1. The *Swift*/BAT light curve in daily averaged flux is from the *Swift*/BAT transient monitor (Krimm et al., 2013). *Swift*/XRT data were reduced following the procedures described in Section 5.2, and the XRT flux was calculated by fitting the spectra with an absorbed power-law model, `TBabs*powerlaw`. In this work, we perform all spectral fitting using XSPEC v12.9.0n (Arnaud, 1996) with  $\chi^2$  statistics, and adopt the cross-sections from Verner et al. (1996) and abundances from Wilms et al. (2000). All parameter uncertainties are reported at the 90% confidence level for one parameter of interest unless otherwise clarified. As shown in Figure 5.1(b), the *NuSTAR* observation caught Swift J1658.2–4242 in the hard state before significant spectral softening occurred.

Three dips are evident in the *NuSTAR* light curve generated by the standard NUPRODUCTS procedure, where the *NuSTAR* full band count rate decreased by  $\sim 45\% - 70\%$  at the dip minima (see Figure 5.2(a)). Dipping has been found to be periodic in the black hole binaries GRO J1655–40 and MAXI J1659–152, and are associated with the binary orbital period in these systems (Kuulkers et al., 1998, 2013). It is possible that the dips observed in Swift J1658.2–4242 are also periodic, but cannot be confirmed with the limited exposure time of our *NuSTAR* observation. We extract source light curves from three energy intervals, 3–6 keV (*S*), 6–10 keV (*M*), 10–

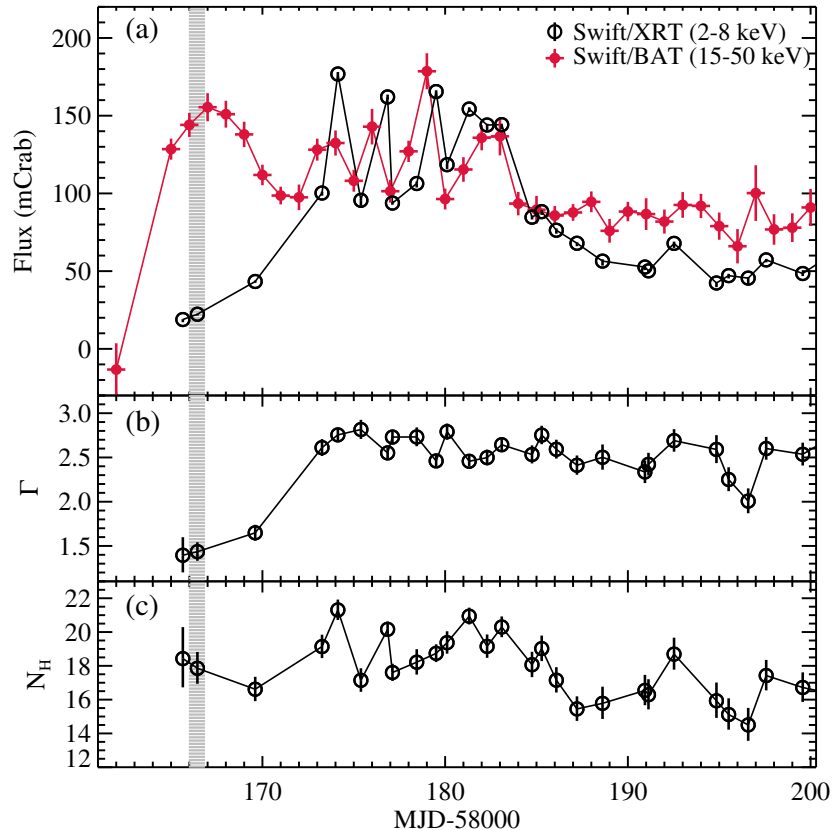


Figure 5.1: *Swift* monitoring of the outburst of Swift J1658.2–4242. (a) *Swift* monitoring lightcurves of the outburst of Swift J1658.2–4242. The BAT light curve is rescaled to the unit mCrab from count rates in the 15–50 keV band. The XRT light curve is converted to mCrab using calculated flux in the 2–8 keV band. (b) (c) Photon index  $\Gamma$  and absorption column density  $N_H$  derived by fitting the XRT spectra with an absorbed power-law model. Gray shaded area marks the duration of the *NuSTAR* observation.

79 keV ( $H$ ), and calculate hardness ratios defined as  $HR1 = (M - S)/(M + S)$  and  $HR2 = (H - M)/(H + M)$ . The dips are clearly detected in all three energy bands. The hardness ratios are found to increase during the dips (see Figure 5.2(b),(c)), indicating that the dips are caused by increased absorption along the line of sight.

The source count rate was rising linearly during the *NuSTAR* observation. Despite the increase in count rate, the hardness ratio, HR1, basically remains constant outside of the dips. The overall change in HR2 is also relatively small (decreased by  $\sim 0.03$  by the end of the exposure), which in this case is mainly due to the change in the high energy cutoff. The cutoff energy,  $E_{\text{cut}}$ , in black hole binaries has been observed to decrease monotonically with the increasing flux during the rising phases of their hard states (e.g., Joinet et al., 2008; Motta et al., 2009). We note here the corresponding changes in the absolute values of spectral parameters are sub-

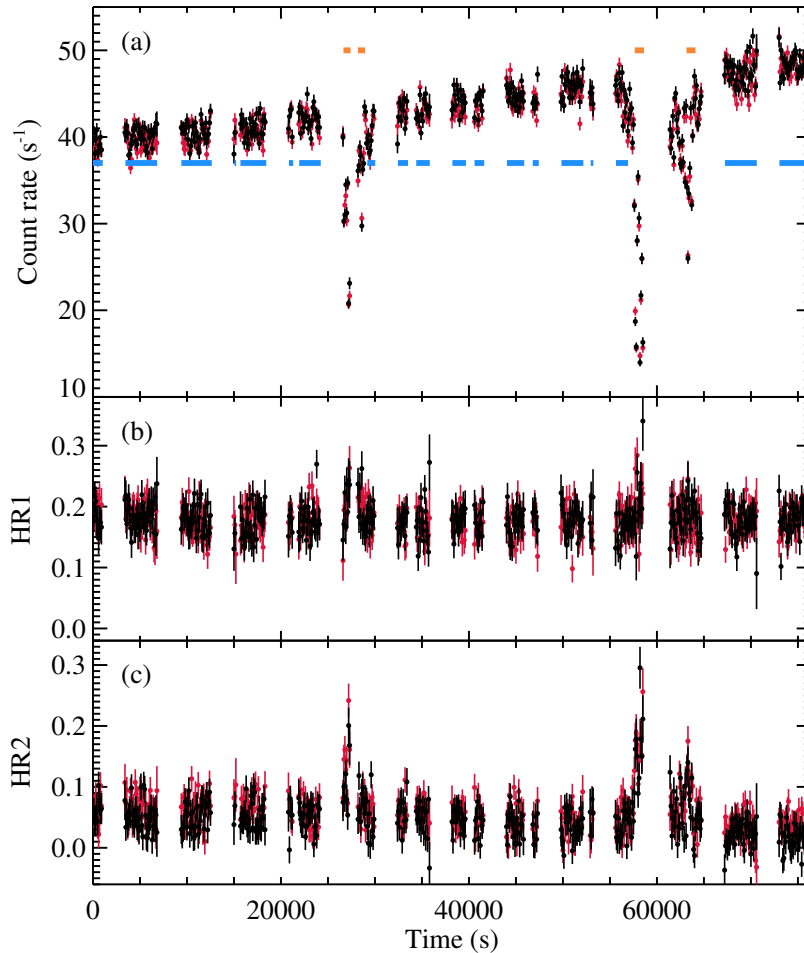


Figure 5.2: *NuSTAR* light curves and hardness ratios of Swift J1658.2–4242. (a) *NuSTAR* full band light curves of Swift J1658.2–4242 in 100s bins (FPMA in black, FPMB in red). Orange and blue lines mark the data intervals selected for the dip and persistent spectra, respectively. The orbital gaps in the light curves are due to occultations and SAA passages. (b) (c) Plots of corresponding hardness ratios. Hardness ratios HR1 and HR2 are defined as  $HR1 = (M - S)/(M + S)$  and  $HR2 = (H - M)/(H + M)$ , where  $S$ ,  $M$ ,  $H$  are the count rates in the energy bands of 3–6 keV, 6–10 keV, and 10–79 keV, respectively.

tle. Therefore, for spectral modeling, we only consider time-averaged spectra and separate the total exposure by dipping and non-dipping phases.

## 5.4 Spectral Analysis

### 5.4.1 Persistent Spectra

We first consider time-averaged spectra excluding the dips, which we refer to as the persistent spectra henceforth. Although the exposure of *Swift*/XRT is much shorter than that of the *NuSTAR* observation, *Swift* caught the second dip observed by *NuSTAR*, which we also excluded from the XRT data when extracting the persistent

spectrum. The accumulated times for the persistent spectra are 30.9 ks, 31.4 ks, and 3.6 ks for *NuSTAR*/FPMA, *NuSTAR*/FPMB, and *Swift*/XRT, respectively.

Relativistic reflection features are clearly detected in the *NuSTAR* spectra, including a broad Fe  $K\alpha$  line and a Compton reflection hump peaking around 30 keV (see Figure 5.3). To highlight the disk reflection features, we first fit the *NuSTAR* spectra with an absorbed cutoff power-law model: TBnew\*cutoffpl, in XSPEC notation, only considering the energy intervals of 3–5, 8–12, and 40–79 keV. We note that in the residual plot, there is some indication for an absorption line around 7 keV (see Figure 5.3(b)), near the absorption edge. Throughout this work, we use the TBnew<sup>1</sup> model to account for neutral absorption, and fix all abundances at solar in TBnew. This updated version of the TBabs model better characterises the shape of the absorption edges, which could be relevant here as the source has a high absorption column density. This approximate fit requires an absorption column density of  $N_{\text{H}} \sim 1.3 \times 10^{23} \text{ cm}^{-2}$ , a photon index of  $\Gamma \sim 1.3$ , and a relatively low cutoff energy of  $E_{\text{cut}} \sim 55 \text{ keV}$ .

To obtain broad-band X-ray coverage so that spectral parameters can be better constrained, we jointly fit the *NuSTAR* and the *Swift*/XRT spectra. We allow the cross-normalization constants to vary freely for *NuSTAR*/FPMB and *Swift*/XRT, and fix the value at unity for *NuSTAR*/FPMA. We use XRT data above 1 keV, as low energy spectral residuals have been reported in heavily absorbed sources observed in the WT mode<sup>2</sup>. Also *NuSTAR* data below 4 keV are ignored during the spectral fitting to avoid possible calibration uncertainties near the low energy end of the band pass. We use the model relxilllpCp in the relxill model family (Dauser et al., 2014; García et al., 2014) to physically model the relativistic reflection spectra. The relxilllpCp model uses an idealized lamp-post geometry for the illuminating source commonly referred to as the corona. In this model, the corona is approximated as a point source located on the spin axis of the black hole above the accretion disk. The reflection fraction,  $R_{\text{ref}}$ , can be self-consistently calculated in the lamp-post model based on the geometry assumed, which helps to reduce the parameter space. It uses the thermal Comptonization model nthcomp (Zdziarski et al., 1996; Życki et al., 1999) as the input continuum, which provides a generally different spectral curvature from the phenomenological cutoffpl model, especially in the case of a low high-energy cutoff. For all spectral fitting with relxilllpCp, we fix the outer radius of the accretion disk  $R_{\text{out}}$  at  $400 r_{\text{g}}$  ( $r_{\text{g}} \equiv \text{GM}/c^2$  is the grav-

<sup>1</sup><http://pulsar.sternwarte.uni-erlangen.de/wilms/research/tbabs/>

<sup>2</sup>[http://www.swift.ac.uk/analysis/xrt/digest\\_cal.php](http://www.swift.ac.uk/analysis/xrt/digest_cal.php)

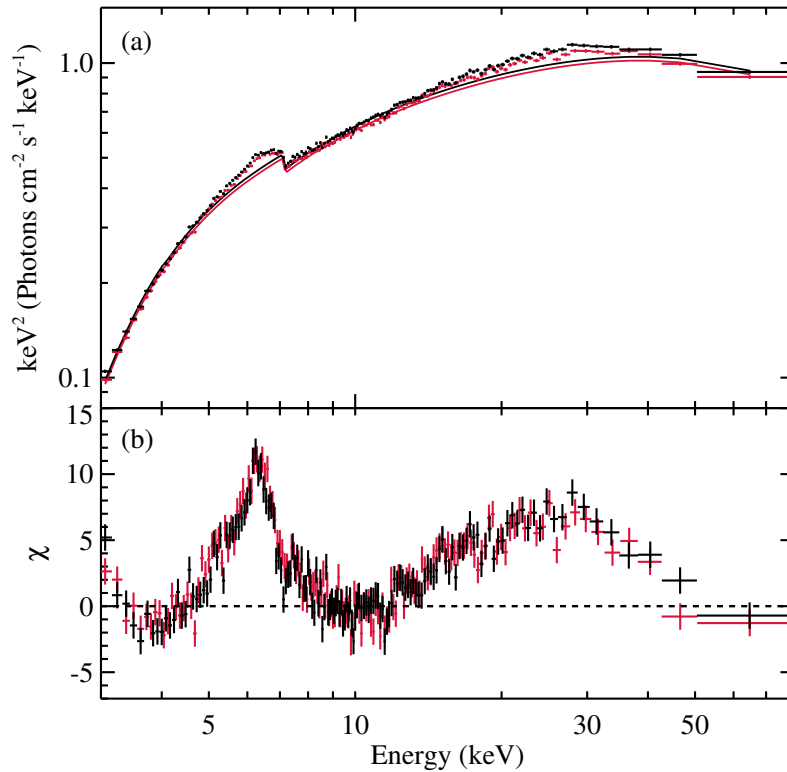


Figure 5.3: *NuSTAR* spectra of Swift J1658.2–4242 during the hard state. (a) Persistent (non-dip) hard state spectra of Swift J1658.2–4242 observed by *NuSTAR*. FPMA and FPMB data are plotted in black and red, respectively. The energy spectra are folded with a cut-off power-law model. (b) Clear relativistic reflection features can be seen in the spectral residuals plotted in  $\chi$ . The spectra have been rebinned for display clarity.

itational radius), and set the value of reflection fraction  $R_{\text{ref}}$  to be self-consistently determined by the model given the combination of the black hole spin parameter  $a^*$ , the inner radius of the accretion disk  $R_{\text{in}}$ , and the lamp-post height  $h$ . The inner disk radius  $R_{\text{in}}$  and the black hole spin parameter  $a^*$  are degenerate, as they both control the effective inner accretion disk radius. Therefore, for simplicity, during the spectral fitting we assume that the inner disk extends down to the ISCO by fixing  $R_{\text{in}}$  at the radius of the ISCO, and fit for the black hole spin as a free parameter (see Section 5.6 for a discussion about disk truncation).

It is clear disk reflection alone `TBabs*relxilllpCp` (Model 1) is not sufficient to describe the data (reduced chi-squared  $\chi^2/\nu = 1808.8/1599 = 1.13$ , where  $\nu$  is the number of degrees of freedom). Secondary features including a narrow iron line and possible absorption around 7 keV can be seen in the residual plot (see Figure 5.4(b)). A narrow iron line component on top of the broad Fe K profile has been found in a number of black hole binaries observed by *NuSTAR* (e.g., Walton

Table 5.1: Spectral Fitting of Swift J1658.2–4242 in the Hard State

Component	Parameter	Persistent (Model 3)	Persistent (Model 4)	Dipping (Model 5)
TBNEW PARCOV*(TBNEW*CABS)	$N_H$ ( $\times 10^{23}$ cm $^{-2}$ )	$1.85^{+0.07}_{-0.10}$	$1.80 \pm 0.08$	—
	$N_H$ ( $\times 10^{24}$ cm $^{-2}$ )	...	...	$1.00^{+0.08}_{-0.07}$
XSTAR	$f_{\text{cov}}$ (%)	...	...	$34 \pm 1$
	$N_H$ ( $\times 10^{22}$ cm $^{-2}$ )	$3.2^{+1.4}_{-1.0}$	$2.0^{+1.2}_{-1.0}$	—
	$\log(\xi)$ (log [erg cm s $^{-1}$ ])	$2.09^{+0.17}_{-0.07}$	$2.00^{+0.27}_{-0.08}$	—
	$v_{\text{out}}/c$	$0.077^{+0.006}_{-0.007}$	$0.080^{+0.007}_{-0.014}$	—
	$h$ ( $r_g$ )	$< 6.6$	$< 3.8$	—
RELXILLPCP	$a^*$ ( $cJ/GM^2$ )	$0.92^{+0.04}_{-0.06}$	$> 0.96$	—
	$i$ ( $^\circ$ )	$61^{+3}_{-4}$	$64^{+2}_{-3}$	—
	$\Gamma$	$1.69 \pm 0.02$	$1.63 \pm 0.02$	—
	$\log(\xi)$ (log [erg cm s $^{-1}$ ])	$3.49^{+0.10}_{-0.08}$	$3.47^{+0.19}_{-0.09}$	—
	$A_{\text{Fe}}$ (solar)	$0.60^{+0.07}_{-0.09}$	$0.91^{+0.54}_{-0.08}$	—
GAUSSIAN	$kT_e$ (keV)	$27 \pm 3$	$22 \pm 1$	—
	$R_{\text{ref}}$	$2.19$	$3.25$	—
	Norm ( $10^{-2}$ )	$1.5^{+1.2}_{-0.7}$	$1.7^{+0.1}_{-0.4}$	—
	$E_{\text{emi}}$ (keV)	...	$6.30 \pm 0.04$	—
	$\sigma$ (keV)	...	$0.23^{+0.08}_{-0.06}$	—
XILLVERCP	Norm ( $10^{-4}$ )	...	$5.7^{+1.4}_{-1.1}$	—
	Norm ( $10^{-2}$ )	$0.18 \pm 0.05$	...	—
	$\chi^2/\nu$	$1650.0/1595$	$1625.7/1593$	$307.6/287$

There is no error estimation for the reflection fraction parameter,  $R_{\text{ref}}$ , as it is self-consistently calculated by the model in the lamp-post geometry. In model 5, we add one extra absorption component,  $\text{parcov}^*$  (TBnew\*cabs), to Model 4 in order to fit the dip spectra. Corresponding parameters in Model 5 are fixed at the best-fit values from Model 4.

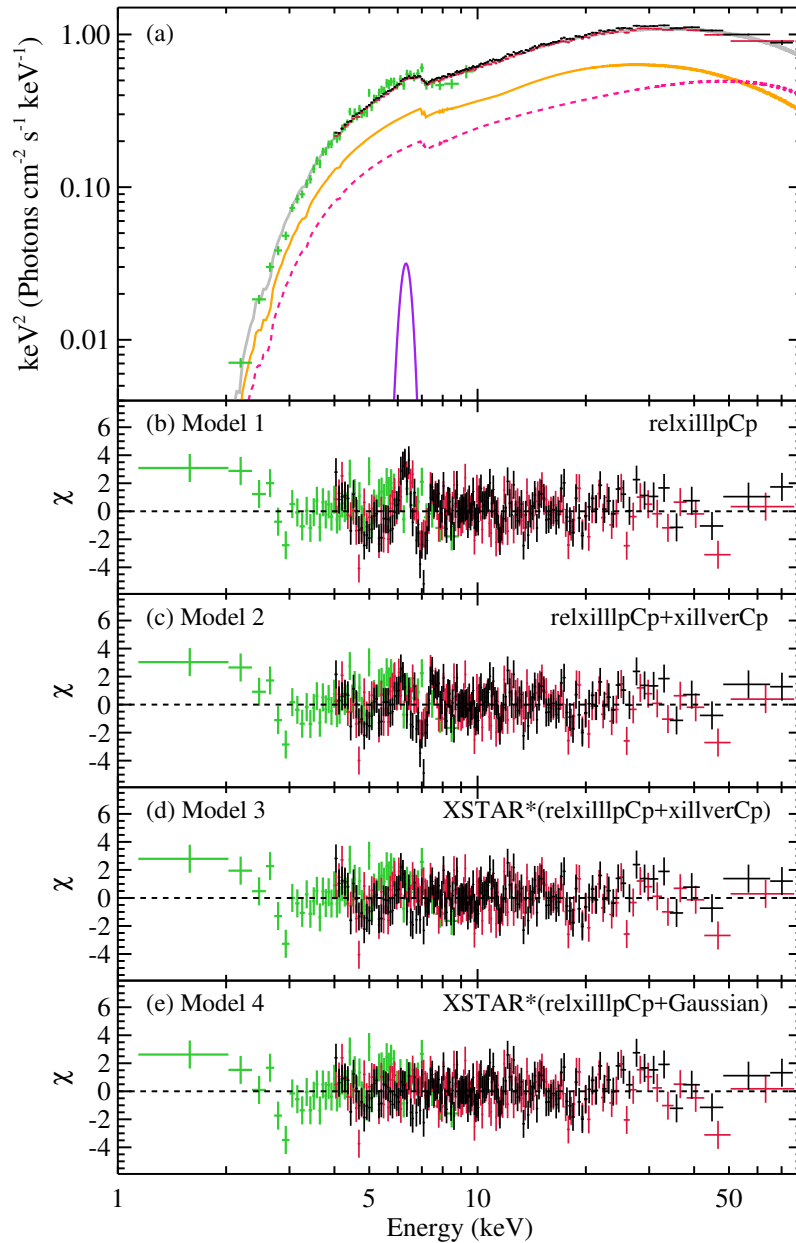


Figure 5.4: Broad-band X-ray spectra of Swift J1658.2–4242. (a) Persistent broad-band X-ray spectra of Swift J1658.2–4242 folded with the best-fit model (Model 4). The total model is marked in gray solid lines, with contributions from the Comptonization continuum (magenta), the disk reflection (orange), and the narrow Fe K line (purple). The *Swift*/XRT spectrum is plotted in green, and the same color scheme is used for the *NuSTAR* data as in previous plots. The spectra are rebinned for display clarity. (b)–(e) Spectral modeling residuals.

et al., 2016, 2017; Xu et al., 2018b; Tomsick et al., 2018), although the narrow line complex cannot be spectrally resolved. The origin of this spectral component is still controversial. Possible scenarios generally considered include distant reflection by a flared disk, line emission from the stellar wind of the donor star, or re-emission from an accretion disk wind if detected along with absorption features. We first tentatively fit for this feature using an unblurred reflection model `xillverCp` (García & Kallman, 2010) to account for possible contribution from distant reflection, with the total model setup as `TBabs*(relxilllpCp+xillverCp)` (Model 2). We assume the narrow iron line to be neutral by setting the ionization parameter in `xillverCp` as  $\log \xi = 0$  ( $\xi = 4\pi F_x/n$ , where  $F_x$  is the ionizing flux, and  $n$  is the gas density). We link other parameters in `xillverCp` with the corresponding parameters in `relxilllpCp`, only allowing the normalization of `xillverCp` to vary freely. This results in an improvement of  $\Delta\chi^2 = 93$  with one additional free parameter ( $\chi^2/\nu = 1715.8/1598 = 1.07$ ). Modeling the narrow iron line with `relxilllpCp` instead results in a similar fit, and it yields a lower limit on the distance of the distant reflection component ( $>300 r_g$ ), which is far enough from the black hole to justify its low ionization state.

An apparent absorption line is still evident in the residuals of Model 2 (see Figure 5.4(c)). Fitting this feature with a simple Gaussian absorption line model brings an improvement of  $\Delta\chi^2 = 67.5$  to the fit with three more parameters. It reveals that the line centroid lies at  $E_{\text{abs}} = 7.03_{-0.03}^{+0.04}$  keV, with an equivalent width (EW) of  $23_{-4}^{+5}$  eV. The absorption line is significantly detected at  $7.5\sigma$  confidence via a simple F-test. Strong absorption features from highly ionized iron are unusual for black hole binaries in the low/hard state, as they are considered as signatures of a powerful disk wind. Complications arise from the fact that the apparent absorption line is right at the Fe K edge. Assuming this is indeed an iron absorption line originating from a disk wind, if associated with blueshifted He-like Fe XXV (6.70 keV), it requires an extreme outflowing velocity of  $0.049_{-0.004}^{+0.006} c$  ( $14800_{-1300}^{+1800}$  km s $^{-1}$ ); alternatively, if this is identified with the more ionized H-like Fe XXVI (6.97 keV), it corresponds to a lower velocity of  $0.009_{-0.004}^{+0.006} c$  ( $2600_{-1300}^{+1800}$  km s $^{-1}$ ), but is still a high outflowing velocity for a disk wind launched by a stellar-mass black hole (e.g., Neilsen & Lee, 2009; Miller et al., 2015a). However, we note that in the latter case, the velocity shift could only be marginal when taking into account the absolute energy calibration uncertainty of *NuSTAR* (Madsen et al., 2015b).

In order to obtain a more physical interpretation, we fit for the absorption feature with an XSTAR table model (Kallman & Bautista, 2001): the full model is setup as `TBabs*XSTAR*(relxilllpCp+xillverCp)` (Model 3). The XSTAR photoionization grid is customized for the hard state of Swift J1658.2–4242 using a power-law input spectrum with the photon index of  $\Gamma = 1.7$ . We also assumed a gas density of  $n = 10^{14} \text{ cm}^{-3}$  following Miller et al. (2015a), a turbulent velocity of  $1000 \text{ km s}^{-1}$  and a source luminosity of  $L = 10^{38} \text{ erg s}^{-1}$ . The grid covers the parameter space of  $1.5 \leq \log(\xi) \leq 4.5$ ,  $10^{21} \text{ cm}^{-3} \leq N_{\text{H}} \leq 10^{23} \text{ cm}^{-3}$  and  $0.1 \leq A_{\text{Fe}} \leq 10.0$ , with the velocity shift as a free parameter. We link the iron abundance of the XSTAR model (in solar units),  $A_{\text{Fe}}$ , with that of the disk reflection component. The XSTAR model successfully accounts for the absorption feature with an ionization parameter of  $\log(\xi) = 2.09_{-0.07}^{+0.17}$ , and a very high outflowing velocity shift of  $v_{\text{out}} = 0.077_{-0.007}^{+0.006} c$  ( $22800 \pm 1800 \text{ km s}^{-1}$ ). We stress that obtaining an unique constraint on the ionization parameter and the velocity shift simultaneously is difficult here. Since only one absorption line can be clearly seen in the Fe K band, the ionization parameter and the velocity shift of the XSTAR grid are degenerate. At  $3\sigma$  confidence level, a velocity of  $v_{\text{out}}$  at  $\sim 0.11 c$  ( $3300 \text{ km s}^{-1}$ ) can still be considered as marginally acceptable (see Figure 5.5 for the constraint on  $v_{\text{out}}$ ). It indicates that associating the absorption feature with more highly ionized Fe K species cannot be completely ruled out. The heavily absorbed nature of the source plus the short XRT exposure time precludes the possibility of detecting corresponding absorption lines in the soft end of the spectra. Model 3 provides an overall satisfying fit of the spectra, the results indicate that the source is a rapidly spinning black hole with the spin parameter of  $a^* = 0.92_{-0.06}^{+0.04}$ , and is viewed at a high inclination angle of  $i = 61_{-4}^{+3^\circ}$ .

In an attempt to further improve the fit, we replace the `xillverCp` component with a simple Gaussian emission line model (Model 4), since there is no clear indication that the narrow core of the Fe  $K\alpha$  profile arises from reflection. This results in a better fit by  $\Delta\chi^2 = 25$ , with the difference mainly lying at the red wing of the narrow iron line around 6 keV (see Figure 5.4). The inclusion of an extra disk blackbody component (`diskbb`) is not statistically required by the data. As the spectra display no obvious bump-like feature at low energies, most likely due to the high absorption column density, the strength or the temperature of the thermal disk emission cannot be well constrained. Although thermal emission from the inner accretion disk is physically required to explain a non-truncated disk, including a `diskbb` model that does not significantly affect the determination of other parameters during the

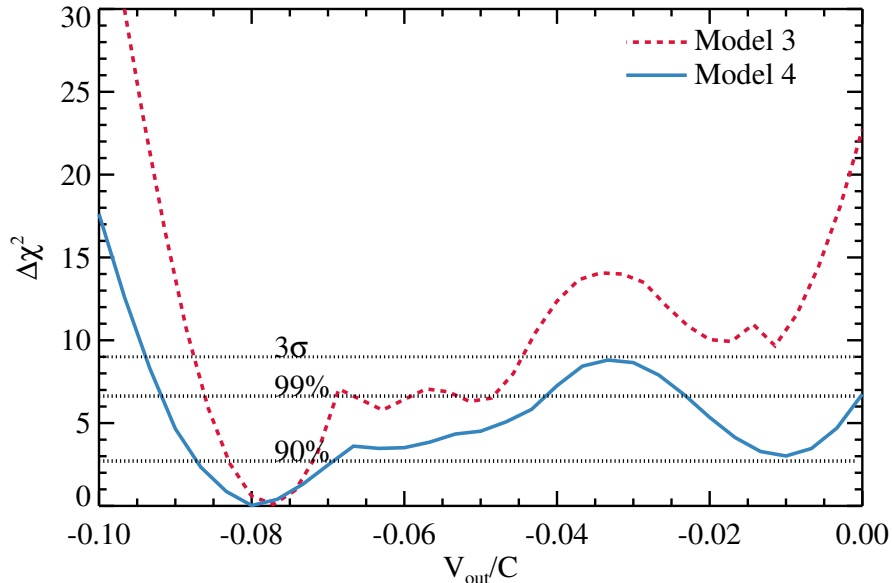


Figure 5.5:  $\Delta\chi^2$  plot of the velocity shift of the ionized absorber. The dashed lines mark the 90%, 99%, and  $3\sigma$  confidence levels for one parameter of interest.

spectral modeling. Therefore, we consider Model 4 as our best-fit model for the persistent broad-band X-ray spectra of Swift J1658.2–4242.

Broadly similar results are obtained with Model 4: a low coronal height of  $h < 3.8 r_g$  and a high spin of  $a^* > 0.96$ , which lead to a high reflection fraction of  $R_{\text{ref}} = 3.25$  calculated self-consistently by the model, signaling strong light-bending effects at the vicinity of the black hole. A high inclination angle of  $i = 64_{-3}^{+2^\circ}$  is measured for the inner accretion disk, which is sensitive to the blue wing of the broad iron line. Similar results are obtained if  $R_{\text{ref}}$  is left to vary freely, and an equally high black hole spin is measured, indicating that the high reflection fraction is indeed required by the data. We note that consistent results are obtained if we replace the lamp-post model used here (`relxilllpCp`) with the model assuming a broken power-law coronal emissivity profile (`relxillCp`); the best-fit values of the key physical parameters (black hole spin, disk ionization and inclination) are all consistent within errors. The constraint on the velocity shift of the XSTAR absorption component with Model 4 is weaker compared to that with Model 3. By allowing both the width and centroid of the line to vary in the Gaussian emission line model, more flexibilities are brought to the spectral modeling near the Fe K edge. However, Model 4 still statistically prefers a considerably large outflowing velocity for the ionized absorber (see Figure 5.5). The most noticeable differences between Model 4 and 3 are the iron abundance  $A_{\text{Fe}}$  and the photon index  $\Gamma$  (see Table 5.1 for

the list of spectral modeling parameters).  $A_{\text{Fe}}$  is driven by the relative flux in the Fe K band and of the Compton hump. Different from the distant reflection model, the narrow iron line component in Model 4 does not contribute to the flux in the high energy band ( $>10$  keV). This would cause a small change in the overall spectral shape, resulting in corresponding changes in  $\Gamma$  and  $A_{\text{Fe}}$ .

The fit confirms that the source is highly absorbed. The best-fit neutral absorption column density,  $N_{\text{H}} = 1.81_{-0.04}^{+0.07} \times 10^{23} \text{ cm}^{-2}$ , is consistent with the measurement reported from initial analysis of the *Swift*/XRT data ( $N_{\text{H}} = (1.9 \pm 0.5) \times 10^{23} \text{ cm}^{-2}$ , Lien et al. (2018)). This value is well in excess of the expected Galactic absorption in the direction of Swift J1658.2–4242,  $N_{\text{H,Gal}} = 1.55 \times 10^{22} \text{ cm}^{-2}$  (Kalberla et al., 2005). Therefore, the extra absorption is intrinsic to the source, and most likely originates from obscuring material near the orbital plane of the system. The parameters of the *nthcomp* continuum are well constrained: a power-law index of  $\Gamma = 1.63 \pm 0.01$ , indicating the source is in the hard state; and a relatively low coronal temperature of  $kT_e = 22 \pm 1$  keV (the value here is as observed, not corrected for gravitational redshift at the vicinity of the black hole), which is determined by the exponential cutoff at the high energy end of the spectrum. Similar low coronal temperatures or equivalently low high-energy cutoffs have been previously measured by *NuSTAR* in black hole binaries during their bright hard states (e.g., Miller et al., 2013, 2015b; Xu et al., 2018b).

#### 5.4.2 Dip Spectra

We extracted the spectra of the three dips collectively to obtain the highest S/N data possible for spectral fitting. The dipping intervals were selected as the periods when the source count rate clearly deviates from the linearly increasing trend (see Figure 5.2 for details). This results in an exposure time of 3.0 ks and 3.3 ks for FPMA and FPMB, respectively. To highlight the spectral difference during the dips, we plot the residuals of the dipping spectra when compared to the best-fit model for the persistent spectra (Model 4) in Figure 5.6(b). It is clear that dip spectra is harder, especially below 10 keV, suggesting that the spectral change is caused by absorption.

An increase in the neutral absorption column density and changes in photon-ionized absorbers are usually invoked to explain spectral change during dipping intervals (e.g., Díaz Trigo et al., 2006; Shidatsu et al., 2013). Evidence has also been found for progressive covering of the accretion disk corona as the dip progresses, dur-

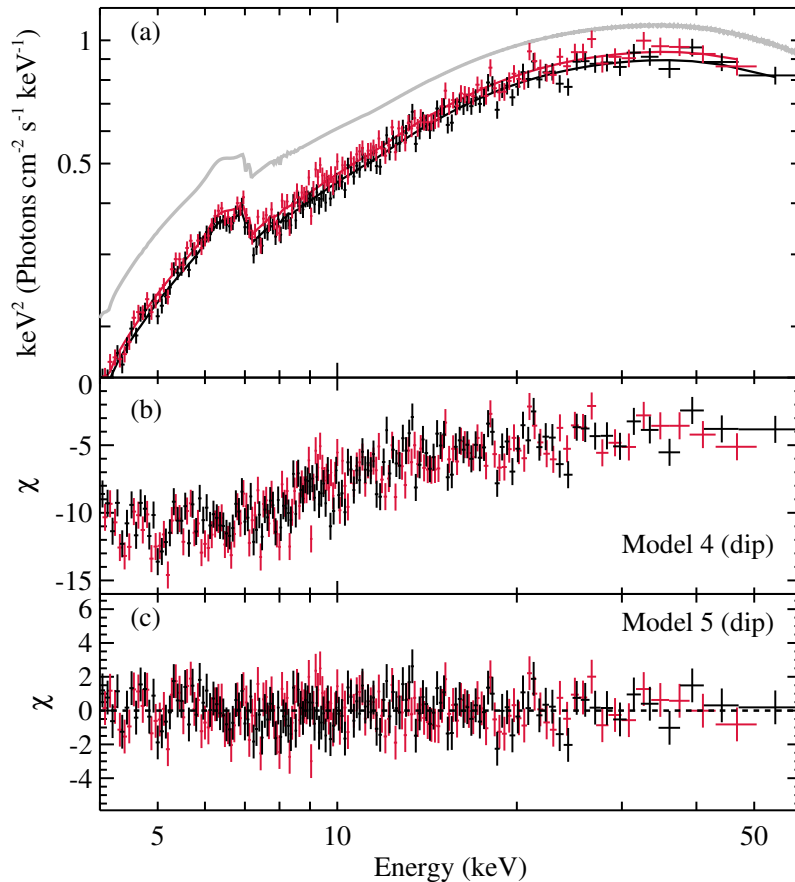


Figure 5.6: The dipping spectra of Swift J1658.2–4242 compared with the persistent spectra. (a) The dipping spectra of Swift J1658.2–4242 observed by *NuSTAR*. FPMA and FPMB data are plotted in black and red, respectively. For comparison, the best-fit model for the persistent spectra is plotted in gray. (b) Residuals of the dipping spectra compared to Model 4 (best model for the persistent spectra). (c) Residuals of the dipping spectra from the best-fit model (Model 5). The spectra have been rebinned for display clarity.

ing which the covering factor of the absorber was measured to increase, approaching the maximum value at the dip minimum (e.g., Smale et al., 2002; Church & Bałucińska-Church, 2004). Our best-fit model for the dip spectra adds one extra partial covering neutral absorber to the persistent spectral model (Model 4). During the dips, electron scattering by the absorber could reduce the Comptonized emission from the corona, producing a nearly energy independent decrease in intensity (e.g., Parmar et al., 1986; Smale et al., 2002). Therefore, we also include a *cabs* model to account for the effects of absorbing material scattering X-ray photons away from the line of sight, and link the absorption column density in the *cabs* model with that of the partial covering absorber. The full model setup is `TBnew*(partcov*(TBnew*cabs))*XSTAR*(relxilllpCp+Gaussian)` (Model

5). Corresponding parameters in Model 5 are fixed at the best-fit values from Model 4, with only two parameters left to vary freely. The dip spectra can be adequately modeled after including the extra absorption component ( $\chi^2/\nu = 307.6/287 = 1.07$ , with no obvious residuals in Figure 5.6(c)). The best fit requires a neutral absorber with the absorption column density of  $N_{\text{H}} = (1.00_{-0.07}^{+0.08}) \times 10^{24} \text{ cm}^2$  and a partial covering factor of  $f_{\text{cov}} = (34 \pm 1)\%$ . The fit confirms that the spectral changes during the dips can be fully accounted for by photoelectric absorption and Compton scattering from an additional neutral absorber.

### 5.5 Low-frequency QPO

For *NuSTAR* timing analysis, we first applied barycenter correction to the event files, transferring the photon arrival times to the barycenter of the solar system using JPL Planetary Ephemeris DE-200. The cross-power density spectra (CPDS) were generated using MaLTPyNT (Bachetti, 2015) following the standard procedure. CPDS measures the signals in phase between the two *NuSTAR* modules (FPMA and FPMB), which helps to reduce dead time distortions to the power density spectra (Bachetti et al., 2015). We selected a light curve binning of  $2^{-8}$  s and calculated the CPDS in 512 s intervals. The power spectra were generated using the root-mean-square (rms) normalization, and were geometrically rebinned by a factor of 1.03 to reach nearly equally spaced frequency bins in the logarithmic scale.

A low-frequency QPO is clearly detected by *NuSTAR*. The QPO frequency steadily increased from  $\sim 0.14$  Hz to  $\sim 0.21$  Hz during the *NuSTAR* exposure, as shown in the dynamical power spectrum (Figure 5.7, left panel). We extract an example CPDS from only the last two orbits, and fit it in XSPEC with a unity response file. We use a multi-Lorentzian model, which is commonly used to fit the power spectra of black hole binaries (e.g., Nowak, 2000). Our model for the power density spectrum includes four Lorentz functions: two Lorentzians with the centroid frequency fixed at zero to fit for the underlying continuum; one Lorentzian for the QPO, and one for the possible sub-harmonic with the frequency linked with half the fundamental QPO frequency. The sample power spectrum can be adequately fitted with no obvious structure left in the residuals,  $\chi^2/\nu = 292.6/243 = 1.20$  (see Figure 5.7, right panel). The QPO peak averaged over the last two orbits can be well constrained to be at the frequency of  $0.207_{-0.002}^{+0.003}$  Hz, with a Q-value of  $4.5 \pm 0.9$  and a fractional rms amplitude of  $12.7 \pm 0.8\%$ . The low QPO frequency, the increasing trend of the centroid frequency with the rising source flux, and the underlying noise continuum in the power density spectrum are consistent with type-C QPOs during hard states

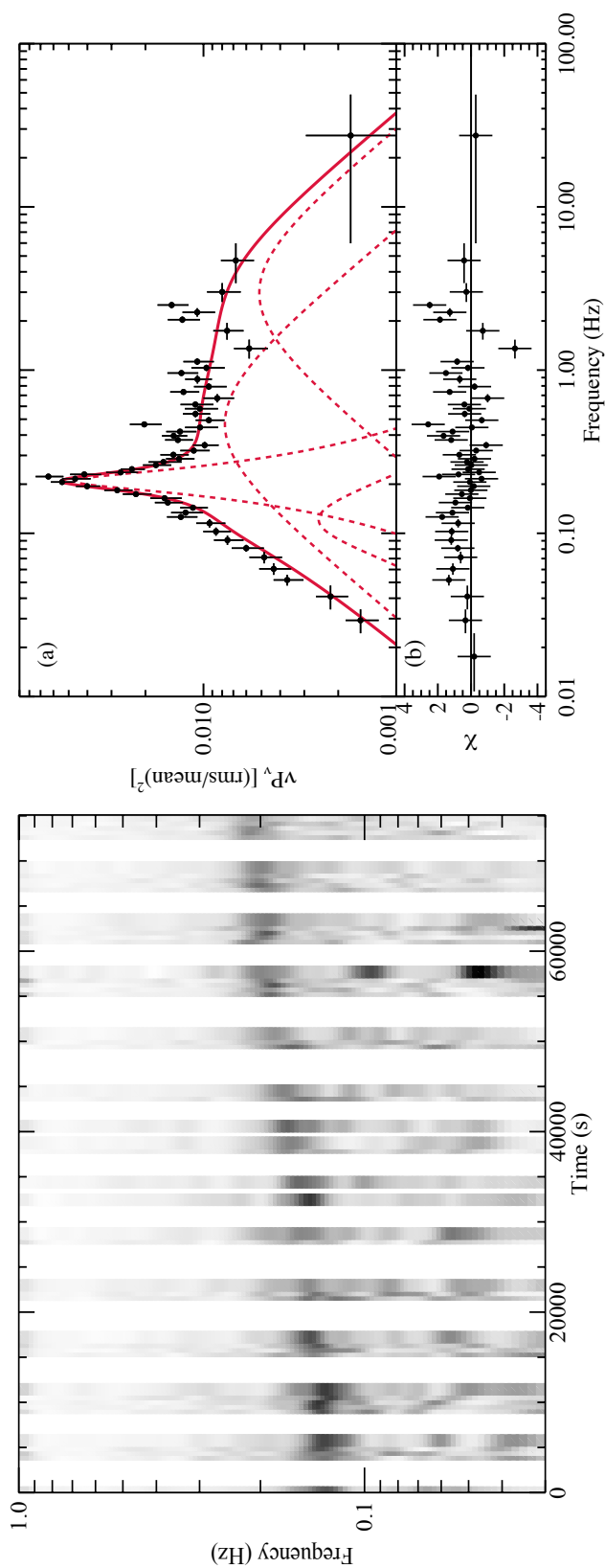


Figure 5.7: Power spectrum of Swift J1658.2-4242 with the QPO. Left: Dynamical power spectrum of Swift J1658.2-4242 from the *NuSTAR* observation. Low-frequency noise is present during the dipping period. Right: Sample power spectrum extracted from the last two orbits fitted with a multi-Lorentzian model. The power spectrum here have been rebinned for display clarity.

of black hole binary outbursts (Wijnands & van der Klis, 1999; Casella et al., 2004, 2005).

## 5.6 Discussion

In this work, we performed an X-ray spectral and timing analysis of the recently discovered X-ray transient Swift J1658.2–4242, using data from joint *NuSTAR* and *Swift* observations. The shape of the broad-band X-ray spectral continuum and the detection of a low-frequency QPO are similar to the properties of black hole binary in the hard state. Given that no coherent pulsation or type I X-ray burst is detected, this suggests that the source is a strong black hole binary candidate. From spectral modeling, the highly absorbed nature of Swift J1658.2–4242 is confirmed, with the neutral absorption column density well measured as  $N_{\text{H}} = (1.80 \pm 0.08) \times 10^{23} \text{ cm}^{-2}$ . The hard photon index of  $\Gamma = 1.63 \pm 0.02$  and the simultaneous detection of a jet in the radio band (Russell et al., 2018) suggests Swift J1658.2–4242 was in the hard state when the observations were taken. It was most likely in the bright phase of the hard state, as the source was reported to enter the hard-intermediate state four days later (Beri et al., 2018). The averaged non-dip flux is about 30 mCrab in the 2–10 keV band during the *NuSTAR* exposure, and the absorption corrected source luminosity is  $L_{\text{x},0.1-500 \text{ keV}} = 3.9 \times 10^{37} \times (D/8 \text{ kpc})^2 \text{ erg s}^{-1}$ . Currently, the distance,  $D$ , to Swift J1658.2–4242 is unknown and the high absorption in the ISM along the line of sight makes it difficult to identify the optical counterpart.

Strong disk reflection features are shown in the *NuSTAR* spectra. Modeling the reflection features with the self-consistent disk reflection model `relxilllpCp` indicates that the central black hole is rapidly spinning with the spin parameter of  $a^* > 0.96$ , and the inner disk is viewed at a high inclination angle of  $i = 64_{-3}^{+2^\circ}$ . The inclination angle measured is consistent with the fact that absorption dips are detected in the light curves.

During spectral modeling of the reflection spectra in Section 5.5, we made the assumption that the inner accretion disk extends to the ISCO, which is not necessarily true considering the possibility of a truncated disk in the hard state. The black hole spin and the inner disk radius are essentially degenerate parameters. The spin parameter is determined by measuring the location of the ISCO, which decreases monotonically from  $9 r_{\text{g}}$  for an extremely retrograde spinning black hole to  $1.235 r_{\text{g}}$  for a black hole with a maximum positive spin. Therefore, by assuming that the disk extends to the ISCO rather than being truncated, we would be conservatively

fitting for a lower limit of the black hole spin. Likewise, a high black hole spin obtained this way rules out the possibility of significant disk truncation. If we fix the spin parameter at the maximum value of  $a^* = 0.998$  and instead fit for  $R_{\text{in}}$ , the best-fit value for the inner disk radius is  $R_{\text{in}} = 1.7_{-0.1}^{+0.2} r_g$ , with other parameters remaining at basically identical values. Solutions with  $R_{\text{in}} > 3.3 r_g$  can be ruled out at a  $5\sigma$  confidence level.

A nearly maximal spin and the lack of significant disk truncation further support the hypothesis that Swift J1658.2–4242 contains a black hole primary. In the case of neutron stars, the Schwarzschild metric is normally a good approximation, and the neutron star spin parameter is expected to be less than 0.3 (e.g., Galloway et al., 2008). Also in neutron stars the disk must be truncated either at the surface of the star or at its magnetospheric radius, with the typical measured truncation radius as  $6\text{--}15 r_g$  (e.g., Cackett et al., 2010; Miller et al., 2013; Ludlam et al., 2017), which significantly exceeds the constraint on the inner disk radius we obtained for Swift J1658.2–4242. The origin of QPOs in black hole binaries is still unclear despite being studied for decades. The lack of disk truncation plus the simultaneous detection of a type-C QPO in the hard state of a black hole binary candidate by *NuSTAR* is in tension with the Lense-Thirring precession model for QPOs, one of the currently promising physical models to explain the origin of low-frequency QPOs, as in the Lense-Thirring precession model, the inner accretion disk is generally required to be truncated (Stella & Vietri, 1998; Stella et al., 1999; Ingram et al., 2009).

An apparent absorption line is detected in the Fe K band centered at  $7.03_{-0.03}^{+0.04}$  keV. If associated with ionized iron absorption, this implies the unusual presence of a disk wind in the hard state of a black hole binary. As only one absorption feature is clearly detected, the velocity shift and the ionization state of the absorber cannot be unambiguously determined, similar to the case of 4U 1630–472 discussed in King et al. (2014). The best fit favors a lower ionization state and a very high outflowing velocity, comparable to the extreme wind velocity reported in the black hole binary candidate IGR J17091–3624 (King et al., 2012). In the case of an extreme disk wind, the relatively narrow Fe K emission line component required in the spectral modeling could be a part of a P-Cygni profile, arising from redshifted ionized iron line emission in the wind. However, we stress that an alternative solution of a higher ionization and moderate outflowing velocity cannot be ruled out from the spectral analysis, where the velocity shift of the ionized absorber is actually close to the absolute energy calibration uncertainty of *NuSTAR*. Swift J1658.2–4242 is an

interesting source for studying the equatorial disk winds in binary systems. Future observations with high spectral resolution would be helpful to resolve this uncertainty.

### **Acknowledgments**

We thank the referee for helpful comments that improved this work. D.J.W. acknowledges support from STFC Ernest Rutherford Fellowship. This work was supported under NASA contract No. NNG08FD60C and made use of data from the *NuSTAR* mission, a project led by the California Institute of Technology, managed by the Jet Propulsion Laboratory, and funded by the National Aeronautics and Space Administration. We thank the *NuSTAR* Operations, Software, and Calibration teams for support with the execution and analysis of these observations. This research has made use of the *NuSTAR* Data Analysis Software (NuSTARDAS), jointly developed by the ASI Science Data Center (ASDC, Italy) and the California Institute of Technology (USA).

## Chapter 6

BROADBAND X-RAY SPECTRAL AND TIMING ANALYSES  
OF THE BLACK HOLE BINARY CANDIDATE SWIFT  
J1658.2–4242: RAPID FLUX VARIATION AND THE TURN-ON  
OF A TRANSIENT QPO

Xu Y., Harrison F. A., Tomsick J. A., Barret D. et al. (2019). “Broadband X-Ray Spectral and Timing Analyses of the Black Hole Binary Candidate Swift J1658.2–4242: Rapid Flux Variation and the Turn-on of a Transient QPO.” *The Astrophysical Journal*, 879(2):93. doi: 0.3847/1538–4357/ab24bf.

**Abstract**

We report results from joint *NuSTAR*, *Swift*, and *XMM-Newton* observations of the newly discovered black hole X-ray binary candidate Swift J1658.2–4242 in the intermediate state. We observe a peculiar event in this source, with its X-ray flux rapidly decreasing by  $\sim 45\%$  in  $\sim 40$  s, accompanied by only subtle changes in the shape of the broadband X-ray spectrum. In addition, we find a sudden turn-on of a transient QPO with a frequency of 6–7 Hz around the time of the flux change, and the total fractional rms amplitude of the power spectrum increases from  $\sim 2\%$  to  $\sim 10\%$ . X-ray spectral and timing analyses indicate that the flux decrease is driven by intrinsic changes in the accretion flow around the black hole, rather than intervening material along the line of sight. In addition, we do not significantly detect any relativistic disk reflection component, indicating that it is much weaker than previously observed while the source was in the bright hard state. We propose accretion disk instabilities triggered at a large disk radius as the origin of the fast transition in spectral and timing properties, and discuss possible causes of the unusual properties observed in Swift J1658.2–4242. The prompt flux variation detected along with the emergence of a QPO makes the event an interesting case for investigating QPO mechanisms in black hole X-ray binaries.

**Keywords:** accretion, accretion disks – X-rays: binaries – X-rays: individual (Swift J1658.2–4242)

## 6.1 Introduction

Most galactic black hole X-ray binaries are discovered as transients, when they go into bright outbursts in the X-ray band. During typical outbursts, these systems are known to undergo a transition from the low/hard to the high/soft state through relatively short-lived intermediate states, with these states exhibiting distinct spectral and timing properties (see Remillard & McClintock, 2006; Belloni & Motta, 2016, for reviews). Swift J1658.2–4242 is a new black hole X-ray binary candidate, first reported by *Swift*-BAT on 2018 February 16 (Barthelmy et al., 2018). Subsequent observations exhibiting dips in the light curve indicate that it is highly absorbed and is viewed at a high inclination angle (Beri et al., 2018; Lien et al., 2018; Xu et al., 2018c). Relativistic disk reflection features, including a broad asymmetric Fe  $K\alpha$  line peaking at 6–7 keV and Compton reflection hump around 30 keV, were detected by *NuSTAR* when Swift J1658.2–4242 was in the low/hard state (Xu et al., 2018c). Relativistic reflection features in the X-ray spectrum of Galactic black hole binaries are believed to arise from reprocessing of hard X-ray emission from the corona by the inner accretion disk (Fabian et al., 1989; Reynolds, 2014). Detailed modeling of the reflection spectra of Swift J1658.2–4242 suggests that the central object in the system is a rapidly spinning black hole ( $a^* > 0.96$ ), and also supported the conclusion that we view the system at high inclination, finding  $\theta = 64_{-3}^{+2^\circ}$  for the inner disc (Xu et al., 2018c).

Variability on a wide range of time scales is characteristic of the accretion process around both stellar-mass and supermassive black holes (e.g., Ulrich et al., 1997; van der Klis, 2006; McHardy, 2010). Rapid flux variations are commonly found in the X-ray light curves of black hole binaries, and are believed to probe the properties of the inner accretion flow in the vicinity of stellar-mass black holes. The power spectrum generated from the X-ray light curve of a black hole X-ray binary is typically characterized by a variable broadband noise component along with transient and discrete peaks superimposed on top of the continuum (e.g., van der Klis, 1989, 2006). The peaks are termed quasi-periodic oscillations (QPOs). Low-frequency QPOs observed in black hole binary systems, with typical frequencies from a few mHz to 30 Hz, can be generally classified into three main types (type-A, B and C), based on their characteristics in the power density spectrum (see Wijnands et al., 1999; Casella et al., 2004, 2005, for details). Type-A QPOs are characterized by a weak and broad peak in the power spectrum. The most common type of low-frequency QPOs are type-C QPOs, which are usually strong and span the frequency range of  $\sim 0.1$ –30 Hz. Type-B QPOs are rarer, limited to a narrow frequency range

(typically  $\sim 5$ -6 Hz), and can be distinguished by the fractional amplitude and underlying noise shape. Type-B QPOs are usually observed during the time of transitions between hard-intermediate (HIMS) and soft-intermediate (SIMS) states (or transitions between hard and soft states), and have been proposed to be associated with major jet ejection events (e.g., Soleri et al., 2008; Fender et al., 2009). There is evidence that type-B QPOs are stronger in systems that are viewed close to face-on, while type-C QPOs are stronger in high-inclination systems (Motta et al., 2015), supporting the idea that the two types have different physical origins. The rapid transitions of QPOs have been found in a few black hole binaries or black hole candidates via time-resolved analysis: GS 1124–684 (Takizawa et al., 1997), XTE J1859+226 (Casella et al., 2004; Belloni et al., 2005), GX 339–4 (Nespoli et al., 2003), XTE J1550–564 (Sriram et al., 2013), XTE J1859+226 (Sriram et al., 2016), and also recently in MAXI J1535–571 (Huang et al., 2018), in most cases type-B QPOs are identified.

Despite the richness in observational phenomenology, the physical origins of QPOs are still highly uncertain. For low-frequency QPOs, the frequency is much longer than the dynamical time scales in the strong gravity regime of stellar-mass black holes. Different theoretical models have been put forward to provide a physical explanation for low-frequency QPOs: some models invoke geometric effects, e.g., Lense-Thirring precession of a radially extended section of the inner accretion flow (e.g., Stella et al., 1999; Ingram et al., 2009; Motta et al., 2018), which is a General-Relativity frame-dragging effect; other models consider intrinsic instabilities in the accretion flow, e.g., oscillations caused by standing shocks (Chakrabarti & Molteni, 1993) or magneto-acoustic wave propagation (Titarchuk & Fiorito, 2004; Cabanac et al., 2010). Similarly, various attempts have also been made to understand the broadband aperiodic noise continuum in the power spectrum (e.g., Lyubarskii, 1997; Arévalo & Uttley, 2006; Ingram & Done, 2010), with the propagation of fluctuating accretion being a popular model, however there is still no consensus on the origin. X-ray spectral-timing studies are believed to be a promising method to investigate the nature of QPOs.

In this work, we present X-ray spectral and timing analyses of the new black hole binary candidate Swift J1658.2–4242 in the intermediate state of its 2018 outburst, observed by *NuSTAR*, *Swift*, and *XMM-Newton*. The paper is structured as follows: in Section 6.2, we describe details of the observations used in this work and the data reduction procedures; results from our X-ray timing and spectral analyses are

present in Section 6.3 and Section 6.4, respectively; finally, we discuss the physical implications from the observations in Section 6.5, and summarize the paper in Section 6.6.

## 6.2 Observations and Data Reduction

*Nuclear Spectroscopic Telescope Array (NuSTAR*; Harrison et al., 2013) and *XMM-Newton* (Jansen et al., 2001) jointly observed Swift J1658.2–4242 on 2018 February 25 (MJD 58175). The outburst of Swift J1658.2–4242 was also monitored daily by the X-ray Telescope (XRT; Burrows et al., 2005) on the Neil Gehrels *Swift* Observatory (*Swift*; Gehrels et al., 2004). The joint *NuSTAR* and *XMM-Newton* observations caught Swift J1658.2–4242 shortly after significant spectral softening occurred during the rising phase of outburst, close to the time of the hard-to-soft state transition (see *Swift* monitoring light curves in Figure 6.1(a)). Based on the hardness-intensity diagram (HID, Figure 6.1(c)), Swift J1658.2–4242 is consistent with being in an intermediate state, transitioning from a canonical hard to a canonical soft state, at a phase of an outburst when some black hole binaries are known to display repeated fast transitions back and forth involving HIMS and SIMS (e.g., Belloni & Motta, 2016).

### 6.2.1 NuSTAR

We reduced the *NuSTAR* data of Swift J1658.2–4242 (OBSID: 80301301002) using NuSTARDAS pipeline v.1.6.0 and CALDB v20180419. After standard data filtering with NUPIPELINE, the exposure times are 31.5 ks and 31.8 ks for the two focal plane modules, FPMA and FPMB, respectively. The source spectra and light curves were extracted from a circular region with the radius of 180'' centered on the location of Swift J1658.2–4242 using NUPRODUCTS. Background was estimated from source-free areas using polygonal regions. The *NuSTAR* spectra were grouped to have a signal-to-noise ratio (S/N) of at least 30 per bin.

### 6.2.2 XMM-Newton

The *XMM-Newton* observation of Swift J1658.2–4242 (OBSID: 0802300201) were processed using the *XMM-Newton* Science Analysis System (SAS) v17.0.0 following standard procedures. The EPIC-MOS1 and EPIC-MOS2 cameras were closed during the observation. The prime instrument we use is EPIC-pn (Strüder et al., 2001). The first part of the observation was carried out in the EPIC-pn Timing Mode, and was later switched to the Burst Mode (a special flavor of the Timing

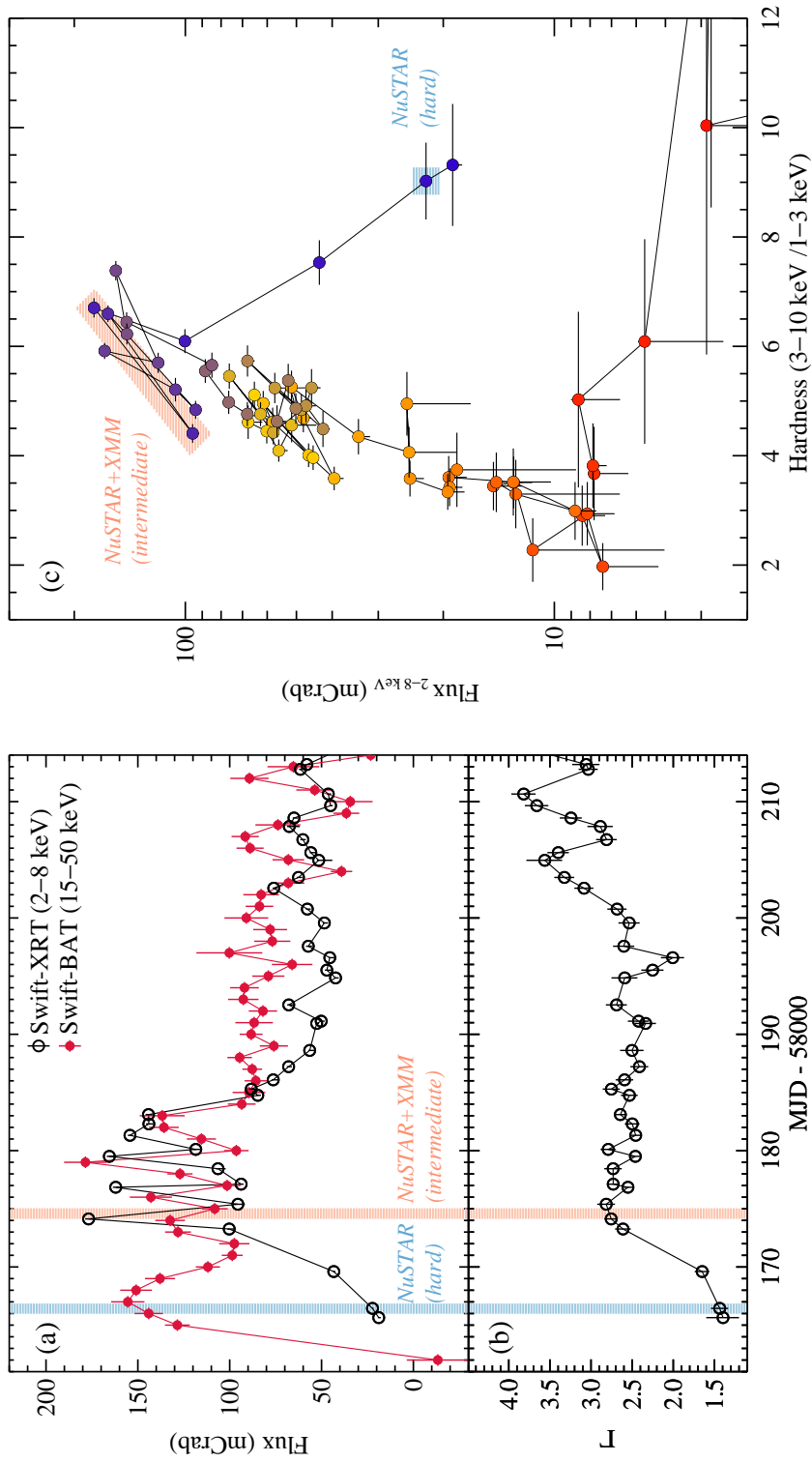


Figure 6.1: Long term *Swift* light curves and HID of Swift J1658.2–4242. (a) Long term *Swift*-XRT and *Swift*-BAT light curves of Swift J1658.2–4242 since the beginning of its 2018 outburst. The BAT light curve in daily averaged flux is from the *Swift*-BAT transient monitor (Krimm et al., 2013), and is rescaled to the unit mCrab from count rates in the 15–50 keV band. The XRT flux was calculated by fitting the spectra with an absorbed power-law model. (c) HID calculated with *Swift*-XRT data. The color scheme indicates the time since the start of the observation. Hardness is calculated by the count rate ratio between 3–10 keV and 1–3 keV. The blue shaded area marks the first *NuSTAR* observation, which caught the source in the rising hard state (see detailed data analysis in Xu et al., 2018c). Our joint *XMM-Newton* and *NuSTAR* observations used in this work is marked in orange, which caught the source in the intermediate state, transitioning from a canonical hard to a canonical soft state.

Mode with low live time) due to the unanticipated high count rate. We selected events with Pattern  $\leq 4$  (singles and doubles) and Quality Flag = 0. The source region was chosen as rows  $20 \leq \text{RAWX} \leq 55$  (Timing Mode),  $25 \leq \text{RAWX} \leq 50$ , and  $\text{RAWY} \leq 142$  (Burst Mode). Corresponding background was extracted from rows  $3 \leq \text{RAWX} \leq 6$ . The resulting exposure times after data filtering are 41 ks for the Timing Mode, and 630 s for the Burst Mode. The source light curves were corrected for dead time, PSF, and other instrumental effects using the `epic1ccorr` tool. Due to an apparent disagreement of *XMM-Newton* data in spectral slope with *NuSTAR* and *Swift-XRT*, we do not use *XMM-Newton* spectra for spectral analysis in this work. The spectral slope disagreement is likely to be associated with pile-up issues along with possible calibration uncertainties for bright targets observed by *XMM-Newton* in the Timing Mode, which cannot be completely solved by excising data from the core of the *XMM-Newton* PSF.

### 6.2.3 Swift

Two *Swift-XRT* observations of Swift J1658.2–4242 (OBSID: 00010571004, 00010571005) were taken close to the time of the joint *NuSTAR* and *XMM-Newton* observations, on 2018 February 25 and 26, respectively. The data were taken in the Windowed Timing mode. We extracted source spectra from a circular region with the radius of  $70''$ , and the background was extracted from an annulus area with the inner and outer radii of  $200''$  and  $300''$ . The averaged *Swift-XRT* count rates are  $\sim 38 \text{ ct s}^{-1}$  and  $\sim 23 \text{ ct s}^{-1}$  for the first and the second observation, respectively, thus the data are not affected by pile-up distortions. After standard data filtering, the exposure times are 857 s and 795 s for the first and second *Swift-XRT* observations. The *Swift-XRT* spectra were rebinned to have a S/N of least 5 per energy bin.

## 6.3 Variability

A dramatic decrease in the flux of Swift J1658.2–4242 was simultaneously observed by *NuSTAR* and *XMM-Newton* at 07:00:14 UTC on 2018 February 25 (around  $1.27 \times 10^4$  s in Figure 6.2). The source count rate decreased by  $\sim 35\%$  in the *XMM-Newton* band (0.3–10 keV), and  $\sim 40\%$  in the *NuSTAR* band (3–79 keV) within only  $\sim 40$  s. The flux levels before and after this sudden flux variation were relatively stable, although increased variability can be seen in the *XMM-Newton* light curve right before the large flux drop around  $1.27 \times 10^4$  s (see Figure 6.2, right panel). The timing of the sharp count rate drop is aligned very well in the *NuSTAR* and *XMM-Newton* light curves, showing no noticeable energy-dependent time delay.

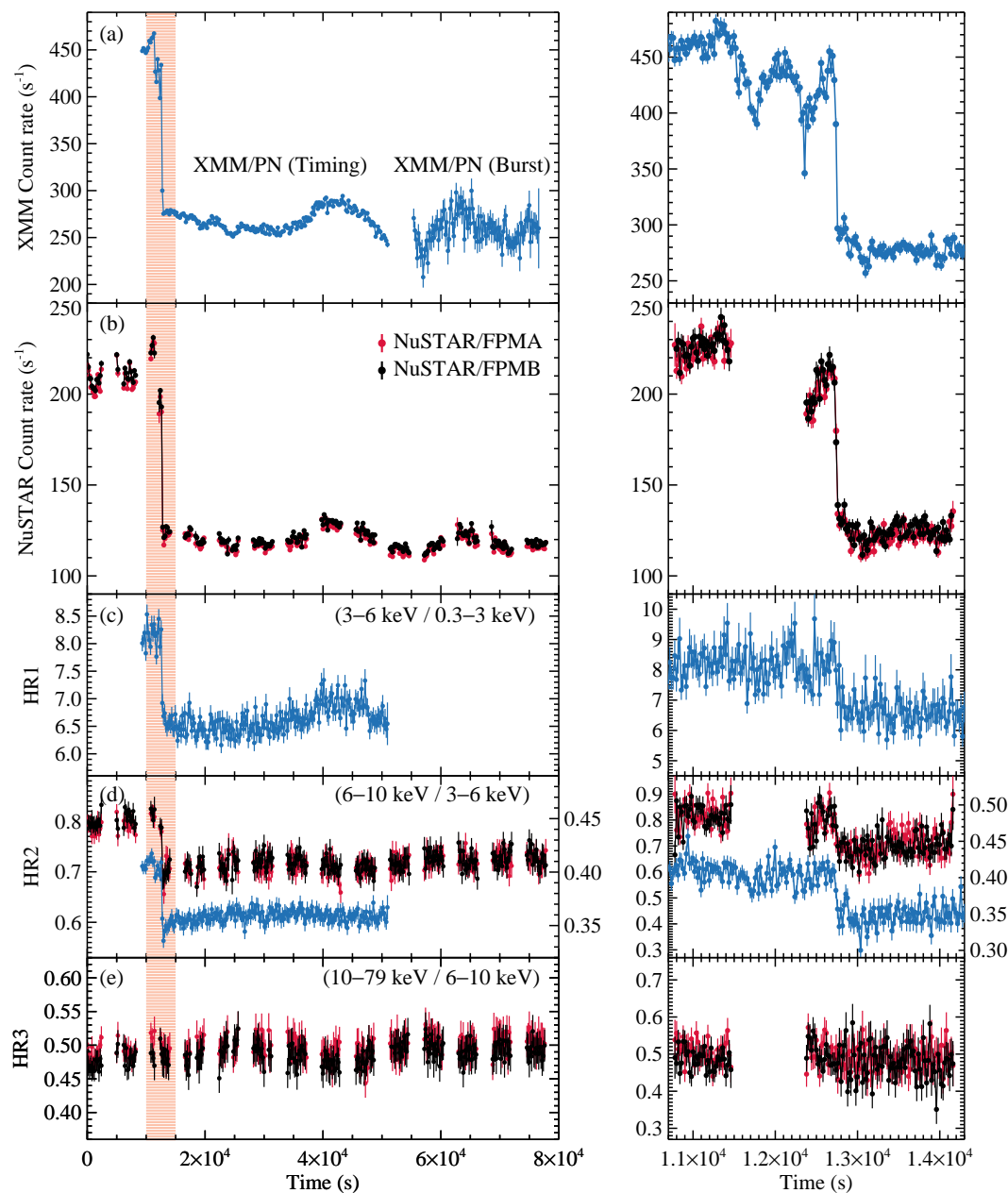


Figure 6.2: *NuSTAR* and *XMM-Newton* light curves of Swift J1658.2–4242. (a) (b) X-ray light curves of Swift J1658.2–4242 from the joint *NuSTAR* and *XMM-Newton* observations. A sharp drop in flux was observed by both telescopes around  $1.27 \times 10^4$  s. Shaded area in the left panel marks the time interval around the flux drop, which is zoomed in for display clarity in the right panel. The left panel is plotted in 100 s bins, the time bins are 20 s for the right panel. *XMM-Newton* EPIC-pn light curve (0.3–10 keV) is plotted in blue. *NuSTAR* FPMA and FPMB light curves (3–79 keV) are plotted in red and black, respectively. The gaps in the *NuSTAR* light curves are due to occultations and SAA passages. (c)–(e) Hardness ratios calculated from count rates in different energy bands. In panel (d), the left y-axis is the *NuSTAR* hardness ratio, and the right y-axis is the *XMM-Newton* hardness ratio. The *XMM-Newton* EPIC-pn Burst Mode data are not displayed in hardness ratios, as the error bars are much larger than those of *NuSTAR* and *XMM-Newton* Timing Mode, which is due to the low instrument live time of the Burst Mode.

We henceforth refer to the time intervals before and after the large flux drop as the high- and the low-flux epoch, respectively. The same trend of flux variation is also reflected in the long term *Swift* light curves of Swift J1658.2–4242 (Figure 6.1), where there is a flux difference of about 50% between the two *Swift*-XRT exposures taken shortly before and after our joint *NuSTAR* and *XMM-Newton* observations.

Despite the dramatic change in flux level, there is only subtle variation in the broadband X-ray spectral energy distribution. We extracted source light curves taken by *NuSTAR* and *XMM-Newton* in four different energy intervals, and calculated hardness ratios based on count rates in the corresponding energy bands, which are defined as:  $\text{HR1} = C_{3-6 \text{ keV}}/C_{0.3-3 \text{ keV}}$ ,  $\text{HR2} = C_{6-10 \text{ keV}}/C_{3-6 \text{ keV}}$ , and  $\text{HR3} = C_{10-79 \text{ keV}}/C_{6-10 \text{ keV}}$ . The sudden drop in count rates around  $1.27 \times 10^4 \text{ s}$  is evident in all four energy bands, and the changes observed in hardness ratios are small. As shown in Figure 6.2, HR1 and HR2 decrease by  $\sim 20\%$  and  $\sim 12\%$ , respectively, at the time of the flux decrease, while HR3 remains constant. The small decrease in hardness ratios below 10 keV (HR1 and HR2) indicates that the source energy spectrum turns slightly softer when the flux is lower, ruling out the possibility that the flux variation is caused by photoelectric absorption from material temporarily obscuring the line of sight. In addition, the constant hardness ratio (HR3) in the hard X-ray band throughout the observations suggests that the non-thermal spectral shape of Swift J1658.2–4242 remains roughly the same despite of the large flux change.

For X-ray timing analysis, we generated power spectra of Swift J1658.2–4242 from *NuSTAR* and *XMM-Newton* data. We first applied barycenter corrections to the event files, transferring the photon arrival times to the barycenter of the Solar system using JPL Planetary Ephemeris DE-200. The *NuSTAR* power spectra were produced using MaLTPyNT in the energy band of 3–79 keV, with a light curve binning size of  $2^{-6} \text{ s}$ , and was averaged in 256 s intervals. The power spectrum generated by MaLTPyNT is the cross-power density spectrum of FPMA and FPMB, which helps to reduce deadtime distortions (Bachetti et al., 2015). We generated an *XMM-Newton* EPIC-pn power spectrum using the powspec tool in the XRONOS package (Stella & Angelini, 1992). The EPIC-pn power spectrum was calculated in the 0.3–10 keV band with a light curve time resolution of 0.01 s, and was averaged from 8 intervals. Both power spectra were generated using the root-mean-square (rms) normalization, and were geometrically rebinned by a factor of 1.03 to reach nearly equally spaced frequency bins in the logarithmic scale.

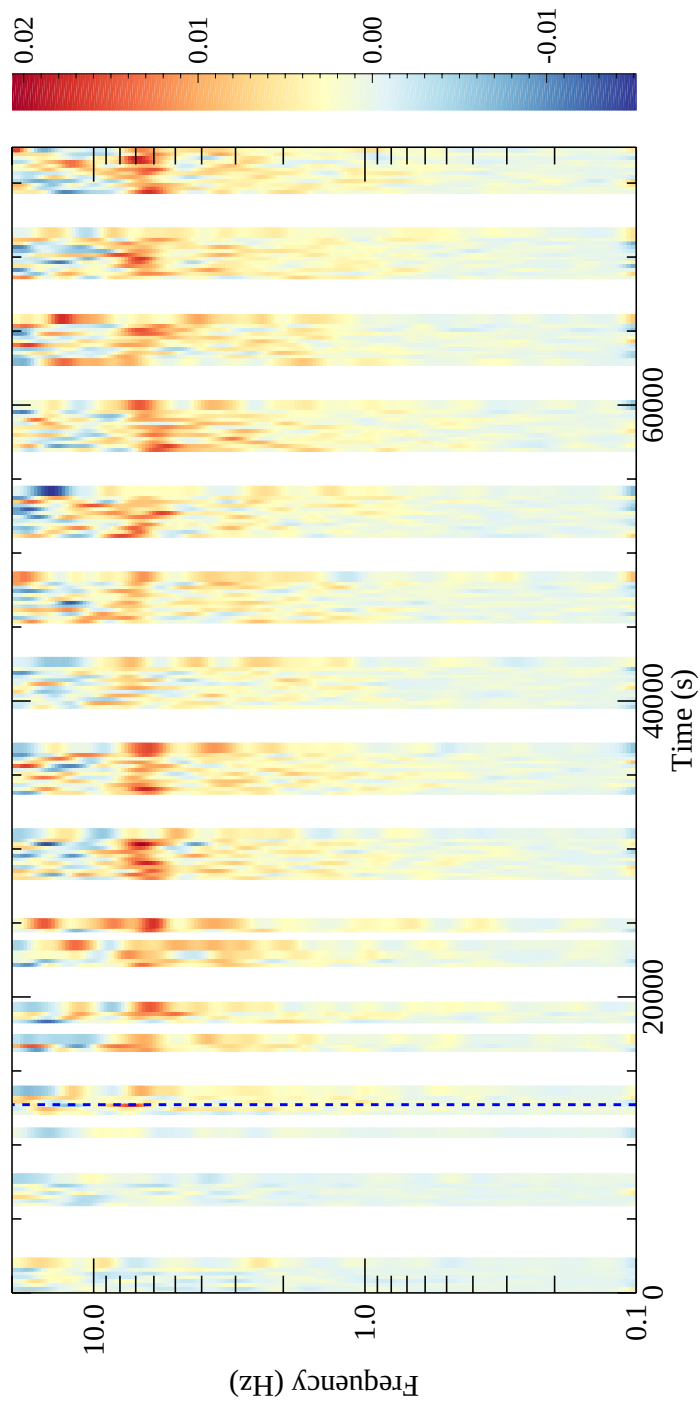


Figure 6.3: Dynamical *NuSTAR* power spectrum in  $\nu P_\nu$  representation, displaying the appearance of a QPO with the frequency of 6–7 Hz starting from  $\sim 1.3 \times 10^4$  s. The appearance of a QPO is found around the same time of the rapid flux variation in the X-ray light curves (marked by a blue dashed line).

Table 6.1: Power Spectra Properties

	$\nu_{\text{qpo}}$ (Hz)	$\text{rms}_{\text{qpo}}$ (%)	$Q$ ( $\nu/\text{FWHM}$ )	$\text{rms}_{\text{tot}}$ (%)	$\chi^2/\nu$
High-flux Epoch					
<i>NuSTAR</i>	6.83 (fixed)	<2.4	3.9 (fixed)	$2.4^{+1.1}_{-0.8}$	0.94
Low-flux Epoch					
<i>XMM</i>	$6.47 \pm 0.15$	$4.7 \pm 0.4$	$4.3 \pm 0.7$	$9.0 \pm 0.2$	1.00
<i>NuSTAR</i>	$6.83 \pm 0.09$	$5.9 \pm 0.4$	$3.9 \pm 0.7$	$10.8 \pm 0.2$	1.05

The timing properties are calculated in the energy band of 3 – 79 keV with *NuSTAR* data, and in the band of 0.3 – 10.0 keV with *XMM-Newton* EPIC-pn Timing Mode data. The total fractional rms amplitude of the power spectra,  $\text{rms}_{\text{tot}}$ , is integrated in the frequency range of 0.1–20 Hz. *XMM-Newton* data in the high-flux epoch are not listed due to its limited exposure time.  $\chi^2/\nu$  is the reduced chi-squared of the best-fit of the power spectra.

The dynamical *NuSTAR* power spectrum is displayed in Figure 6.3. The first two orbits of data lack any significant periodicity. A QPO appears in the power spectrum at  $\sim 6\text{--}7$  Hz from  $\sim 1.3 \times 10^4$  s, coinciding with the time of the rapid flux decrease found in Figure 6.2. For further analysis, we generate *NuSTAR* and *XMM-Newton* power density spectra for the high-flux and low-flux epochs separately.

We fit the time-averaged power spectra of Swift J1658.2–4242 during the two epochs with a unity response file in XSPEC v12.9.0n (Arnaud, 1996). In this work, we perform all spectral fitting in XSPEC using  $\chi^2$  statistics, and all parameter uncertainties are reported at the 90% confidence level for one parameter of interest unless otherwise clarified. The power density spectra of Swift J1658.2–4242 can be adequately fitted with a multi-Lorentzian model, which is commonly used for black hole binaries (Belloni et al., 2002). We use three Lorentzians to fit for the noise continuum, with the centroid frequency fixed at zero; one Lorentz function for the QPO, and one for the possible sub-harmonic with the frequency linked with half the fundamental QPO frequency.

Comparing the time-averaged *NuSTAR* power spectra at the high- and low-flux epochs (see Figure 6.4), it is evident that the source variability increased significantly after the rapid flux drop: the total fractional rms variability ( $\text{rms}_{\text{tot}}$ , integrated in the frequency range of 0.1–20 Hz) in the *NuSTAR* band increases from  $2.4^{+1.0}_{-0.8}\%$  to  $10.8 \pm 0.2\%$ , and a QPO peak emerges in the power spectra along with increased noise continuum above 0.1 Hz.

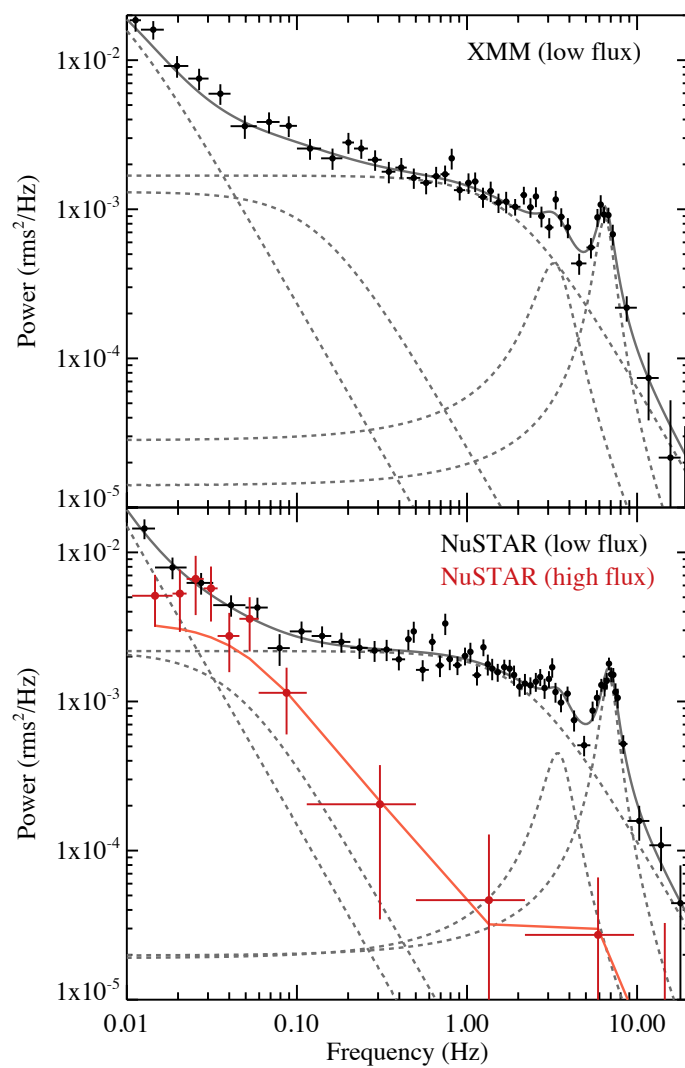


Figure 6.4: Time-averaged power spectra of Swift J1658.2–4242 in the intermediate state with the best-fit model. The *NuSTAR* and *XMM-Newton* power spectra are calculated in the energy band of 3–79 keV and 0.3–10 keV, respectively. The *NuSTAR* power spectra is plotted in black for the low-flux epoch, and in red for the high-flux epoch. The dashed lines mark the individual Lorentzian model components.

The time-averaged QPO frequency measured at the low-flux epoch is  $\nu_{3-79 \text{ keV}} = 6.83 \pm 0.09 \text{ Hz}$  in the *NuSTAR* band, and is  $\nu_{0.3-10 \text{ keV}} = 6.47 \pm 0.15 \text{ Hz}$  in the *XMM-Newton* band. The quality factor  $Q$  ( $\nu/\text{FWHM}$ ) of the QPO is  $4.3 \pm 0.7$  measured by *NuSTAR*, and is  $3.9 \pm 0.7$  measured by *XMM-Newton*, with the fractional rms amplitude,  $\text{rms}_{\text{qpo}}$ , of  $5.9 \pm 0.4\%$  and  $4.7 \pm 0.4\%$ , respectively (see details in Table 6.1). The characteristics of the QPO are similar to those of type-B or type-C low-frequency QPOs in black hole binaries (e.g., Casella et al., 2004, 2005; Motta et al., 2015). Type-C QPOs are usually strong, but can also be weak when appear in the soft state (fractional rms amplitude  $\sim 1\text{--}25\%$ ). They are variable in the frequency range of  $\sim 0.1\text{--}30 \text{ Hz}$ , and have a strong flat-top noise continuum in the power spectrum. Type-B QPOs are typically weaker (fractional rms amplitude  $\sim 1\text{--}10\%$ ), characterized by a weak red noise continuum, and are usually detected in a narrow frequency range around  $5\text{--}6 \text{ Hz}$ . We note that considering that the QPO peak lies on top of a strong noise continuum in the power spectra in Figure 6.4, the low-frequency QPO detected in Swift J1658.2–4242 is most likely to be a type-C QPO. The lack of a type-B QPO here is unusual, as a switch between a type-B QPO and a type-A/type-C QPO or noise is expected during fast transitions between HIMS and SIMS (e.g., Belloni, 2010; Belloni & Motta, 2016). The QPO frequency and strength increase at higher energies, as can be seen by comparing the QPO properties in the two different instrument bands, which is typical for QPOs observed in black hole binaries (e.g., Rodriguez et al., 2002; Casella et al., 2004).

The QPO is absent in the high-flux epoch. By using a Lorentzian function to fit for the possible presence of a QPO in the high-flux epoch, with the centroid and width of the Lorentzian fixed at the low-flux values, we can put an upper limit on the fractional rms amplitude of the QPO of  $<2.4\%$  (90% confidence level, in the  $3\text{--}79 \text{ keV}$  band of *NuSTAR*). We can rule out the possibility that the non-detection of QPO in the high-flux epoch is simply due to dilution by increased X-ray photons: the rms amplitude of the QPO in the low-flux epoch is  $5.9\%$ , the value would be  $3.5\%$  if diluted by extra  $40\%$  of non-variable photons, which exceeds the upper limit obtained. Therefore, the non-detection of a QPO during the start of the observation when the count rate is high is because of the intrinsic weakness of the QPO signal.

#### 6.4 Spectral Analysis

For spectral modeling, we separately extracted *NuSTAR* energy spectra accumulated before and after the flux change. The *NuSTAR* exposure times during the high- and the low-flux epoch are  $\sim 3.7 \text{ ks}$  and  $\sim 27.4 \text{ ks}$ , respectively. We first fit the *NuSTAR*

spectra in the two epochs jointly with a simple absorbed cutoff power-law model plus a thermal disk blackbody component, `TBnew*(diskbb+cutoffpl)` (Model 1), in XSPEC notation. The `cutoffpl` model is widely used to fit the non-thermal X-ray emission in black hole binaries. It is used as a phenomenological spectral description of the Comptonized emission generated in the corona in the vicinity of a black hole. Neutral absorption is accounted for by using the `TBnew` absorption model, with the cross-sections from Verner et al. (1996) and abundances from Wilms et al. (2000). In the case of Swift J1658.2–4242, neutral absorption is mostly intrinsic to the source, as the absorption column density,  $N_{\text{H}}$ , measured by modeling the X-ray spectrum, greatly exceeds the Galactic value of  $N_{\text{H,Gal}} = 1.55 \times 10^{22} \text{ cm}^{-2}$  (Kalberla et al., 2005). All abundances are fixed at the Solar value in the `TBnew` model. Changes in the shape of the non-thermal spectra of Swift J1658.2–4242 before and after the large flux variation are minimal, as revealed by the constant values of HR3 (see Figure 6.2(e)). Therefore, we link the parameters of the `cutoffpl` model between epochs, including the power-law index,  $\Gamma$ , and the exponential high-energy cutoff,  $E_{\text{cut}}$ , while allow the normalization of the `cutoffpl` model to vary independently.

As shown in Figure 6.5, Model 1 fits the spectral continuum well, with the reduced chi-squared of  $\chi^2/\nu = 2151/1698 = 1.27$  ( $\nu$  is the number of degrees of freedom). Allowing the parameters of  $E_{\text{cut}}$  and  $\Gamma$  to have different values at the two epochs brings no significant improvement to the fit. The prominent spectral residuals of Model 1 are a narrow Fe  $K\alpha$  emission line at  $\sim 6.4$ – $6.5$  keV, and a narrow absorption feature at  $\sim 7.1$  keV (see Figure 6.5). The narrow emission line is only seen after the drop in flux, while the absorption line is seen in both the high- and low-flux epochs.

In order to achieve broadband X-ray coverage, we further include two contemporaneous *Swift*-XRT spectra in the spectral modeling, so that the parameters sensitive to the soft X-ray band (i.e., absorption column density,  $N_{\text{H}}$ , and disk blackbody temperature,  $T_{\text{in}}$ ) can be better constrained. We use *NuSTAR* spectra in the energy range of 4–79 keV and *Swift*-XRT spectra in 1.0–10.0 keV, following Xu et al. (2018c). We allow the cross-normalization constants to vary freely for *NuSTAR*/FPMB and *Swift*-XRT, and fix the value at unity for *NuSTAR*/FPMA. To improve the fit, we add a Gaussian absorption line model, `gabs` and a Gaussian emission line model, `Gaussian`, to account for the spectral residuals of Model 1 shown in Figure 6.5, with the total model set up in XSPEC as: `TBnew*gabs*(diskbb+cutoffpl +Gaussian)` (Model 2). For simplicity, we fix the line width,  $\sigma$ , of the `gabs` model at

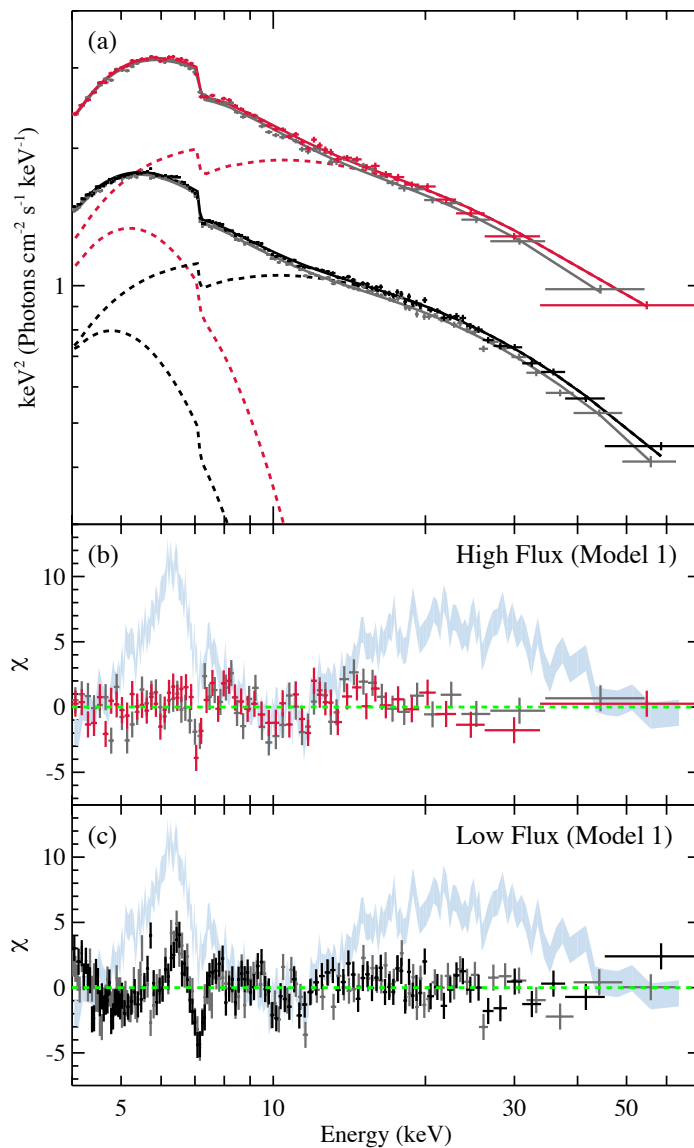


Figure 6.5: *NuSTAR* spectra of Swift J1658.2–4242 during the intermediate state. (a) Folded *NuSTAR* spectra of Swift J1658.2–4242 in the intermediate state. FPMA data in the high- and low-flux epochs are plotted in red and black, respectively. FPMB data are both plotted in gray. Dashed lines mark the individual model components, a thermal disk blackbody and a cutoff power-law. (b) (c) Spectral residuals of Model 1. There is no evidence for relativistic reflection features (i.e., a broad and asymmetric Fe  $K\alpha$  line and Compton reflection hump) in the data. For comparison, strong relativistic reflection features from the earlier *NuSTAR* observation of Swift J1658.2–4242 in the hard state reported in Xu et al. (2018c) are overplotted in light blue.

Table 6.2: Spectral Fitting Results: Part I

Component	Parameter	High-flux Epoch	Low-flux Epoch
Model 1: TBnew*(diskbb+cutoffpl) [ <i>NuSTAR</i> ]			
TBNEW	$N_{\text{H}} (\times 10^{23} \text{ cm}^{-2})$	$1.60 \pm 0.04$	$1.48 \pm 0.03$
DISKBB	$kT_{\text{in}} (\text{keV})$	$1.46 \pm 0.02$	$1.28 \pm 0.01$
	Norm	$74 \pm 5$	$84 \pm 3$
CUTOFFPL	$\Gamma$		$2.09 \pm 0.03$
	$E_{\text{cut}} (\text{keV})$		$52 \pm 4$
	Norm	$3.1 \pm 0.2$	$1.7 \pm 0.1$
$\chi^2/\nu$		$2151/1698 = 1.27$	
Model 2: TBnew*gabs*(diskbb+cutoffpl+Gaussian) [ <i>Swift</i> + <i>NuSTAR</i> ]			
TBNEW	$N_{\text{H}} (\times 10^{23} \text{ cm}^{-2})$	$1.75 \pm 0.03$	$1.41 \pm 0.02$
GABS	$E_{\text{gabs}} (\text{keV})$		$7.09 \pm 0.04$
	Norm	$(1.3 \pm 0.4) \times 10^{-2}$	$(1.3 \pm 0.2) \times 10^{-2}$
DISKBB	$kT_{\text{in}} (\text{keV})$	$1.44 \pm 0.01$	$1.29 \pm 0.01$
	Norm	$86 \pm 4$	$78 \pm 3$
CUTOFFPL	$\Gamma$		$2.07 \pm 0.03$
	$E_{\text{cut}} (\text{keV})$		$50 \pm 4$
	Norm	$3.0 \pm 0.2$	$1.6 \pm 0.1$
GAUSSIAN	$E_{\text{gauss}} (\text{keV})$		$6.48 \pm 0.04$
	Norm	$< 2 \times 10^{-4}$	$(9 \pm 1) \times 10^{-4}$
$\chi^2/\nu$		$2900/2580 = 1.12$	
Model 3: TBnew*gabs*(diskbb+relxillp+Gaussian) [ <i>Swift</i> + <i>NuSTAR</i> ]			
TBNEW	$N_{\text{H}} (\times 10^{23} \text{ cm}^{-2})$	$1.84 \pm 0.03$	$1.55 \pm 0.02$
GABS	$E_{\text{gabs}} (\text{keV})$		$7.09 \pm 0.03$
	Norm	$(2.0_{-0.4}^{+0.5}) \times 10^{-2}$	$(1.8 \pm 0.3) \times 10^{-2}$
DISKBB	$kT_{\text{in}} (\text{keV})$	$1.38 \pm 0.02$	$1.17 \pm 0.03$
	Norm	$83_{-8}^{+6}$	$103_{-10}^{+7}$
RELXILLP	$\Gamma$		$2.32_{-0.03}^{+0.04}$
	$E_{\text{cut}} (\text{keV})$		$91_{-14}^{+17}$
	$h (r_{\text{g}})$		$18 \pm 8$
	$a^* (cJ/GM^2)$		0.998 (fixed)
	$R_{\text{in}} (r_{\text{g}})$		$< 6.7$
	$A_{\text{Fe}} (\text{solar})$		0.91 (fixed)

Continued on Next Page

Table 6.2 – Continued

Component	Parameter	High-flux Epoch	Low-flux Epoch
	$\theta$ ( $^\circ$ )		64 (fixed)
	$\log(\xi)$		$3.7^{+0.4}_{-0.3}$
	$R_{\text{ref}}$		$0.4 \pm 0.3$
	Norm ( $10^{-2}$ )	$6.5^{+1.3}_{-1.1}$	$3.5 \pm 0.6$
GAUSSIAN	$E_{\text{gauss}}$ (keV)		$6.45 \pm 0.06$
	Norm	$< 1 \times 10^{-4}$	$(7 \pm 1) \times 10^{-4}$
	$\chi^2/\nu$	2837/2576 = 1.10	
	$F_{\text{disk}}$ ( $\text{erg cm}^{-2} \text{s}^{-1}$ ) <sup>a</sup>	$5.66 \times 10^{-9}$	$3.09 \times 10^{-9}$
	$F_{\text{powerlaw}}$ ( $\text{erg cm}^{-2} \text{s}^{-1}$ ) <sup>a</sup>	$1.19 \times 10^{-8}$	$6.51 \times 10^{-9}$
	$F_{\text{total}}$ ( $\text{erg cm}^{-2} \text{s}^{-1}$ ) <sup>a</sup>	$1.75 \times 10^{-8}$	$9.60 \times 10^{-9}$

a. Unabsorbed flux in 0.1–500 keV calculated based on the normalization of *NuSTAR*/FPMA.

0.1 keV and the width of the Gaussian model at 0.2 keV. During the joint spectral fitting, we link the centroid energies of gabs and Gaussian between epochs, while allow their corresponding strength to vary independently. The addition of these two extra model components reduces the reduced chi-squared of the fit ( $\chi^2/\nu = 2900/2580 = 1.12$ ), and leaves no visually evident spectral residuals (see Figure 6.6).

The shape of the broadband X-ray continuum is consistent with black hole binaries in the intermediate state (Remillard & McClintock, 2006; Belloni & Motta, 2016). The spectral fitting measures a soft power-law index ( $\Gamma = 2.07 \pm 0.03$ ) and a high disk blackbody temperature ( $kT_{\text{in}} \simeq 1.2\text{--}1.4$  keV, the value varies between epochs), whereas the contribution of the thermal disk to the total unabsorbed flux in 0.1 – 500 keV is only  $\sim 32\%$ , indicating that Swift J1658.2–4242 was yet to enter a canonical soft (thermal dominant) state. The changes in the shape of the broadband X-ray spectrum after the large flux decrease are subtle (see Figure 6.6(a)), which are reflected by the similar values of the best-fit parameters measured for the two epochs (see Table 6.2). The values of the inner disk temperature,  $kT_{\text{in}}$ , are measured to be  $1.44 \pm 0.01$  keV and  $1.29 \pm 0.01$  keV for the high- and the low-flux epoch, respectively. The absorption column density,  $N_{\text{H}}$ , slight decreases from  $(1.75 \pm 0.03) \times 10^{23} \text{ cm}^{-2}$  to  $(1.41 \pm 0.02) \times 10^{23} \text{ cm}^{-2}$  after the flux drop. The variation in hardness ratios described in Section 6.3 is caused by this simultaneous decrease in the inner disk temperature and the absorption column density.

Via modeling the broadband X-ray spectra, we can confidently rule out increased photoelectric absorption as the origin of the large decrease in X-ray flux.

One key difference when comparing the *NuSTAR* spectra of Swift J1658.2–4242 in the intermediate state with that from an earlier observation in the hard state (Xu et al., 2018c), besides spectral softening, is the disappearance of strong relativistic reflection features (see Figure 6.5 for a comparison). Strong relativistic reflection features, including a broad and asymmetric Fe  $K\alpha$  line and Compton reflection hump, are commonly found in bright black hole binaries during intermediate and soft states, enabling a measurement of the black hole spin in those systems (e.g., Tomsick et al., 2014; Walton et al., 2016; Miller et al., 2018). In the case of Swift J1658.2–4242, although relativistic disk reflection features were clearly detected in the bright hard state in Xu et al. (2018c), there is no clear indication for such a component on top of the Comptonization continuum in the intermediate state. Considering that the flux of the hard X-ray coronal emission in the intermediate state is comparable to that in the hard state, reflection features should be easily detectable in the intermediate state as long as the reflection fraction is comparably high. Therefore, the non-detection of relativistic reflection features in this work is because of the intrinsic weakness of the relativistic reflection component rather than the source being too faint.

Lacking prominent relativistic reflection features in the data, we cannot obtain a robust measurement of the inner accretion disk parameters via reflection spectral modeling. Thus, we simply calculate the upper limit of the strength of any reflection component that comes from the inner disk. To do so, we add a relativistic disk reflection component modeled by the `relxilllp` model (`relxill` v1.0.2; Dauser et al., 2014; García et al., 2014) to the fit, with the total model set up in XSPEC as: `TBnew*gabs*(diskbb+relxilllp+Gaussian)` (Model 3). The `relxilllp` model assumes a lamp-post geometry for the corona, which parameterizes the disk emissivity profile by the height of the corona,  $h$ , above the accretion disk. A cutoff power-law continuum is included in the `relxilllp` model, and is used as input for the reflection spectrum. To reduce the number of free parameters, we fix the black hole spin,  $a^* = 0.998$ , the inclination of the accretion disk,  $\theta = 64^\circ$ , and the iron abundance in the disk,  $A_{\text{Fe}} = 0.91$ , according to the best-fit values found in Xu et al. (2018c), as  $a^*$  and  $A_{\text{Fe}}$  do not change between states and the  $\theta$  is also usually assumed to remain constant. The best-fit reflection fraction measured by Model 3 is low,  $R_{\text{ref}} = 0.4 \pm 0.3$ , confirming the lack of a strong relativistic reflection

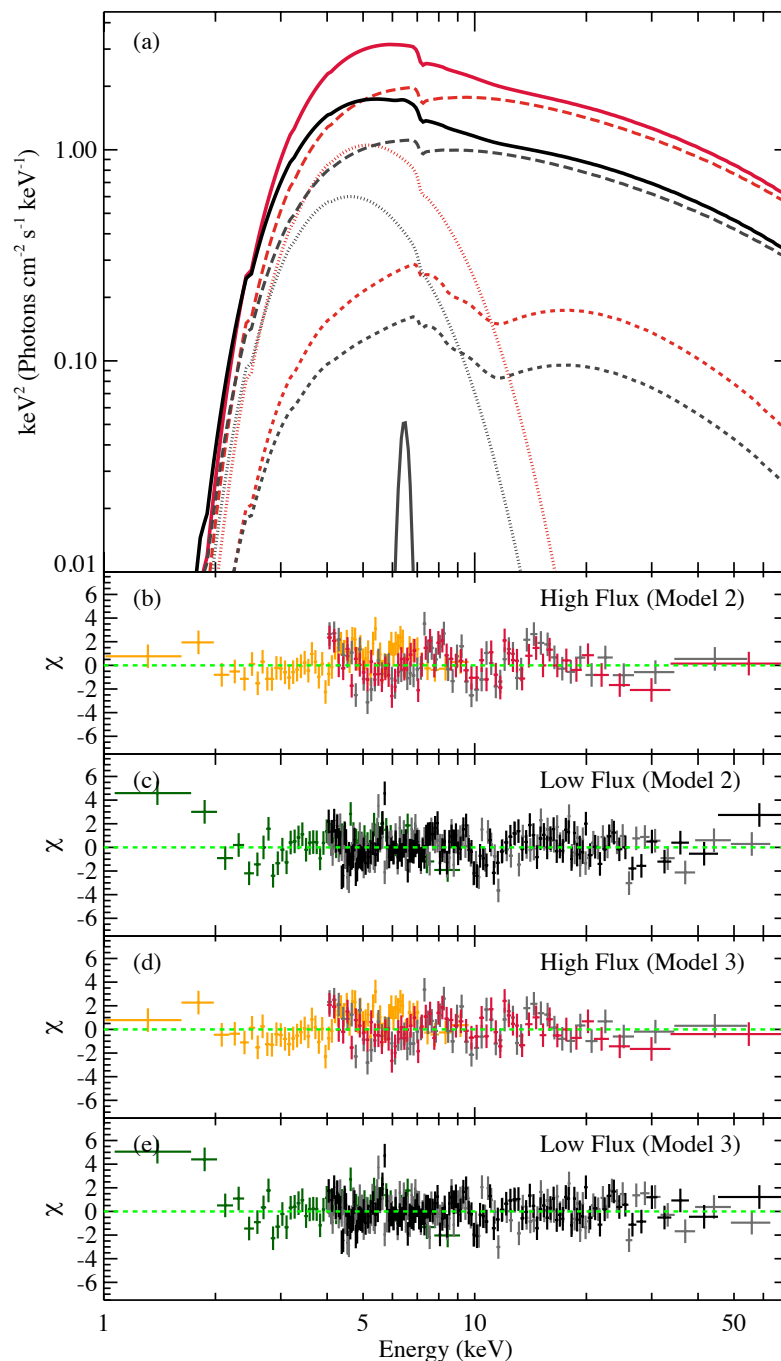


Figure 6.6: The broadband X-ray spectra of Swift J1658.2–4242 in the intermediate state with best-fit models. (a) Best-fit model (Model 3) of the broadband X-ray spectra of Swift J1658.2–4242, plotted in red for high-flux epoch and in black for low-flux epoch. The total model (solid lines) is plotted together with contributions from the putative weak relativistic disk reflection component (dashed lines), the coronal emission component (long dashed lines), the thermal disk (dotted lines), and the narrow Fe  $K\alpha$  emission line (solid line). (b)–(e) Spectral residuals from Model 2 and Model 3. The *Swift*-XRT spectra are plotted in orange and green for the high- and the low-flux epoch, respectively. The same color scheme is used for the *NuSTAR* data as in previous plots.

component in the spectra (see also in Figure 6.6(a), the contribution of the putative relativistic reflection component is weak when compared to the total spectra).

We note that although the addition of a relativistically blurred reflection component improves the fit slightly with four extra parameters by  $\Delta\chi^2/\Delta\nu = 63/-4$ , we do not consider it as significantly detected. As shown in Figure 6.6, the addition of a `relxill` component in Model 3 only slightly reduces the residuals between 10 keV and 20 keV, which are likely to come from small spectral curvature not perfectly accounted for in Model 2, rather than being related to relativistic reflection features. We stress that when fitting spectra with the `relxill` model, the constraint on the inner disk radius can only be confidently achieved in cases where the profile of the broad Fe  $K\alpha$  line is clearly visible. Since there is no broad Fe  $K\alpha$  line present in the spectral residuals in Figure 6.5, the small inner disk radius,  $R_{\text{in}}$ , measured (see Table 6.2) could be driven by the lack of prominent blurred reflection features in the spectra. Thus the model tends to artificially make the line broad to mimic part of the continuum in the Fe  $K\alpha$  band. Therefore, we consider the best-fit reflection fraction obtained in Model 3 as a crude upper limit, and do not discuss physical implications of the rest of the reflection parameters to avoid over-interpretation of the data.

The high S/N of the *NuSTAR* spectra of Swift J1658.2–4242 used in this work allows a comparison of the strength of secondary spectral features in the two epochs: the strength of the narrow absorption line at  $\sim 7.1$  keV modeled by `gabs` can be considered as constant within errors; whereas the absolute flux of the narrow Fe  $K\alpha$  emission line at 6.4–6.5 keV modeled by `Gaussian` clearly increases after the flux drop (the emission line is not detected in the high-flux epoch, see best-fit parameters in Table 6.2). Both features were also observed in Swift J1658.2–4242 with *NuSTAR* early on during its 2018 outburst in the hard state, and were discussed in detail in Xu et al. (2018c).

Absorption lines in the Fe K band of the X-ray spectrum of black hole binaries are commonly associated with blueshifted absorption lines from highly ionized iron (e.g., Fe XXV and Fe XXVI) generated in an accretion disk wind, which are frequently found when the accretion rate is high in the soft state (e.g., Miller et al., 2008; Ponti et al., 2012; Miller et al., 2016b). The constant strength we measured of the narrow absorption line implies an invariant disk wind component during the high- and low-flux epochs.

Narrow Fe  $K\alpha$  emission lines in the spectra of black hole binaries are believed to be produced by distant reprocessing of the hard X-ray photons from the corona, which may arise from distant reflection of the coronal emission by the outer edge of a flared accretion disk, or re-emission in a disk wind. We can get an estimate of the location of the narrow Fe  $K\alpha$  line emission in terms of the distance from the black hole based on the Fe  $K\alpha$  line width. We replace the simple Gaussian emission line model in Model 3 with a second `relxilllp` model component (by setting `relf_frac = -1`, only the reflected part is used). As the line energy is consistent with being neutral, we fix the ionization parameter<sup>1</sup>,  $\log(\xi)$ , of this `relxilllp` model component at 0, allow the parameter of the inner disk radius,  $R_{\text{in}}$ , to vary freely, and link all other parameters with those of the relativistic disk reflection component. We can get a lower limit of the inner radius of this `relxilllp` component to be  $406 r_g$  (where  $r_g \equiv GM/c^2$ , is the gravitational radius), which we use to represent the disk radius responsible for the narrow Fe  $K\alpha$  line. The emergence of a narrow Fe  $K\alpha$  emission line in the low-flux epoch indicates the appearance of reprocessing material at a large distance from the central black hole after the flux drop.

## 6.5 Discussion

We have presented analyses of the coordinated *NuSTAR* and *XMM-Newton* observations with contemporaneous *Swift-XRT* data of the new black hole binary candidate Swift J1658.2–4242, which caught the source in the intermediate state during its 2018 outburst. A rapid decrease in the source flux is observed by both telescopes, accompanied by the turn-on of a transient low-frequency QPO. The dramatic variation in flux and timing properties together with only minor changes in the broadband X-ray spectra are unusual for black hole X-ray binaries, and the physical driver of the event is uncertain. We discuss possible causes of the uncommon properties observed in Swift J1658.2–4242 based on results from our X-ray spectral and timing analyses.

### 6.5.1 Invariance of Coronal Properties

The power-law component extending to high energies in the X-ray spectra of black hole binaries is believed to originate from the so-called corona in the vicinity of black holes. Hot electrons in the corona up-scatter soft disk photons into the hard X-ray band. The parameters characterizing the spectral shape of the coronal emission

---

<sup>1</sup>The ionization parameter,  $\xi$ , is defined as  $\xi = 4\pi F_x/n$ , where  $F_x$  is the ionizing flux, and  $n$  is the gas density.

is the photon-index,  $\Gamma$ , and exponential cutoff at the high energy end,  $E_{\text{cut}}$ , which are associated with physical properties of the corona, its optical depth, and the electron temperature (Lightman & Zdziarski, 1987; Petrucci et al., 2001).

In order to measure the physical properties of the corona, we replace the `cutoffpl` component in Model 2 with the Comptonization model, `compPS` (Poutanen & Svensson, 1996). We assume a thermal electron distribution in the `compPS` model, and perform spectral fitting assuming a slab and a spherical geometry for the corona. We link the seed photon temperature in the `compPS` model with the disk blackbody temperature,  $kT_{\text{in}}$ , in the `diskbb` model. The physical model, `compPS`, fits the data equally well as the phenomenological model, `cutoffpl`. We cannot distinguish between the two coronal geometries based on the spectral modeling. The optical depth,  $\tau$ , and electron temperature,  $kT_e$ , of the corona can be well constrained (see Table 6.3 for the best-fit parameters). We find  $\tau = 1.6 \pm 0.1$  and  $kT_e = 24^{+2}_{-1}$  keV assuming a slab geometry, and  $\tau = 2.1 \pm 0.2$  and  $kT_e = 25 \pm 2$  keV assuming a spherical geometry, which is similar to the typical values reported in other black hole X-ray binaries (e.g., Del Santo et al., 2013; Sánchez-Fernández et al., 2017). Allowing  $\tau$  and  $kT_e$  to have different values for the two epochs does not bring significant improvement to the fit, indicating that these parameters which define the coronal properties are invariant in spite of the large flux variation.

The corona has also been proposed to be associated with the base of a jet (e.g., Markoff et al., 2001, 2005). There is evidence that transient QPOs and fast changes in X-ray timing properties of black hole binaries are related to jet ejection activity observed in the radio band (e.g., Fender et al., 2009; Miller-Jones et al., 2012), which could be a potential physical explanation for the transient low-frequency QPO observed in Swift J1658.2–4242. Radio flaring was indeed detected by ATCA around February 24, one day before our joint *NuSTAR* and *XMM-Newton* observations, when Swift J1658.2–4242 was in the same state. The source continued to be detected by subsequent radio observations in February and March (T. Russell, private communication). However, we note that associating the driver of the changes in X-ray flux and timing properties with dynamical activity of the jet or corona is hard to be reconciled with the invariant physical properties of the corona, i.e., its optical depth and electron temperature.

The turnover at the high energy end of the X-ray spectra of Swift J1658.2–4242 enables a good measurement of  $E_{\text{cut}}$  within the *NuSTAR* band. Studies of the evolution of cutoff energy during black hole X-ray binary outbursts reveal that the

Table 6.3: Spectral Fitting Results: Part II

Component	Parameter	High-flux Epoch	Low-flux Epoch
Slab corona geometry: TBnew*gabs*(diskbb+compPS+Gaussian)			
TBNEW	$N_{\text{H}} (\times 10^{23} \text{ cm}^{-2})$	$1.64 \pm 0.02$	$1.33 \pm 0.02$
GABS	$E_{\text{gabs}} (\text{keV})$	$7.11 \pm 0.04$	
	Norm	$(1.3 \pm 0.4) \times 10^{-2}$	$(1.2 \pm 0.2) \times 10^{-2}$
DISKBB	$kT_{\text{in}} (\text{keV})$	$1.38 \pm 0.01$	$1.23 \pm 0.01$
	Norm	$108 \pm 5$	$96 \pm 3$
COMPSS	$\tau$	$1.6 \pm 0.1$	
	$kT_{\text{e}} (\text{keV})$	$24_{-1}^{+2}$	
	Norm	$169_{-9}^{+16}$	$150_{-8}^{+10}$
GAUSSIAN	$E_{\text{gauss}} (\text{keV})$	$6.48 \pm 0.04$	
	Norm	$< 3 \times 10^{-4}$	$(1.0 \pm 0.1) \times 10^{-3}$
$\chi^2/\nu$		$2901/2580 = 1.12$	
Spherical corona geometry: TBnew*gabs*(diskbb+compPS+Gaussian)			
TBNEW	$N_{\text{H}} (\times 10^{23} \text{ cm}^{-2})$	$1.63 \pm 0.02$	$1.33 \pm 0.02$
GABS	$E_{\text{gabs}} (\text{keV})$	$7.11 \pm 0.04$	
	Norm	$(1.3 \pm 0.4) \times 10^{-2}$	$(1.3_{-0.1}^{+0.2}) \times 10^{-2}$
DISKBB	$kT_{\text{in}} (\text{keV})$	$1.38 \pm 0.01$	$1.24 \pm 0.01$
	Norm	$110 \pm 5$	$98 \pm 3$
COMPSS	$\tau$	$2.1 \pm 0.2$	
	$kT_{\text{e}} (\text{keV})$	$25 \pm 2$	
	Norm	$60 \pm 5$	$54_{-4}^{+5}$
GAUSSIAN	$E_{\text{gauss}} (\text{keV})$	$6.48_{-0.02}^{+0.04}$	
	Norm	$< 3 \times 10^{-4}$	$(1.0 \pm 0.1) \times 10^{-3}$
$\chi^2/\nu$		$2899/2580 = 1.12$	

spectral turnover at high energies usually disappears after the the sources make the transition to the soft state (e.g., Joinet et al., 2008; Motta et al., 2009). The measurement of  $E_{\text{cut}}$  further supports that Swift J1658.2–4242 is yet to enter a canonical soft state during the time of our observations. We note that the spectral shape resembles the very high state (more generally classified as intermediate state here) reported in some black hole binaries (named the steep power-law state in the review by McClintock & Remillard, 2006), considering that the power-law and the disk component are both strong and the spectrum is dominated by the steep power-law component. Therefore, Swift J1658.2–4242 could be accreting at a high Eddington rate during

the time of the observations, although the exact number is uncertain as the black hole mass and the distance are currently unknown.

### 6.5.2 Weakness of Relativistic Disk Reflection

Relativistic disk reflection, arising from the innermost edge of the accretion disk, is common in the X-ray spectra of bright black hole binaries observed by *NuSTAR* during recent years (e.g., Tomsick et al., 2014; Fürst et al., 2015; Walton et al., 2017; Xu et al., 2018b), and has been observed in several sources in their very high/intermediate states (e.g., King et al., 2014; Parker et al., 2016). We note that although we detected a narrow Fe  $K\alpha$  line in this work, it is probably produced by reflection from distant material, thus is not an indicator for the innermost edge of the accretion disk. The presence of a distant reflection component in Swift J1658.2–4242 is demonstrated by the detection of a narrow Fe  $K\alpha$  core on top of the broad Fe  $K\alpha$  line profile by *NuSTAR* during the hard state (Xu et al., 2018c), indicating that there are two separate reflection zones in the system. However, contrary to the earlier observation in the hard state, there is no unambiguous relativistically blurred disk reflection component detected in this work, when Swift J1658.2–4242 is in the intermediate state. The reflection fraction from the inner accretion disk we estimated here,  $R_{\text{ref,intermediate}} = 0.4 \pm 0.3$ , is significantly lower than the value measured in the bright hard state 8 days earlier ( $R_{\text{ref,hard}} = 3.25$ , Xu et al. (2018c)). The significant decrease in relativistic reflection strength during the rising phase of a black hole binary outburst is unusual, as the relative strength of the reflection component has been known to scale positively with the X-ray spectral photon index in black hole binaries (e.g., Zdziarski et al., 1999, 2003; Steiner et al., 2016).

Earlier detection of strong relativistic disk reflection features in Swift J1658.2–4242 led to the conclusion that the inner edge of the accretion disk reached the innermost stable circular orbit (ISCO) during its bright hard state (Xu et al., 2018c). One possibility for the weakness of relativistic disk reflection in the intermediate state is that the accretion disk is truncated later on during the rising phase of the outburst, close to the time of the hard-to-soft state transition. Due to light-bending effects at the vicinity of a black hole (preferentially bending light towards the accretion disk and away from the observer), the value of the reflection fraction,  $R_{\text{ref}}$ , should be greater than unity<sup>2</sup>, assuming that the accretion disk extends down to the ISCO. The low reflection fraction from the inner disk measured in this work could be most

<sup>2</sup>The reflection fraction  $R_{\text{ref}}$  is defined as the ratio of the coronal intensity illuminating the disk to that reaching the observer in the *relxill* model (Dauser et al., 2016).

straightforwardly explained by a truncated accretion disk, so that a large portion of the photons from the corona falls directly into the black hole without being reflected by an optically thick accretion disk. If true, this would challenge the canonical picture for state evolutions in black hole X-ray binaries (e.g., Done et al., 2007), which assumes that the accretion disk is truncated at a large radius and is replaced by an advection-dominated accretion flow (ADAF) in the hard state; as the outburst develops, the inner edge of the disk gradually moves inward, and reaches the ISCO after the source makes the transition to the soft state.

However, attributing the apparent weakness of relativistic reflection in Swift J1658.2–4242 to a truncated accretion disk is problematic, as the scenario of an optically thin ADAF inside the truncated disk would break down when the accretion rate is high in the intermediate/very high state of black hole X-ray binaries (e.g., Esin et al., 1997; Meyer et al., 2007). The high temperature and strength of the thermal disk emission also imply that the accretion disk cannot be significantly truncated.

Alternatively, it is possible that the strength of reflection from the inner accretion disk is reduced by the fact that the system is viewed at high inclination. Due to obscuration by the accretion disk when viewed close to the disk plane, most of the coronal emission reflected by the innermost edge of the accretion disk may not be directly visible to the observer, with only the part scattered into the line of sight being observed. This greatly reduces the apparent reflection strength from the inner disk (e.g., Wilkins & Gallo, 2015; Steiner et al., 2017). Under this scenario, explaining the significant change in the relativistic reflection fraction between the hard and the intermediate state requires invoking some change in the disk-corona geometry as the X-ray spectral state evolves, e.g., an increase in the scale-height of the accretion disk due to enhanced accretion rate. This would be a natural consequence of the puffing up of the inner disk at relatively high Eddington ratios. In this case, we note that it is likely that part of the thermal disk emission is also blocked from view.

In addition, as radio observations show jet activities around the time of our X-ray observations, an outflowing corona at relativistic speeds could also potentially weaken relativistic reflection features, because most photons would be beamed away from the accretion disk. Only considering special relativity effects, the reflection fraction could be reduced from 1 to as low as  $\sim 0.05$  for a viewing angle  $>60^\circ$ , depending on the the bulk velocity of the plasma (Beloborodov, 1999).

### 6.5.3 Interpretation of Rapid Flux Variation

The broadband X-ray spectra we obtained of Swift J1658.2–4242 enable a good measurement of the absorption column density before and after the flux change, which rules out increased photoelectric absorption as the cause of the rapid decrease in X-ray flux. The generation of low-frequency QPOs is believed to be tied to matter in the inner accretion flow. The association of the rapid flux variation with the emergence of a transient QPO indicates that the physical origin of the flux variation involves fundamental changes in the inner accretion flow around the central black hole, rather than being purely caused by geometrical effects, e.g., a partial eclipse of the X-ray emission region by the donor star.

The connection of the appearance of QPOs to step-function-like rapid changes in count rates is reminiscent of the “flip-flop” transitions detected in some black hole X-ray binaries in their very high states (e.g., Miyamoto et al., 1991; Takizawa et al., 1997; Casella et al., 2004; Belloni et al., 2005), which have been proposed to have a jet origin. However, they are phenomenologically distinct from the case being discussed here in Swift J1658.2–4242, as the “flip-flop” transitions are found to be repetitive over much shorter time scales ( $\sim 100$ – $1000$  s), and QPOs are usually detected during the local peaks of the flux. Rapid transitions of QPOs along with flux variations have also been observed and studied in detail in the highly variable Galactic microquasar GRS 1915+105 (e.g., Belloni et al., 2000; Rodriguez et al., 2002). However, the fast transitions observed in GRS 1915+105 are accompanied by significant changes in the spectral shape: soft X-ray flux (from the accretion disk) is anti-correlated with the hard X-ray flux (from the corona) (Rodriguez et al., 2002; Ueda et al., 2002). Therefore, changes in electron cooling rate in the corona, driven by the variable number of thermal photons emitted from the inner disk, provides a possible physical explanation for the overall flux variation in GRS 1915+105. In contrast, in the case of Swift J1658.2–4242, emission from the thermal disk and the power-law component both dropped by  $\sim 45\%$  at the time of the rapid flux decrease, which indicates a different physical origin.

In terms of the X-ray spectral analysis of Swift J1658.2–4242, we note that the most salient change in spectral parameters after the flux drop is a decrease in disk temperature by  $\sim 15\%$ . The normalization parameters of the `diskbb` model for the two epochs are consistent within errors, which are proportional to  $\propto R_{\text{in}}^2 \cos\theta$  by definition (where  $R_{\text{in}}$  is the apparent inner disk radius, and  $\theta$  is the disk inclination). Therefore, the observable inner edge of the accretion disk should remain at the same

radius at the two flux levels, and the reduced disk blackbody emission is caused by a decrease in disk temperature at this radius.

As shown in the long term monitoring light curve in Figure 6.1(a), the broadband X-ray flux of Swift J1658.2–4242 recovered after our joint observations, and underwent several similar large amplitude flux fluctuations during subsequent days until its flux level stabilized around MJD 58184. In the Galactic black hole X-ray binary GRS 1915+105, which is known to be accreting close to the Eddington limit, similar fast transitions occurring on much shorter time scales have been proposed to be associated with the Lightman & Eardley (1974) instability. Specifically, they have been proposed to be caused by the rapid removal and replenishment of matter forming the inner part of an optically thick accretion disk (Belloni et al., 1997a). Although the constant inner disk radius estimated by our spectral modeling of Swift J1658.2–4242 clearly indicates a different picture, it is still reasonable to attribute the origin of fast changes in spectral and timing properties observed in Swift J1658.2–4242 to certain instabilities in the accretion disk. Thermal and viscous instabilities in accretion disks were discussed in the Shakura-Sunyaev  $\alpha$ -disk model (Shakura & Sunyaev, 1976). Assuming  $\alpha = 1$ , Miyamoto et al. (1994) estimated the thermal and viscous time scales for a  $10 M_{\odot}$  black hole to be 0.01 s and 1 s at the radius of  $6 r_g$ , respectively, scaling with the disk radius as  $\propto R^{\frac{3}{2}}$ . Given that the count rate of Swift J1658.2–4242 dropped rapidly in 40 s as shown in Figure 6.2, we can get a rough estimate of the radius where the instability is triggered, which corresponds to a radius of  $\sim 1500 r_g$  for thermal instability, and  $\sim 70 r_g$  for viscous instability. Thus, in the case of Swift J1658.2–4242, it is most likely that disk instability arises from a relatively large distance from the central black hole. Then this propagates inwards, causing a change in the temperature of inner accretion disk in the X-ray emitting region, and triggering the QPO in the inner accretion flow.

Therefore, we propose accretion disk instability stimulated at a large radius, which propagates to affect the inner disk, as a coherent explanation for the various changes in X-ray spectral and timing properties along with the rapid flux variation observed in Swift J1658.2–4242. It is in principle possible for the propagating instability to alter the global structure of the accretion disk. A change in the outer disk geometry, e.g., increased disk scale-height, could help account for the emergence of distant reflection features in the X-ray spectra after the large flux drop. It could also provide a possible explanation for the decrease in the observed coronal emission through

occultation of coronal X-ray photons by an inflated inner disk along the disk plane, without invoking intrinsic changes in the physical properties of the corona.

## 6.6 Summary

In this work, we report a fast transition of spectral and timing properties observed in the new black hole binary candidate Swift J1658.2–4242 in the intermediate state. During the joint *NuSTAR* and *XMM-Newton* observations, the source flux decreased rapidly by  $\sim 45\%$  in 40 s, and simultaneously we observed a sudden turn-on of a low-frequency QPO. However, the rapid variation of X-ray flux and timing properties is accompanied by only subtle changes in the shape of the broadband X-ray spectrum, thus making it difficult to identify its physical origin.

The event observed in Swift J1658.2–4242 is phenomenologically new, distinct from reported behavior of previously known black hole X-ray binaries. We discuss disk instabilities triggered at a larger radius as a possible explanation for the various changes in the spectral and timing properties at the time of the rapid flux variation. In addition, strong relativistic disk reflection features previously reported in the bright hard state of Swift J1658.2–4242 in Xu et al. (2018c) disappear in the intermediate state, although the hard X-ray coronal emission in the intermediate state is comparably strong, which is unusual for black hole binaries. We propose that the significant weakening in the apparent reflection from the inner disk could be related to the fact the source is viewed at high inclination, along with a possible change in the the accretion disk geometry during the hard-to-soft state transition. The appearance of a transient QPO together with the large X-ray flux variation makes Swift J1658.2–4242 interesting for the investigations of the nature of QPOs in black hole X-ray binaries.

## Acknowledgments

We thank the anonymous referee for helpful comments that improved the paper. We thank Tom Russell and James Miller-Jones for providing information about ATCA radio observations. D.J.W. acknowledges support from STFC Ernest Rutherford Fellowship. This work was supported under NASA contract No. NNG08FD60C and made use of data from the *NuSTAR* mission, a project led by the California Institute of Technology, managed by the Jet Propulsion Laboratory, and funded by the National Aeronautics and Space Administration. We thank the *NuSTAR* Operations, Software, and Calibration teams for support with the execution and analysis of these observations. This research has made use of the *NuSTAR* Data Analysis Software

(NuSTARDAS), jointly developed by the ASI Science Data Center (ASDC, Italy) and the California Institute of Technology (USA).

STUDYING THE REFLECTION SPECTRA OF THE NEW  
BLACK HOLE X-RAY BINARY CANDIDATE MAXI J1631–479  
OBSERVED BY *NUSTAR*: A VARIABLE BROAD IRON LINE  
PROFILE

Xu Y., Harrison F. A., Tomsick J. A., Walton D. J. et al. (2020). “Studying the Reflection Spectra of the New Black Hole X-Ray Binary Candidate MAXI J1631–479 Observed by *NuSTAR*: A Variable Broad Iron Line Profile.” *The Astrophysical Journal*, 893(1):30. doi: 0.3847/1538–4357/ab7dc0.

**Abstract**

We present results from the *Nuclear Spectroscopic Telescope Array* (*NuSTAR*) observations of the new black hole X-ray binary candidate MAXI J1631–479 at two epochs during its 2018–2019 outburst, which caught the source in a disk dominant state and a power-law dominant state. Strong relativistic disk reflection features are clearly detected, displaying significant variations in the shape and strength of the broad iron emission line between the two states. Spectral modeling of the reflection spectra reveals that the inner radius of the optically-thick accretion disk evolves from  $<1.9 r_g$  to  $12 \pm 1 r_g$  (statistical errors at 90% confidence level) from the disk dominant to the power-law dominant state. Assuming in the former case that the inner disk radius is consistent with being at the ISCO, we estimate a black hole spin of  $a^* > 0.94$ . Given that the bolometric luminosity is similar in the two states, our results indicate that the disk truncation observed in MAXI J1631–479 in the power-law dominant state is unlikely to be driven by a global variation in the accretion rate. We propose that it may instead arise from local instabilities in the inner edge of the accretion disk at high accretion rates. In addition, we find an absorption feature in the spectra centered at  $7.33 \pm 0.03$  keV during the disk dominant state, which is evidence for a rare case that an extremely fast disk wind ( $v_{\text{out}} = 0.067^{+0.001}_{-0.004} c$ ) is observed in a low-inclination black hole binary, with the viewing angle of  $29^\circ \pm 1^\circ$  as determined by the reflection modeling.

**Keywords:** accretion – black hole physics – X-ray binary stars – X-ray transient sources

## 7.1 Introduction

The majority of Galactic black hole X-ray binaries are found as X-ray transients (Corral-Santana et al., 2016; Tetarenko et al., 2016). These are mostly low-mass X-ray binaries (LMXBs), which are stellar-mass black holes accreting from low-mass donor stars that go into recurrent outbursts due to thermal-viscous instabilities in the accretion disc (e.g., Frank et al., 2002). During a typical outburst, lasting from months to years, a black hole X-ray binary displays characteristic evolution in its X-ray spectral and timing properties, which are classified into different spectral states (see Remillard & McClintock, 2006; Belloni & Motta, 2016, for reviews). The outburst usually starts from a low/hard state, transitions to a high/soft state, then returns to the low/hard state at the end of the outburst. In addition, intermediate states are often found close to the time of the state transitions.

The X-ray emission from Galactic black hole X-ray binaries comes primarily from two components: blackbody radiation from the accretion disk and inverse Compton emission from the hot and tenuous corona, and they are believed to be coupled in the framework of the disk-corona model (Haardt & Maraschi, 1991, 1993). Reprocessing of the hard X-ray continuum emission by the optically thick accretion disk also imprints characteristic features in the X-ray spectrum, most prominently, the ionized Fe  $K\alpha$  fluorescence emission lines, the Fe K absorption edge, and the Compton reflection hump arising from absorption and Compton back-scattering (Guilbert & Rees, 1988; Lightman & White, 1988; Fabian et al., 1989). Relativistic effects at a few gravitational radii from the central black hole distort and blend the reflection features, giving rise to a broad and asymmetric line profile.

Modeling the relativistic disk reflection features helps to probe the physical conditions of inner accretion flow around the central black hole (see Miller; Fabian & Ross, 2007; 2010 for reviews and references within). Notably, via fitting the spectrum with physically self-consistent reflection models, it offers a method to locate the innermost edge of the optically-thick accretion disk by measuring the degree of gravitational redshift that modifies the reflection spectrum. Assuming that the innermost disk radius is associated with the innermost stable circular orbit (ISCO) around the black hole, we can directly estimate the spin of the black hole. Recently, with high sensitivity and broadband spectral coverage, *NuSTAR* detected strong relativistic reflection features in several known or new black hole X-ray binaries or binary candidates, where the broad iron line profiles are resolved (e.g., Tomsick et al., 2014; Miller et al., 2015b; Parker et al., 2016; Walton et al., 2017; Xu et al.,

2018b,c; Buisson et al., 2019). These high-quality datasets of bright black hole X-ray binaries are free from pile-up distortions and enable detailed studies of the inner accretion flow of black holes based on the diagnostics of relativistic disk reflection features.

MAXI J1631–479 is a new Galactic black hole X-ray binary candidate discovered when the source went into outburst in late 2018. It is only about  $8.9'$  away from the known X-ray pulsar AX J1631.9–4752. X-ray monitoring observations by MAXI revealed enhanced X-ray emission from an area consistent with the position of AX J1631.9–4752 from December 2018, but greatly exceeding the maximum historically recorded flux of AX J1631.9–4752 (Kobayashi et al., 2018). We performed two short *NuSTAR* observations on December 28, 2018 to explore the possibility of another source residing within the MAXI error circle (radius of  $0.17^\circ$ ). Indeed, *NuSTAR* clearly resolved two point sources within the MAXI error region, and confirmed that the enhanced X-ray emission came from a bright uncatalogued X-ray transient at a flux of about 0.8 Crab (2.0–10.0 keV), which was named MAXI J1631–479 (Miyasaka et al., 2018). The characteristics of the light curve and the shape of the energy spectrum of MAXI J1631–479 are both typical for Galactic X-ray binaries in outburst. In addition, the lack of pulsations and the detection of a strong broad Fe  $K\alpha$  emission line from the preliminary analysis of the *NuSTAR* data made the source a strong black hole candidate. Subsequent radio, optical and X-ray observations have been performed to further investigate the characteristics of this new black hole binary candidate (e.g., Russell et al., 2019; Eijnden et al., 2019; Kong, 2019). A radio observation on January 13, 2019 by ATCA suggests the detection of an optically-thin radio flare in a soft state black hole binary (Russell et al., 2019).

## 7.2 Observations and Data Reduction

The new black hole binary candidate MAXI J1631–479 was observed by *NuSTAR* (Harrison et al., 2013) on January 17, January 27, and January 30, 2019 (see Table 7.1 for details). We reduced the *NuSTAR* data following standard procedure using NuSTARDAS pipeline v.1.6.0 and CALDB v20170817. The source spectra were extracted from a circular region with the radius of  $200''$  from the two *NuSTAR* focal plane modules (FPMA and FPMB). Corresponding background spectra were extracted using polygonal regions from source-free areas in the detectors. We also extracted spectra from mode 6 data following the procedures described in Walton et al. (2016) to maximize the available exposure time. Mode 6 data are taken

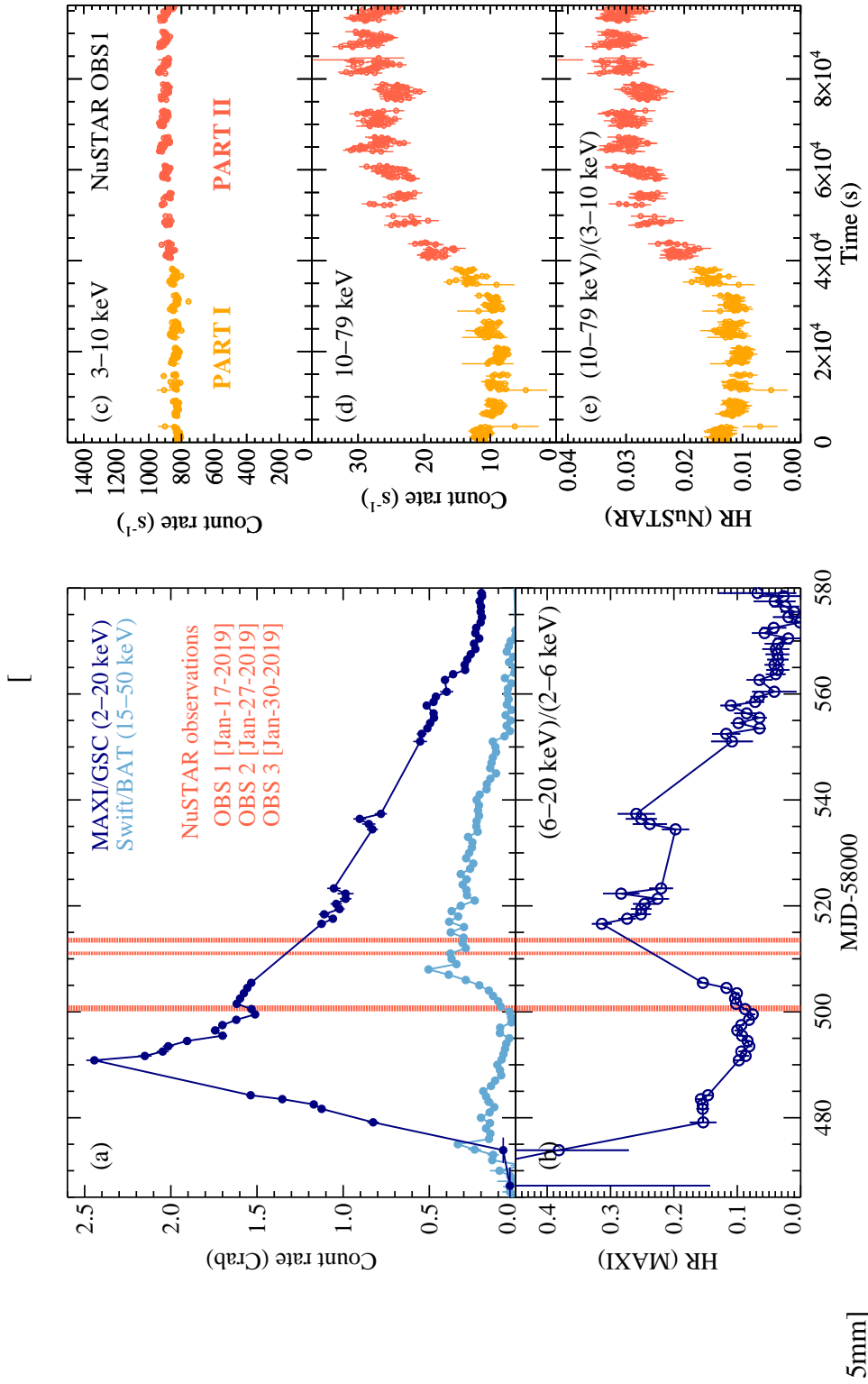


Figure 7.1: MAXI and *Swift*/BAT monitoring light curves of MAXI J1631–479. Left panels: (a) Long-term MAXI and *Swift*/BAT monitoring light curves of the 2018–2019 outburst of the new black hole binary candidate MAXI J1631–479. The flux in Crab unit is estimated from count rates in the corresponding energy bands. The orange shaded areas mark our *NuSTAR* observations. (b) Hardness ratio (HR) estimated by count rates in the energy bands of 2–10 keV and 10–20 keV of MAXI. Right panels: *NuSTAR* light curves and HR of MAXI J1631–479 for one module (FPMB) during OBS1, when significant flux variation is detected in the hard X-ray band. The *NuSTAR* count rates have been corrected for deadtime.

Table 7.1: *NuSTAR* Observations of MAXI J1631–479

	ObsID	Start Time (UTC)	Exposure (ks)
OBS1	90501301001	Jan-17-2019 02:16	7.5 (PART I)
			8.8 (PART II)
OBS2	80401316002	Jan-27-2019 16:56	10.1
OBS3	80401316004	Jan-30-2019 01:26	14.4

Exposure time is deadtime corrected on-source live time for one *NuSTAR* module, FPMA. Mode 6 data accounts for about 10% of the exposure time.

when an aspect solution is not available from the star tracker on the optics bench (CHU4), but solutions are available from the star trackers on the main spacecraft bus (CHU1,2,3), sufficient for spectral analysis of point sources (see Walton et al., 2016 for further details). MAXI J1631–479 was very bright during the three *NuSTAR* observations. The deadtime corrected count rates are  $\sim 850$ – $1000$  ct s<sup>-1</sup> for one module, exceeding the Crab count rate in the *NuSTAR* band. For spectral analysis, we coadded the FPMA and FPMB spectra from each observation using the `addspec` tool in HEASOFT v6.19. The *NuSTAR* spectra were grouped to have a signal-to-noise ratio (S/N) of 20 per energy bin.

Significant spectral variability was found during the first *NuSTAR* observation (OBS1, see Figure 7.1, right panel), when the count rate in the hard X-ray band ( $>10$  keV) increases by a factor of  $\sim 3$  and the count rate in the soft X-ray band ( $<10$  keV) remains roughly constant. For spectral modeling, we separated spectra corresponding to the first and second half of the observation, noted as the OBS1 PART I and PART II henceforth. No strong spectral variation was detected during OBS2 and OBS3, which enables a time-averaged spectral analysis. We use the *NuSTAR* spectrum up to 40 keV for OBS1 PART I, as the spectrum starts to become background dominated above 40 keV due to the weakness of power-law tail during this period. For OBS2 and OBS3, we ignore spectra in the band of 11–12 keV due to the presence of a narrow dip centered at 11.5 keV, which is calibration related and not intrinsic to the source. The apparent dip is weak ( $EW \approx 10$  eV) and only noticeable in very bright sources with a hard energy spectrum. For other observations, we use *NuSTAR* spectra in the full energy band of 3–79 keV.

To address the spectral states during our *NuSTAR* observations in a broader context, we plot the duration of the *NuSTAR* observations with the long-term MAXI/GSC (Matsuoka et al., 2009) and *Swift*/BAT (Krimm et al., 2013) monitoring light curves

(Figure 7.1, left panel). The MAXI/GSC light curve and hardness ratio were produced by the MAXI/GSC on-demand web interface<sup>1</sup>. We extracted source counts from a circular region with a radius of  $1.6^\circ$  centered on the source position and extracted background counts from a region with a radius of  $2^\circ$ , using auto bright-source exclusion with a minimum exclusion radius of  $1^\circ$ . The *Swift*/BAT light curve was obtained from the *Swift*/BAT Hard X-ray Transient Monitor<sup>2</sup>. We note that AX J1631.9–4752 was found to be faint ( $\sim 2$  mCrab in 2–10 keV) by the *NuSTAR* observation on December 28, 2018. Therefore, although MAXI and BAT cannot resolve MAXI J1631–479 and AX J1631.9–4752, the contamination from AX J1631.9–4752 is negligible. From the monitoring light curves, it is clear that *NuSTAR* OBS1 caught the source in a disk dominant state, when soft X-ray emission from the accretion disk dominates the spectrum. OBS2 and OBS3 were triggered during the phase when the source was undergoing significant spectral hardening, on the declining phase of the outburst.

### 7.3 Spectral Modeling

We detect strong relativistic disk reflection features in the spectra of MAXI J1631–479. To highlight the relativistic disk reflection features, we fit the *NuSTAR* spectrum with a disk blackbody model (`diskbb`; Mitsuda et al., 1984) plus a power-law model modified by neutral absorption, `TBabs*(diskbb+powerlaw)` (Model 1), in XSPEC notation, avoiding energy ranges corresponding to prominent reflection features (4–8 keV and 12–30 keV). In this work, we perform all spectrum modeling in XSPEC v12.9.0n (Arnaud, 1996), and use the cross-sections from Verner et al. (1996) and abundances from Wilms et al. (2000) in the TBabs neutral absorption model. All uncertainties are reported at the 90% confidence level. We fit the spectra with an absorbed disk blackbody model, `TBabs*diskbb` in XSPEC. As shown in Figure 7.2, a broad and asymmetric iron line peaking at  $\sim 6$ –7 keV and Compton hump at  $\sim 20$ –30 keV are evident in the spectral residuals.

Comparing the relative strength of the `diskbb` and `powerlaw` component in Figure 7.2, we note that OBS1 caught MAXI J1631–479 in a state when thermal emission from the accretion disk dominates, consistent with the canonical soft state of black hole binaries. OBS2 and OBS3 were taken when the steep power-law component is dominant, which is similar to the characteristics of the intermediate state/very high state/steep power-law state in some black hole binaries (e.g., Remil-

<sup>1</sup><http://maxi.riken.jp/mxondem/>

<sup>2</sup><https://swift.gsfc.nasa.gov/results/transients/>

lard & McClintock, 2006; Belloni & Motta, 2016). For simplicity, we henceforth refer to the spectral state during the first and second epoch as the disk dominant and the power-law dominant state, respectively, to avoid possible ambiguities in terms of the state classification.

The broad Fe  $K\alpha$  line profile clearly varies between the two states: it appears to be broader and stronger in the disk dominant state when compared with the power-law dominant state. As shown in Figure 7.3(a), the red wing of the line extends to  $\sim 4$  keV and  $\sim 5$  keV for the disk dominant and the power-law dominant states, respectively. The line equivalent width (EW)<sup>3</sup> decreased from  $\sim 180$ – $210$  eV to  $\sim 70$  eV from the disk dominant state to the power-law dominant state. We note that by the broad Fe  $K\alpha$  line here, we are referring to the blurred reflection feature that comes from the iron emission lines and the Fe K absorption edge, whose contribution to the reflection feature in the Fe K band varies with the ionization state (Ross & Fabian, 2005). The shape of the broad Fe  $K\alpha$  line profile is relatively constant over shorter time intervals (between OBS1 PART I and PART II, and between OBS2 and OBS3), although the spectral continuum varies considerably. Therefore, for more detailed spectral modeling, we fit the spectra of the two states separately, and link the relativistic reflection parameters between OBS1 PART I and PART II, and between OBS2 and OBS3.

We plot the evolution of the iron line flux with the power-law flux in the 10–79 keV band during our *NuSTAR* observations in Figure 7.3(b), which represent the strength of the observed reflection feature in the Fe K band and the strength of the hard X-ray illumination from the corona, respectively. The broad iron line flux does not correlate positively with the flux of the non-thermal power-law component, which is in contradiction to the general trend found by previous studies of black hole X-ray binaries observed by *RXTE* (e.g., Park et al., 2004; Rossi et al., 2005; Reis et al., 2013; Steiner et al., 2016). The ratio of the iron line flux to the power-law flux in the 10–79 keV band varies by a factor of  $\sim 50$  during our *NuSTAR* observations. Although the effects of gravitational light bending would possibly produce an anti-correlation, the effect is not predicted to be this large in the lamp-post coronal geometry (e.g., Miniutti et al., 2004; Reis et al., 2013). The broad iron line we observed in MAXI J1631–479 during OBS 1 PART I is unusually strong when compared with the weakness of the coronal emission, despite that reflection features are generally believed to be weak in disk dominant states. This implies

---

<sup>3</sup>EW and flux of the broad iron line is estimated by adding a Gaussian emission line model to Model 1 with other model parameters fixed at the best-fit values in Model 1.

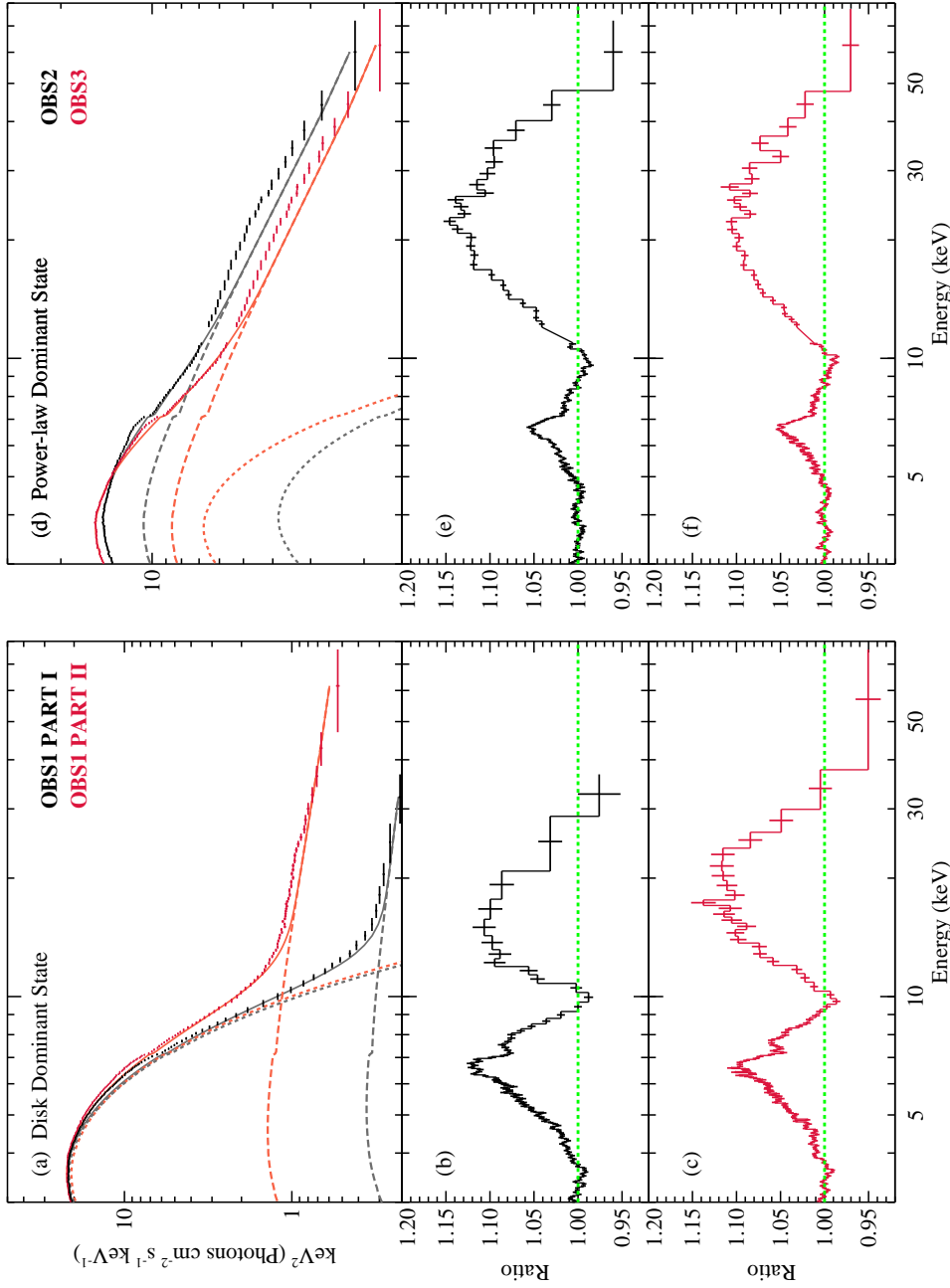


Figure 7.2: *NuSTAR* spectra of MAXI J1631–479 in the disk dominant and the power-law dominant state. Top panels: Unfolded *NuSTAR* spectra of MAXI J1631–479 in the disk dominant and the power-law dominant state, with the model of a disk blackbody and a non-thermal power-law component modified by neutral absorption, TBabs\* (di.kbb+powerLaw) (Model 1). The disk blackbody and the power-law model component are plotted in dashed and long-dashed lines, respectively. Middle and bottom panels: Strong relativistic reflection features (i.e., a broad iron line and the Compton reflection hump) are shown in the residuals. The spectra are rebinned for display clarity.

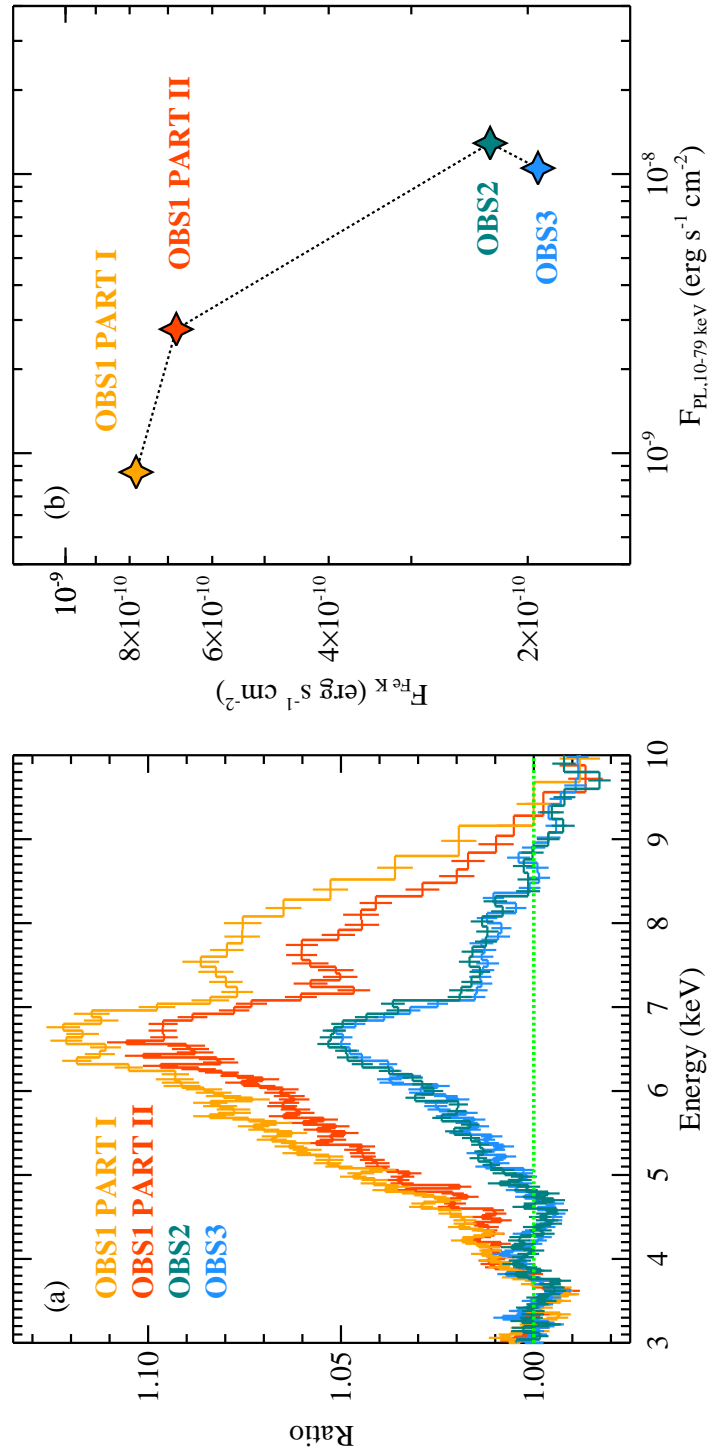


Figure 7.3: Variations in the profile and the strength of the Fe K $\alpha$  line. Left panel: Zoom-in plot of the Fe K band in the spectral residuals of Figure 7.2. The spectra are rebinned for display clarity. Right panel: Evolution of the Fe K line flux with the hard X-ray flux from the corona, the latter is represented by the flux of the power-law model component in the 10–79 keV band.

that the conventional picture that the apparent reflection features solely originate from the reprocessed non-thermal coronal emission may not be true for the case of MAXI J1631–479 in the disk dominant state.

### 7.3.1 Disk Dominant State

The shape and the strength (EW) of the Fe  $K\alpha$  line in MAXI J1631–479 remains relatively constant between OBS1 PART I and PART II, despite the large flux variation of the non-thermal emission in the hard X-ray band, implying that the strong and constant thermal disk emission plays a major role in shaping the reflected emission. In this case, the thermal disk component is dominant up to  $\sim 10$  keV (see Figure 7.2, left panel), which should provide the majority of the high energy X-ray photons that are able to ionize Fe K-shell electrons and produce the Fe  $K\alpha$  emission line (i.e., photons with energies above 7.1 keV), when transmitting through the disk atmosphere. Thus, thermal disk photons can also cause iron fluorescence and cause an increase in the observed iron line flux above what would be expected from the coronal illumination alone. Therefore, we propose that this reprocessing of high energy disk photons could explain the anti-correlation observed in Figure 7.3(b). This would explain why the iron line flux in the disk dominant state is not correlated with the power-law flux without the need to invoke light bending effects on the coronal emission. In addition, strong disk emission should have a significant effect on determining the ionization structure of the disk atmosphere.

Therefore, in the disk dominant state of MAXI J1631–479, thermal radiation from the hot accretion disk is important to the reflection process. We use the `refbhb` (Ross & Fabian, 2007) reflection model to fit the reflection spectra observed here. The `refbhb` reflection model takes into account the interaction between thermal disk photons and the disk atmosphere by directly including disk emission entering the surface layer from below. Thus the model is suitable for the disk dominant states of black hole binaries, when the thermal disk emission is hot and strong. The model self-consistently calculates the emergent spectrum that results from illumination of the hot inner portion of a constant density disc atmosphere and takes into account line broadening due to Compton scattering. The parameters of the model are the number density of hydrogen in the illuminated surface layer,  $H_{\text{den}}$ , the blackbody temperature of the thermal disk emission entering the disk surface layer from below,  $kT_{\text{BB}}$ , the power-law index of the coronal emission illuminating the surface layer from above,  $\Gamma$ , and the flux ratio of the coronal emission illuminating the disk and

the thermal emission radiating from the disk, `Illum/BB`. Elemental abundances are fixed at solar values in the `refbhb` model.

We convolve the disk reflection component with the `relconv_lp` model (Dauser et al., 2010, 2013) to measure the relativistic blurring effects on the reflection component. The `relconv_lp` model assumes an idealized lamp-post geometry (i.e., the corona is a point source located on the spin axis of the black hole above the accretion disk). It parameterizes the disk emissivity profile by the height of the corona,  $h$ , with a lower  $h$  corresponding to a steeper disk emissivity profile (e.g., Wilkins & Fabian, 2012; Dauser et al., 2013). We note that even in cases where the lamp-post geometry may not be the most realistic assumption,  $h$  can still be viewed as a proxy for the general shape of disk emissivity profile (Dauser et al., 2013), as currently even very high quality data cannot distinguish between the disk emissivity calculated in the lamp-post geometry and that assumed in the form of a broken power-law (e.g., Miller et al., 2015b; Xu et al., 2018b; Parker et al., 2015). Other parameters of the `relconv_lp` model are the black hole spin,  $a^*$ , the inner radius,  $R_{\text{in}}$ , and the inclination,  $i$ , of the accretion disk.

The total spectral model is set up as `TBabs*(relconv_lp*(refbhb+powerlaw))` in XSPEC (Model 2). The `powerlaw` model component is used here to account for the coronal emission that goes directly towards the observer without being reflected. We link the power-law index,  $\Gamma$ , in `powerlaw` and `refbhb`. As the black hole spin,  $a^*$ , and inner disk radius,  $R_{\text{in}}$ , are degenerate parameters, we fix  $R_{\text{in}}$  at the radius of the ISCO, aiming to obtain a measurement of the black hole spin. All parameters are linked between OBS1 PART I and PART II, except  $\Gamma$ , `Illum/BB`, and the normalization of the model components.

As shown in Figure 7.4(b), Model 2 is able to account for most of the reflection features and greatly improves the fit ( $\chi^2/\nu = 1825.8/800$ , where  $\nu$  is the number of degrees of freedom), leaving only a narrow Fe  $K\alpha$  emission line centered at  $6.50 \pm 0.03$  keV, some excess in the Compton hump region, and a narrow absorption feature centered at  $7.33 \pm 0.03$  keV in the spectral residuals. The narrow absorption feature can also be clearly seen in Figure 7.3(a), as a dip in 7–8 keV superposed on the broad iron line profile. We add an unblurred reflection component to fit the weak and narrow iron emission line, which possibly originates from distant reprocessing of the hard X-ray photons. Absorption features in the Fe K band are commonly associated with blueshifted Fe XXV/Fe XXVI lines, but the narrow absorption line complex cannot be resolved by *NuSTAR*. They are believed to arise

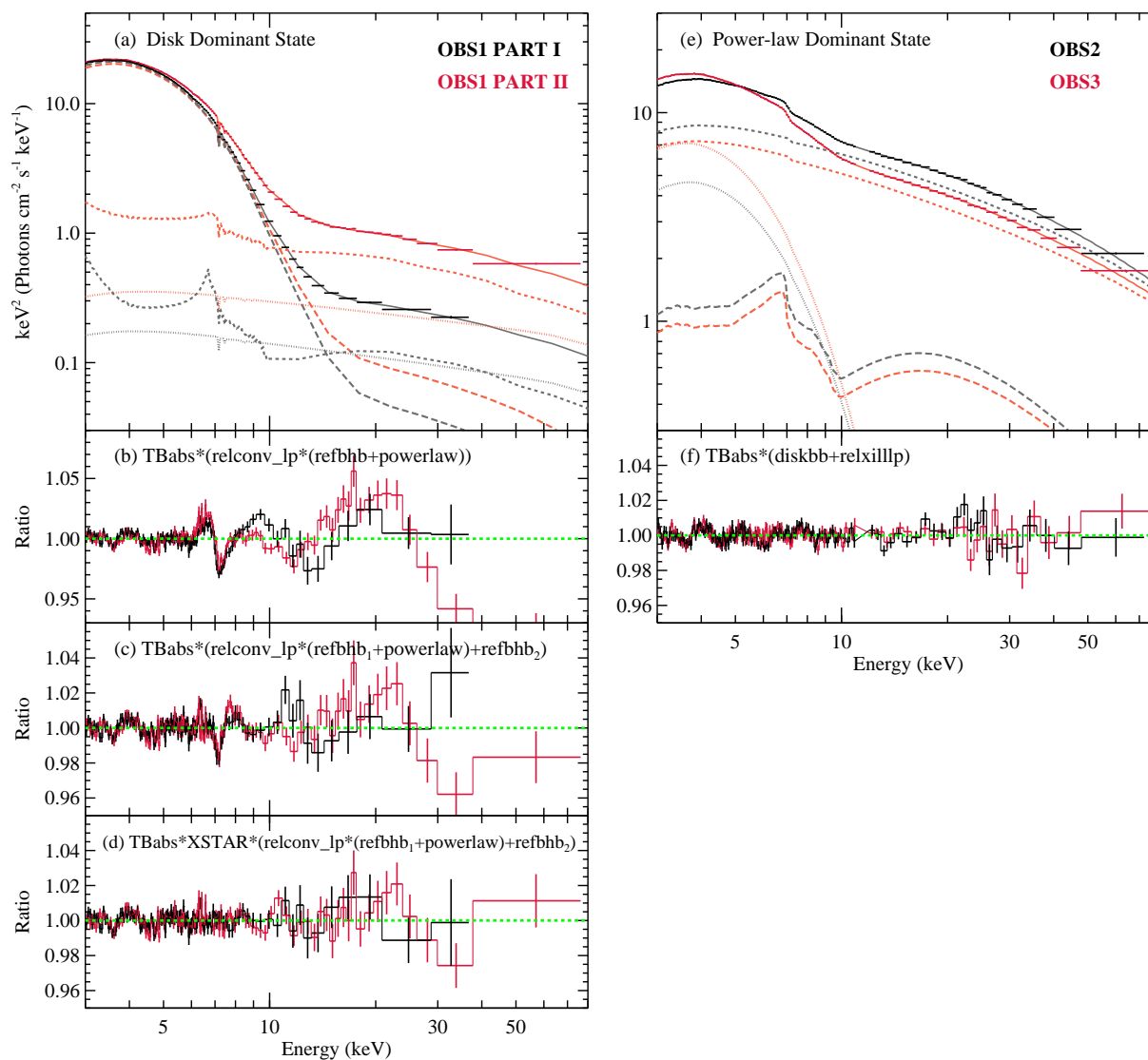


Figure 7.4: *NuSTAR* spectra of MAXI J1631–479 with the best-fit models. Top panels: Unfolded *NuSTAR* spectra of MAXI J1631–479 with the best-fit models (Model 3 for the disk dominant state, Model 4 for the power-law dominant state). In panel (a), the total model is plotted in solid lines together with the non-thermal coronal emission, powerlaw (dotted lines), the distant reflection component, refbhb<sub>2</sub> (dashed lines), and the thermal disk emission with relativistic disk reflection, refbhb<sub>1</sub> (long-dashed lines). In panel (e), the individual model components are the thermal disk emission (dotted lines), the non-thermal coronal emission (dashed lines), and the relativistic reflection component (long-dashed lines). Bottom panels: Data/model residuals. The spectra are rebinned for display clarity.

from absorption by outflowing material launched from the accretion disk (e.g., Ponti et al., 2012; Díaz Trigo & Boirin, 2016). If the absorption feature at  $7.33 \pm 0.03$  keV is associated with blueshifted He-like Fe XXV (6.70 keV), it requires an outflowing velocity of  $0.094 \pm 0.004 c$ ; or a lower velocity of  $0.052 \pm 0.004 c$  if identified with the more ionized H-like Fe XXVI. For a physical modeling of the absorption feature, we include an ionized absorption table model calculated by the XSTAR photoionization code (Kallman & Bautista, 2001). We use the same XSTAR grid as the one constructed for the soft state of Cygnus X-1 used in Tomsick et al. (2014). The free model parameters are the absorption column density,  $N_{\text{H,XSTAR}}$ , the ionization parameter,  $\xi$ , and the outflowing velocity,  $v_{\text{out}}$ . We set up the model in XSPEC as `TBabs*XSTAR*(relconv_lp*(refbhb1+powerlaw) +refbhb2)` (Model 3).

Model 3 adequately describes the data, leaving no obvious structures in the residuals ( $\chi^2/\nu = 1027.9/791$ , see Figure 7.4(d)). The addition of an XSTAR grid improves the fit by  $\Delta\chi^2 \sim 160$ , indicating that the narrow absorption feature is significantly detected (see the comparison between Figure 7.4(c) and (d)). The best fit reveals an outflowing velocity of  $v_{\text{out,XSTAR}} = 0.067^{+0.001}_{-0.004} c$  for the ionized absorber, which is extremely fast for a disk wind detected in a black hole X-ray binary (e.g., King et al., 2012; Miller et al., 2015b). Mostly driven by the clear broad iron line profile, the black hole spin and physical parameters related to the inner accretion flow are well constrained (see Table 7.2). The fitting results reveal that the central compact object in MAXI J1631–479 is a rapidly spinning black hole with the spin parameter of  $a^* > 0.94$ , and the inner accretion disk is viewed at a low inclination of  $i = 29^\circ \pm 3^\circ$ . By fixing the spin parameter at the maximum value of 0.998 and instead fitting for the inner disk radius, we can get an estimate of the inner disk radius of  $R_{\text{in}} < 1.9 r_g$  ( $r_g \equiv GM/c^2$ , is the gravitational radius). The ionization state of the gas is self-consistently derived by radiative transfer equations in the `refbhb` model, which is determined by the disk temperature,  $kT_{\text{BB}}$ , the disk density,  $H_{\text{den}}$ , and strength of the illuminating flux from the corona, `Illum/BB`. We can also get a reasonable constraint on the disk density and temperature based on the spectral modeling. The values are high for the relativistic reflection component, `refbhb1`, and decrease significantly for the unblurred reflection component, `refbhb2` (see best-fit parameters in Table 7.2). This is in accordance with the unblurred reflection occurring at a large distance from the black hole, as both the disk density and temperature are predicted to drop with increasing disk radius in the standard Shakura & Sunyaev (1973) disk model.

Table 7.2: Spectral Fitting of MAXI J1631–479 (Disk Dominant State)

Model 3: $TBabs * XSTAR * (relconv\_lp * (refbhb_1 + powerlaw) + refbhb_2)$		
Parameter	OBS1(PART I)	OBS1(PART II)
$N_{H,TBabs}$ ( $\times 10^{22}$ cm $^{-2}$ )		$3.3^{+0.4}_{-0.3}$
$N_{H,XSTAR}$ ( $\times 10^{22}$ cm $^{-2}$ )		$1.48^{+0.15}_{-0.12}$
$\log(\xi)_{XSTAR}$ (log [erg cm s $^{-1}$ ])		$4.81^{+0.18}_{-0.12}$
$v_{out,XSTAR}$ ( $c$ )		$0.067^{+0.001}_{-0.004}$
$h$ ( $r_g$ ) <sup>a</sup>		$< 3.7$
$a^*$ ( $cJ/GM^2$ )		$> 0.94$
$R_{in}$ ( $r_g$ )		$R_{ISCO}^f$ ( $< 1.9 r_g$ )
$i$ ( $^\circ$ )		$29 \pm 3$
$\Gamma$	$2.38^{+0.09}_{-0.04}$	$2.32^{+0.06}_{-0.05}$
Norm (powerlaw)	$9^{+12}_{-5}$	$17^{+25}_{-11}$
$kT_{BB,1}$ (keV)		$0.94 \pm 0.01$
$H_{den,1}$ (cm $^{-3}$ )		$1.7^{+0.3}_{-0.4} \times 10^{21}$
Illum/BB <sub>1</sub>	$0.04^{+0.04}_{-0.01}$	$0.07^{+0.05}_{-0.01}$
Norm (refbhb <sub>1</sub> ) <sup>b</sup>	$7^{+2}_{-1}$	$10 \pm 1$
$kT_{BB,2}$ (keV)		$0.22^{+0.06}_{-0.02}$
$H_{den,2}$ (cm $^{-3}$ )		$4^{+13}_{-1} \times 10^{17}$
Illum/BB <sub>2</sub>	$0.08^{+0.06}_{-0.03}$	$0.4^{+0.3}_{-0.1}$
Norm (refbhb <sub>2</sub> )	$0.7 \pm 0.1$	$2.6^{+0.2}_{-0.3}$
$\chi^2/\nu$	1027.9/791=1.30	
$F_{3-10}$ keV (erg cm $^{-2}$ s $^{-1}$ ) <sup>c</sup>	$2.5 \times 10^{-8}$	$2.6 \times 10^{-8}$
$F_{10-79}$ keV (erg cm $^{-2}$ s $^{-1}$ ) <sup>c</sup>	$9.7 \times 10^{-10}$	$2.9 \times 10^{-9}$
$F_{0.1-100}$ keV (erg cm $^{-2}$ s $^{-1}$ ) <sup>d</sup>	$1.7 \times 10^{-7}$	$1.6 \times 10^{-7}$

Parameters marked with a superscript  $f$  are fixed during the spectral fitting. <sup>a</sup>  $r_g \equiv GM/c^2$ , is the gravitational radius. <sup>b</sup> The `refbhb` model is normalized based on the power-law incident flux in 1–100 keV. <sup>c</sup> Observed flux in the corresponding energy bands. <sup>d</sup> Flux corrected for absorption.

For the spectral fitting above, we linked the disk temperature and the parameters about the relativistic blurring effects between OBS1 PART I and PART II, which is motivated by the constant thermal disk component and the similarity of the observed broad iron line profile. Allowing these parameters to have different values between epochs does not cause any significant change to the fitting results; therefore we keep them linked to obtain tighter constraints on the key physical parameters of interest. In this case, the strong and hot thermal disk component has a major role in shaping

the reflection features rather than non-thermal emission from the corona, so the relative strength of the different non-thermal components above 20 keV cannot be well constrained (e.g., see the poorly constrained normalization of the `powerlaw` model in Table 7.2). Therefore, we do not discuss the physical implications about the fraction of the power-law emission that is reflected by the inner disk, the distant reprocessing material, and the emission that goes directly to the observer as inferred from the best-fit parameters, to avoid over-interpreting the data.

We note that within  $3\sigma$  errors, the flux of the distant reflection component can be either higher or lower than that of the direct power-law component above 20 keV, but it is always constrained to be higher than that of the relativistic reflection component. The changes to the quality of the fits and the fit parameters are only negligible if we force the power-law flux to be higher than the flux of `reflbb2` above 20 keV. We have tried replacing the `powerlaw` component in Model 3 with a power-law model with a high-energy cutoff, `cutoffpl`, a power-law model with a low-energy cutoff, `expabs*powerlaw`, and a Comptonization model with both low-energy and high-energy rollovers, `nthcomp` (Zdziarski et al., 1996; Życki et al., 1999), which do not cause any significant difference to the fitting results and the cutoff is not required for the spectral continuum. It is difficult to understand the geometry that could cause the distant reflection to receive more coronal illumination than the relativistic one. We are currently uncertain if this is due to oversimplifications in the current version of the `reflbb` model, e.g., the fixed iron abundance and the self-consistently calculated ionization assuming a constant accretion rate and disk surface radius (Ross & Fabian, 2007), which might cause a bias in the relative strength of the iron line and Compton reflection hump and make the origin of the `reflbb2` component questionable. If this is the case, the role of the `reflbb2` model component in the spectral fitting might only be phenomenological in some sense. However, as shown in Figure 7.5, `reflbb2` only contributes to the narrow core of the iron line profile, thus would not affect the base of the broad iron line profile that we use to deduce the black hole spin.

The single-temperature blackbody description of the accretion disk in the `reflbb` model is not as realistic as the multi-color blackbody disk model. As discussed in Reis et al. (2008), this simplification might lead to biased values for the inner disk temperature, but would not have a significant effect on the key physical parameters determined by the reflection modeling, such as the inner radius of the accretion disk (or the black hole spin). Modeling the *NuSTAR* spectra of MAXI J1631–479

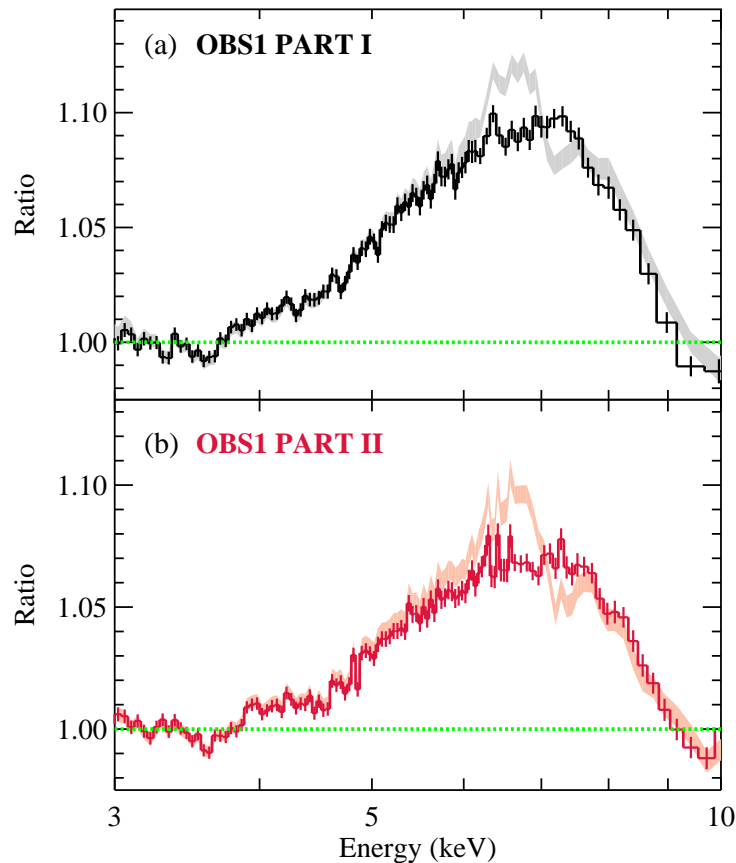


Figure 7.5: The broad iron line profiles of MAXI J1631–479 observed during the disk dominant state, corrected for the absorption feature at  $\sim 7.33$  keV and the narrow iron emission line at  $\sim 6.50$  keV. The spectral residuals in the Fe K band here are estimated by adding the *XSTAR* and *reflbb<sub>2</sub>* components to Model 1, with their parameters fixed at the best-fit values in Table 7.2, and fitting the *NuSTAR* spectra in 3–79 keV avoiding the energy range of 4–9 keV. For comparison, the line profiles without this correction are plotted in shaded regions.

above 4 keV, mostly only covering the Wien tail of the blackbody distribution, leads to similar fitting results; therefore we stress that the measurement of a rapid black hole spin here is robust.

For comparison, we also made an attempt to fit the data with a disk reflection model that does not directly include thermal disk emission, *relxilllp* (see detailed description of the model in Section 7.3.2). We add a *diskbb* model to account for the thermal disk component. The fit leads to extreme parameters, a high iron abundance,  $A_{\text{Fe}} \sim 5$ , and a reflection fraction,  $R_{\text{ref}} > 10$ , for OBS1 PART I, which is driven by the strong iron line, but such high reflection fraction is probably unphysical. Also, the model fails to describe the data, leaving prominent spectral residuals.

### 7.3.2 Power-law Dominant State

For the power-law dominant state, the flux of the illuminating coronal emission is significantly higher than that of the thermal disk emission, which exceeds the range of parameters covered in the `refbhb` model. We instead use the `relxilllp` model (`relxill`; Dauser et al.; García et al., 2014; 2014) to fit the reflection spectra, which is a combination of the ionized disk reflection model `xillver` (García et al., 2013), which implements the XSTAR code (Kallman & Bautista, 2001) to solve the ionization structure of the disk atmosphere, and the relativistic blurring kernel `relconv_lp` (Dauser et al., 2010, 2013). The `relxilllp` model intrinsically includes the illuminating corona emission in the shape of a power-law with an exponential high-energy cutoff,  $E_{\text{cut}}$ . The `xillver` reflection model is calculated based on the assumption of a slab geometry for the accretion disk, and does not include thermal disk photons entering the surface layer of the accretion disk from below. The model assumes a constant density ( $H_{\text{den}} = 10^{15} \text{ cm}^{-3}$ ) for the surface layer of the accretion disk with the disk temperature fixed at 10 eV. Therefore, the model neglects the role of thermal disk emission on determining the physical conditions in the disk atmosphere and thus the emergence reflection spectrum, which suits the case of cool accretion disks in AGNs. The model underestimates the effect of a hot accretion disk on the reflection spectrum for black hole binaries, but it seems to be a reasonable simplification for black hole binaries in the hard and intermediate states, when the thermal disk emission is weak and non-thermal power-law component dominates the spectrum. The iron abundance,  $A_{\text{Fe}}$  (in solar units), and the ionization parameter  $\xi$  (defined as  $\xi = 4\pi F_x/n$ , where  $F_x$  is the illuminating flux and  $n$  is the gas density) are free parameters in the `xillver` model.

In addition, we include a separate multicolor disk blackbody component, `diskbb`, to fit for the thermal emission from the accretion disk. We set up the total model in XSPEC as `TBabs*(diskbb+relxilllp)` (Model 4). We note that the broad iron line becomes narrower in the power-law dominant state (see Figure 7.3(a)), implying that the gravitational redshift is weaker in the line emission region, which implies that the Fe  $K\alpha$  emission line is produced at a larger disk radius than that in the disk dominant state. Therefore, we fix the black hole spin at the maximum value of  $a^* = 0.96$  (best-fit value in the disk dominant state), and instead fit for the inner disk radius,  $R_{\text{in}}$ . We note that the choice of the fixed spin parameter here would not affect the determination of other model parameters. If the accretion disk is truncated at a larger radius than the ISCO, the data would not be sensitive to the black hole spin parameter, as the frame-dragging effect from black holes of different spins would

Table 7.3: Spectral Fitting of MAXI J1631–479 (Power-law Dominant State)

Model 4: $TBabs^*(diskbb+relxillp)$		
Parameter	OBS2	OBS3
$N_{H,TBabs}$ ( $\times 10^{22}$ cm $^{-2}$ )		$3.84^{+0.10}_{-0.09}$
$h$ ( $r_g$ )		$4.3^{+0.5}_{-0.3}$
$a^*$ ( $cJ/GM^2$ )		$0.96^f$
$R_{in}$ ( $r_g$ )		$12 \pm 1$
$i$ ( $^\circ$ )		$29 \pm 1$
$\Gamma$	$2.45 \pm 0.02$	$2.51 \pm 0.02$
$E_{cut}$ (keV)	$110 \pm 11$	$156 \pm 22$
$\log(\xi)_{,ref}$ ( $\log$ [erg cm s $^{-1}$ ])		$3.56^{+0.15}_{-0.09}$
$A_{Fe}$ (solar)		$1.0^{+0.3}_{-0.1}$
$R_{ref}$		0.49
Norm (relxillp)	$0.8 \pm 0.1$	$0.8 \pm 0.1$
$kT_{in}$ (keV)	$1.19^{+0.01}_{-0.02}$	$1.14 \pm 0.01$
Norm (diskbb)	$454^{+32}_{-20}$	$859^{+38}_{-27}$
$\chi^2/\nu$	1669.6/1491=1.12	
$F_{3-10}$ keV (erg cm $^{-2}$ s $^{-1}$ )	$2.3 \times 10^{-8}$	$2.3 \times 10^{-8}$
$F_{10-79}$ keV (erg cm $^{-2}$ s $^{-1}$ )	$1.3 \times 10^{-8}$	$1.1 \times 10^{-8}$
$F_{0.1-100}$ keV (erg cm $^{-2}$ s $^{-1}$ )	$2.5 \times 10^{-7}$	$2.5 \times 10^{-7}$

only cause very small differences to the emission line profile produced at large disk radii (e.g., Dauser et al., 2013). Model 4 fits the *NuSTAR* spectra well and leaves no prominent structures in the spectral residuals ( $\chi^2/\nu = 1669.6/1491 = 1.12$ , see Figure 7.4(f)). The fitting results confirm that the source is not in a canonical hard state during the time of the *NuSTAR* observation, despite the significant spectral hardening observed in the monitoring light curves in Figure 7.1(b). From the best-fit parameters (see Table 7.3), we find the disk temperature is still high and the spectral slope remains soft in the power-law dominant state. The spectral hardening is caused by a large change in the relative strength of the thermal disk and the power-law component, the disk fraction of the total flux in 0.1–100 keV decreases from  $\sim 60\%$  to  $\sim 10\%$  from the disk dominant to the power-law dominant state.

In terms of the reflection parameters, the best-fit results of Model 4 (see Table 7.3) indicate significant truncation of the inner edge of the accretion disk at  $R_{in} = 12 \pm 1 r_g$ , larger than the ISCO radius for any given black hole spin (the ISCO radius depends on the black hole spin,  $R_{ISCO} = 1.235 r_g$  for  $a^* = 0.998$ ,  $R_{ISCO} = 6 r_g$

for  $a^* = 0$ , and  $R_{\text{ISCO}} = \sim 9 r_g$  for  $a^* = -0.998$ ; Bardeen et al.; Thorne, 1972; 1974). The disk inclination determined by the reflection method is driven by the relativistic Doppler shift of iron line, which is sensitive to the blue wing of the line profile (e.g., Brenneman & Reynolds, 2006). The inclination of the inner accretion disk is measured to be  $29 \pm 1^\circ$ , which agrees well with the value obtained in the disk dominant state from the `refbhb` model. The iron abundance measured by the `relxilllp` model is consistent with the solar value,  $A_{\text{Fe}} = 1.0_{-0.1}^{+0.3}$ , which is also in agreement with the value of elemental abundances fixed in the `refbhb` model. We note that certain systematic uncertainties could be introduced when fitting the spectra with different reflection models (e.g., see the discussion in Middleton et al., 2016), but the good agreement we find in  $i$  and  $A_{\text{Fe}}$  determined by the `refbhb` and `relxilllp` reflection models indicates such uncertainties are probably minimal here.

In addition, we find a reflection fraction of  $R_{\text{ref}} = 0.49$  for the power-law dominant state, significantly lower when compared with that of other black hole binaries displaying strong reflection features (e.g., Xu et al., 2018b,c; Miller et al., 2018). In the `relxilllp` model, the value is defined as the ratio of the coronal intensity illuminating the disk to that reaching the observer, self-consistently calculated by the model in the lamp-post geometry (Dauser et al., 2016). Leaving the reflection fraction as a free parameter does not cause any significant change to the fit, indicating that a truncated accretion disk is indeed required by the shape of broad iron profile. The low reflection fraction is consistent with the relative weakness of the broad iron line in the power-law dominant state, which is a natural outcome from the scenario where the accretion disk is truncated, as X-ray photons would be lost in the gap between the black hole and the inner edge of the truncated accretion disk, without being reprocessed by the optically-thick accretion disk.

#### 7.4 Discussion

We have performed detailed modeling of the reflection spectra of the new black hole binary candidate MAXI J1631–479 during its 2018–2019 outburst, which displays clear variation in the Fe  $K\alpha$  emission line profile between the two epochs observed by *NuSTAR*. The inclination of the inner part of accretion disk is measured to be low in MAXI J1631–479 ( $i \approx 29^\circ$ , closer to being face-on than edge-on). Therefore, we probably have a relatively clear view of the inner regions around the black hole without being blocked by e.g., a geometrically-thick accretion disk. Detailed modeling of the reflection spectra suggests that the variation of the broad iron line

profile is caused by a change in the radius of the inner edge of the optically thick accretion disk,  $R_{\text{in}}$ , from  $<1.9 r_g$  to  $12 \pm 1 r_g$ , which consistently explains the changes in the iron line width and strength (see constraints of the inclination and the inner disk radius in Figure 7.6).

Assuming that the small inner disk radius measured during the first epoch is associated with the ISCO radius of the black hole, we can get an estimate of the spin of the black hole of  $a^* > 0.94$ , close to the maximum value. The high spin measured indicates that the central compact object in MAXI J1631–479 is likely a black hole instead of a neutron star. In accreting neutron stars, the inner edge of accretion disk is observed to be truncated at a typically larger radius of  $\sim 6\text{--}15 r_g$ , due to either the magnetic field of the neutron star or the existence of a solid stellar surface (e.g., Cackett et al., 2010; Ludlam et al., 2017, 2019). During the second epoch, however, the inner radius measured via the reflection method becomes significantly larger, which suggests a change in the accretion mode in MAXI J1631–479: the innermost part of the optically-thick accretion disk is replaced by an optically-thin accretion flow, which is unable to produce clear reflection features inside of the disk truncation radius.

#### 7.4.1 The Iron Line Profile and Disk Truncation

The inner edge of the accretion disk around black holes is predicted to vary with the mass accretion rate, which is inferred from the source luminosity, in units of the Eddington luminosity. The mass accretion rate is thought to influence the disk surface density, and thus determine the transitional inner edge of the accretion disk where the matter becomes thin to Thomson scattering, defined as the “reflection edge” (e.g., Krolik & Hawley, 2002). When the accretion rate is high, the optically-thick accretion disk is predicted to reach down to the ISCO, and its innermost part would be replaced by an optically-thin advection-dominated accretion flow (ADAF) at low accretion rates (e.g., Esin et al., 1997, 1998). Different theoretical models have been proposed to discuss the mechanisms facilitating the disk truncation (e.g., Narayan & Yi, 1995; Honma, 1996; Meyer et al., 2000; Yuan & Narayan, 2004). However, what triggers disc truncation in accreting black hole systems and the typical disk truncation radius is still debated.

From observations, the outburst of a black hole binary is considered ideal to explore the relationship between the accretion disk inner disk radius and the accretion rate, as its X-ray luminosity varies by several orders of magnitude during a typical

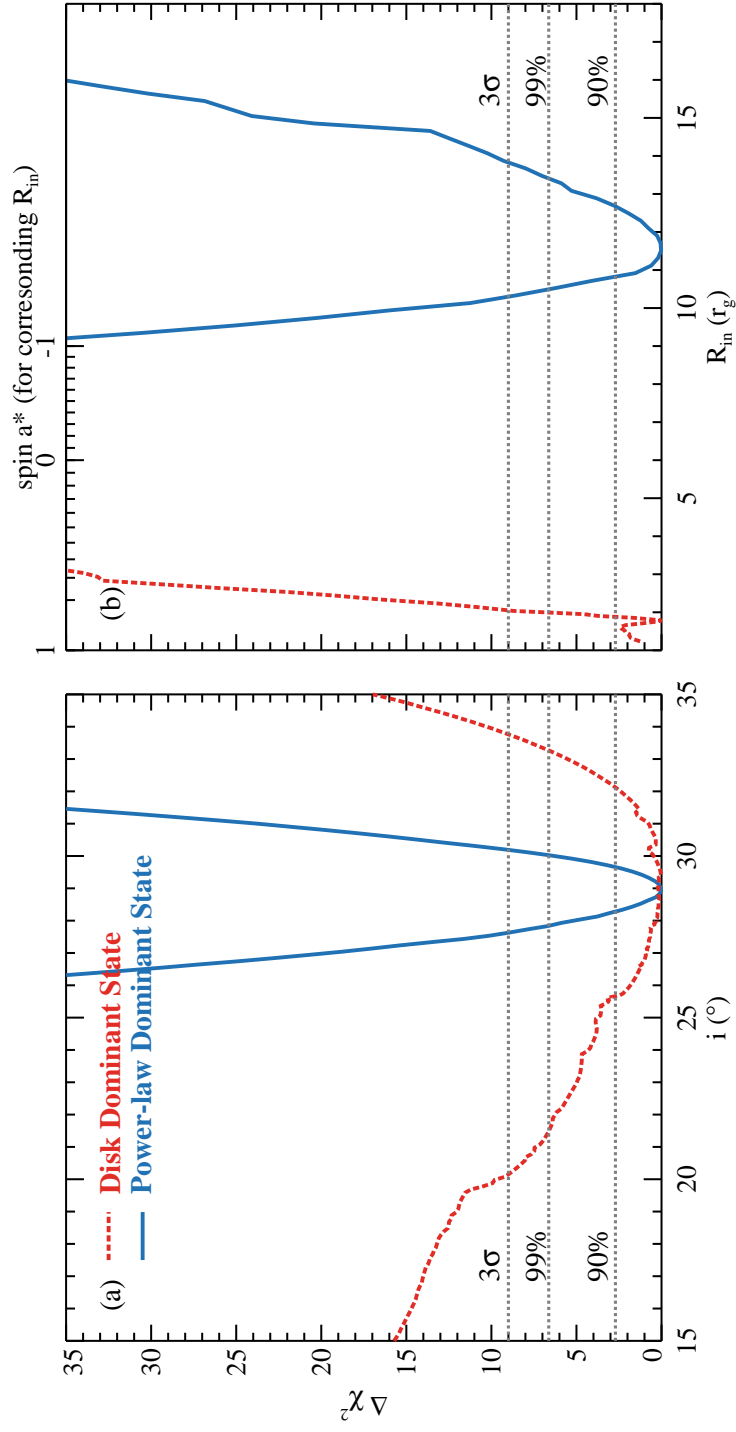


Figure 7.6:  $\Delta\chi^2$  plots for the black hole spin parameter  $a^*$  and inner accretion disk radius  $R_{\text{in}}$ . The constraints for the disk dominant state and power-law dominant state are marked in red dashed and blue solid lines. The horizontal lines indicate the 90%, 99%, and  $3\sigma$  confidence levels for one parameter of interest.

outburst. Recently, there have been numerous observational campaigns of black hole X-ray binaries aiming to use the reflection method to track the evolution of the inner accretion disk radius (e.g., Fürst et al., 2015; Walton et al., 2016, 2017; Xu et al., 2017; García et al., 2019; Kara et al., 2019; Buisson et al., 2019). However, in most cases, the change in the inner disk radius measured at multiple epochs is only marginally significant, and can often be considered as consistent within errors. The best cases regarding variations in the Fe  $K\alpha$  line profile are the narrow lines detected in the very low states of GX 339–4 (Tomsick et al., 2009) and V404 Cygni (Motta et al., 2017), given that relativistically broadened lines are known to be present in their high states (e.g., Parker et al., 2016; Walton et al., 2017). We note that in the previous cases the Fe  $K\alpha$  lines are sufficiently narrow and symmetric that they do not require general relativity effects to explain, signaling a line emission region at a large distance of  $\gtrsim 10^2\text{--}10^3 r_g$ . As proposed in Motta et al. (2017), it is possible that they arise from reprocessing by distant obscuring material, making them an analogue to obscured AGNs. Thus it is debated whether they constrain the inner edge of the accretion disk. The possibility of the existence of two reflection zones (inner accretion disk and distant reprocessing material) is also supported by the narrow core found on top of the broad Fe  $K\alpha$  emission line profile in several black hole binaries (e.g., Walton et al., 2017; Miller et al., 2018; Tomsick et al., 2018; Xu et al., 2018b,c). In general, high S/N detections of a relativistically broadened Fe  $K\alpha$  emission line changing in line width, which could be used as a strong evidence for a variable inner accretion disk radius in a black hole X-ray binary, are still lacking.

In this work, we obtained high S/N *NuSTAR* spectra of the new black hole binary candidate MAXI J1631–479 revealing a broad Fe  $K\alpha$  emission line variable in line width and strength. Spectral modeling suggests a change in the inner disk radius from  $R_{\text{in}} < 1.9 r_g$  to  $R_{\text{in}} = 12 \pm 1 r_g$  between the two epochs observed by *NuSTAR*, despite the small variance in the bolometric luminosity<sup>4</sup> of the source at  $L_{\text{bol}} \sim (1.3 \times 10^{39} - 1.9 \times 10^{39}) \times (D/8 \text{ kpc})^2 \text{ erg s}^{-1}$ . The Eddington rate at the time of the observations is uncertain, as both the black hole mass and distance are currently unknown. Assuming a typical source distance of 8 kpc and black hole mass of  $10 M_{\odot}$ , we estimate the Eddington rate of  $L/L_{\text{Edd}} \sim (100\% - 150\%) \times (10 M_{\odot}/M) \times (D/8 \text{ kpc})^2$ . Our spectral analysis of MAXI J1631–479 indicates that it is possible for the accretion disk to become significantly truncated at this high accretion rate. In addition, the results suggest that in the case of MAXI J1631–479, the change in

---

<sup>4</sup>The bolometric luminosity is estimated from the absorption corrected flux in 0.1–100 keV from the best-fit spectral models.

the accretion mode between the two epochs is not driven by a variation in the global accretion rate of the system.

At high accretion rates, it is predicted that disk truncation could be triggered by thermal instabilities due to the dominance of radiation pressure in the inner accretion disk (e.g., Takeuchi & Mineshige, 1998; Gu & Lu, 2000; Lu et al., 2004). Observational evidence for temporal disappearance of the innermost part of the accretion disk, believed to be associated with the Lightman & Eardley (1974) instability, has been found in the black hole X-ray binary GRS 1915+105 (e.g., Belloni et al., 1997b) and V404 Cygni (Walton et al., 2017), which are known to be accreting close to the Eddington limit. In the case of GRS 1915+105, the disappearance and follow up replenishment of the inner accretion disk has been reported to be associated with the formation of relativistic expanding clouds and jet ejections (e.g., Pooley & Fender, 1997; Mirabel et al., 1998).

#### **7.4.2 The Spectral Continuum**

Based on the shape of the spectral continuum, the spectral state during the second epoch is similar to the very high/steep power-law state reported in some black hole X-ray binaries, when the luminosity is high and the spectrum is dominated by a steep power-law component (e.g., Remillard & McClintock, 2006; Belloni & Motta, 2016). There is evidence that the inner accretion disk in black hole X-ray binaries is sometimes truncated at the very high state. During the very high state, the constant disk emission area inferred from the relation between observed temperature and disc luminosity breaks down (e.g., Kubota & Done, 2004; McClintock & Remillard, 2006). Detailed modeling of the thermal disk component, taking into account the coupled energetics of the disk and corona, also reveals that the inner disk radius in the very high state is larger than the location of the ISCO (e.g., Kubota & Done, 2004; Done & Kubota, 2006; Tamura et al., 2012). By modeling the disk reflection spectra, we have measured a significantly truncated disk in MAXI J1631–479 during the second epoch, supporting this interpretation of the disk structure in the very high state based on previous studies of the thermal disk component. However, because the distance and black hole mass of MAXI J1631–479 are currently unknown, we are unable to obtain an accurate measurement of the inner disk radius via modeling the thermal disk component and directly compare that with the value obtained from the reflection method.

For an approximate estimation, we tried fitting the spectra with the model, TBabs \*simpl\*diskbb, only aiming to describe the shape of the spectral continuum without self-consistently modeling the reflection features. We use the `simpl` convolution model (Steiner et al., 2009b) to account for the effect that a fraction of the input disk seed photons are redistributed by Comptonization into a power-law component (e.g., Nakahira et al., 2018; Shidatsu et al., 2019). We only model the disk dominant state spectra, as the simplified Comptonization model, `simpl`, is not applicable to the power-law dominant state based on the model assumptions (Steiner et al., 2009a). In order to reveal the intrinsic temperature and luminosity of the thermal disk component during the power-law dominant state, more complicated calculations may be required depending on the disk-corona geometry (e.g., Kubota & Done, 2004; Done & Kubota, 2006; Gierliński et al., 2008). The spectral fit yields  $kT_{\text{in}} \sim 1.0$  keV,  $N_{\text{diskbb}} \sim 4000$  for the disk dominant state. Based on the definition of the normalization parameter of `diskbb`,  $N_{\text{diskbb}}$ , and assuming a spectral hardening factor of  $f = 1.7$  (Shimura & Takahara, 1995)<sup>5</sup>, we estimate the inner disk radius to be  $\sim 10 \times (10 M_{\odot}/M) \times (D/8 \text{ kpc}) r_g$ . We note that there are several possible uncertain factors regarding the thermal disk modeling here. It has been proposed that the spectral hardening factor is likely to be variable (e.g., Merloni et al., 2000; Salvesen et al., 2013; Davis & El-Abd, 2019). Also, at high accretion rates, thermal disk emission deviates from that of an idealized thin accretion disk, which makes the inner disk radius inferred by a thin-disk model problematic at high luminosities (e.g., McClintock & Remillard, 2006; Straub et al., 2011).

It is also interesting to consider how the reflection component corresponds to changes of the spectral continuum. Statistical studies of the reflection component in AGNs reveal that disk reflection tends to be less variable than the illuminating continuum (e.g., Miniutti et al., 2003; Miller, 2007; Parker et al., 2014). From our observations of MAXI J1631–479, we find that the reflection component stays constant across short time intervals (between OBS1 PART I and II, and between OBS2 and OBS3), the variation of the corona emission has only a negligible effect on the shape of the broad iron line. Significant variation in the reflection spectra occurs at the time of state transition, which arises from dynamical changes in the disk structure. However, considering the fact that in several black hole X-ray binaries, previous studies show that the broad iron line remains relatively unchanged in different spectral

---

<sup>5</sup> $R_{\text{in, km}} = f^2 D_{10 \text{ kpc}} \sqrt{N_{\text{diskbb}} / \cos i}$ , where  $R_{\text{in}}$  is the inner disc radius in km,  $f$  is the spectral hardening factor,  $D_{10 \text{ kpc}}$  is the distance to the source in units of 10 kpc,  $N_{\text{diskbb}}$  is the normalization of the `diskbb` model, and  $i$  is the inner disc inclination. We assume a disk inclination angle of  $i = 30^\circ$  for MAXI J1631–479 when estimating  $R_{\text{in}}$ .

states (e.g., Reis et al., 2008; Walton et al., 2012; Parker et al., 2015). It is possible that the significant change in the shape of the broad iron line we find in MAXI J1631–479 is a peculiar case.

### 7.4.3 Fast Disk Wind with a Narrow Opening Angle

Disk winds are believed to be ubiquitous in X-ray binaries and important to the accretion process, that might trigger instabilities in the accretion flow (Begelman et al., 1983) and even lead to accretion state changes (Shields et al., 1986). Disk wind launched in X-ray binaries is generally known to have an equatorial geometry, flowing radially at small angles above the accretion disk. Among LMXBs, blueshifted ionized absorption lines in the X-ray spectrum signaling outflowing material are preferentially found in systems viewed close to edge-on (e.g., Ponti et al., 2012; Díaz Trigo & Boirin, 2016), the majority being “dippers” with an inclination estimate of  $60^\circ - 80^\circ$  (Frank et al., 1987).

From the *NuSTAR* observations of MAXI J1631–479, we find a blueshifted ionized absorption feature in the Fe K band in the disk dominant state, which disappears later during the power-law dominant state. The transient nature indicates that MAXI J1631–479 is most likely to be a LMXB. Therefore, the absorption feature found in MAXI J1631–479 probably arises from disk wind rather than the stellar wind from a massive companion star. It is uncommon for strong disk wind features to be detected in a low-inclination black hole binary. We note that the detection of blueshifted ionized iron absorption feature in MAXI J1631–479 (with the disk inclination angle of  $i \approx 29^\circ$ , close to face-on) implies that the disk wind observed in MAXI J1631–479 is collimated to be nearly perpendicular to the disk, or has a narrow opening angle assuming a conical geometry. The presence of disk wind supports that MAXI J1631–479 is accreting at a high accretion rate at the time of our *NuSTAR* observations. The disappearance of absorption features at the second epoch might be caused by a geometric change of the wind due to the state transition, or over-ionization of the outflowing material due to increased hard X-ray illumination from the central engine (e.g., Miller et al., 2006b; Ueda et al., 2010; Díaz Trigo et al., 2014). It supports a change in the accretion mode between the two epochs.

In addition, we note that the disk wind velocity we find from the best-fit results is very high,  $v_{\text{out}} = 0.067^{+0.001}_{-0.004} c$  ( $20100^{+300}_{-1200} \text{ km s}^{-1}$ ), significantly exceeding the typical range for disk winds detected in black hole X-ray binaries (e.g., King et al., 2013; Shidatsu et al., 2013; Díaz Trigo & Boirin, 2016). This velocity is comparable

to some of the most extreme cases that have been reported in black hole X-ray binaries (King et al., 2012; Chiang et al., 2012; Xu et al., 2018c; Miller et al., 2019), and might be an analogue to the ultra-fast outflows (UFOs) detected in a number of AGNs (e.g., Tombesi et al., 2010, 2013; Nardini et al., 2015).

## 7.5 Conclusion

In this work, we report strong and variable relativistic disk reflection features in the new black hole binary candidate MAXI J1631–479 detected by *NuSTAR*. Significant difference is found in the strength and the red wing of the broad iron line observed at two epochs, which caught the source in the disk dominant and the power-law dominant state. The iron line flux in the disk dominant state is unusually high when compared with the flux of the weak power-law component, and the iron line flux is not correlated with the strength of the coronal emission. These suggest that the reprocessing of high energy disk photons plays an important role in shaping the disk reflection spectra we observe in the disk dominant state.

By fitting the *NuSTAR* spectra with self-consistent reflection models, the change in the line profile can be explained by an increase in the inner radius of the optically thick accretion disk: the inner edge of the accretion disk extends down to the ISCO in the disk dominant state and becomes truncated at a larger radius during the power-law dominant state. We discuss the possible physical mechanism (local disk instabilities) that could trigger disk truncation without a significant change in the luminosity/accretion rate. In addition, the results indicate that the central object in MAXI J1631–479 is a rapidly spinning black hole with a spin parameter of  $a^* > 0.94$ , and the accretion disk is viewed at a low inclination angle of  $i = 29^\circ \pm 1^\circ$ . This is also an uncommon case that a disk wind feature is detected in a black hole X-ray binary viewed close to face-on, where the disk wind is found to be extremely fast for a black hole X-ray binary.

## Acknowledgments

We thank the referee for constructive comments that improved the paper. D.J.W. acknowledges support from an STFC Ernest Rutherford fellowship. J.A.G. acknowledges support from NASA grant NNX17AJ65G and from the Alexander von Humboldt Foundation. J.H. acknowledges support from an appointment to the NASA Postdoctoral Program at the Goddard Space Flight Center, administered by the USRA through a contract with NASA. M.L.P. is supported by European Space Agency (ESA) Research Fellowship. This work was supported under NASA con-

tract No. NNG08FD60C and made use of data from the *NuSTAR* mission, a project led by the California Institute of Technology, managed by the Jet Propulsion Laboratory, and funded by the National Aeronautics and Space Administration. We thank the *NuSTAR* Operations, Software, and Calibration teams for support with the execution and analysis of these observations. This research has made use of the *NuSTAR* Data Analysis Software (NuSTARDAS), jointly developed by the ASI Science Data Center (ASDC, Italy) and the California Institute of Technology (USA). This research has also made use of MAXI data provided by RIKEN, JAXA, and the MAXI team.

EVIDENCE FOR DISK TRUNCATION AT LOW ACCRETION  
STATES OF THE BLACK HOLE BINARY MAXI J1820+070  
OBSERVED BY *NUSTAR* AND *XMM-NEWTON*

Xu Y., Harrison F. A., Tomsick J. A., Hare J. et al. (2020). “Evidence for Disk Truncation at Low Accretion States of the Black Hole Binary MAXI J1820+070 Observed by *NuSTAR* and *XMM-Newton*.” *The Astrophysical Journal*, 893(1): 42. DOI: 10.3847/1538-4357/ab7cdb.

**Abstract**

We present results from *NuSTAR* and *XMM-Newton* observations of the new black hole X-ray binary MAXI J1820+070 at low accretion rates (below 1% of the Eddington luminosity). We detect a narrow Fe  $K\alpha$  emission line, in contrast to the broad and asymmetric Fe  $K\alpha$  line profiles commonly present in black hole binaries at high accretion rates. The narrow line, with weak relativistic broadening, indicates that the Fe  $K\alpha$  line is produced at a large disk radius. Fitting with disk reflection models assuming standard disk emissivity finds a large disk truncation radius (a few tens to a few hundreds of gravitational radii, depending on the disk inclination). In addition, we detect a quasi-periodic oscillation (QPO) varying in frequency between  $11.6 \pm 0.2$  mHz and  $2.8 \pm 0.1$  mHz. The very low QPO frequencies suggest a large size for the optically-thin Comptonization region according to the Lense-Thirring precession model, supporting that the accretion disk recedes from the ISCO and is replaced by advection-dominated accretion flow at low accretion rates. We also discuss the possibility of an alternative accretion geometry that the narrow Fe  $K\alpha$  line is produced by a lamppost corona with a large height illuminating the disk.

**Keywords:** accretion – black hole physics – X-ray binary stars – X-ray transient sources

### 8.1 Introduction

Low-mass black hole X-ray binaries contain stellar-remnant black holes accreting from donor stars with a mass of  $<1 M_{\odot}$  that transfer mass by Roche lobe overflow. Most known Galactic black hole X-ray binaries are low-mass X-ray binaries

(LMXBs) and are discovered as transients. These systems exhibit recurrent outbursts on year to decade time scales, during which their flux increases by several orders of magnitude in the optical and X-ray bands (e.g., Corral-Santana et al., 2016). During a typical outburst, lasting for a few months, a black hole binary transitions between different X-ray spectral states, and displays distinct X-ray spectral and timing properties (see Remillard & McClintock, 2006, for a review).

MAXI J1820+070 (=ASASSN-18ey) is a new transient black hole X-ray binary discovered in 2018. The outburst was first reported in optical by the All-Sky Automated Survey for SuperNovae on UT 2018 March 06.58 (ASAS-SN; Tucker et al., 2018), and subsequently in the X-ray band by MAXI a week later (Kawamuro et al., 2018). The source reached a peak X-ray luminosity (2–20 keV) of about 2 Crab, becoming one of the brightest X-ray nova discovered. Its outburst was well covered by multi-wavelength observations from the radio to the gamma-ray band (e.g., Bright et al., 2018; Shidatsu et al., 2019; Paice et al., 2019; Hoang et al., 2019). The distance of MAXI J1820+070 is estimated as  $5.1 \pm 2.7$  kpc or  $4.4 \pm 2.4$  kpc (Atri et al., 2020), and  $3.46^{+2.18}_{-1.03}$  kpc (Gandhi et al., 2019) based on different distance priors from the *Gaia* DR2 parallax (Gaia Collaboration et al., 2018). From radio parallax, the distance is measured to be  $2.96 \pm 0.03$  kpc (Atri et al., 2020). MAXI J1820+070 is recently dynamically confirmed as a black hole binary (BHB) accreting from a K3-5 type donor star with a 0.68 day orbit, and the mass estimate of the central black hole is  $7\text{--}8 M_{\odot}$  (Torres et al., 2019). Due to its high X-ray flux, MAXI J1820+070 is an ideal new target for the study of the inner accretion flow properties around black holes via X-ray spectral and timing analyses. X-ray timing analysis of *NICER* observations provides clues about the evolution in the coronal geometry (Kara et al., 2019). *NuSTAR* observations of MAXI J1820+070 during the bright phases of the hard state display relativistic disk reflection features, including a broad Fe  $K\alpha$  line that is nearly invariant in the line profile over multiple observations at different fluxes. Detailed modeling of the reflection spectra reveals that the inner edge of the accretion disk remains stable at about 5 gravitational radii, which indicates that the central black hole is likely to have a low spin (Bharali et al., 2019; Buisson et al., 2019). In addition, a low-frequency QPO varying in frequency is detected in MAXI J1820+070 in both optical and X-ray bands (e.g., Yu et al., 2018; Buisson et al., 2019).

Black hole accretion is generally studied in two regimes, cold accretion flows of optically-thick material at high mass accretion rates; and optically-thin hot accre-

tion flows at low accretion rates. The latter is thought to contain an advection-dominated accretion flow (ADAF and its variants, see Yuan & Narayan, 2014 for a review). The ADAF model explains the hard X-ray emission from black holes accreting at low accretion rates, e.g., BHBs in quiescence and low/hard states, low luminosity AGNs (LLAGNs), and also Sgr A\*. In BHBs, the accretion geometry is deduced to be in the form of an optically-thick accretion disk at large disk radii, which evaporates and is replaced by ADAF close to the black hole (e.g., Esin et al., 1997). The transitional radius, or the truncation radius of the optically-thick accretion disk, is predicted to increase with decreasing accretion rate (e.g., Meyer et al., 2000; Taam et al., 2012).

Observationally, the inner radius of the accretion disk in BHBs can be measured by modeling the strength and temperature of the thermal disk emission component (Zhang et al., 1997), or modeling the profile of Fe  $K\alpha$  emission line that originates from reflection of hard X-ray photons from the corona by the accretion disk (Fabian et al., 1989). The line profile becomes broad and asymmetric, with an extended red wing originating from the vicinity of the black hole due to combinational effects of Doppler shift, relativistic beaming and gravitational redshift (see Miller, 2007, for a review). Recent observations of several bright BHBs by *NuSTAR* reveal clearly broad Fe  $K\alpha$  lines, indicating that the accretion disk extends all the way down to the ISCO in the bright hard state (BHS) (e.g., Miller et al., 2015b; Xu et al., 2018b,c; Buisson et al., 2019). In the low hard state (LHS), the detection of a narrow Fe  $K\alpha$  line, the evidence for disk truncation, is usually hindered by the faintness of the targets, the weakness of the reflection features, and the limited instrumental spectral resolution. So far, narrow Fe  $K\alpha$  emission has only been convincingly detected in the BHB candidate from a long *Suzaku* observation taken in 2008 (Tomsick et al., 2009).

## 8.2 Observation and Data Reduction

We triggered *NuSTAR* (Harrison et al., 2013) and *XMM-Newton* (Jansen et al., 2001) observations of MAXI J1820+070 during the second rebrightening period after the end of its 2018 main outburst (Xu et al., 2019). During this rebrightening period, the source stayed in the LHS at a low accretion rate (below 1% of the Eddington limit), but reached an X-ray flux level high enough to enable the detection of the Fe  $K\alpha$  emission line.

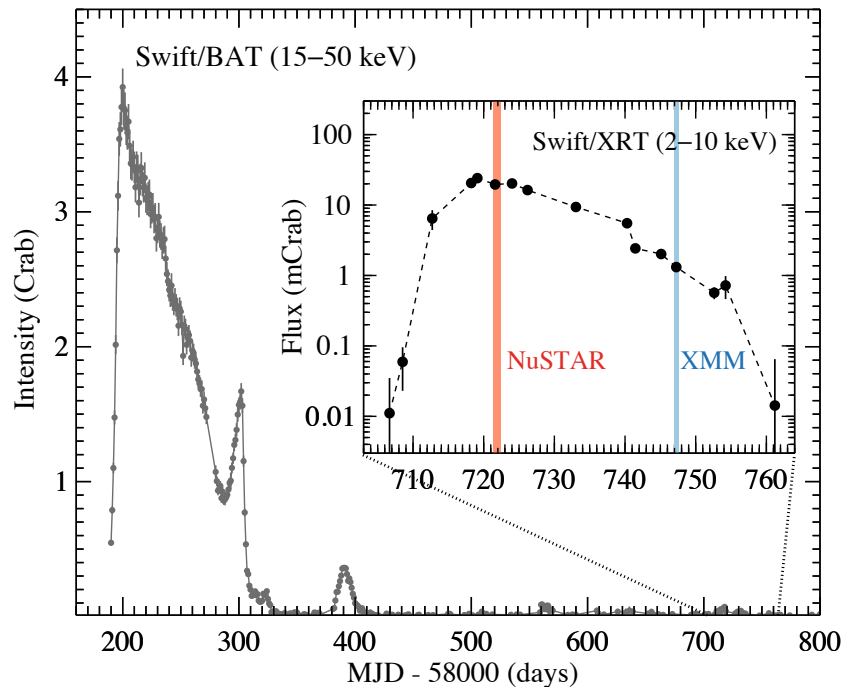


Figure 8.1: Long-term *Swift*/BAT monitoring light curve of the outburst of MAXI J1820+070. The BAT count rate is divided by the Crab count rate. The insert is the X-ray flux of MAXI J1820+070 measured by *Swift*/XRT close to the rebrightening period. The shaded areas mark the duration of the *NuSTAR* and *XMM-Newton* observations analyzed in this work.

We show the time of the *NuSTAR* and *XMM-Newton* observations in the *Swift*/BAT (Krimm et al., 2013) and XRT (Burrows et al., 2005) monitoring light curves of MAXI J1820+070 (see Figure 8.1). The *Swift*/BAT light curve was obtained from the *Swift*/BAT Hard X-ray Transient Monitor<sup>1</sup> (Krimm et al., 2013). We reduced the *Swift*/XRT data using `xrtpipeline` v.0.13.5 with CALDB v20190910. We extracted source spectra from a circular region with a radius of 60'', and the background was extracted from an annulus with inner and outer radii of 160'' and 300''. The X-ray flux in 2–10 keV measured by XRT was estimated by fitting the spectra in the energy range of 0.3–10 keV with an absorbed power-law model.

### 8.2.1 NuSTAR

*NuSTAR* observed MAXI J1820+070 on Aug 26, 2019 starting from UT 07:16:09 (ObsID: 90501337002). We reduced the data using NuSTARDAS pipeline v.1.8.0 and CALDB v20191008. The source spectra were extracted from a circular region with the radius of 180'' from the two focal plane modules (FPMA and FPMB).

<sup>1</sup><https://swift.gsfc.nasa.gov/results/transients/>

Corresponding background spectra were extracted using polygonal regions from source-free areas. We also extracted spectra from mode 6 data to maximize the available exposure time following the method outlined in Walton et al. (2016). The resulting exposure times are 48.6 ks and 48.4 ks for FPMA and FPMB, respectively. We coadded the FPMA and FPMB spectra using the `addspec` tool in HEASOFT. The *NuSTAR* spectra were grouped to have a signal-to-noise ratio (S/N) of at least 10 per bin. We applied barycenter corrections to the event files, transferring the photon arrival times to the barycenter of the solar system using JPL Planetary Ephemeris DE-200, and extracted source light curve from the same region as the energy spectra.

### 8.2.2 XMM-Newton

The *XMM-Newton* observation of MAXI J1820+070 (ObsID: 0851181301) started on September 20, 2019 from UT 22:45:46. Data reduction is performed using the *XMM-Newton* Science Analysis System v17.0.0 following standard procedures. EPIC-MOS1, MOS2, and EPIC-pn operated in the timing mode, but EPIC-MOS1 experienced full scientific buffer during the whole observation. EPIC-pn (Strüder et al., 2001) is the prime instrument we use due to its large effective area in the Fe K band. The net exposure time of EPIC-pn is 56 ks after filtering out periods of high background flaring activity. The data is free from pile-up effects at a mean count rate of  $\sim 20$  cts  $s^{-1}$ . We selected events with pattern  $\leq 4$  (singles and doubles) and quality flag = 0. The source spectrum and light curve were extracted from the columns of  $27 \leq \text{RAWX} \leq 47$ , and the corresponding background was extracted from  $58 \leq \text{RAWX} \leq 60$ . We used `rmfgen` and `arfgen` to generate the redistribution matrix files and ancillary response files. We grouped the EPIC-pn spectrum to have a minimum S/N of 10 for spectral modeling. The collected source light curve was barycenter corrected using the `barycen` tool, and corrected for instrumental effects by `epiclccorr`.

### 8.3 Spectral Analysis

In this work, we perform all spectral modeling in XSPEC v12.10.1f (Arnaud, 1996). We use the cross-sections from Verner et al. (1996) and abundances from Wilms et al. (2000) in the TBabs neutral absorption model. All uncertainties are reported at the 90% confidence level unless otherwise clarified. We fit *NuSTAR* spectra from 3.5–79 keV, and *XMM-Newton* EPIC-pn spectrum from 0.6–10 keV.

We first model the *NuSTAR* (=EPOCH 1) and *XMM-Newton* (=EPOCH 2) spectra with an absorbed power-law model, `TBabs*powerlaw`, in XSPEC. The *NuSTAR* and *XMM-Newton* observations were taken in two epochs separated by 25 days, thus we fit the spectra individually with no linked parameters. We freeze the absorption column density,  $N_{\text{H}}$ , at zero when modeling the *NuSTAR* spectra, as the small amount of absorption towards MAXI J1820+070 does not affect energies above 3 keV.

The absorbed power-law model leaves systematic residuals, with a reduced chi-squared of  $\chi^2/\nu_{\text{EPOCH1}} = 1557.1/941 = 1.65$  and  $\chi^2/\nu_{\text{EPOCH2}} = 1248.3/1127 = 1.11$ . Reflection features are evident in the spectral residuals (see Figure 8.2, panel (b) and (e)): an Fe  $K\alpha$  emission line is clearly detected by both *NuSTAR* and *XMM-Newton* centered around 6.4–6.5 keV, and a Compton reflection hump is evident in the *NuSTAR* spectra peaking around 30 keV. The prominent Compton reflection hump confirms that the Fe  $K\alpha$  line originates from reflection by cold optically-thick gas (e.g., Lightman & White, 1988). Accounting for the Fe  $K\alpha$  line with a Gaussian model improves the fit by  $\Delta\chi^2 = 384$  for the *NuSTAR* spectrum, and  $\Delta\chi^2 = 88$  for *XMM-Newton*. The best-fit Gaussian model indicates that the Fe  $K\alpha$  line is narrow, with a line width of  $\sigma_{\text{EPOCH1}} = 0.29^{+0.05}_{-0.04}$  keV measured by *NuSTAR* and  $\sigma_{\text{EPOCH2}} = 0.24^{+0.09}_{-0.06}$  keV measured by *XMM-Newton*, and equivalent width (EW) is constrained to be  $64 \pm 7$  eV and  $98^{+20}_{-21}$  eV (see Table 8.1 for details). The line width and EW are significantly smaller than those measured with *XMM-Newton* EPIC-pn during the BHS ( $\sigma_{\text{BHS}} \approx 0.9$  keV and  $EW_{\text{BHS}} \approx 270 \pm 30$  eV; Kajava et al., 2019). The narrow and symmetric line profile we observe here indicates weak relativistic effects, which is direct evidence for the Fe  $K\alpha$  line being produced far from the central black hole.

In order to physically model the reflection features, and to get a constraint of the disk truncation radius, we fit the spectra with the `relxill` relativistic disk reflection model (`relxill` v1.3.3, Dauser et al.; García et al., 2014; 2014). We fix the disk emissivity indices,  $q_{\text{in,out}}$  at 3, the value expected for the outer part of a Shakura & Sunyaev disk (Laor, 1991; Dauser et al., 2013). This is a reasonable assumption, considering that the reflection features are produced at a large distance from the black hole. The emissivity indices cannot be constrained if left free. We fix the black hole spin,  $a^*$ , at the default value of 0.998. This parameter is irrelevant here as the inner disk is truncated outside of the ISCO. The outer disk radius,  $R_{\text{out}}$ , is fixed at the maximum value of the model at  $1000 r_{\text{g}}$  ( $r_{\text{g}} \equiv GM/c^2$  is the gravitational radius).

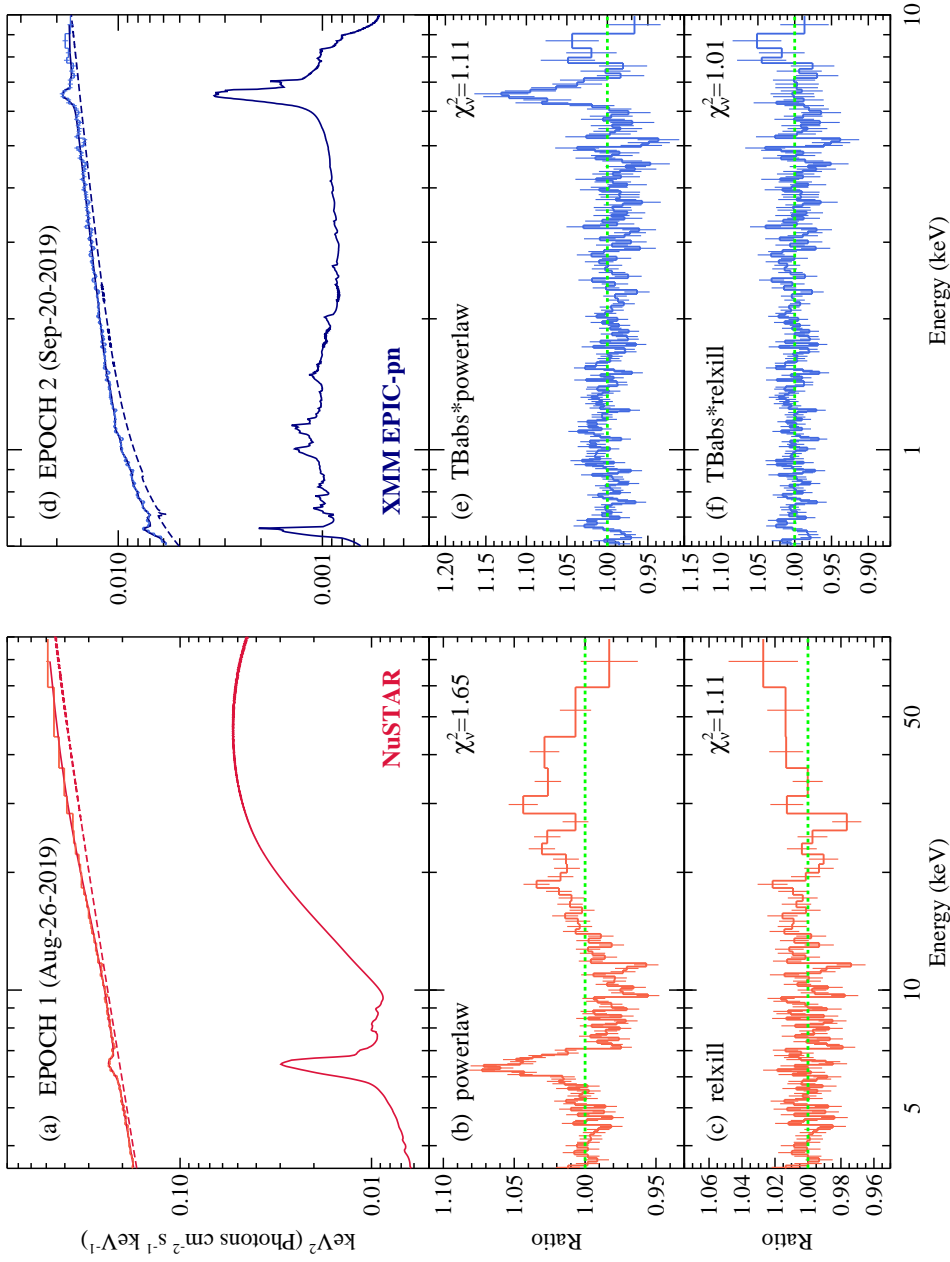


Figure 8.2: *NuSTAR* and *XMM-Newton* spectra of the MAXI J1820+070 in the LHS. Top: *NuSTAR* (EPOCH 1, left) and *XMM-Newton* (EPOCH 2, right) spectra of the MAXI J1820+070 in the LHS, unfolded with the best-fit model. The coronal emission directly observed and the disk reflection component are plotted in dashed and solid lines, respectively. Middle and bottom: data/model spectral residuals. The spectra are rebinned for display clarity. The dips in the *NuSTAR* spectrum at about 11 keV and 26 keV and the excess in the *XMM-Newton* EPIC-pn spectrum around 8 keV are calibration related.

Table 8.1: Energy Spectral Parameters of MAXI J1820+070 in the LHS

Parameter	EPOCH 1	EPOCH 2
Fe $K\alpha$ line modeled with Gaussian: TBabs*(powerlaw+gauss)		
$N_{\text{H}}$ ( $\times 10^{21}$ cm $^{-2}$ )	...	$0.93 \pm 0.03$
$E_{\text{Fe}}$ (keV)	$6.37 \pm 0.04$	$6.54 \pm 0.06$
$\sigma_{\text{Fe}}$ (keV)	$0.29^{+0.05}_{-0.04}$	$0.24^{+0.09}_{-0.06}$
$\text{EW}_{\text{Fe}}$ (eV)	$64 \pm 7$	$98^{+20}_{-21}$
$\Gamma$	$1.667 \pm 0.006$	$1.799 \pm 0.006$
$\chi^2/\nu$	1173.4/939=1.25	1160.3/1124=1.03
Best-fit model: TBabs*relxill		
$N_{\text{H}}$ ( $\times 10^{21}$ cm $^{-2}$ )	...	$1.03 \pm 0.04$
$q$	$3^f$	$3^f$
$\Gamma$	$1.660^{+0.008}_{-0.007}$	$1.765 \pm 0.008$
$E_{\text{cut}}$ (keV)	$> 697$	$> 328$
$i$ ( $^\circ$ )	$< 20$	$< 39$
$R_{\text{in}}$ ( $r_{\text{g}}$ )	$27^{+10}_{-6}$	$> 38$
$\log(\xi)$ ( $\log$ [erg cm s $^{-1}$ ])	$2.99^{+0.02}_{-0.17}$	$3.08 \pm 0.06$
$A_{\text{Fe}}$ (solar)	$3.0^{+0.6}_{-0.5}$	$6 \pm 2$
$R_{\text{ref}}$	$0.060^{+0.005}_{-0.007}$	$0.06 \pm 0.01$
$\chi^2/\nu$	1033.8/936=1.10	1135.4/1121=1.01
$F_{2-10 \text{ keV}}$ (erg cm $^{-2}$ s $^{-1}$ )	$5.0 \times 10^{-10}$	$3.9 \times 10^{-11}$
$L_{0.1-100 \text{ keV}}$ (erg s $^{-1}$ )	$2.6 \times 10^{36}$	$1.9 \times 10^{35}$
$L_{\text{Edd}}$ (%)	0.25	0.018

Fixed parameters are marked with the superscript  $f$ . In this work, we adopt the distance estimate of 3 kpc and black hole mass estimate of  $8 M_{\odot}$  when calculating the source luminosity and Eddington ratio of MAXI J1820+070.

As the majority of the X-ray flux comes from the inner part of the accretion disk, the spectral modeling is not sensitive to  $R_{\text{out}}$ . The `relxill` model includes a coronal illuminating continuum in the shape of a power-law with an exponential cutoff at high energies, parameterized by the power-law index,  $\Gamma$ , and the high energy cutoff,  $E_{\text{cut}}$ . Other free model parameters are the inner disk radius,  $R_{\text{in}}$ , the disk inclination,  $i$ , the ionization parameter,  $\xi$ , the iron abundance,  $A_{\text{Fe}}$ , and the reflection fraction,  $R_{\text{ref}}$ .

The model, `TBabs*relxill` in XSPEC notation, describes the data well, leaving no systematic structures in the residuals with  $\chi^2/\nu_{\text{EPOCH1}} = 1033.8/936 = 1.10$  and

$\chi^2/\nu_{\text{EPOCH2}} = 1135.4/1122 = 1.01$  (see Figure 8.2(c) and (f)). We measure a low absorption column density,  $N_{\text{H}} = (1.03 \pm 0.04) \times 10^{21} \text{ cm}^{-2}$  with *XMM-Newton*, consistent with the value obtained early-on during the outburst (Shidatsu et al., 2019; Kajava et al., 2019). The spectral continuum is well described by a power-law with a hard photon-index of  $\Gamma \approx 1.6\text{--}1.8$ , with no prominent high energy cutoff required (see Table 8.1 for best-fit parameters). The observed flux of MAXI J1820+070 in 2–10 keV decreased from  $5.0 \times 10^{-10} \text{ erg cm}^{-2} \text{ s}^{-1}$  to  $3.9 \times 10^{-11} \text{ erg cm}^{-2} \text{ s}^{-1}$  between EPOCH 1 and EPOCH 2, corresponding to a change in Eddington ratio of 0.35% to 0.026%. Adding an extra thermal disk component modeled by `diskbb` does not improve the fit, implying that thermal emission from the accretion disk is either too weak to be detected, or the disk is sufficiently cool that the peak of the disk blackbody distribution moves below the *XMM-Newton* band.

The fitting results indicate that the disk is moderately ionized, with an ionization parameter of  $\log(\xi) \approx 3$ . We measure the truncation radius of the optically-thick accretion disk to be  $R_{\text{in, EPOCH1}} = 27_{-6}^{+10} r_{\text{g}}$ , and  $R_{\text{in, EPOCH2}} > 38 r_{\text{g}}$ . Based on the definition of the ionization parameter<sup>2</sup>, we estimate the density of the accretion disk,  $n$ , at the radius where the Fe K line is generated, decreases from  $\sim 10^{18} \text{ cm}^{-3}$  to  $\sim 10^{16} \text{ cm}^{-3}$  from EPOCH 1 to EPOCH 2. The best fit prefers a low inclination angle of the accretion disk, and only upper limits are obtained:  $i_{\text{EPOCH1}} < 20^\circ$  and  $i_{\text{EPOCH2}} < 39^\circ$ . This is expected given the presence of a narrow Fe  $K\alpha$  line, as line broadening caused by relativistic effects would become less apparent when the disk is viewed close to face-on (Laor, 1991).  $R_{\text{in}}$  and  $i$  are degenerate, as they are both related to the width of the Fe  $K\alpha$  line. Without a more complicated line profile like the broad and asymmetric lines detected during the BHS, the two parameters cannot be uniquely constrained. To investigate the correlation between  $R_{\text{in}}$  and  $i$ , we plot the  $\Delta\chi^2$  contour in Figure 6.3. As shown in panel (b), similar to the case of GX 339–4 discussed in Tomsick et al. (2009), the model tends to prefer a larger inner disk radius with increasing disk inclination. Therefore, we note that by letting both  $R_{\text{in}}$  and  $i$  vary freely, we are quoting a conservatively small value for the disk truncation radius.

In addition, the best fit leads to a super-solar iron abundance, similar to that found in the BHS (Bharali et al., 2019; Buisson et al., 2019). It is currently uncertain whether the high iron abundance, frequently found when performing spectral modeling with ionized disk reflection models, represents the true elemental abundance in the ac-

<sup>2</sup> $\xi$  is defined as  $\xi = L_{\text{x}}/(nr^2)$ , where  $L_{\text{x}}$  is the X-ray luminosity,  $r$  is the distance between the gas and the X-ray source, and  $n$  is the gas density (hydrogen nucleus density).

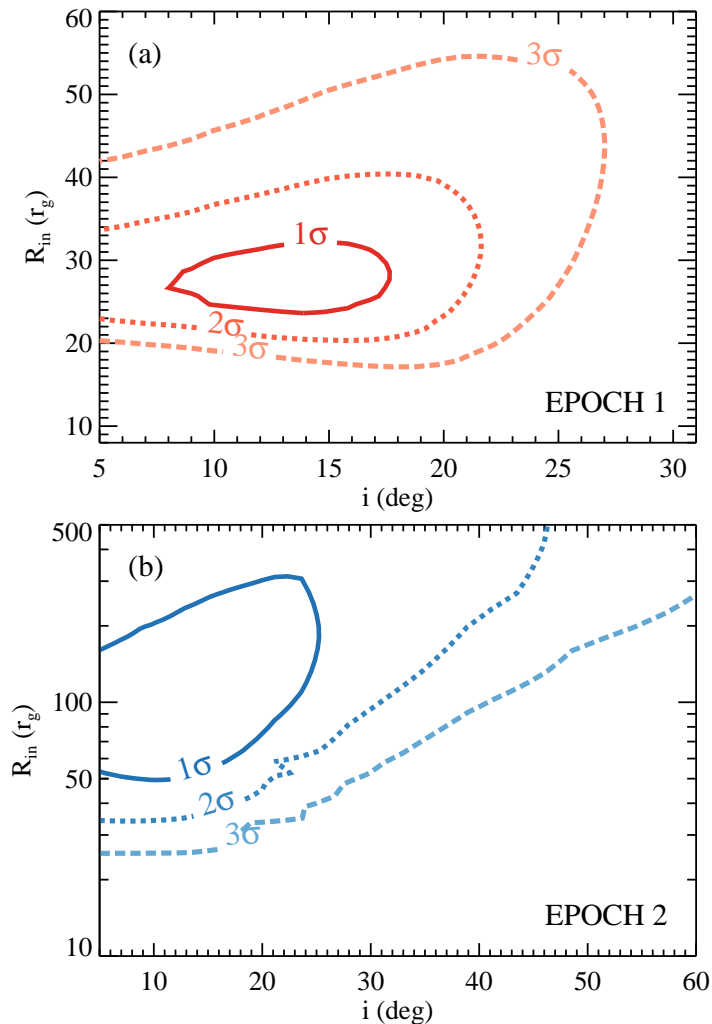


Figure 8.3: Confidence contours of the inner disk radius,  $R_{\text{in}}$ , and the disk inclination,  $i$ .  $1\sigma$ ,  $2\sigma$ , and  $3\sigma$  corresponds to  $\Delta\chi^2$  of 1, 4, and 9, respectively.

cretion disk, or is an overestimation resulting from physical processes overlooked in the calculation of the reflection models. There is evidence that this issue might be mitigated by using reflection models assuming high disk density (e.g., Tomsick et al., 2018; Jiang et al., 2019). We note that the iron abundance is known to be mostly related to the line strength rather than the line width, thus it is unlikely to have a significant effect on the estimate of the disk truncation radius here.

The best-fit reflection fraction is  $R_{\text{ref}} \approx 0.06$ , significantly lower than that measured in the BHS of BHBs, which often requires a reflection fraction greater than unity. This reflection fraction in the BHS is believed to be enhanced by strong light-bending effects near the black hole (e.g., Miniutti et al., 2004; Reis et al., 2013; Xu et al., 2018b,c). The reflection fraction parameter in the `relxill` model is defined

as the ratio of the coronal intensity illuminating the disk to that reaching the observer. The extremely low value we find here in the LHS of MAXI J1820+070 indicates that the solid angle extended by the reflector is small, which is consistent with the scenario that the inner accretion disk is significantly truncated.

#### 8.4 Timing Analysis

We produced the power spectral density (PSD) from the *NuSTAR* (EPOCH 1) and *XMM-Newton* EPIC-pn (EPOCH 2) light curves, in the energy band of 3–79 keV and 0.6–10 keV. The *NuSTAR* light curves of FPMA and FPMB are added using the `lcmath` tool in XRONOS. We produce the PSD from light curves with the time bins of 0.5 s, averaged in intervals of  $2^{13}$  bins. The PSD is calculated in the rms normalization using `powspec`, with white noise subtracted. The *NuSTAR* and *XMM-Newton* PSD is geometrically rebinned by a factor of 1.03 and 1.05, respectively, to reach nearly equally spaced frequency bins in logarithmic scale. We fit the PSD in XSPEC with a multi-Lorentzian model using a unity response file: several zero-centered broad Lorentzians for the band-limited noise continuum, one narrow Lorentzian for the QPO, and one for its possible sub-harmonic.

As shown in Figure 8.4, we find a QPO in the *NuSTAR* and *XMM-Newton* PSD at the frequency of  $\nu_{\text{EPOCH1}} = 11.6 \pm 0.2$  mHz and  $\nu_{\text{EPOCH2}} = 2.8 \pm 0.1$  mHz, detected at  $5.3\sigma$  and  $3.2\sigma$  via the F-test. The QPO has rms variability of  $13 \pm 1\%$  and  $11 \pm 3\%$  in EPOCH 1 and EPOCH 2, respectively. The QPO is detected in the mHz range, lower than the typical frequency range of low-frequency QPOs found in BHBs (0.1–30 Hz). But the shape of the noise continuum and the fact that QPO is located close to the low-frequency break are consistent with type-C QPOs commonly found in BHBs (Belloni & Motta, 2016). The PSD is similar to that detected in MAXI J1820+070 during the BHS (Buisson et al., 2019), only with the QPO and the low-frequency break extending to even lower frequencies in the LHS.

#### 8.5 Discussion and Conclusion

We detect a narrow Fe  $K\alpha$  emission line with high S/N from *NuSTAR* and *XMM-Newton* observations of the black hole X-ray binary MAXI J1820+070 during the second rebrightening period after its 2018 main outburst. The X-ray spectral and timing properties indicate that the source was in the LHS during the time of the observations. Spectral modeling reveals a very low absorption column density, combined with the moderate ionization state of the reflection material, confirming that the Fe  $K\alpha$  line is produced from reflection by the accretion disk rather than that by

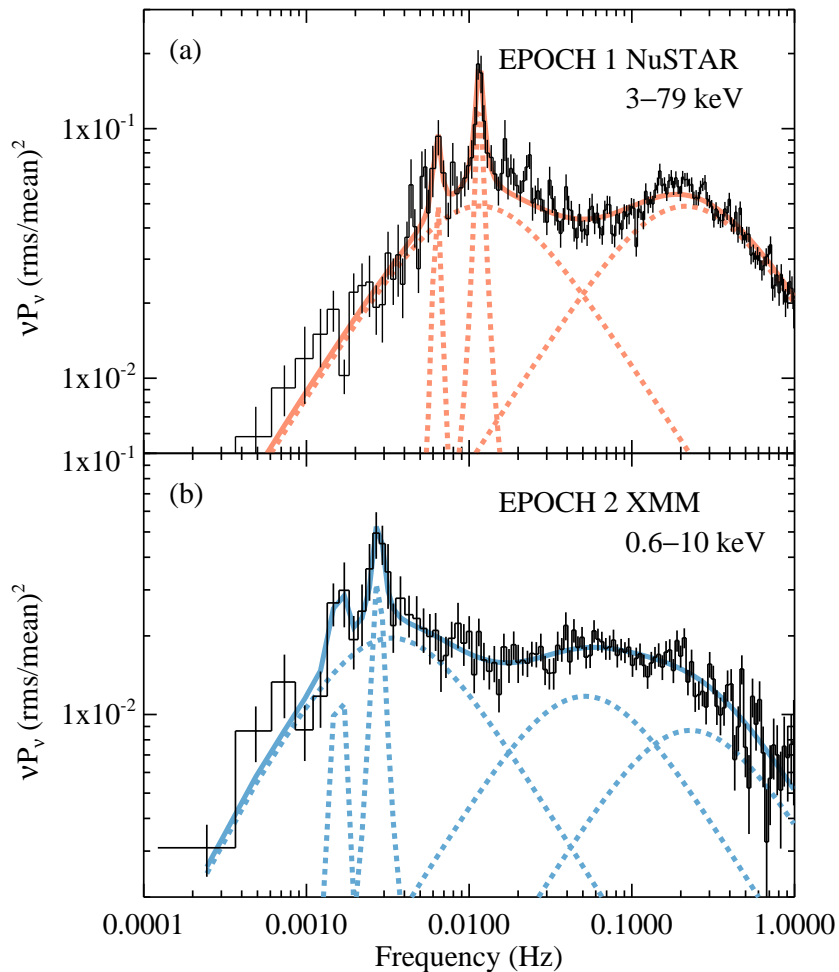


Figure 8.4: *NuSTAR* and *XMM-Newton* PSD of MAXI J1820+070 in the LHS. The best-fit models and their individual Lorentzian components are marked in solid and dashed lines.

torus-like Compton thick obscuring material commonly found in AGNs (Hickox & Alexander, 2018) and in the BHB V404 Cygni (Motta et al., 2017). The line is visibly narrow and lacks significant relativistic broadening, in contrast to the broad line profile observed during the BHS (see Figure 8.4(a) for a comparison of the line profile<sup>3</sup>), providing direct evidence for significant truncation of the inner accretion disk at low accretion rates in a BHB.

There are disparities in the literature about the estimate of the disk inclination in MAXI J1820+070. X-ray dips were observed during early phases of the outburst (Kajava et al., 2019), and a sharp increase in the  $H\alpha$  emission line EW was reported

<sup>3</sup>We choose the representative Fe  $K\alpha$  line profile of MAXI J1820+070 in the BHS from the *NuSTAR* observation on March 21, 2018 (ObsID: 90401309006); detailed analysis of this dataset is published in Buisson et al., 2019.

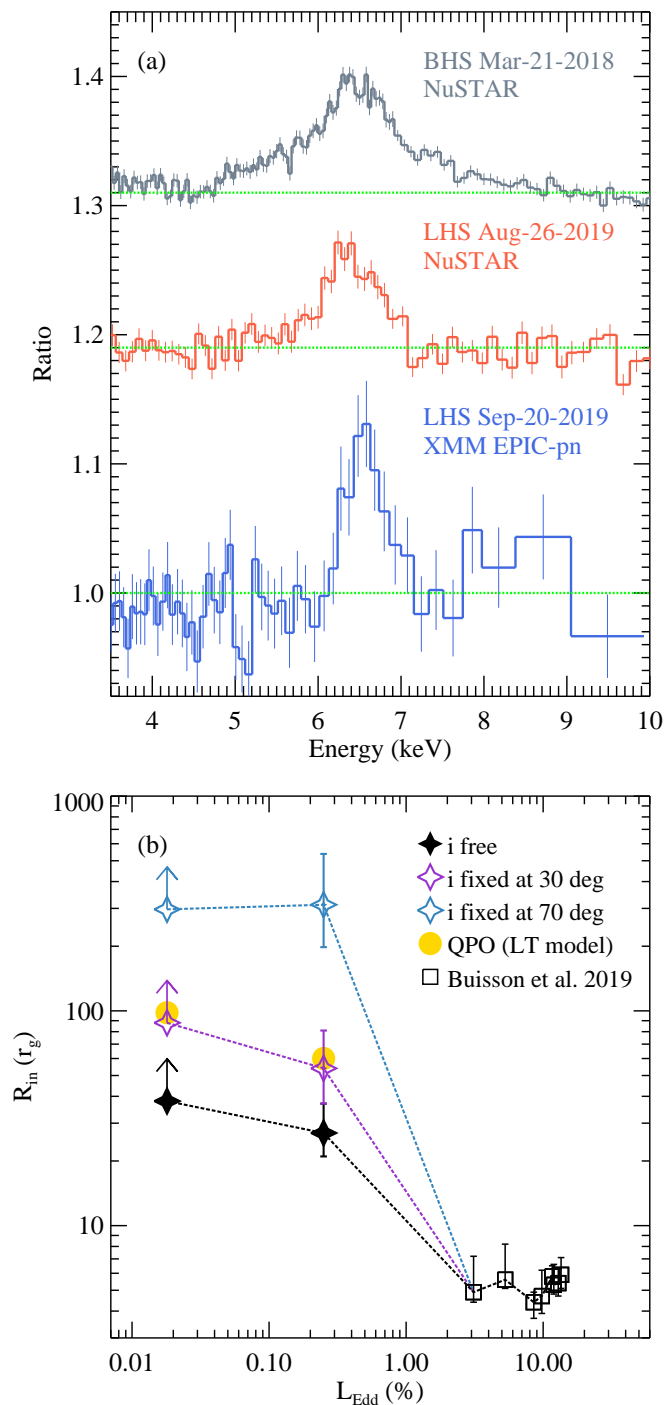


Figure 8.5: The Fe  $K\alpha$  line profile of MAXI J1820+070 observed at different epochs, and the evolution of the inner accretion disk radius with the Eddington ratio measured in MAXI J1820+070. (a) A comparison of the Fe  $K\alpha$  line profile of MAXI J1820+070 observed at different epochs. The Fe  $K\alpha$  becomes visually narrower during the LHS when compared that during the BHS (Buisson et al., 2019). We caution that the apparent difference in the narrow line profile observed by *NuSTAR* and *XMM-Newton* during the LHS is at least partially due to the different energy resolution of the instruments, which is about 400 eV for *NuSTAR* and 100 eV for EPIC-pn on *XMM-Newton*. (b) Evolution of the inner accretion disk radius with the Eddington ratio measured in MAXI J1820+070.

and interpreted as a grazing eclipse of the accretion disk (Torres et al., 2019), suggesting a high inclination of  $i \approx 60^\circ\text{--}80^\circ$  for the outer part of the accretion disk. We note that the inclination of this system is also unlikely to be very low (e.g.,  $<10^\circ$ ) because radial velocity (RV) measurements are significant in amplitude (Torres et al., 2019). The measured jet inclination angle of  $62^\circ \pm 3^\circ$  also indicates that the system is viewed at high inclination (Atri et al., 2020). In contrast, modeling the relativistic reflection spectra during the BHS yields a low inclination of  $i \approx 30^\circ$  for the inner part of the accretion disk (Buisson et al., 2019; Bharali et al., 2019). If both inclination estimates are robust, this implies a strong disk warp of  $\sim 30^\circ\text{--}50^\circ$ . Our spectral fitting of the narrow Fe K $\alpha$  line in the LHS also prefers a very low inclination. However, as discussed above, it is expected for the spectral modeling to bias towards low inclinations in the presence of a narrow line profile. Without strong relativistic distortion effects, the inclination is poorly constrained as only upper limits are obtained. Therefore, we tried fitting the spectra with a fixed disk inclination angle instead, and still assuming a disk emissivity index of  $q = 3$ . This results in a larger disk truncation radius and slightly degraded quality of the fits: when  $i$  is frozen at  $30^\circ$ , we get  $R_{\text{in, EPOCH1}} = 54_{-17}^{+27} r_g$  and  $R_{\text{in, EPOCH2}} > 88 r_g$  with  $\Delta\chi_{\text{EPOCH1}}^2 = 11.7$  and  $\Delta\chi_{\text{EPOCH2}}^2 = 1.6$ ; when  $i$  is fixed at  $70^\circ$ , the constraint on the inner disk radius becomes  $R_{\text{in, EPOCH1}} = 312_{-114}^{+226} r_g$  and  $R_{\text{in, EPOCH2}} > 297 r_g$  with  $\Delta\chi_{\text{EPOCH1}}^2 = 9.9$  and  $\Delta\chi_{\text{EPOCH2}}^2 = 5.2$ . These fits, although statistically slightly worse, leave no clear residuals with physical implications, thus may still be considered acceptable within calibration uncertainties.

There have been a number of observational campaigns aiming at investigating the evolution of the inner disk radius with the accretion rate in BHBs via the reflection method (e.g., Petrucci et al., 2014; Fürst et al., 2016a). However, the results are often poorly constrained or highly model-dependent due to low statistics, especially at low flux states. In this work, we find evidence for a large inner disk radius in MAXI J1820+070 at low accretion rates (a few tens to a few hundreds of  $r_g$ , depending on the disk inclination). Combined with earlier measurements during the BHS by *NuSTAR* (Buisson et al., 2019; Bharali et al., 2019), it suggests that the inner edge of the accretion disk remains stable around the ISCO when the accretion rate is high, and starts to recede from the ISCO as the luminosity drops below  $\sim 1\%$  of the Eddington luminosity (see Figure 8.5(b)). The critical accretion rate when significant disk truncation occurs is consistent with that measured in the well-studied source GX 339–4 via the reflection method (Tomsick et al., 2009), and that found based on the study of several BHBs by systematically modeling their

thermal disk components (Cabanac et al., 2009). In terms of the disk recessing with accretion rate, the results agree well with the theoretical prediction that the inner part of accretion disk becomes replaced by ADAF at low accretion rates ( $<1\%$  of the Eddington limit; Esin et al., 1997), although the model predicts that the optically-thick accretion disk should be truncated in all hard states.

In addition, we detected a QPO at  $\nu_{\text{EPOCH1}} = 11.6 \pm 0.2$  mHz and  $\nu_{\text{EPOCH2}} = 2.8 \pm 0.1$  mHz. The QPO and low-frequency break are found at lower frequencies than those in the BHS. Qualitatively, the longer time scales imply a physically larger size for the hot optically-thin Comptonization regions around black holes, where the QPO is believed to be generated. In the propagating mass accretion rate fluctuations model, the low-frequency break marks the viscous time scale at the outer edge of the Comptonization region (e.g., Ingram & Done, 2010; Ingram & van der Klis, 2013). There have been various theoretical models put forward to explain the low-frequency QPOs in BHBs, but the exact mechanism is still highly uncertain. One of the currently promising models is the Lense-Thirring (LT) precession model. Adopting the simplified assumption that the QPO is caused by the effect of the Lense-Thirring precession of a test particle orbiting a spinning black hole at the disk truncation radius (Motta et al., 2018), we calculate the inner disk radius inferred from the QPO frequencies using the black hole mass of  $8 M_{\odot}$  and the spin of  $a^* = 0.3$ . This leads to the characteristic truncation radius of  $R_{\text{in, EPOCH1}} \sim 60 r_g$  and  $R_{\text{in, EPOCH2}} \sim 100 r_g$ . As a crude estimate, these are broadly similar to the spectral modeling results, in support of the inner accretion disk being significantly truncated in the LHS. During the BHS, however, we note that there is usually disagreement in the measurements from the two methods (e.g., Fürst et al., 2016a; Xu et al., 2017; Buisson et al., 2019); especially, Buisson et al. (2019) find that the QPO frequency and the disc inner radius are not connected. As discussed in Ingram & Done (2011), it is possible that the discrepancy is related to physical complexities currently not well understood and thus not included in the QPO models, or complexities related to intrinsic properties of the corona.

Additional uncertainties in the measurement of the inner disk radius come from the poorly known nature of the corona, which affects the illumination pattern of the disk (Fabian et al., 2014). During the above analysis, we assume the disk emissivity of  $\epsilon \propto r^{-q}$  ( $q = 3$ ), which is expected for a standard accretion disk in the Newtonian regime. An alternative explanation for the narrow Fe K line that does not involve disk truncation is a low disk emissivity index ( $q < 2$ ), so that most of the contri-

bution to the reflection features come from the outer disk. One possible accretion geometry that yields such a low emissivity index is a large lamppost height for the corona, which is believed to be associated with the base of a jet (Dauser et al., 2013). The emissivity expected for a lamppost geometry in Newtonian gravity is  $q \sim 0$  for  $r < h$ , and  $q \sim 3$  for  $r > h$  (Vaughan et al., 2004). The spectra can be equally well fitted by the reflection model assuming a lamppost geometry, `relxilllp`, with a lamppost height of  $h_{\text{EPOCH1}} \sim 40 r_g$  and  $h_{\text{EPOCH2}} > 70 r_g$ , without the need to invoke disk truncation. But the model cannot self-consistently explain the low reflection fraction, unless significant beaming away from the accretion disk is involved. For a reflection fraction of  $\sim 0.1$ , it requires bulk motion with a Lorentz factor of  $\gamma \sim 1.2$  when viewed at the inclination of  $30^\circ$ , and  $\gamma \sim 1.6$  at the inclination of  $60^\circ$  (Beloborodov, 1999). It is uncertain whether strong beaming and the accretion geometry of a compact corona with a large lamppost height above the accretion disk are realistic descriptions of the system. There is evidence that significant beaming is absent in X-ray emissions of BHBs in the LHS (Narayan & McClintock, 2005). Although the case at low accretion rates is less clear, previous successful applications of the lamppost model to X-ray spectra of bright BHBs and AGNs measures a low lamppost height of  $< 10 r_g$ , or a steep disk emissivity profile (Fabian et al., 2015). Thus the physical implications of such a large lamppost height or low emissivity index required by the spectral fitting here are currently unclear and require further investigation. The extended disk-corona model and the lamppost corona model are two competing coronal geometries that have been proposed (Chauvin et al., 2018). The QPO frequency and low-frequency break in the PSD suggest a physically large size for the Comptonization region, consistent with the extended corona and receding accretion disk scenario. The inner disk being truncated at a large radius also naturally explains the non-detection of any thermal disk emission. Disk truncation provides a straightforward and physically reasonable explanation for the narrow Fe  $K\alpha$  line we detected in MAXI J1820+070. However, we note that an alternative accretion geometry of a high lamppost corona cannot be ruled out by our dataset and may also be plausible.

### Acknowledgments

We thank the anonymous referee for helpful comments that improved the paper. We thank Norbert Schartel for approving the *XMM-Newton* DDT observation and the *XMM-Newton* SOC for prompt scheduling of the observation. J.H. acknowledges support from an appointment to the NASA Postdoctoral Program at the Goddard

Space Flight Center, administered by the USRA through a contract with NASA. D.J.W. acknowledges support from an STFC Ernest Rutherford Fellowship. This work was supported under NASA contract No. NNG08FD60C and made use of data from the *NuSTAR* mission, a project led by the California Institute of Technology, managed by the Jet Propulsion Laboratory, and funded by the National Aeronautics and Space Administration. We thank the *NuSTAR* Operations, Software, and Calibration teams for support with the execution and analysis of these observations.

## SUMMARY AND FUTURE PROSPECTS

### 9.1 Summary of Previous Research

In this thesis, I have conducted detailed X-ray spectral and timing analysis of one AGN and several Galactic black hole X-ray binaries. The physical interpretations are concentrated on the following aspects: 1) the black hole accretion geometry at different accretion states (or mass accretion rates); 2) the spin of supermassive and stellar-mass black holes; 3) the physical properties of the various structures around an accreting black hole: the accretion disk, the corona, the disk wind, the jet, and any obscuration materials if present. Due to the appearance of several very bright uncatalogued black hole X-ray transients during the past few years and the new capabilities brought by the recent *NuSTAR* X-ray mission, the data quality exceeds what have been obtained before in the sense that subtle atomic features on top of the X-ray spectral continua have been systematically detected with good S/N, especially the detailed shapes (and variations) of the broad Fe  $K\alpha$  line profile, the Compton reflection hump, and the high energy power-law cutoff. The clear detection of these observable features present great opportunities for us to gain new insights on the physical process about accretion and the nature of the compact objects. I summarize the main findings from my thesis work and discuss their astrophysics implications below:

#### *Accretion Geometry*

One of the main goals of modeling the relativistic disk reflection features is to investigate the accretion geometry around black holes at different mass accretion rates and accretion states. It provide a means to measure the location of the inner edge of the optically-thick accretion disk, which is sensitive to the width and red wing of the broad Fe  $K\alpha$  line profile, while the disk inclination is sensitive to the blue wing of the line profile. Therefore the disk inclination and the inner disk radius can be simultaneously constrained, without obvious parameter degeneracy. The reflection features are produced in the surface layers of the accretion disk, therefore they mostly reflect the physical properties of the accretion disk while their connection with the illuminating source (the corona) can be expected to be somewhat more subtle. Based on current observational constraints, we cannot distinguish

among existing theoretical models with different coronal geometries. A very idealized lamppost geometry for the corona with a varying height above the accretion disk seems to be sufficient to describe all the data, but this simplified parameter is mainly used to adjust the emissivity distribution of the accretion disk; its physical meaning may not be straightforward. The safe conclusion based on our findings is merely that in cases where an extremely broadened Fe  $K\alpha$  line is detected, the disk emissivity seems to be quite centralized, which indicates a corona compact in size, consistent with previous findings (e.g., Wilkins & Fabian, 2012).

About the location of the inner accretion disk, we have measured a truncated inner accretion disk in IGR J17091–3624 during the bright hard state (Chapter 3), in MAXI J1631–479 during the steep power-law/intermediate state (Chapter 7), and in MAXI J1820+070 during the low hard state (Chapter 8). On the other hand, we have found a non-truncated inner accretion disk in MAXI J1535–571 (Chapter 4) and Swift J1658.2–4242 (Chapter 5) in their bright hard states, and in MAXI J1631–479 in the soft state (Chapter 7). The differences in the Fe  $K\alpha$  line profiles and line strengths between the two classes are visually evident, with the latter being significantly broader and stronger. We made no attempt to derive the inner disk radius independently with the thermal disk modeling method (Mitsuda et al., 1984; Makishima et al., 1986), which would be driven by the strength and temperature of the thermal disk emission, although disk components under most circumstances were strong enough that we could tightly constrain their basic parameters by only fitting their high energy tails above 3 keV in the *NuSTAR* spectra. Firstly, it is because the non-thermal power-law spectral component is not negligible in any of the cases that we studied. The power-law component is believed to arise from Comptonization of the thermal disk photons, therefore the intrinsic strength and shape of the thermal disk component are highly uncertain when the power-law component is strong. Secondly, it is because most of these newly discovered black hole transients currently lack mass and distance measurements, and it is therefore questionable whether their disk spectra should be modeled with the standard thin disk model given that their mass accretion rates are largely unknown. The advantage of the reflection modeling method is that it is not restricted by the above limitations, thus uncertainties are considerably smaller.

From a comprehensive view of my studies of these individual sources, the results that we currently have regarding the inner radius of the optically-thick accretion disk with accretion states is at least partially *inconsistent* with the theoretical pre-

dictions illustrated in Figure 1.8. Especially for the bright phases of the hard state or the very high state, the measurements indicate that the inner accretion disk is truncated in some cases, while it is not in others. Therefore, the degree of the extension of the inner edge of the accretion disk is not necessarily related to the obvious relative strength of the thermal and non-thermal components in the X-ray spectrum, which is the main factor used to classify the accretion states, contrary to what has been long believed. This indicates that the optically-thin and optically-thick phases of the accretion flow (Shapiro et al., 1976) are probably not simply transforming into each other at a certain disk radius as predicted in Esin et al. (1997); reality seems to prefer a more complicated scenario of them co-existing with vertical structures, such as an optically-thick accretion disk underneath the corona as outlined in some recent theoretical calculations (e.g., Meyer-Hofmeister et al., 2009). Low-frequency QPOs have been detected both when the inner accretion disk is truncated (Chapter 3) and non-truncated (Chapter 5). QPOs are known to be associated with the non-thermal component in the X-ray spectrum. Therefore, this may also imply that the innermost part of the optically-thick accretion disk and the corona could behave independently at least to some level.

The relationship of inner disk radius with the Eddington ratio of the sample is currently uncertain. Most of newly discovered black hole transients still lack distance and mass measurements, as it is notoriously difficult to determine the distance of Galactic objects especially when heavy extinction along the line of sight is involved. A possible approximate estimation can be given based on the hard and soft state transition luminosity, as state transitions have been believed to occur around a certain critical mass accretion rate (Esin et al., 1997). However, there is now increasing evidence showing that the mass accretion rate during transitions between these two states varies greatly from source to source, or even for the same source during different outbursts. The soft-to-hard transition luminosities are known to have a wide distribution (e.g., Yu & Yan, 2009). Although there is some evidence that hard-to-soft transition luminosities may have smaller variations (Maccarone, 2003), the study is based on a very small sample. Given the uncertainties, I defer accurate descriptions of the accretion flow geometry with the accretion rate to future work, when more reliable distance and mass estimates become available. But considering that at least we have gathered some evidence supporting that the degree of disk truncation is not solely determined by the accretion state, it is likely that the inner disk radius is more closely connected with the mass accretion rate instead, which then raises the question of how the accretion state is related to mass accretion rate

and what fundamentally causes the accretion state changes. It is now known that the accretion state is not a simple function of the mass accretion rate, and the same accretion state can appear in the same object at different luminosities. Even in one outburst, the hard-to-soft state transition usually occurs at a significantly higher flux level than soft-to-hard state transition, the so-called “hysteretic” behavior, which is not well understood but has been proposed to be related to the magnetic fields threaded in the disk and the corona (e.g., Begelman & Armitage, 2014; Begelman et al., 2015). In all, these imply that there is an independent factor, other than the mass accretion rate, that is modulating the variations of the accretion states and the accretion flow geometry in accreting black holes.

In the case of the new black hole binary candidate, Swift J1658.2–4242, we observed a dramatic change in its X-ray flux with a novel combination of variations in X-ray spectral and timing properties (Chapter 6), and more similar events were detected during subsequent observations (e.g., Bogensberger et al., 2020). We have proposed a picture that invokes a change in the accretion geometry (mainly a change in the scale-height of the accretion disk) arising from propagating instabilities triggered at a large disk radius to coherently explain the X-ray spectral, timing, and flux variations observed in this source. We also discuss the possible role of jet activities during this process as routinely done in this area of research, but did not extend much further to prevent over-interpretation of the data. Because by all means, jets observed in these systems are a result of accretion, and thus just by attributing variations in observable properties triggered by accretion instabilities to jet activities would not properly address the question of their origin.

### *Black Hole Spin*

The measurement of the spin parameter of a black hole is of obvious importance as it is one of the two physical parameters that defines a black hole, besides its mass. The black hole spin is believed to have potentially broad influences on the accretion and outflow processes around black holes, and encode information about their formation and evolution channels. For black hole X-ray binaries, it is thought that neither accretion nor angular momentum extraction would significantly modify the black hole mass and spin (King & Kolb, 1999), so the values probably retain close to those at formation. The spin of a black hole is also of particular interest because it has been theoretically predicted to be possible to extract power from the rotational energy of spinning black holes (Penrose & Floyd, 1971); in a more realistic scene, that could power jets by the magnetic fields threading through the black

hole and held onto the black hole by the surrounding disk (Blandford & Znajek, 1977). But there has been arguments favoring that the energy extracted from the black hole in this way would never exceeds that from the inner regions of the accretion disk (Livio et al., 1999). So far, observational evidence for clear connections between the black hole spin and the jet power is generally lacking in both AGNs and black hole X-ray binaries (e.g., Fender et al., 2010; King et al., 2013), and studies claiming that such connection is found are based on very small samples using observations from certain accretion states (Narayan & McClintock, 2012; Steiner et al., 2013).

Using the relativistic disk reflection modeling method, I have measured the black hole spins in the Seyfert 1h Galaxy/ULIRG IRAS 05189–2524 (Chapter 2), the black hole X-ray binaries MAXI J1535–571 (Chapter 4), Swift J1658.2–4242 (Chapter 5), and MAXI J1631–479 (Chapter 7) using *NuSTAR* observations. Such measurements are feasible in these cases because no significant disk truncation is found and the disks are consistent with extending all the way down to the ISCO. The measurements all yield statistically well constrained high spin parameters, close to the maximum value. These add to the relatively short but slowly growing list of stellar-mass and supermassive black holes with existing spin measurements, the majority of which are found to be rapidly spinning (e.g., Miller, 2007; Reynolds, 2020). There are various selection effects that might be involved in these kinds of studies, partially because it is much more difficult to constrain a low than a high spin parameter via modeling the broad Fe  $K\alpha$  line profile, and also essentially we cannot distinguish between a black hole accreting with a slightly truncated disk (inner disk radius within  $9 r_g$ ) and a slowly spinning black hole this way. So in some sense, the measured black hole spin could be viewed as lower limits, depending on whether the assumption of an non-truncated accretion disk is solid.

We note that caution should be taken when comparing black spin measurements from the literature, as in a few cases very different results have been reported for the same source based on different observations. It is mainly because relativistic disk reflection features are generally weak features, thus are approaching the calibration accuracy limits of some instruments (such as *RXTE/PCA*); also photon pile up could be an issue for observations taken with CCD detectors aboard *XMM-Newton* and *Chandra* of bright sources, despite the efforts to mitigate the pile-up distortion effects. In addition to disk reflection modeling, there are other independent ways to measure the spin parameters in black hole X-ray binaries from obser-

vations at electromagnetic wavelengths, via modeling the thermal disk component (e.g., Zhang et al., 1997) or inferring from the QPO frequencies (e.g., Abramowicz & Kluźniak, 2001; Motta et al., 2014). However, the former method is limited to the thermal dominant states and requires prior knowledge of the black mass and distance, which are currently unknown for most of the new black hole transients that we studied, and the latter is model-dependent as the physical origin of QPOs is still highly debated. Therefore, we made no attempt in this thesis to compare measurements using different methods, but it would be expected that no easy consent could be achieved as they suffer from different systematic uncertainties. Yet the majority of rapidly spinning stellar-mass black holes measured in black hole X-ray binaries are still in great contrast with the growing number of black holes with spin estimates from gravitational detectors, most of which are with spins that are significantly lower and masses systematically higher (Abbott et al., 2019, 2020a,b). This implies different formation channels for the stellar-mass black holes in Galactic black hole X-ray binaries and those found in much more distant binary black hole merger events, and thus they are likely to be formed in different galactic environments. The answer to the origin of this discrepancy is still largely unknown, but see some possibilities with relevant references discussed in e.g., Abbott et al. (2020c). The underlying question is intriguing, but in general we do not have much of any further observational information at the current stage.

### *Disk Wind*

While studying the broad Fe  $K\alpha$  line arising from the relativistic disk reflection process, I have also searched for absorption features in the Fe K band and investigated their physical properties, which are believed to be produced by either high-velocity disk wind launched from the vicinity of the black hole or slightly outflowing accretion disk atmosphere. Absorption features have been significantly detected around 7 keV in the black hole X-ray binary Swift J1658.2–4242 during the bright hard state (Chapter 5) and the intermediate state (Chapter 6), and also in MAXI J1631–479 during the soft state (Chapter 7). The blueshifted absorption line ( $EW \sim 25$  eV, comparable in the strength to the strong disk winds detected during soft states in e.g., GRS 1915+105 in Neilsen & Lee, 2009 and 4U 163047 in Díaz Trigo et al., 2014) found in the hard state of Swift J1658.2–4242 is unexpected, because disk winds are thought to be weak or absent during hard states when jets act as the dominant form of outflow. The apparent absorption feature that we observed in MAXI J1631–479 is also interesting if indeed originates from disk winds, as disk winds

are generally believed to be equatorial, and thus it is unusual for such features to be observed in systems viewed at a low inclination angle of  $\sim 30^\circ$ .

Before *NuSTAR*, disk winds have only been detected and studied in a relatively small number of black hole X-ray binaries ( $\sim 10$ , e.g. see Ponti et al., 2012). The generally well accepted trend predicting that disk winds and jets are mutually exclusive and that disk winds are equatorial and have wide opening angles (e.g., Ponti et al., 2012), should still be subject to scrutiny. And I note that the disk wind features that we detected using *NuSTAR* in these new black hole X-ray binaries have already started to display different behaviors, and therefore probably a renewed way is required of how we think about the relationship between the disk wind, the jet, and the accretion state variations around black holes, and also the physical mechanism by which the disk wind is launched from the accretion disk. In addition, we found evidence (marginal detection) for ionized absorption features, indicating the presence of an ultra-fast outflow, in the Seyfert 1h Galaxy/ULIRG IRAS 05189–2524 between 7–8 keV from *NuSTAR* and *XMM-Newton* observations (Chapter 2). Similar features were detected with slightly better statistics in subsequent observations of this source with longer exposure times (Smith et al., 2019). The potential presence of an energetic high-velocity disk wind from the nucleus of this source (and in ULIRGs in general) is important, because it could be responsible for driving the molecular outflow at galactic scales, providing a direct link between the supermassive black holes and the large-scale gas in the galaxy out of which stars form (e.g., Tombesi, 2016). Considering its energy resolution, *NuSTAR* is capable to detect but cannot resolve the narrow absorption line complex caused by disk winds around these accreting black holes, which prevents the simultaneous and confident determination of the ionization state, the intrinsic broadening, and the shift velocity of the outflowing materials. Future observations with X-ray missions like *XRISM* and *Athena*, combining high energy resolution and large effective area, will help confirm whether these absorption-line-like features are indeed caused by outflowing materials, better characterize the detailed physical properties of disk winds, and enable the study of outflowing materials in a larger sample of accreting black hole systems using X-ray spectroscopy.

## 9.2 Future Prospects

For any field of observational astronomy, advances come with developments of new technologies that enhance our abilities to observe the celestial objects. As a large part of this thesis is focused on studying the atomic features in the X-ray spec-

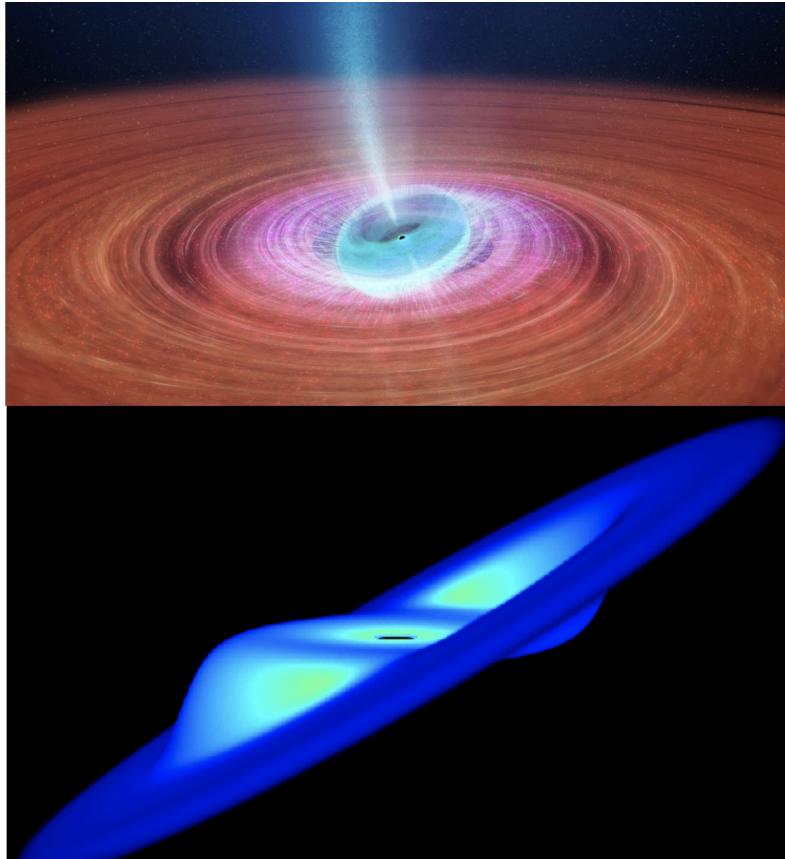


Figure 9.1: Top panel: Wildly wobbling jets observed in V404 Cyg (Miller-Jones et al., 2019), which is thought to be caused by the warped inner part of the accretion disk under frame-dragging effects (image credit: ICRAR). Bottom panel: 3D geometry of a warped accretion disk from particle simulations in Lodato & Price (2010).

tra of accreting black holes (either from the disk reflection process or the ionized absorption by disk winds), in this ending section, I illustrate one promising direction to extend my research with the upcoming X-ray observatory, *XRISM*, expected to be launched next year. The X-ray microcalorimeter aboard *XRISM* combines high effective area with high energy resolution (a factor of a few tens in improvement when compared with the CCD level detector resolution, comparable to the standards of optical spectroscopy), will greatly enhance the scientific potentials of X-ray spectroscopy.

*Probing the Geometry and Dynamics of Warped Disks in Accreting Black Holes Using Disk Reflection X-ray Spectroscopy*

The standard steady thin accretion disk is one common simplification used nowadays in the study of black hole accretion, although more sophisticated disk structures are theoretically predicted to be more realistic descriptions. Warped accretion

disks, where the disk is misaligned with the orbital plane, are believed to exist in a variety of accreting astrophysical systems (see Figure 9.1), including X-ray binaries, AGNs, as well as young stellar objects. Observational evidence for disk warping and precessing have been obtained in several representative systems via different approaches, including the 164-day precession of the jet in the microquasar SS 433 (Margon et al., 1979), the kinematics of water masers detected at subparsec scales in the spiral galaxy NGC 4258 (e.g., Miyoshi et al., 1995), and the super-orbital flux modulations observed in some X-ray binaries, e.g., LMC X-4, Her X-1 (e.g., Priedhorsky & Holt, 1987). In terms of black hole accretion, it is still unclear where the warps occur in the accretion disks, what physical mechanism is driving the disk warping and precessing, and whether or under what conditions the warps are able to reach a steady state. These questions remain to be answered with future observations. Associated with the geometry and stability of disk structures, they have a fundamental influence on the accretion history and evolution of black holes.

Disk warping and precessing have been widely studied by analytic calculations and numerical simulations. The standard Bardeen & Petterson (1975) model attributes the warp to the competition between the Lense-Thirring torque from the central black hole and the viscous angular-momentum transport within the disk. Specifically, several mechanisms have been theoretically proposed that could excite, maintain, and propagate disk warps in accretion disks: self-induced disk warping by radiation pressure (Pringle, 1996), warps driven by irradiation-driven disk winds (Schandl & Meyer, 1994), or magnetic fields in the accretion disk (Lai, 2003). From recent particle simulations of black hole accretion disks, the warps are found to reach a steady state under certain circumstances and the characteristic transition radius of disk orientation is estimated to be at  $\sim 10\text{--}20 r_g$ , where disk emission peaks in the X-ray band. In addition, the warps are thought to modulate the accretion efficiency, and thus are important to the growth of black holes (Nealon et al., 2015).

Accretion phenomena have been widely studied in X-rays in both stellar-mass black holes ( $\sim 5\text{--}30 M_\odot$ ), i.e., black hole X-ray binaries, and supermassive black holes ( $\sim 10^5\text{--}10^{10} M_\odot$ ), i.e., AGNs. Different from AGNs, most black hole X-ray binaries are X-ray transients, which go into recurrent outbursts that cover a broad range of Eddington fractions. The typical time scales associated with these accreting stellar-mass black hole systems are much shorter than those in supermassive black holes, making it easier to observe their accretion state variations. Because

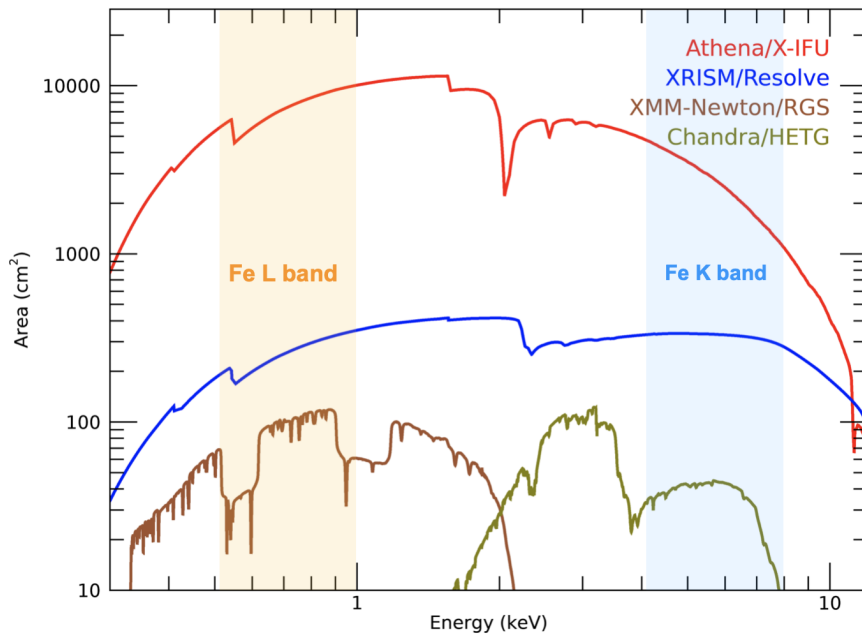


Figure 9.2: The effective areas of high-resolution X-ray spectroscopy instruments aboard currently operating and future X-ray missions; figure from Guainazzi & Tashiro (2018). *XRISM/Resolve* will have almost an order-of-magnitude increase in the effect area over the Fe K band when compared with *Chandra/HETG*.

X-rays are produced deep within the gravitational potential in the accretion disk corona, a few gravitational radii from the central black holes, X-ray spectroscopy provides powerful diagnostic for probing the inner accretion flow properties. Broad Fe  $K\alpha$  emission lines, detected in both AGNs and black hole X-ray binaries, are believed to be generated from reprocessing of the hard X-ray coronal photons by the optically-thick accretion disk in the vicinity of black holes, known as the disk reflection process. These lines with their associated spectral continua are unique and valuable diagnostic tools to uncover the geometry and dynamics of the inner accretion flow around black holes. It would be promising to conduct further research to systematically search for features of warped accretion disks and to study the geometry and dynamics of such warps in AGNs and black hole X-ray binaries, via modeling the disk reflection spectrum, using both CCD and calorimeter resolution X-ray spectra. This kind of study would be mostly driven by fine structures in the broad Fe  $K\alpha$  line profile.

With observations from *XMM-Newton* and *NuSTAR*, relativistic disk reflection features (the broad and asymmetric Fe  $K\alpha$  line centered at 6–7 keV, and the Compton reflection hump peaking at 20–30 keV) have been detected in a number of bright

AGNs (e.g., Nandra et al., 2007; Fabian, 2016), and have also been routinely found in known and new Galactic black hole X-ray binary transients, e.g., see Chapter 3, 4, 5, and 7 in this thesis. Modeling of the broadband X-ray spectra confirms that the observed broad Fe  $K\alpha$  line is caused by reflection by the inner accretion disk around the black hole, rather than a combination of complex absorption effects (Risaliti et al., 2013). In addition, some high S/N reflection spectra reveal secondary features/distinct narrow components on top of the broad Fe  $K\alpha$  line profiles (e.g., Miller et al., 2018, and also see Chapter 4 and 6), whose origin is uncertain. Interesting explanations invoke that the weak and narrow features could arise from relative distant reprocessing of hard X-ray coronal photons by the tilted or warped part of the accretion disk. In general, secondary fine features in the broad Fe  $K\alpha$  line profile may be evidence for more complicated disk geometries, beyond the simplified assumption of an accretion disk being steady and geometrically-thin, such as a warped and precessing disk.

High-resolution X-ray spectroscopy is crucial for resolving the detailed shape of the Fe  $K\alpha$  line profile, maximizing our ability to extract the encoded information regarding the dynamics and geometry of the accretion disk. X-ray grating spectrometers, the High Energy Transmission Grating Spectrometer (HETGS) aboard *Chandra*, and the Reflection Grating Spectrometer (RGS) aboard *XMM-Newton* have demonstrated the potential power of high-resolution X-ray spectroscopy. However, the limited effective areas make them insensitive to the relativistic disk reflection features (e.g., Tzanavaris & Yaqoob, 2018), which result in relatively weak curvatures superimposed on the spectral continuum. The situation will be significantly improved with the high-resolution, large effective area calorimeters of future X-ray missions, the Resolve aboard X-ray Imaging and Spectroscopy Mission (*XRISM*), and the X-IFU aboard Advanced Telescope for High Energy Astrophysics (*Athena*) (see Figure 9.2). *XRISM*, anticipated to be launched in 2022, will soon open some new discovery space of high-resolution X-ray spectroscopy. Combining high energy resolution with an effective area comparable to *NuSTAR* and *XMM-Newton*/EPIC, *XRISM*/Resolve will be good at detecting and resolving the detailed shape of the broad Fe  $K\alpha$  line profile in bright AGNs and black hole X-ray binaries to an unprecedentedly high precision.

Theoretically, disk warping is predicted to leave detectable features in emission lines generated in the accretion disks (e.g., Hartnoll & Blackman, 2000; Fragile et al., 2005), manifesting as multiple horns or broad blue wings in the integrated

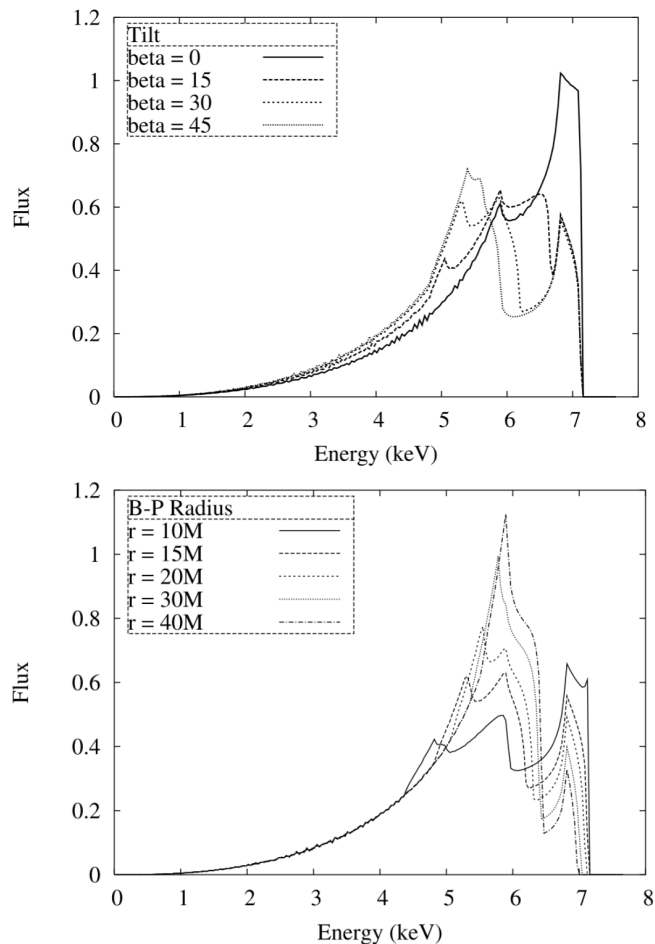


Figure 9.3: Example Fe  $K\alpha$  emission line profiles arising from warped accretion disks, from theoretical calculations in Fragile et al. (2005). The contours indicate the line profiles produced in warped disks with different tilt angles (upper panel) and Bardeen-Petterson transition radii (lower panel).

line profiles (see Figure 9.3). Observationally, studies have been performed in the optical band in AGNs showing broad double-peak  $H\alpha$  emission lines, believed to be produced in the accretion disk, which probe potential warps in the outer parts of the disk (e.g., Strateva et al., 2003; Gezari et al., 2007). Similar investigations with Fe  $K\alpha$  lines in the X-ray band would provide unique views into the inner accretion disk around black holes, where a warped and precessing disk is most likely to be coupled with jet production, and the strong GR effects associated with the disk warping may be responsible for the physical origins of QPOs in black hole X-ray binaries (e.g., Dexter & Fragile, 2011).

Evidence for complicated components in the broad Fe  $K\alpha$  line profile have been found by *NICER* (e.g., Miller et al., 2018) and *NuSTAR* (e.g., see Chapter 4, 5,

and 7), which can be interpreted to originate from the reflected emission and self-shadowing from a warped accretion disk. High-resolution X-ray spectroscopy enabled by *XRISM/Resolve* (resolution  $<10$  eV FWHM) will bring great improvement in resolving the detailed shape and the low-velocity components in the broad Fe  $K\alpha$  line profiles, compared with that achievable with current detectors with CCD-level energy resolution ( $\sim 400$  eV for *NuSTAR* and  $\sim 100$  eV for *XMM-Newton/EPIC-pn*). High spectral resolution is also essential for separating the line profile from narrow absorption/emission lines produced in disk winds to reveal the intrinsic shape of the broad line generated in the accretion disk. By modeling the X-ray disk reflection spectrum, in particular the Fe  $K\alpha$  line profile, it is promising to obtain robust measurements of the key physical parameters about the geometry of a warped disk around black holes, such as the Bardeen-Petterson transition radius and the tilt angle between the inner and outer part of the accretion disk if the warps are to reach a simple steady state, or to test whether the disk is teared into multiple independently precessing rings (e.g., Nixon et al., 2012). There are ongoing efforts to produce self-consistent disk reflection spectral models compatible for the use with the X-ray spectral fitting software XSPEC, which consider warped and misaligned disk geometries around black holes (e.g., Abarr & Krawczynski, 2021). Such models will facilitate the quantitative description and physical interpretation of sophisticated features in the broad Fe  $K\alpha$  line profile.

The time scales associated with stellar-mass black holes permit the study about the stability and dynamics of warped accretion disk in black hole X-ray binaries using multi-epoch observations. Such monitoring campaigns will reveal the typical time scales of disk wobbling, precession, and realignment, and help investigate the physical mechanisms driving the disk warping and precession. It will also be interesting to investigate if and how the disk warping phenomena are related to the nature of transient QPOs, or the appearance of disk wind features. If such association can be established, disk warping features may provide a method to estimate the prevalence of disk winds in accreting black holes, and their overall influence on larger environments via feedback. In addition, for AGNs, it will be interesting to compare system inclinations measured in multi-wavelengths covering different galactic scales, e.g., the inclination inferred from relativistic disk reflection in X-rays, from resolved jets in the radio band, from ionization cones in the narrow line regions observed in the optical band, and the orientation of host galaxies, which may provide a new angle for studying the co-evolution of supermassive black holes and their host galaxies.

It is natural to expect that such disk warps only occur during certain phases over the accreting history of black holes. If future X-ray observations reveal clear spectral signatures of warps in the inner accretion disks in several AGNs, or in just one black hole X-ray binary displaying variations due to precession consistent with theoretical predictions, that should be enough to make the case. Similar investigations could also be conducted in accreting neutron star systems with low magnetic fields, where the accretion disks extend close to the neutron stars. But the relativistic Fe  $K\alpha$  lines observed in these accreting neutron star systems (e.g., Bhattacharyya & Strohmayer, 2007; Cackett et al., 2008; Ludlam et al., 2017) are typically narrower in width and weaker in strength compared to those in black holes, so the corresponding observational signatures might appear less clear if present.

## BIBLIOGRAPHY

- Abarr, Q., & Krawczynski, H. 2021, *ApJ*, 906, 28
- Abbott, B. P., Abbott, R., Abbott, T. D., et al. 2019, *ApJL*, 882, L24
- Abbott, R., Abbott, T. D., Abraham, S., et al. 2020a, *PhRvL*, 125, 101102
- Abbott, R., Abbott, T. D., Abraham, S., et al. 2020b, *ApJL*, 896, L44
- Abbott, R., Abbott, T. D., Abraham, S., et al. 2020c, *ApJL*, 900, L13
- Abramowicz, M. A., & Kluźniak, W. 2001, *A&A*, 374, L19
- Altamirano, D., & Belloni, T. 2012, *ApJL*, 747, L4
- Altamirano, D., Linares, M., van der Klis, M., et al. 2011a, *ATel*, 3225
- Altamirano, D., Belloni, T., Linares, M., et al. 2011b, *ApJL*, 742, L17
- Arévalo, P., & Uttley, P. 2006, *MNRAS*, 367, 801
- Arnaud, K. A. 1996, in *ASP Conf. Ser. 101, Astronomical Data Analysis Software and Systems V*, ed. G. H. Jacoby & J. Barnes (San Francisco, CA: ASP), ed. G. H. Jacoby & J. Barnes, 17
- Atri, P., Miller-Jones, J. C. A., Bahramian, A., et al. 2020, *MNRAS*, 493, L81
- Axelsson, M., & Done, C. 2016, *MNRAS*, 458, 1778
- Axelsson, M., Done, C., & Hjalmarsdotter, L. 2014, *MNRAS*, 438, 657
- Bañados, E., Connor, T., Stern, D., et al. 2018, *ApJL*, 856, L25
- Bachetti, M. 2015, *MaLTPyNT: Quick look timing analysis for NuSTAR data*, *Astrophysics Source Code Library*, ascl:1502.021
- Bachetti, M., Harrison, F. A., Walton, D. J., et al. 2014, *Natur*, 514, 202
- Bachetti, M., Harrison, F. A., Cook, R., et al. 2015, *ApJ*, 800, 109
- Ballantyne, D. R., Ross, R. R., & Fabian, A. C. 2002, *MNRAS*, 336, 867
- Bardeen, J. M., & Petterson, J. A. 1975, *ApJL*, 195, L65
- Bardeen, J. M., Press, W. H., & Teukolsky, S. A. 1972, *ApJ*, 178, 347
- Barr, P., White, N. E., & Page, C. G. 1985, *MNRAS*, 216, 65P
- Barthelmy, S. D., D’Avanzo, P., Deich, A., et al. 2018, *GCN*, 22416

- Basak, R., & Zdziarski, A. A. 2016, *MNRAS*, 458, 2199
- Basak, R., Zdziarski, A. A., Parker, M., & Islam, N. 2017, *MNRAS*, 472, 4220
- Begelman, M. C., & Armitage, P. J. 2014, *ApJL*, 782, L18
- Begelman, M. C., Armitage, P. J., & Reynolds, C. S. 2015, *ApJ*, 809, 118
- Begelman, M. C., McKee, C. F., & Shields, G. A. 1983, *ApJ*, 271, 70
- Bellocchi, E., Arribas, S., Colina, L., & Miralles-Caballero, D. 2013, *A&A*, 557, A59
- Belloni, T., Homan, J., Casella, P., et al. 2005, *A&A*, 440, 207
- Belloni, T., Klein-Wolt, M., Méndez, M., van der Klis, M., & van Paradijs, J. 2000, *A&A*, 355, 271
- Belloni, T., Méndez, M., King, A. R., van der Klis, M., & van Paradijs, J. 1997a, *ApJ*, 488, L109
- Belloni, T., Méndez, M., King, A. R., van der Klis, M., & van Paradijs, J. 1997b, *ApJL*, 479, L145
- Belloni, T., Psaltis, D., & van der Klis, M. 2002, *ApJ*, 572, 392
- Belloni, T., Parolin, I., Del Santo, M., et al. 2006, *MNRAS*, 367, 1113
- Belloni, T. M. 2010, in *States and Transitions in Black Hole Binaries*, ed. T. Belloni (Berlin: Springer), 53
- Belloni, T. M., & Motta, S. E. 2016, in *Astrophysics of Black Holes: From Fundamental Aspects to Latest Developments*, ed. C. Bambi, Vol. 440 (Berlin: Springer), 61
- Beloborodov, A. M. 1999, *ApJL*, 510, L123
- Beri, A., Belloni, T., Vincentelli, F., Gandhi, P., & Altamirano, D. 2018, *ATel*, 11375
- Berti, E., & Volonteri, M. 2008, *ApJ*, 684, 822
- Bharali, P., Chauhan, J., & Boruah, K. 2019, *MNRAS*, 487, 5946
- Bhattacharyya, S., & Strohmayer, T. E. 2007, *ApJL*, 664, L103
- Blandford, R., Meier, D., & Readhead, A. 2019, *ARA&A*, 57, 467
- Blandford, R. D., & Znajek, R. L. 1977, *MNRAS*, 179, 433
- Bogensberger, D., Ponti, G., Jin, C., et al. 2020, *A&A*, 641, A101

- Boissay, R., Ricci, C., & Paltani, S. 2016, *A&A*, 588, A70
- Brenneman, L. W., & Reynolds, C. S. 2006, *ApJ*, 652, 1028
- Bright, J., Fender, R., & Motta, S. 2018, *ATel*, 11420
- Brightman, M., Masini, A., Ballantyne, D. R., et al. 2016, *ApJ*, 826, 93
- Brightman, M., & Nandra, K. 2011, *MNRAS*, 413, 1206
- Brightman, M., Silverman, J. D., Mainieri, V., et al. 2013, *MNRAS*, 433, 2485
- Buisson, D. J. K., Fabian, A. C., Barret, D., et al. 2019, *MNRAS*, 490, 1350
- Burrows, D. N., Hill, J. E., Nousek, J. A., et al. 2005, *SSRv*, 120, 165
- Cabanac, C., Fender, R. P., Dunn, R. J. H., & Körding, E. G. 2009, *MNRAS*, 396, 1415
- Cabanac, C., Henri, G., Petrucci, P. O., et al. 2010, *MNRAS*, 404, 738
- Cackett, E. M., Miller, J. M., Bhattacharyya, S., et al. 2008, *ApJ*, 674, 415
- Cackett, E. M., Miller, J. M., Ballantyne, D. R., et al. 2010, *ApJ*, 720, 205
- Capitanio, F., Del Santo, M., Bozzo, E., et al. 2012, *MNRAS*, 422, 3130
- Casella, P., Belloni, T., Homan, J., & Stella, L. 2004, *A&A*, 426, 587
- Casella, P., Belloni, T., & Stella, L. 2005, *ApJ*, 629, 403
- Chakrabarti, S. K., & Molteni, D. 1993, *ApJ*, 417, 671
- Chauvin, M., Florén, H. G., Friis, M., et al. 2018, *NatAs*, 2, 652
- Chiang, C.-Y., Reis, R. C., Walton, D. J., & Fabian, A. C. 2012, *MNRAS*, 425, 2436
- Church, M. J., & Bałucińska-Church, M. 2004, *MNRAS*, 348, 955
- Corral-Santana, J. M., Casares, J., Muñoz-Darias, T., et al. 2016, *A&A*, 587, A61
- Corral-Santana, J. M., Casares, J., Muñoz-Darias, T., et al. 2013, *Sci*, 339, 1048
- Court, J. M. C., Altamirano, D., Pereyra, M., et al. 2017, *MNRAS*, 468, 4748
- Dasyra, K. M., Tacconi, L. J., Davies, R. I., et al. 2006, *ApJ*, 651, 835
- Dauser, T., García, J., Parker, M. L., Fabian, A. C., & Wilms, J. 2014, *MNRAS*, 444, L100
- Dauser, T., García, J., Walton, D. J., et al. 2016, *A&A*, 590, A76

- Dauser, T., Garcia, J., Wilms, J., et al. 2013, MNRAS, 430, 1694
- Dauser, T., Svoboda, J., Schartel, N., et al. 2012, MNRAS, 422, 1914
- Dauser, T., Wilms, J., Reynolds, C. S., & Brenneman, L. W. 2010, MNRAS, 409, 1534
- Davis, S. W., & El-Abd, S. 2019, ApJ, 874, 23
- Del Santo, M., Malzac, J., Belmont, R., Bouchet, L., & De Cesare, G. 2013, MNRAS, 430, 209
- Dexter, J., & Fragile, P. C. 2011, ApJ, 730, 36
- Di Salvo, T., Done, C., Życki, P. T., Burderi, L., & Robba, N. R. 2001, ApJ, 547, 1024
- Díaz Trigo, M., & Boirin, L. 2016, AN, 337, 368
- Díaz Trigo, M., Migliari, S., Miller-Jones, J. C. A., & Guainazzi, M. 2014, A&A, 571, A76
- Díaz Trigo, M., Parmar, A. N., Boirin, L., Méndez, M., & Kaastra, J. S. 2006, A&A, 445, 179
- Díaz Trigo, M., Parmar, A. N., Boirin, L., et al. 2009, A&A, 493, 145
- Dincer, T. 2017, ATel, 10716
- Done, C., & Diaz Trigo, M. 2010, MNRAS, 407, 2287
- Done, C., Gierliński, M., & Kubota, A. 2007, A&ARv, 15, 1
- Done, C., & Kubota, A. 2006, MNRAS, 371, 1216
- Draine, B. T. 2003, ApJ, 598, 1026
- Eijnden, J. v. d., Ludlam, R. M., Homan, J., et al. 2019, ATel, 12440
- El-Batal, A. M., Miller, J. M., Reynolds, M. T., et al. 2016, ApJL, 826, L12
- Esin, A. A., McClintock, J. E., & Narayan, R. 1997, ApJ, 489, 865
- Esin, A. A., Narayan, R., Cui, W., Grove, J. E., & Zhang, S.-N. 1998, ApJ, 505, 854
- Fabian, A. C. 2012, ARA&A, 50, 455
- Fabian, A. C. 2016, AN, 337, 375
- Fabian, A. C., Iwasawa, K., Reynolds, C. S., & Young, A. J. 2000, PASP, 112, 1145
- Fabian, A. C., Kara, E., Walton, D. J., et al. 2013, MNRAS, 429, 2917

- Fabian, A. C., Lohfink, A., Kara, E., et al. 2015, *MNRAS*, 451, 4375
- Fabian, A. C., Parker, M. L., Wilkins, D. R., et al. 2014, *MNRAS*, 439, 2307
- Fabian, A. C., Rees, M. J., Stella, L., & White, N. E. 1989, *MNRAS*, 238, 729
- Fabian, A. C., & Ross, R. R. 2010, *SSRv*, 157, 167
- Farrell, S. A., Webb, N. A., Barret, D., Godet, O., & Rodrigues, J. M. 2009, *Natur*, 460, 73
- Fender, R., & Belloni, T. 2012, *Sci*, 337, 540
- Fender, R. P., Belloni, T. M., & Gallo, E. 2004, *MNRAS*, 355, 1105
- Fender, R. P., Gallo, E., & Russell, D. 2010, *MNRAS*, 406, 1425
- Fender, R. P., Homan, J., & Belloni, T. M. 2009, *MNRAS*, 396, 1370
- Feruglio, C., Fiore, F., Carniani, S., et al. 2015, *A&A*, 583, A99
- Fragile, P. C., Miller, W. A., & Vandernoot, E. 2005, *ApJ*, 635, 157
- Frank, J., King, A., & Raine, D. J. 2002, *Accretion Power in Astrophysics* (3rd ed.; Cambridge: Cambridge Univ. Press)
- Frank, J., King, A. R., & Lasota, J. P. 1987, *A&A*, 178, 137
- Fürst, F., Nowak, M. A., Tomsick, J. A., et al. 2015, *ApJ*, 808, 122
- Fürst, F., Tomsick, J. A., Yamaoka, K., et al. 2016a, *ApJ*, 832, 115
- Fürst, F., Grinberg, V., Tomsick, J. A., et al. 2016b, *ApJ*, 828, 34
- Gaia Collaboration , Brown, A. G. A., Vallenari, A., et al. 2018, *A&A*, 616, A1
- Galloway, D. K., Munro, M. P., Hartman, J. M., Psaltis, D., & Chakrabarty, D. 2008, *ApJS*, 179, 360
- Gandhi, P., Rao, A., Johnson, M. A. C., Paice, J. A., & Maccarone, T. J. 2019, *MNRAS*, 485, 2642
- Gandhi, P., Dhillon, V. S., Durant, M., et al. 2010, *MNRAS*, 407, 2166
- García, J., Dauser, T., Lohfink, A., et al. 2014, *ApJ*, 782, 76
- García, J., Dauser, T., Reynolds, C. S., et al. 2013, *ApJ*, 768, 146
- García, J., & Kallman, T. R. 2010, *ApJ*, 718, 695
- García, J. A., Dauser, T., Steiner, J. F., et al. 2015a, *ApJL*, 808, L37
- García, J. A., Steiner, J. F., McClintock, J. E., et al. 2015b, *ApJ*, 813, 84

- García, J. A., Tomsick, J. A., Sridhar, N., et al. 2019, *ApJ*, 885, 48
- Gehrels, N., Chincarini, G., Giommi, P., et al. 2004, *ApJ*, 611, 1005
- Gendreau, K., Arzoumanian, Z., Markwardt, T., et al. 2017, *ATel*, 10768
- George, I. M., & Fabian, A. C. 1991, *MNRAS*, 249, 352
- Gezari, S., Halpern, J. P., & Eracleous, M. 2007, *ApJS*, 169, 167
- Gierliński, M., & Done, C. 2004, *MNRAS*, 349, L7
- Gierliński, M., Done, C., & Page, K. 2008, *MNRAS*, 388, 753
- Grebenev, S. A., Mereminskiy, I. A., Prosvetov, A. V., et al. 2018, *ATel*, 11306
- Grinberg, V., Eikmann, W., Kreykenbohm, I., & Wilms, J. 2018, *ATel*, 11318
- Gu, W.-M., & Lu, J.-F. 2000, *ApJL*, 540, L33
- Guainazzi, M., & Tashiro, M. S. 2018, arXiv:1807.06903
- Guilbert, P. W., & Rees, M. J. 1988, *MNRAS*, 233, 475
- Haardt, F., & Maraschi, L. 1991, *ApJ*, 380, L51
- Haardt, F., & Maraschi, L. 1993, *ApJ*, 413, 507
- Halpern, J. P. 1984, *ApJ*, 281, 90
- Harrison, F. A., Craig, W. W., Christensen, F. E., et al. 2013, *ApJ*, 770, 103
- Hartnoll, S. A., & Blackman, E. G. 2000, *MNRAS*, 317, 880
- Hawley, J. F., & Krolik, J. H. 2001, *ApJ*, 548, 348
- Hickox, R. C., & Alexander, D. M. 2018, *ARA&A*, 56, 625
- Hoang, J., Molina, E., Lopez, M., et al. 2019, *Proc. ICRC (Madison, WI)*, 36, 696
- Honma, F. 1996, *PASJ*, 48, 77
- Hopkins, P. F., Hayward, C. C., Narayanan, D., & Hernquist, L. 2012, *MNRAS*, 420, 320
- Hopkins, P. F., Hernquist, L., Cox, T. J., et al. 2006, *ApJS*, 163, 1
- Huang, Y., Qu, J. L., Zhang, S. N., et al. 2018, *ApJ*, 866, 122
- Hynes, R. I., Haswell, C. A., Cui, W., et al. 2003, *MNRAS*, 345, 292
- Ingram, A., & Done, C. 2010, *MNRAS*, 405, 2447
- Ingram, A., & Done, C. 2011, *MNRAS*, 415, 2323

- Ingram, A., Done, C., & Fragile, P. C. 2009, MNRAS, 397, L101
- Ingram, A., & Motta, S. 2014, MNRAS, 444, 2065
- Ingram, A., & Motta, S. 2020, arXiv:2001.08758
- Ingram, A., & van der Klis, M. 2013, MNRAS, 434, 1476
- Ingram, A., & van der Klis, M. 2015, MNRAS, 446, 3516
- Ingram, A., van der Klis, M., Middleton, M., et al. 2016, MNRAS, 461, 1967
- Iwasawa, K., Fabian, A. C., Mushotzky, R. F., et al. 1996, MNRAS, 279, 837
- Iyer, N., Nandi, A., & Mandal, S. 2015, ApJ, 807, 108
- Jansen, F., Lumb, D., Altieri, B., et al. 2001, A&A, 365, L1
- Jiang, J., Fabian, A. C., Wang, J., et al. 2019, MNRAS, 484, 1972
- Joinet, A., Kalemci, E., & Senziani, F. 2008, ApJ, 679, 655
- Kajava, J. J. E., Motta, S. E., Sanna, A., et al. 2019, MNRAS, 488, L18
- Kalberla, P. M. W., Burton, W. B., Hartmann, D., et al. 2005, A&A, 440, 775
- Kallman, T., & Bautista, M. 2001, ApJS, 133, 221
- Kara, E., Fabian, A. C., Lohfink, A. M., et al. 2015, MNRAS, 449, 234
- Kara, E., Steiner, J. F., Fabian, A. C., et al. 2019, Natur, 565, 198
- Kawamuro, T., Negoro, H., Yoneyama, T., et al. 2018, ATel, 11399
- Kennea, J. A. 2017, ATel, 10731
- Kennea, J. A., Evans, P. A., Beardmore, A. P., et al. 2017, ATel, 10700
- King, A., & Lasota, J.-P. 2020, MNRAS, 494, 3611
- King, A., & Pounds, K. 2015, ARA&A, 53, 115
- King, A. L., Miller, J. M., Raymond, J., Reynolds, M. T., & Morningstar, W. 2015, ApJL, 813, L37
- King, A. L., Miller, J. M., Raymond, J., et al. 2012, ApJL, 746, L20
- King, A. L., Miller, J. M., Raymond, J., et al. 2013, ApJ, 762, 103
- King, A. L., Walton, D. J., Miller, J. M., et al. 2014, ApJL, 784, L2
- King, A. R., & Kolb, U. 1999, MNRAS, 305, 654
- King, A. R., Kolb, U., & Burderi, L. 1996, ApJL, 464, L127

- Kobayashi, K., Maruyama, W., Negoro, H., et al. 2018, ATel, 12320
- Kolehmainen, M., Done, C., & Díaz Trigo, M. 2014, MNRAS, 437, 316
- Komossa, S. 2008, RevMexAA Conf. Ser., 32, 86
- Komossa, S. 2015, JHEA, 7, 148
- Kong, A. K. H. 2019, ATel, 12504
- Kotani, T., Ebisawa, K., Dotani, T., et al. 2000, ApJ, 539, 413
- Krimm, H. A., Barthelmy, S. D., Baumgartner, W., et al. 2011, ATel, 3144
- Krimm, H. A., Holland, S. T., Corbet, R. H. D., et al. 2013, ApJS, 209, 14
- Krolik, J. H. 1998, Active Galactic Nuclei: From the Central Black Hole to the Galactic Environment (Princeton, NJ: Princeton Univ. Press)
- Krolik, J. H., & Hawley, J. F. 2002, ApJ, 573, 754
- Kubota, A., & Done, C. 2004, MNRAS, 353, 980
- Kuulkers, E., Lutovinov, A., Parmar, A., et al. 2003, ATel, 149
- Kuulkers, E., Wijnands, R., Belloni, T., et al. 1998, ApJ, 494, 753
- Kuulkers, E., Kouveliotou, C., Belloni, T., et al. 2013, A&A, 552, A32
- Lai, D. 2003, ApJL, 591, L119
- Laor, A. 1991, ApJ, 376, 90
- Leahy, D. A., Elsner, R. F., & Weisskopf, M. C. 1983, ApJ, 272, 256
- Lehmer, B. D., Alexander, D. M., Bauer, F. E., et al. 2010, ApJ, 724, 559
- Lehto, H. J. 1989, in Proc. ESLAB Symp., ed. J. Hunt & B. Bottrick (Paris : ESA), 499
- Lien, A. Y., Kennea, J. A., Barthelmy, S. D., et al. 2018, ATel, 11310
- Lightman, A. P., & Eardley, D. M. 1974, ApJL, 187, L1
- Lightman, A. P., & White, T. R. 1988, ApJ, 335, 57
- Lightman, A. P., & Zdziarski, A. A. 1987, ApJ, 319, 643
- Livio, M., Ogilvie, G. I., & Pringle, J. E. 1999, ApJ, 512, 100
- Lodato, G., & Price, D. J. 2010, MNRAS, 405, 1212
- Lu, J.-F., Lin, Y.-Q., & Gu, W.-M. 2004, ApJL, 602, L37

- Ludlam, R. M., Miller, J. M., Bachetti, M., et al. 2017, *ApJ*, 836, 140
- Ludlam, R. M., Miller, J. M., Barret, D., et al. 2019, *ApJ*, 873, 99
- Lyubarskii, Y. E. 1997, *MNRAS*, 292, 679
- Maccarone, T. J. 2003, *A&A*, 409, 697
- Madsen, K. K., Reynolds, S., Harrison, F., et al. 2015a, *ApJ*, 801, 66
- Madsen, K. K., Harrison, F. A., Markwardt, C. B., et al. 2015b, *ApJS*, 220, 8
- Magdziarz, P., & Zdziarski, A. A. 1995, *MNRAS*, 273, 837
- Makishima, K., Maejima, Y., Mitsuda, K., et al. 1986, *ApJ*, 308, 635
- Malzac, J. 2018, *NatAs*, 2, 623
- Malzac, J., Beloborodov, A. M., & Poutanen, J. 2001, *MNRAS*, 326, 417
- Margon, B., Ford, H. C., Grandi, S. A., & Stone, R. P. S. 1979, *ApJL*, 233, L63
- Markoff, S., Falcke, H., & Fender, R. 2001, *A&A*, 372, L25
- Markoff, S., Nowak, M. A., & Wilms, J. 2005, *ApJ*, 635, 1203
- Martocchia, A., & Matt, G. 1996, *MNRAS*, 282, L53
- Matsumoto, H., Tsuru, T. G., Koyama, K., et al. 2001, *ApJL*, 547, L25
- Matsuoka, M., Kawasaki, K., Ueno, S., et al. 2009, *PASJ*, 61, 999
- McClintock, J. E., Narayan, R., & Steiner, J. F. 2014, *SSRv*, 183, 295
- McClintock, J. E., & Remillard, R. A. 2006, in *Black hole Binaries*, ed. W. Lewin & M. van der Klis, Vol. 39 (Cambridge: Cambridge Univ. Press), 157
- McHardy, I. 2010, in *The Jet Paradigm: From Microquasars to Quasars*, ed. T. Belloni (Berlin: Springer), 203
- Mehdipour, M., Branduardi-Raymont, G., Kaastra, J. S., et al. 2011, *A&A*, 534, A39
- Mereminskiy, I. A., & Grebenev, S. A. 2017, *ATel*, 10734
- Merloni, A., Fabian, A. C., & Ross, R. R. 2000, *MNRAS*, 313, 193
- Meyer, F., Liu, B. F., & Meyer-Hofmeister, E. 2000, *A&A*, 361, 175
- Meyer, F., Liu, B. F., & Meyer-Hofmeister, E. 2007, *A&A*, 463, 1
- Meyer-Hofmeister, E., Liu, B. F., & Meyer, F. 2009, *A&A*, 508, 329

- Middleton, M., Done, C., Gierliński, M., & Davis, S. W. 2006, MNRAS, 373, 1004
- Middleton, M. J., Parker, M. L., Reynolds, C. S., Fabian, A. C., & Lohfink, A. M. 2016, MNRAS, 457, 1568
- Miller, J. M. 2007, ARA&A, 45, 441
- Miller, J. M., Fabian, A. C., Kaastra, J., et al. 2015a, ApJ, 814, 87
- Miller, J. M., Homan, J., Steeghs, D., et al. 2006a, ApJ, 653, 525
- Miller, J. M., Raymond, J., Reynolds, C. S., et al. 2008, ApJ, 680, 1359
- Miller, J. M., Reynolds, M., Kennea, J., King, A. L., & Tomsick, J. 2016a, ATel, 8742
- Miller, J. M., Zoghbi, A., Gandhi, P., & Paice, J. 2019, ATel, 13012
- Miller, J. M., Fabian, A. C., Wijnands, R., et al. 2002, ApJ, 578, 348
- Miller, J. M., Raymond, J., Homan, J., et al. 2006b, ApJ, 646, 394
- Miller, J. M., D'Ai, A., Bautz, M. W., et al. 2010, ApJ, 724, 1441
- Miller, J. M., Raymond, J., Fabian, A. C., et al. 2012, ApJL, 759, L6
- Miller, J. M., Parker, M. L., Fuerst, F., et al. 2013, ApJL, 775, L45
- Miller, J. M., Tomsick, J. A., Bachetti, M., et al. 2015b, ApJL, 799, L6
- Miller, J. M., Raymond, J., Fabian, A. C., et al. 2016b, ApJL, 821, L9
- Miller, J. M., Gendreau, K., Ludlam, R. M., et al. 2018, ApJL, 860, L28
- Miller, J. M., Zoghbi, A., Raymond, J., et al. 2020, ApJ, 904, 30
- Miller, L., Turner, T. J., & Reeves, J. N. 2008, A&A, 483, 437
- Miller, L., Turner, T. J., & Reeves, J. N. 2009, MNRAS, 399, L69
- Miller-Jones, J. C. A., Sivakoff, G. R., Altamirano, D., et al. 2012, MNRAS, 421, 468
- Miller-Jones, J. C. A., Tetarenko, A. J., Sivakoff, G. R., et al. 2019, Natur, 569, 374
- Miniutti, G., & Fabian, A. C. 2004, MNRAS, 349, 1435
- Miniutti, G., Fabian, A. C., Goyder, R., & Lasenby, A. N. 2003, MNRAS, 344, L22
- Miniutti, G., Fabian, A. C., & Miller, J. M. 2004, MNRAS, 351, 466
- Mirabel, I. F. 2006, Sci, 312, 1759

- Mirabel, I. F., Dhawan, V., Chaty, S., et al. 1998, *A&A*, 330, L9
- Mitsuda, K., Inoue, H., Koyama, K., et al. 1984, *PASJ*, 36, 741
- Miyamoto, S., Kimura, K., Kitamoto, S., Dotani, T., & Ebisawa, K. 1991, *ApJ*, 383, 784
- Miyamoto, S., Kitamoto, S., Iga, S., Hayashida, K., & Terada, K. 1994, *ApJ*, 435, 398
- Miyasaka, H., Tomsick, J. A., Xu, Y., & Harrison, F. A. 2018, *ATel*, 12340
- Miyoshi, M., Moran, J., Herrnstein, J., et al. 1995, *Natur*, 373, 127
- Motta, S., Belloni, T., & Homan, J. 2009, *MNRAS*, 400, 1603
- Motta, S., Homan, J., Muñoz Darias, T., et al. 2012, *MNRAS*, 427, 595
- Motta, S. E., Casella, P., Henze, M., et al. 2015, *MNRAS*, 447, 2059
- Motta, S. E., Franchini, A., Lodato, G., & Mastroserio, G. 2018, *MNRAS*, 473, 431
- Motta, S. E., Kajava, J. J. E., Sánchez-Fernández, C., Giustini, M., & Kuulkers, E. 2017, *MNRAS*, 468, 981
- Motta, S. E., Munoz-Darias, T., Sanna, A., et al. 2014, *MNRAS*, 439, L65
- Murphy, K. D., & Yaqoob, T. 2009, *MNRAS*, 397, 1549
- Nakahira, S., Negoro, H., Mihara, T., et al. 2017, *ATel*, 10729
- Nakahira, S., Shidatsu, M., Makishima, K., et al. 2018, *PASJ*, 70, 95
- Nandra, K., George, I. M., Mushotzky, R. F., Turner, T. J., & Yaqoob, T. 1997, *ApJ*, 477, 602
- Nandra, K., O'Neill, P. M., George, I. M., & Reeves, J. N. 2007, *MNRAS*, 382, 194
- Nandra, K., & Pounds, K. A. 1994, *MNRAS*, 268, 405
- Narayan, R., & McClintock, J. E. 2005, *ApJ*, 623, 1017
- Narayan, R., & McClintock, J. E. 2012, *MNRAS*, 419, L69
- Narayan, R., & Yi, I. 1995, *ApJ*, 452, 710
- Nardini, E., Reeves, J. N., Gofford, J., et al. 2015, *Sci*, 347, 860
- Nealon, R., Price, D. J., & Nixon, C. J. 2015, *MNRAS*, 448, 1526
- Negoro, H., Kawase, T., Sugizaki, M., et al. 2017, *ATel*, 10708
- Neilsen, J., & Lee, J. C. 2009, *Natur*, 458, 481

- Nespoli, E., Belloni, T., Homan, J., et al. 2003, *A&A*, 412, 235
- Netzer, H. 2015, *ARA&A*, 53, 365
- Nixon, C., King, A., Price, D., & Frank, J. 2012, *ApJL*, 757, L24
- Noda, H., & Done, C. 2018, *MNRAS*, 480, 3898
- Novikov, I. D., & Thorne, K. S. 1973, in *Black Holes (Les Astres Occlus)*, ed. C. DeWitt & B. DeWitt (New York: Gordon and Breach), 343
- Nowak, M. A. 2000, *MNRAS*, 318, 361
- Nowak, M. A., & Wagoner, R. V. 1995, *MNRAS*, 274, 37
- Padovani, P., Alexander, D. M., Assef, R. J., et al. 2017, *A&ARv*, 25, 2
- Page, M. J., Simpson, C., Mortlock, D. J., et al. 2014, *MNRAS*, 440, L91
- Pahari, M., Bhattacharyya, S., Yadav, J. S., & Pandey, S. K. 2012, *MNRAS*, 422, L87
- Paice, J. A., Gandhi, P., Shahbaz, T., et al. 2019, *MNRAS*, 490, L62
- Park, S. Q., Miller, J. M., McClintock, J. E., et al. 2004, *ApJ*, 610, 378
- Parker, M. L., Marinucci, A., Brenneman, L., et al. 2014, *MNRAS*, 437, 721
- Parker, M. L., Tomsick, J. A., Miller, J. M., et al. 2015, *ApJ*, 808, 9
- Parker, M. L., Tomsick, J. A., Kennea, J. A., et al. 2016, *ApJL*, 821, L6
- Parker, M. L., Pinto, C., Fabian, A. C., et al. 2017, *Natur*, 543, 83
- Parmar, A. N., White, N. E., Giommi, P., & Gottwald, M. 1986, *ApJ*, 308, 199
- Patrick, A. R., Reeves, J. N., Lobban, A. P., Porquet, D., & Markowitz, A. G. 2011, *MNRAS*, 416, 2725
- Patrick, A. R., Reeves, J. N., Porquet, D., et al. 2012, *MNRAS*, 426, 2522
- Penrose, R., & Floyd, R. M. 1971, *NatPhS*, 229, 177
- Pepe, C., Vila, G. S., & Romero, G. E. 2015, *A&A*, 584, A95
- Petrucci, P. O., Cabanac, C., Corbel, S., Koerding, E., & Fender, R. 2014, *A&A*, 564, A37
- Petrucci, P. O., Haardt, F., Maraschi, L., et al. 2001, *ApJ*, 556, 716
- Ponti, G., Fender, R. P., Begelman, M. C., et al. 2012, *MNRAS*, 422, L11
- Pooley, G. G., & Fender, R. P. 1997, *MNRAS*, 292, 925

- Pottschmidt, K., Wilms, J., Nowak, M. A., et al. 2003, *A&A*, 407, 1039
- Pounds, K. A., & King, A. R. 2013, *MNRAS*, 433, 1369
- Pounds, K. A., King, A. R., Page, K. L., & O'Brien, P. T. 2003, *MNRAS*, 346, 1025
- Pounds, K. A., Reeves, J. N., King, A. R., et al. 2003, *MNRAS*, 345, 705
- Poutanen, J., & Fabian, A. C. 1999, *MNRAS*, 306, L31
- Poutanen, J., & Svensson, R. 1996, *ApJ*, 470, 249
- Predehl, P., & Schmitt, J. H. M. M. 1995, *A&A*, 500, 459
- Priedhorsky, W. C., & Holt, S. S. 1987, *SSRv*, 45, 291
- Pringle, J. E. 1981, *ARA&A*, 19, 137
- Pringle, J. E. 1996, *MNRAS*, 281, 357
- Rao, A., & Vadawale, S. V. 2012, *ApJL*, 757, L12
- Rees, M. J. 1988, *Natur*, 333, 523
- Reis, R. C., Fabian, A. C., Ross, R. R., et al. 2008, *MNRAS*, 387, 1489
- Reis, R. C., Miller, J. M., King, A. L., & Reynolds, M. T. 2012, *ATel*, 4382
- Reis, R. C., Miller, J. M., Reynolds, M. T., et al. 2013, *ApJ*, 763, 48
- Remillard, R. A., & McClintock, J. E. 2006, *ARA&A*, 44, 49
- Reynolds, C. S. 2014, *SSRv*, 183, 277
- Reynolds, C. S. 2020, *arXiv:2011.08948*
- Reynolds, M. T., & Miller, J. M. 2013, *ApJ*, 769, 16
- Reynolds, M. T., Miller, J. M., Homan, J., & Miniutti, G. 2010, *ApJ*, 709, 358
- Ricci, C., Tazaki, F., Ueda, Y., et al. 2014, *ApJ*, 795, 147
- Ricci, C., Kara, E., Loewenstein, M., et al. 2020, *ApJL*, 898, L1
- Risaliti, G., Harrison, F. A., Madsen, K. K., et al. 2013, *Natur*, 494, 449
- Risaliti, G., Miniutti, G., Elvis, M., et al. 2009, *ApJ*, 696, 160
- Rivers, E., Markowitz, A., & Rothschild, R. 2013, *ApJ*, 772, 114
- Rodriguez, J., Corbel, S., Caballero, I., et al. 2011, *A&A*, 533, L4
- Rodriguez, J., Durouchoux, P., Mirabel, I. F., et al. 2002, *A&A*, 386, 271

- Ross, R. R., & Fabian, A. C. 2005, MNRAS, 358, 211
- Ross, R. R., & Fabian, A. C. 2007, MNRAS, 381, 1697
- Rossi, S., Homan, J., Miller, J. M., & Belloni, T. 2005, MNRAS, 360, 763
- Rothberg, B., Fischer, J., Rodrigues, M., & Sanders, D. B. 2013, ApJ, 767, 72
- Ruan, J. J., Anderson, S. F., Eracleous, M., et al. 2019, ApJ, 883, 76
- Rupke, D. S., Veilleux, S., & Sanders, D. B. 2005, ApJ, 632, 751
- Rupke, D. S. N., & Veilleux, S. 2015, ApJ, 801, 126
- Rupke, D. S. N., Veilleux, S., & Baker, A. J. 2008, ApJ, 674, 172
- Russell, T. D., Miller-Jones, J. C. A., Sivakoff, G. R., & Tetarenko, A. J. 2018, ATel, 11322
- Russell, T. D., Miller-Jones, J. C. A., Sivakoff, G. R., Tetarenko, A. J., & Jacpot Xrb Collaboration. 2017, ATel, 10711
- Russell, T. D., van den Eijnden, J., & Degenaar, N. 2019, ATel, 12396
- Rykoff, E. S., Miller, J. M., Steeghs, D., & Torres, M. A. P. 2007, ApJ, 666, 1129
- Salvesen, G., Miller, J. M., Reis, R. C., & Begelman, M. C. 2013, MNRAS, 431, 3510
- Sánchez-Fernández, C., Kajava, J. J. E., Motta, S. E., & Kuulkers, E. 2017, A&A, 602, A40
- Sanders, D. B., Soifer, B. T., Elias, J. H., et al. 1988, ApJ, 325, 74
- Scaringi, S., & ASTR211 Students. 2017, ATel, 10702
- Schandl, S., & Meyer, F. 1994, A&A, 289, 149
- Severgnini, P., Risaliti, G., Marconi, A., Maiolino, R., & Salvati, M. 2001, A&A, 368, 44
- Shakura, N. I., & Sunyaev, R. A. 1973, A&A, 500, 33
- Shakura, N. I., & Sunyaev, R. A. 1976, MNRAS, 175, 613
- Shapiro, S. L., Lightman, A. P., & Eardley, D. M. 1976, ApJ, 204, 187
- Shemmer, O., Brandt, W. N., Netzer, H., Maiolino, R., & Kaspi, S. 2008, A&A, 682, 81
- Shidatsu, M., Nakahira, S., Murata, K. L., et al. 2019, ApJ, 874, 183
- Shidatsu, M., Ueda, Y., Nakahira, S., et al. 2013, ApJ, 779, 26

- Shields, G. A., McKee, C. F., Lin, D. N. C., & Begelman, M. C. 1986, *ApJ*, 306, 90
- Shimura, T., & Takahara, F. 1995, *ApJ*, 445, 780
- Smale, A. P., Church, M. J., & Bałucińska-Church, M. 2002, *ApJ*, 581, 1286
- Smith, R. N., Tombesi, F., Veilleux, S., Lohfink, A. M., & Luminari, A. 2019, *ApJ*, 887, 69
- Soleri, P., Belloni, T., & Casella, P. 2008, *MNRAS*, 383, 1089
- Sriram, K., Rao, A. R., & Choi, C. S. 2013, *ApJ*, 775, 28
- Sriram, K., Rao, A. R., & Choi, C. S. 2016, *ApJ*, 823, 67
- Steiner, J. F., García, J. A., Eikmann, W., et al. 2017, *ApJ*, 836, 119
- Steiner, J. F., McClintock, J. E., & Narayan, R. 2013, *ApJ*, 762, 104
- Steiner, J. F., McClintock, J. E., Remillard, R. A., et al. 2010, *ApJL*, 718, L117
- Steiner, J. F., McClintock, J. E., Remillard, R. A., Narayan, R., & Gou, L. 2009a, *ApJL*, 701, L83
- Steiner, J. F., Narayan, R., McClintock, J. E., & Ebisawa, K. 2009b, *PASP*, 121, 1279
- Steiner, J. F., Remillard, R. A., García, J. A., & McClintock, J. E. 2016, *ApJL*, 829, L22
- Stella, L., & Angelini, L. 1992, in *ASP Conf. Ser. 25, Astronomical Data Analysis Software and Systems I*, ed. D. M. Worrall, C. Biemesderfer, & J. Barnes (San Francisco, CA: ASP), 103
- Stella, L., & Vietri, M. 1998, *ApJL*, 492, L59
- Stella, L., Vietri, M., & Morsink, S. M. 1999, *ApJL*, 524, L63
- Strateva, I. V., Strauss, M. A., Hao, L., et al. 2003, *AJ*, 126, 1720
- Straub, O., Bursa, M., Sądowski, A., et al. 2011, *A&A*, 533, A67
- Strüder, L., Briel, U., Dennerl, K., et al. 2001, *A&A*, 365, L18
- Taam, R. E., Liu, B. F., Yuan, W., & Qiao, E. 2012, *ApJ*, 759, 65
- Takeuchi, M., & Mineshige, S. 1998, *ApJL*, 505, L19
- Takizawa, M., Dotani, T., Mitsuda, K., et al. 1997, *ApJ*, 489, 272
- Tamura, M., Kubota, A., Yamada, S., et al. 2012, *ApJ*, 753, 65
- Tan, Y., Wang, J. X., Shu, X. W., & Zhou, Y. 2012, *ApJL*, 747, L11

- Tanaka, Y., & Shibazaki, N. 1996, *ARA&A*, 34, 607
- Tanaka, Y., Nandra, K., Fabian, A. C., et al. 1995, *Natur*, 375, 659
- Teng, S. H., Rigby, J. R., Stern, D., et al. 2015, *ApJ*, 814, 56
- Teng, S. H., Veilleux, S., Anabuki, N., et al. 2009, *ApJ*, 691, 261
- Teng, S. H., Veilleux, S., & Baker, A. J. 2013, *ApJ*, 765, 95
- Terrell, N. James, J. 1972, *ApJL*, 174, L35
- Tetarenko, B. E., Sivakoff, G. R., Heinke, C. O., & Gladstone, J. C. 2016, *ApJS*, 222, 15
- Thorne, K. S. 1974, *ApJ*, 191, 507
- Titarchuk, L., & Fiorito, R. 2004, *ApJ*, 612, 988
- Tombesi, F. 2016, *AN*, 337, 410
- Tombesi, F., Cappi, M., Reeves, J. N., et al. 2013, *MNRAS*, 430, 1102
- Tombesi, F., Cappi, M., Reeves, J. N., et al. 2011, *ApJ*, 742, 44
- Tombesi, F., Cappi, M., Reeves, J. N., et al. 2010, *A&A*, 521, A57
- Tombesi, F., Meléndez, M., Veilleux, S., et al. 2015, *Natur*, 519, 436
- Tomsick, J. A., Lapshov, I., & Kaaret, P. 1998, *ApJ*, 494, 747
- Tomsick, J. A., Yamaoka, K., Corbel, S., et al. 2009, *ApJL*, 707, L87
- Tomsick, J. A., Nowak, M. A., Parker, M., et al. 2014, *ApJ*, 780, 78
- Tomsick, J. A., Parker, M. L., García, J. A., et al. 2018, *ApJ*, 855, 3
- Torrejón, J. M., Schulz, N. S., Nowak, M. A., & Kallman, T. R. 2010, *ApJ*, 715, 947
- Torres, M. A. P., Casares, J., Jiménez-Ibarra, F., et al. 2019, *ApJL*, 882, L21
- Tortosa, A., Marinucci, A., Matt, G., et al. 2017, *MNRAS*, 466, 4193
- Tremaine, S., Gebhardt, K., Bender, R., et al. 2002, *ApJ*, 574, 740
- Tucker, M. A., Shappee, B. J., Holoién, T. W. S., et al. 2018, *ApJL*, 867, L9
- Turner, M. J. L., Abbey, A., Arnaud, M., et al. 2001, *A&A*, 365, L27
- Tzanavaris, P., & Yaqoob, T. 2018, *ApJ*, 855, 25
- U, V., Sanders, D. B., Mazzarella, J. M., et al. 2012, *ApJS*, 203, 9

- Ueda, Y., Inoue, H., Tanaka, Y., et al. 1998, *ApJ*, 492, 782
- Ueda, Y., Yamaoka, K., Sánchez-Fernández, C., et al. 2002, *ApJ*, 571, 918
- Ueda, Y., Honda, K., Takahashi, H., et al. 2010, *ApJ*, 713, 257
- Ulrich, M.-H., Maraschi, L., & Urry, C. M. 1997, *ARA&A*, 35, 445
- Ursini, F., Boissay, R., Petrucci, P.-O., et al. 2015, *A&A*, 577, A38
- van der Klis, M. 1989, *ARA&A*, 27, 517
- van der Klis, M. 2006, in *Compact Stellar X-ray Sources*, ed. W. H. G. Lewin & M. van der Klis (Cambridge: Cambridge Univ. Press), 39
- van Paradijs, J. 1998, in *The Many Faces of Neutron Stars*, ed. R. Buccheri, J. van Paradijs, & M. A. Alpar (Dordrecht: Kluwer Academic Publisher), 279
- Vaughan, S., Fabian, A. C., Ballantyne, D. R., et al. 2004, *MNRAS*, 351, 193
- Veilleux, S., Kim, D.-C., Sanders, D. B., Mazzarella, J. M., & Soifer, B. T. 1995, *ApJS*, 98, 171
- Veilleux, S., Meléndez, M., Sturm, E., et al. 2013, *ApJ*, 776, 27
- Veilleux, S., Sanders, D. B., & Kim, D.-C. 1999, *ApJ*, 522, 139
- Veledina, A., Poutanen, J., & Ingram, A. 2013, *ApJ*, 778, 165
- Verner, D. A., Ferland, G. J., Korista, K. T., & Yakovlev, D. G. 1996, *ApJ*, 465, 487
- Véron-Cetty, M.-P., & Véron, P. 2006, *A&A*, 455, 773
- Wada, K. 2012, *ApJ*, 758, 66
- Walton, D. J., Nardini, E., Fabian, A. C., Gallo, L. C., & Reis, R. C. 2013, *MNRAS*, 428, 2901
- Walton, D. J., Reis, R. C., Cackett, E. M., Fabian, A. C., & Miller, J. M. 2012, *MNRAS*, 422, 2510
- Walton, D. J., Risaliti, G., Harrison, F. A., et al. 2014, *ApJ*, 788, 76
- Walton, D. J., Tomsick, J. A., Madsen, K. K., et al. 2016, *ApJ*, 826, 87
- Walton, D. J., Mooley, K., King, A. L., et al. 2017, *ApJ*, 839, 110
- Westmoquette, M. S., Clements, D. L., Bendo, G. J., & Khan, S. A. 2012, *MNRAS*, 424, 416
- White, N. E., & Swank, J. H. 1982, *ApJL*, 253, L61
- Wijnands, R., Homan, J., & van der Klis, M. 1999, *ApJL*, 526, L33

- Wijnands, R., & van der Klis, M. 1999, *ApJ*, 514, 939
- Wilkins, D. R., & Fabian, A. C. 2012, *MNRAS*, 424, 1284
- Wilkins, D. R., & Gallo, L. C. 2015, *MNRAS*, 448, 703
- Wilms, J., Allen, A., & McCray, R. 2000, *ApJ*, 542, 914
- Winter, L. M., Mushotzky, R. F., Reynolds, C. S., & Tueller, J. 2009, *ApJ*, 680, 1322
- Xu, Y., Harrison, F., & Tomsick, J. 2019, *ATel*, 13025
- Xu, Y., Kennea, J. A., Harrison, F. A., & Forster, K. 2018a, *ATel*, 11321
- Xu, Y., García, J. A., Fürst, F., et al. 2017, *ApJ*, 851, 103
- Xu, Y., Harrison, F. A., García, J. A., et al. 2018b, *ApJL*, 852, L34
- Xu, Y., Harrison, F. A., Kennea, J. A., et al. 2018c, *ApJ*, 865, 18
- Young, S., Hough, J. H., Efstathiou, A., et al. 1996, *MNRAS*, 281, 1206
- Yu, W., & Yan, Z. 2009, *ApJ*, 701, 1940
- Yu, W., Zhang, J., Yan, Z., Wang, X., & Bai, J. 2018, *ATel*, 11510
- Yuan, F., & Narayan, R. 2004, *ApJ*, 612, 724
- Yuan, F., & Narayan, R. 2014, *ARA&A*, 52, 529
- Zdziarski, A. A., Johnson, W. N., & Magdziarz, P. 1996, *MNRAS*, 283, 193
- Zdziarski, A. A., Lubiński, P., Gilfanov, M., & Revnivtsev, M. 2003, *MNRAS*, 342, 355
- Zdziarski, A. A., Lubiński, P., & Smith, D. A. 1999, *MNRAS*, 303, L11
- Zhang, S. N., Cui, W., & Chen, W. 1997, *ApJL*, 482, L155
- Życki, P. T., Done, C., & Smith, D. A. 1999, *MNRAS*, 309, 561